The Interactions and Reactions of Atoms and Molecules on the Surfaces of Model Interstellar Dust Grains

A thesis submitted for the degree of Doctor of Philosophy

Helen Jessica Kimber

Department of Chemistry

University College London

2016

-I, Helen Jessica Kimber, confirm that the work presented in this thesis is my own. Where information has been derived from other sources, I confirm that this has been indicated in the thesis.

Signed,

Abstract

The elemental composition of the known universe comprises almost exclusively light atoms (~99.9% hydrogen and helium). However, to date, close to 200 different molecules have been detected in the interstellar medium (ISM) where their distribution is far from uniform. The vast majority of these molecules are contained within vast clouds of gas and dust referred to as interstellar clouds. Within these interstellar clouds, many of the molecules present are formed *via* gas-phase ion-neutral reactions. However, there are several molecules for which known gas-phase kinetics cannot account for observed gas-phase abundances. As a result, reactions occurring on the surface of interstellar dust grains are invoked to account for the observed abundances of some of these molecules. This thesis presents results of experimental investigations into the interaction and reactions of atoms and molecules on the surface of model interstellar dust grains.

Chapters three and four present results for the reaction of (^{3}P)O on molecular ices. Specifically, the reaction of (^{3}P)O and propyne or acrylonitrile. After a one hour dosing period, temperature programmed desorption (TPD), coupled with time-of-flight mass spectrometry (TOFMS), are used to identify (^{3}P)O addition products. Each reaction is studied at a series of fixed surface temperatures between 15 K and 100 K and a kinetic model is used to determine desorption energies of reactants and reaction probabilities of reaction. In the case of the reaction of (^{3}P)O and propyne two products with the empirical formulae C_3H_4O and $C_3H_4O_2$ are observed. Transmission infrared spectroscopy (TIR) identified two isomers of the single addition product (propenal and methyl ketene) whilst only one isomer of the double addition product (glycidaldehyde) was observed. Furthermore, the TIR data reveals a product which remains on the surface under vacuum at room temperature which is assigned to the polymer β-propiolactone. In the case of the surface reaction of O(^{3}P) and acrylonitrile (C_3H_3N) on a acrylonitrile/O_2 matrix a single addition product is identified as cyanoethylene oxide.

Finally, Chapter five presents results for the desorption characteristics of O_2 and CO_2 from amorphous porous fullerene-like carbonaceous dust grains produced in laser ablation experiments. In these experiments O_2 and CO_2 are found to have significantly larger binding energies to the surface when compared to the traditional carbonaceous dust grain analogue graphite. The effect of these large binding energies on the desorption characteristics under interstellar conditions is modelled.

Acknowledgements

Firstly I would like to thank my supervisor Professor Stephen Price. His support and encouragement throughout my PhD has been paramount especially whilst writing this thesis.

I am also grateful to the present and past members of the Price group who have allowed me to discuss, sometimes at great lengths, the results presented in this thesis. In particular Felicity Gossan, Catherine Higgins, Dr Courtney Ennis and Dr Michael Parkes.

During my PhD I visited the Friedrich-Schiller-University in Jena to collaborate with the Jäger group. I am particularly grateful to Dr Cornelia Jäger, Dr Daniele Fulvio and Hagen Walter for their help performing these experiments.

I am also grateful to my family and friends who have listened to, and supported, me throughout my PhD. In particular my mum, Julia Callender, and my sister, Kristy Kimber. Finally, I would like to thank my husband Hamish Mcdougall, who has taken the brunt of my thesis writing, I intend to be a more present wife from now on. Thank you for being understanding.

List of Publications

Listed below are previous and expected future publications of the work presented in this thesis.

Single and double addition of oxygen atoms to propyne on surfaces at low temperatures

H. J. Kimber, C. P. Ennis and S. D. Price, *Faraday Discuss.*, 2014, **168**, 167-184.

Addition of oxygen atoms to acrylonitrile on surfaces at low temperatures does not lead to saturation

In preparation

Contributions to interstellar dust grains from the addition of oxygen atoms to propyne on surfaces at low temperatures

In preparation

The desorption of O_2 and CO_2 from fullerene-like amorphous porous carbonaceous interstellar dust grain analogues

In preparation

Table of Contents

List of Acronyms and Abbreviations

AGB	Asymptotic Giant Branch
APCDG	Amorphous Porous Carbonaceous Dust Grains
ASW	Amorphous Solid Water
B3LYP	Becke's three-parameter nonlocal exchange functional with the nonlocal correlation functional of Lee, Yang, Parr
ER	Eley - Rideal
FESEM	Field Emission Scanning Electron Microscopy
FUV	Far Ultra Violet
HOPG	Highly Oriented Pyrolytic Graphite
HRTEM	High Resolution Tunnelling Electron Microscopy
HV	High Vacuum
IR	Infrared
ISC	Intersystem Crossing
ISM	Interstellar Medium
LH	Langmuir-Hinshelwood
MCP	Microchannel Plate
ML	Monolayer (1×10^{15} molecules cm^{-2})
m/z	mass-to-charge ratio
PIC	Partial Ionisation Cross Section
PTFE	Polytetrafluoroethylene
QMS	Quadrupole Mass Spectrometry
RAIRS	Reflection-Absorption IR Spectroscopy
REMPI	Resonance Enhanced Multi-Photon Ionisation
SEM	Secondary Electron Multiplier
SWCNT	Single Walled Carbon Nanotubes
TDC	Time to Digital Converter
TIR	Transmission Infrared Spectroscopy
TMP	Turbomolecular Pump
TOF	Time of Flight
TOFMS	Time of Flight Mass Spectrometry
TP-DED	Temperature Programmed During-Exposure Desorption
TPD	Temperature Programmed Desorption
UHV	Ultra-High Vacua
UMIST	University of Manchester Institute of Science and Technology

List of Figures

List of Tables

Chapter 1 – Introduction

1.1 Overview

The space in between stars is called the interstellar medium (ISM) and these regions of space represent the emptiest areas of the known universe. In the ISM pressures and temperatures are extremely low and so molecular synthesis is expected to be limited. Furthermore, destructive energetic light from surrounding stars is likely to result in high rates of molecular dissociation in these regions. It is therefore tempting to assume that the chemistry of the ISM is non-existent. However, the detection of approximately two hundred molecular species in the ISM has provided overwhelming evidence that these assumptions are incorrect.[1] A large proportion of these interstellar molecules are contained within vast clouds of gas and dust. These relatively dense regions of the ISM are referred to as interstellar clouds. The penetration depth of destructive light, from surrounding stars, is often smaller than the radius of these clouds. The photons are therefore completely absorbed by the molecules on the outer edges of these clouds and so do not penetrate to their centre. As a result, gas and dust temperatures in the dense clouds are reduced to approximately 10 K and molecular lifetimes are extended when compared to other regions of the ISM. The cold gas also accretes onto the surface of the dust grains building up icy mantles. These mantles provide a meeting ground for reactive species and facilitate reactions which, ordinarily, would require a third body to carry away any excess energy. Over the lifetime of an interstellar cloud these extended molecular lifetimes, at the cloud's centre, result in an increase in the cloud's density with respect to other regions in the ISM. Once a cloud reaches a critical density, gravity can act on the cold gas and dust causing it to contract. The contraction increases the pressure of the gas and therefore the cloud's temperature rises. For further contraction to occur the molecules present are essential for irradiating away the thermal energy that builds up during the gravitational collapse. The collapsing mass is called a protostar and can be identified in the ISM *via* the IR radiation emitted by the molecules present. As further contraction of the protostar occurs, the temperature increases and molecules eventually dissociate into atomic species which provide fuel for the star. Once the temperature reaches approximately four million kelvin, atomic nucleosynthesis begins and the star is born. The star converts the light elements present into heavier elements *via* nuclear fusion. Once the star has burnt all of its fuel its fate is dependent on its solar mass. Massive stars result in Red Super Giants which undergo supernova explosions. Supernova explosions disperse the atoms produced during nucleosynthesis across the interstellar medium enriching the ISMs elemental composition.

The motivation for studying molecular formation in the interstellar medium is two-fold. Firstly, molecular formation pathways can be used in astrochemical models to predict the rate of star formation depending upon initial interstellar cloud conditions. Secondly, since the matter present

in interstellar clouds aggregates around small stars to form planets, it is possible that prebiotic molecules essential for life have interstellar origins. However, the formation pathways for many molecules in the interstellar medium are still unknown. It is the aim of a laboratory astrochemist to study factors effecting molecular synthesis under astronomical conditions. The insight of a laboratory astrochemist can then be used by modellers to predict star and planetary formation. This thesis presents studies of the interactions and reactions of atoms and molecules on the surfaces of model interstellar dust grains. In particular, the surface reactions of oxygen atoms with simple unsaturated organic species and the thermal desorption of small molecules from amorphous porous dust grains. This Chapter will begin by describing the structure of the interstellar medium. This description of the ISM will be followed by a detailed discussion of the laboratory work that has advanced our understanding of the complex network of thermal surface chemistry at play on interstellar ices. The discussion of previous laboratory studies places the results presented in this thesis into context within the literature.

1.2 A Brief Chemical History of the Universe

When Edwin Hubble gazed into the cosmos he discovered that there were not only stars but entire galaxies outside of the Milky Way. Furthermore, it appeared that these galaxies were moving away from one another. He concluded that the universe is expanding and so at some point in the past the universe was smaller. It can therefore be inferred that the universe began life as a singularity. A singularity is a dimensionless object with infinite energy. It is thought that the universe came into existence from this singularity in a colossal explosion of energy that gave birth to space and time. This event is called the 'Standard Big Bang' and this model is successful in accounting for elemental abundances and cosmic background radiation. At $t = 10^{-35}$ s after the Big Bang, the universe had cooled by a factor of 10,000 to 10^{28} K. At this temperature the first building blocks of atoms, quarks, came into existence. At $t = 10^{-5}$ s a quark-hadron transition is believed to have occurred.[3] In this phase change the quarks became bound by the strong nuclear force, through gluons, to form hadrons (protons and neutrons).[4] At around the same time leptons came into existence, and so the building blocks for atoms had been born. Chemically speaking the universe consisted of ionised hydrogen atoms and free electrons.

A few minutes after the big bang, the universe underwent a brief period of nucleosynthesis in which the protons and neutrons combined to form nuclei.[5, 6] Nucleosynthesis requires high pressures and since the universe had vastly expanded the pressure was only sufficient to form nuclei with an atomic mass of eight and below: only hydrogen (H), deuterium (D), tritium (T) helium (He) and lithium (Li) nuclei were produced. The relative abundances of He and Li were 0.1 and 10^{-10} respectively when compared to hydrogen.[7] It was not until the universe was 10,000 years old and had cooled to approximately 4000 K that nuclei and electrons combined to form the

first atoms. This period is often called the recombination era, and represents the transition from an ionised opaque universe, in which matter and radiation were strongly coupled, to a transparent universe in which the two are decoupled.[7] However, when an electron and a nuclei combine a photon is emitted which can ionise an electron from another nuclei and so no net recombination occurs. For net recombination to occur, a single recombination event must result in an atom in an excited state that then 'cascades down'. The cascade relaxation process must occur in two or more steps and so emit two, or more, lower energy photons. The photons emitted do not have sufficient energy to ionise an electron bound to a hydrogen nuclei, this process is called B recombination.[7] The recombination of the nuclei and electrons occurred in order of their ionisation potentials. The first bound electrons occurred in the recombination reaction of Li^{3+} and an electron to form Li^{2+}. The first neutral atom formed was helium arising from the recombination of an electron with He^{+}.[7]

After this period of recombination, the only elements available for molecular synthesis were hydrogen, helium and lithium. Hydrogen was by far the most abundant atom and so one might suggest molecular synthesis would occur *via* the combination of two hydrogen atoms to form H_2. When two H atoms combine 4.5 eV of energy is released upon bond formation. For the resulting molecule to be stable this energy must be irradiated away sufficiently quickly for the molecule to be trapped in its potential well. However, since molecular hydrogen does not have a dipole moment, it is inefficient at radiating away this excess energy and so formation of H_2 by radiative association is very slow. At ambient pressures, three-body interactions facilitate reactions which produce molecules without dipole moments, since the third body can carry away the excess energy. However, in the interstellar medium three-body interactions are not possible in the gas-phase due to the low number densities. Hence, the first pathway that produced a significant quantity of molecular hydrogen is believed to have been catalysed by helium atoms.[7]

$$H^+ + He \rightarrow HeH^+ + h\nu \quad (1.2.1)$$

$$HeH^+ + H \rightarrow H_2^+ + He \quad (1.2.2)$$

$$H_2^+ + H \rightarrow H_2 + H^+ \quad (1.2.3)$$

However, most of the H_2 formed in this way would have been quickly destroyed by cosmic background radiation.[7] Later, after further cooling, the reactions believed responsible for the creation of molecular hydrogen are catalysed by electrons or protons:

$$H + e^- \rightarrow H^- + h\nu \quad (1.2.4)$$

$$H^- + H \rightarrow H_2 + e^- \quad (1.2.5)$$

and

$$H + H^+ \rightarrow H_2^+ \quad (1.2.6)$$

$$H_2^+ + H \rightarrow H_2 + H^+ \quad (1.2.7)$$

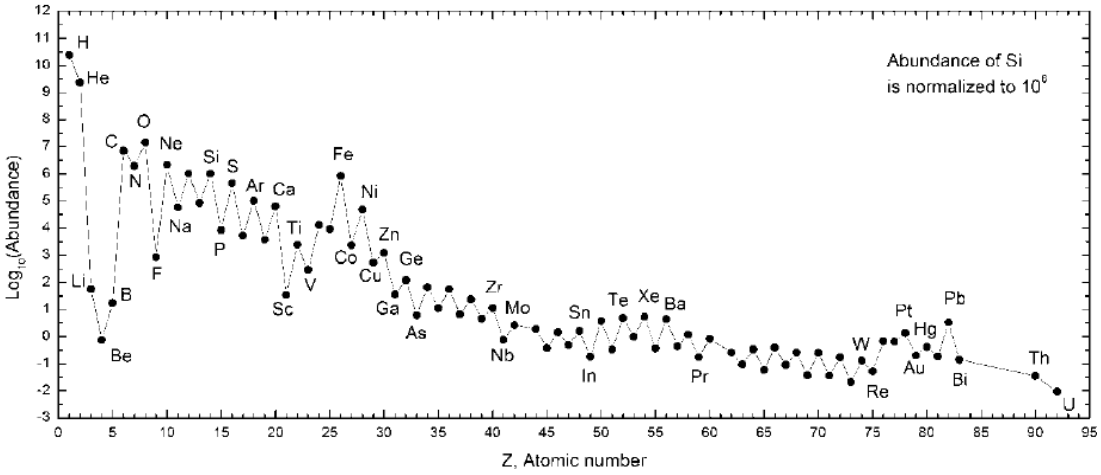

Figure 1.2.1: The abundances of the elements in the Solar System (taken from reference 2).

The next milestone for the universe was the formation of stars. Stars start to form when matter becomes dense enough for it to start collapsing under its own gravitational field. When the centre of the collapsing mass reaches a critical density, nuclear fusion begins and a star is born. A star can only form if the kinetic energy gained by the gravitational attraction of matter can be irradiated away.[7] Atoms can act as a cooling agent when heated to excite a ground state electron to a higher energy orbital. The promoted electron then relaxes to lower levels (sometimes in stages) emitting photon(s). In the case of hydrogen, this cooling by the available atoms cannot occur below 8000 K, since below this temperature there is not enough thermal energy to excite ground state electrons to the first available excited state (2s). For further cooling to occur, molecular vibrations and rotations are needed to radiate away the heat. Vibrational and rotational excited energy levels lie at lower energies than the atomic electronic excitation energies. Hence, these vibrational and rotational excited states can be thermally excited at lower temperatures. The radiative emission of these states can provide cooling at lower temperatures than atomic excitations. As the abundance of molecules increased in the universe, their ability to radiate away energy allowed gravitational collapse to occur which facilitated star formation. Stars synthesise elements, with atomic numbers up to and including iron, *via* nucleosynthesis. Nucleosynthesis is an exothermic reaction and prevents the star from collapsing under its own gravitational field. In the case of stars larger than our sun, once the available hydrogen has burnt the star will enter a supernova phase. During the supernova phase nucleosynthesis for atoms heavier than iron will occur.[8] This process is endothermic and so leads to gravitational collapse and the end of a star's life. The gravitational collapse of the star leads to a supernova explosion which distributes the products of nuclear synthesis throughout the ISM. Stars larger than our sun therefore increase the elemental variety in the ISM. This increased elemental variety increases the range of molecular species that can be formed. More complex molecules are more efficient at irradiating away energy and so star formation becomes more efficient. However, despite all the stars that have existed since the

formation of the universe 13.77 billion years ago, the universe is still composed of 99% hydrogen and helium. The current elemental composition of the universe can be seen in Figure 1.2.1.

1.3 Interstellar Clouds

The vast majority of the molecules present in the interstellar medium are contained within interstellar clouds. These clouds are composed of gas and dust and can measure several light years in diameter. The gas is 99.9 % hydrogen and helium with trace amounts of heavier atoms. Molecular hydrogen is by far the most abundant gas-phase molecular species, followed by carbon monoxide which has an abundance of 1×10^{-5} relative to H_2.[9] Interstellar clouds are broadly categorised into two types, depending upon their atomic and molecular number densities. Diffuse clouds have typical number densities of 10^7-10^9 m^{-3}, gas temperatures of approximately 100 K and dust temperatures of 10 K.[10] Dense clouds are characterised by higher number densities of 10^9-10^{10} m^{-3}, which are comparable to the best ultra-high vacua (UHV) available on Earth (10^{-14} Torr). The relatively low number density in diffuse clouds allows UV photons from surrounding stars to penetrate the entire cloud resulting in high rates of molecular dissociation. In dense clouds where molecular densities are higher, the UV photons are completely absorbed by molecules on the edges of the cloud. The dense clouds are said to be self-sheilding.[10] The lack of photons at the centre of dense interstellar clouds results in extended molecular lifetimes and reduced gas temperatures, when compared to diffuse clouds. As a result dense clouds contain a much larger proportion of the complex molecules observed in the interstellar medium than diffuse clouds.[10]

1.4 Interstellar Dust

In 1784 William Herchel observed dark patches in the night sky (Figure 1.4.1). He had made the first observation of interstellar clouds although he incorrectly identified them as empty starless regions of space. It was not until Trumpler's investigations in 1930 that these dark patches were identified as dust clouds containing particles with a diameter comparable to the wavelength of visible light.[11] The dust clouds cause Rayleigh scattering of the visible light from the stars behind the cloud. As a result, when the clouds are observed using the visible region of the spectrum the clouds appear to be empty regions of space. The stars obscured by the dust cloud can be observed using the infrared region of the electromagnetic spectrum, light which is not scattered by the dust particles (Figure 1.4.2). Trumpler observed discrepancies between the angular distance and the luminosity distance of stars at long distances (Figure 1.4.3). The luminosity distance is defined as the relationship between the absolute magnitude and apparent magnitude of an astronomical

Figure 1.4.1: The central area of globule B68 in a colour composite of visible and near-infrared region (taken from reference 12).

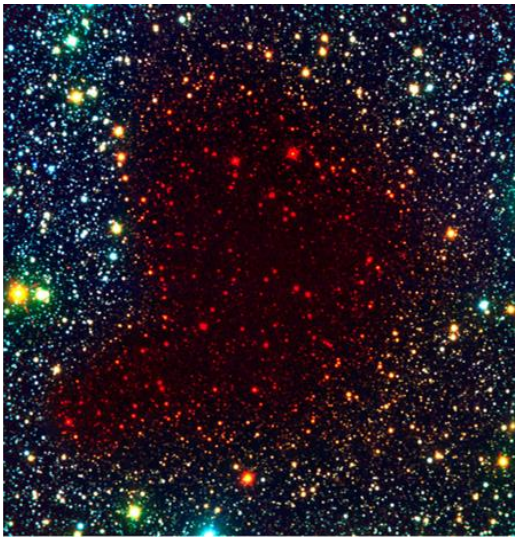

Figure 1.4.1: A false-colour composite based on a visible (here rendered as blue), a near-infrared (green) and an infrared (red) (taken from reference 13).

object. The angular distance is the distance calculated using the angle between two objects as perceived by an observer. As an observer's distance from a light emitting object increases the luminosity distance and the angular distance should increase linearly. From Figure 1.4.2 it can be seen that as the luminosity distance increases the angular distance does not increase by the same amount. It was concluded that the light travelling from more distant stars undergoes more extinction than light travelling from closer stars. This extinction is believed to be caused by areas of space that contained dust grains which scatter the light.

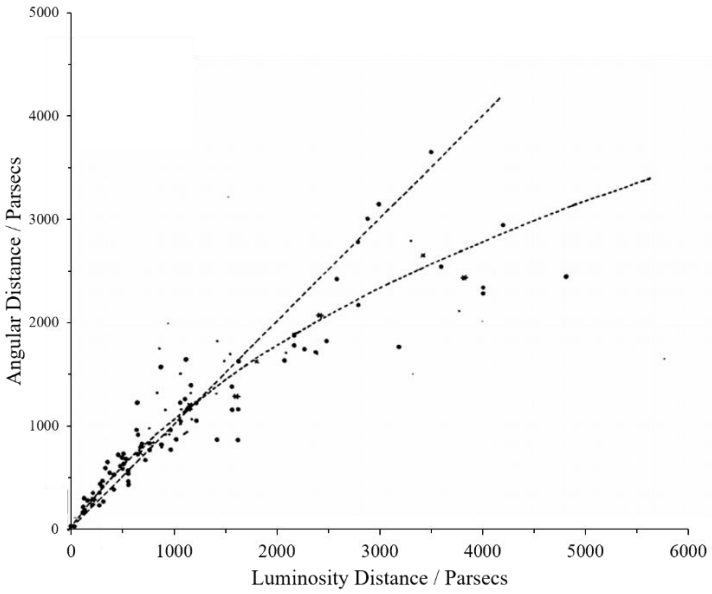

Figure 1.4.3: Trumpler's evidence for the discrepancy between the angular distance and the luminosity distance at long distances (taken from reference 11).

Further evidence for dust grains can be seen when the inverse wavelength of starlight is plotted against the extinction of the starlight (Figure 1.4.4). Extinction curves along particular lines of sight can vary significantly but do share some key features. The inverse of the wavelength is roughly proportional to the extinction with a pronounced bump centred around 2175 Å. The proportionality of the inverse of the wavelength to the extinction is characteristic of light scattered by particles which have a radius similar to the wavelength of the light.[9] Early models suggested the profile of the extinction curve could be due to a mixture of graphite and silicate dust particles.[14] The proportional behaviour is attributed to the silicate dust and the bump to the graphite dust.

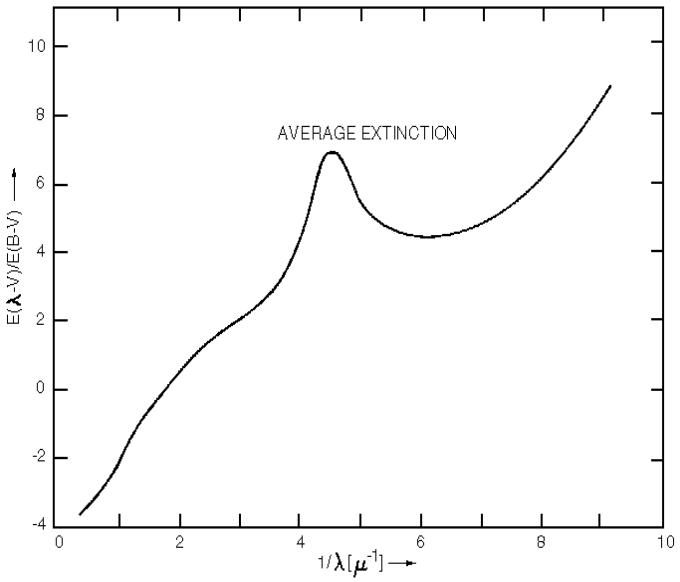

Figure 1.4.4: The mean for the UV extinction curve of Bless and Savage (taken from reference 15).

There are several more indirect pieces of evidence for interstellar dust grains. The first of which is the observed depletion of elements in the gas-phase. Estimations of elemental abundances from stellar nuclear fusion predict larger quantities of some elements than are observed in the gas-phase in the ISM. Furthermore, the depletion seems to be correlated to the condensation temperatures of the elements. It is therefore believed that these depleted elements are present in the solid phase in the interstellar medium as dust grains. Particularly high depletions are observed for silicon, oxygen, carbon and iron. A second indirect piece of evidence for dust grains involves the diffuse light in the interstellar medium. The diffuse light does not appear to originate from one source but rather across the entire night sky. This diffuse light can arise from the scattering of starlight. However, H atoms dominate the gas-phase but their cross section for scattering starlight is much too low to account for the diffuse light observed. It is therefore predicted that dust grains are responsible for this Rayleigh scattering of starlight. Another feature of the light in the night sky, that supports the hypothesis of dust grains in the ISM, is the presence of reflection nebula. Reflection nebula are clouds that do not emit light themselves but reflect light from nearby young stars. The light does not possess enough energy to ionise the gas in the nebula and so the observed light must be attributed to scattering from dust grains. The light from sources of this type is

partially polarised. This polarised-light indicates that the dust particles are likely to be aligned non-spherical particles or aligned particles with an anisotropic crystal structure. An example of a carbonaceous material with an anisotropic crystal structure is graphite.

A final piece of indirect evidence for dust grains is the observed column densities of some molecules. In particular the abundance of molecular hydrogen in the interstellar medium. The column densities of H_2 measured by astronomers cannot be accounted for by gas-phase kinetics. It is now believed that these large column densities are achieved *via* the reaction of H atoms to form H_2 on the surface of dust particles.[16] This hypothesis is strengthened by the observed direct correlation between molecular hydrogen column densities and the extinction of star light.[17] Furthermore, solid-phase water and CO_2 are observed in the ISM *via* broad bands at 3.1 μm for the O-H stretch in water and 15.3 μm for CO_2.[18-21] These bands are attributed to water and carbon dioxide in the solid phase on the surface of dust particles.

There is direct spectral evidence for silicate dust grains in the interstellar medium *via* a set of broad absorptions in the mid-infrared region: a strong absorption feature peaking at approximately 9.7 μm is observed.[22] Silicate materials generally have a strong absorption at approximately 10 μm and so this absorption at 9.7 μm is assigned to Si-O stretching in olivine. This conclusion is strengthened by the observation of the 9.7 um feature near outflows from oxygen-rich stars where silicates are expected to condense. This 9.7 μm absorption is not observed in the outflow from carbon-rich stars where silicates are not expected to form due to the oxygen reacting with carbon to produce CO.[22] There is also a broad absorption observed at 18 μm that is assigned to the O-Si-O bending mode in silicates.[23, 24] The lack of structure of these bands more closely resembles amorphous rather than crystalline silicates. Furthermore, in some cases amorphous and glassy silicates prepared in the laboratory have been shown to have similar IR absorptions to those observed in the ISM.[22] Silicate dust grains in the ISM are therefore predicted to be largely amorphous materials.

Direct spectral evidence for the molecular structure of the carbonaceous grains is elusive. It is clear that graphite alone cannot truly model the extinction "bump" at 2175Å and so it has been proposed that nano-sized amorphous carbon structures could be responsible for this UV-feature.[25] Other possibilities include naphthalene aggregates and strongly dehydrogenated polyaromatic hydrocarbons (PAHs).[26-28] Using *ab initio* calculations, mixtures of PAHs in different charge states have also been shown to be possible carriers of the UV-feature.[28] Laser ablation experiments, which produce PAH films give a slightly blue-shifted UV bump when compared to astronomical data. The PAHs produced in these experiments contain 22-38 carbon atoms per PAH. Calculations based on these experiments have estimated that to produce the red shift required to reproduce the UV bump, around 50-60 carbon atoms would be needed per PAH.[29] Further spectral evidence for carbonaceous dust grains lies in a complex collection of IR absorption bands around 3.4 μm. These absorptions have been observed along lines of sight in

the diffuse interstellar medium where large quantities of dust grains are expected to be present. These absorptions are now commonly attributed to the CH stretching of sp^3 hybridised carbon.[30-34] These absorptions are believed to be due to an organic refractory material primarily composed of hydrocarbons and so these bands represent another possible signature of carbonaceous dust grains. The material responsible for these absorptions at 3.4 μm contains little nitrogen, oxygen or long-chain alkanes.[35] These IR absorptions are attributed to a material which possesses around 50% more methylene groups than methyl groups as well as diamond-like CH groups.[36-38] The IR absorption at 3.3 μm, attributed to the CH stretching of methylene groups, can be reproduced by nanometer-sized carbon grains of PAHs produced in laser ablation experiments.[39] Whilst the true chemical structure for carbonaceous dust grains is elusive, PAHs and nanometer sized dust grains represent promising structures.

In conclusion, there is overwhelming evidence for the presence of dust grains in the interstellar medium. These dust grains are estimated to account for 1 % of the mass of an interstellar cloud. The grains are likely to be composed of silicates and carbonaceous material and have a diameter on the same order of the wavelength of visible light. The grains are either elliptical in shape or are composed of a material with an anisotropic crystal structure. It is generally believed that dust grain surfaces play an important role in the chemical complexity of the interstellar medium, particularly in dense clouds where their surfaces can accommodate icy mantles of H_2O, CO_2 and CO.

1.5 Interstellar Ice Composition

Due to the self-shielding of dense interstellar clouds, photons cannot penetrate to their centre. This lack of photons results in a reduced gas-temperatures when compared to diffuse interstellar clouds. Furthermore, the low temperatures and low photon flux result in little to no thermal desorption or photo-desorption from the grains. As a result gas-phase species can aggregate on the surface of dust grains to form ices. Over the lifetime of a cloud these ices can reach a thickness of a few hundred monolayers.[40] There is a robust amount of observational data to allow us to develop a picture of the composition and structure of interstellar ices. On top of the 2.4 μm - 45 μm extinction curve of interstellar light sources, are superimposed IR absorptions of molecular ices.[41, 42] It is clear, with the exception of carbon monoxide, that observed ice abundances cannot be accounted for by simply the accretion of gas-phase molecules onto the dust grain surfaces.[40] Gas-phase column densities in the interstellar medium are low, collisions are infrequent, and three-body interactions are negligible. However, grain surfaces can provide a ‘meeting ground’ for reactive species and offer relaxation pathways for energetic products of association reactions

not available in the gas-phase.[40] It therefore follows that surface chemistry of the grains is contributing to the molecular abundances observed in the ISM.

The observed IR absorptions indicate that water accounts for 60 – 70 % of interstellar ice in most lines of sight.[43] Water ice is primarily identified by its strong O-H stretching mode at 3279 cm^{-1}, but also by weaker bending modes, combination modes and libations at 1667 cm^{-1}, 2222 cm^{-1} and 7692 cm^{-1} respectively. The remaining major components of the ice are carbon monoxide,[44] methanol,[45] methane,[46] carbon dioxide,[18] ammonia and formaldehyde.[47] Other molecular species typically make up only a few percent of the ices.[41] The ices are thought to consist of two phases, a polar phase dominated by water and carbon dioxide and a non-polar phase dominated by carbon monoxide.[41] These two phases were first identified by the two components of the 2141 cm^{-1} fundamental vibrational band of carbon monoxide. Carbon monoxide's IR profile, in the ISM, consists of a broad (polar) component centred at 2136.5 cm^{-1} and a narrow (nonpolar) band centred around 2140.0 cm^{-1}.[48, 49] It was previously thought that the polar component broadening the 2136.5 cm^{-1} feature was water. However, laboratory experiments with CO:H_2O ices could not reproduce the 2136.5 cm^{-1} feature without introducing a shoulder centred at 2151 cm^{-1}.[50] It was thought that this shoulder may not be observable in the ISM,[51] but later laboratory spectroscopic work showed that an ice mixture containing H_2O:CO:CO_2 could also not account for the broad feature at 2136.5 cm^{-1}. It is now thought that the broadening of the feature at 2136.5 cm^{-1} is due to CO:CH_3OH ice, indicating that methanol is almost exclusively present in the non-polar phase of interstellar ice.[52] Methanol is identified by its features at 2833 cm^{-1}, 2532 cm^{-1}, 1471 cm^{-1}, and 1026 cm^{-1}. In TMC-1, methanol is observed to have an ice abundance of < 2.9% relative to that of water.[53] Carbon dioxide is identified by its two strong bands the ν_3 (2342 cm^{-1}) asymmetric stretch and the ν_2 (6579 cm^{-1}) bending mode. In TMC-1 carbon dioxide has polar and apolar abundances of 24.2% and <0.8% compared with that of water.[54] Methane is observed *via* its ν_4 deformation-mode at 1304 cm^{-1}. Ammonia is identified by its N-H stretch at 3378 cm^{-1}, its N-H deformation mode at 6192 cm^{-1} and an umbrella mode at 1075 cm^{-1}.[41] Despite the overwhelming dominance of water, and other simple molecules, it is believed that most of the complex and exotic species in the ISM, such as amino acids, are produced in or on the ice mantles of dust grains.

1.6 Interstellar Ice Reactivity

The surface chemistry of the interstellar ices can be categorised into two classes: thermal and non-thermal reactions. Non-thermal reactions are initiated by UV photons or energetic particles. The interaction of these energetic particles with interstellar ice causes dissociation of molecules generating suprathermal fragments. These suprathermal fragments are capable of undergoing further reactions with reasonably large activation energies. Conversely, thermal reactions occur when both reactants are in thermal equilibrium with their surroundings. Given the low

temperatures of the gas and ice (10K) in dense interstellar clouds, there is very little thermal energy available to overcome activation barriers. At these temperatures thermal reactions typically occur when one reactant has an open shell electronic structure, such as H or O atoms. Reactions in which at least one reactant is an open shell species tend to have low activation energies. This thesis focuses on the thermal reactions in the interstellar medium and so it is beyond it's scope to discuss non-thermal reactions in detail. However, reviews of non-thermal reactions in the interstellar medium are available in the literature.[55]

In general, bimolecular reactions on surfaces are thought to follow one of three prototypical reaction pathways. The first is the Langmuir-Hinshelwood (LH) mechanism where both reactive species are initially adsorbed and thermalised on the surface.[56] One or both of the reactants, which are only weakly bound in physisorption sites, will diffuse across the surface either by a classical random walk or by tunnelling through diffusion barriers. Upon encountering a suitable reaction partner, a product is formed. The second surface reaction mechanism, the Eley-Rideal (ER) pathway, involves a thermalised surface molecule undergoing a direct reaction with an incident, and potentially energetic, gas-phase species.[56] The third surface reaction mechanism is the hot atom pathway in which the incident gas-phase species is partially thermalized with the surface upon encountering and reacting with a surface species. In the interstellar medium cross sections for the ER mechanism are often low due to the low surface coverages of reactants. What is more, in dense clouds the gas and dust temperatures are in thermal equilibrium and so impinging molecules are already thermalized with the surface. It is therefore believed that surface chemistry on dust grains proceeds predominantly *via* the LH mechanism.[40]

1.7 Hydrogen Atom Surface Reactivity

1.7.1 H_2 Formation

Early studies of the thermal surface chemistry of the interstellar medium focused on hydrogen atom recombination. Not only are H atoms the most abundant species in the ISM, but H_2 is the most abundant molecular species in the ISM. As discussed in Section 1.2, simple radiative association of H atoms is slow and three-body gas-phase reactions are not possible. However, in 1961 it was shown that, on a water ice, H atom recombination occurred when surface temperatures were below 30 K.[57] The efficiency of the reaction was increased when a fresh water surface was prepared. Subsequent modelling used this experimental observation to predict that H atom recombination would be efficient on interstellar dust grains between 5 K and 20 K. This high efficiency was shown to account for the high H_2 abundance in the interstellar medium.[58, 59] The upper limit of 20 K represents the surface temperature at which H atoms have a high sticking coefficient and the lower limit of 5 K represents the temperature at which H_2 will adsorb onto the surface, building up a monolayer and quenching the reaction on the surface. Subsequent

experimental studies reported that the efficiency of H atom recombination on an olivine surface was a factor of 10 lower than theoretical predictions.[60, 61] This discrepancy between theory and experiments is attributed to the theoretical calculations considering a perfect surface. It was proposed that defects on the surface may alter the sticking coefficient or reduce the rate of tunnelling of H atoms. Further experimental work by Pirronello *et al.* showed that during a temperature programmed desorption (TPD) experiment, second order desorption kinetics of HD were observed when low coverages of H and D atoms were dosed onto a surface held at 6 K.[60] Second order desorption kinetics are characteristic of associative desorption. For a general explanation of a TPD experiment see Section 2.1. The second order desorption kinetics of the HD detected by Pirronello *et al.* indicates it was formed by associative desorption during the warm up phase of the TPD. This indicates that, at 6 K, the H and D atoms are relatively immobile on the surface. When high, although still sub-monolayer, coverages of H and D atoms were dosed onto the same surface first order desorption kinetics were observed for HD. The first order desorption observed at high coverages indicates that HD formed on the surface at 6 K will remain bound to the surface until heating is applied. This observation is at odds with the previous hypothesis that the 4.5 eV binding energy released upon recombination would redistribute amongst vibrational modes in such a way that the HD would be ejected from the surface upon formation. Later studies showed that hydrogen recombination was approximately twice as efficient on a graphite surface than an olivine surface.[62] Although, this efficiency on graphite is still five times smaller than theoretical predictions.

Later experiments at UCL were designed to determine the fate of the 4.5 eV binding energy released upon the formation of HD.[63, 64] Both the H and D atoms were co-dosed onto a graphite surface held at a temperature of 15 - 20 K. The rovibrational populations of HD molecules desorbing from the surface were probed using resonance enhanced multi-photon ionisation (REMPI) and time of flight mass spectrometry (TOFMS). The experiments revealed the HD molecules were formed in excited vibrational states peaking at $v = 4$ with states populated up to $v = 7$. Conversely only rotational states $J = 0$ and 1 were populated. The results show that the 4.5 eV binding energy released upon H atom recombination is efficiently redistributed throughout vibrational modes but not into rotational modes.

1.7.2 H_2O Formation

Water is the dominant constituent of interstellar ices. It has even been hypothesised that the water formed on interstellar ices is the same water that fills our Earth's oceans. The H/D ratios observed for gas-phase water observed in proto-planetary discs exceeds the H/D ratio of the Earth's oceans. Conversely, the H/D ratios of gas-phase cometary water in the Oort cloud, an extended shell of icy objects that exist in the outermost reaches of our solar system, are comparable to the H/D ratio in the Earth's oceans. Clearly the water observed in proto-planetary discs and comets have

different origins and it seems the water in the Earth's oceans more closely resembles the water associated with comets. It has therefore been hypothesised that the water in the Earth's oceans may have been delivered to Earth *via* comets. However, a direct comparison to the H/D ratio in interstellar ices cannot yet conclusively determine that the cometary water has interstellar origins.[1] Nevertheless, the gas-phase formation and subsequent freeze out of water cannot account for the observed abundancies of H_2O in interstellar ices. Therefore, the thermal formation of water on interstellar dust grains has been extensively studied in the laboratory over the last two decades. The idea of water formation *via* surface hydrogenation of O_2 was first put forward by Van de Hulst in 1949.[65] In 1982 Tielens and Hagen extended this idea to include three pathways, involving oxygen and hydrogen, for the formation of water on surfaces.[66] The reactions are listed below in equations (1.7.2.1), (1.7.2.2) and (1.7.2.3).

$$2H + O \rightarrow H_2O \qquad (1.7.2.1)$$

$$4H + O_2 \rightarrow 2H_2O \qquad (1.7.2.2)$$

$$6H + O_3 \rightarrow 3H_2O \qquad (1.7.2.3)$$

Experimental work began in 1998 when Hiraoka and co-workers observed that D and O atoms react to produce water in the condensed phase.[67] Oxygen atoms were generated using a microwave discharge in N_2O. The resulting gas (N_2O and O atoms) was deposited onto a surface held at 12 K generating a matrix 13 monolayers thick. The matrix was then dosed with D atoms. A TPD experiment confirmed the production of D_2O with a yield of 1.3 %. This study provided the first evidence that D atoms can migrate and react with O atoms to form water at temperatures relevant to the ISM. However, a matrix of N_2O is not representative of interstellar ice, and so later work by Dulieu *et al.* extended this study to the reaction of O and D atoms on the surface of a porous water ice substrate.[68] A 100-layer thick film of non-porous water was first deposited at 120 K and the substrate was then cooled to 10 K where a further 10 monolayers of amorphous porous ice (ASW) were grown. The ice was then annealed to 90 K to avoid any further collapse of the pores during the subsequent TPD experiments. The atomic species, O and D, were generated using a microwave discharge in O_2 and D_2 respectively. D atoms were first dosed onto the water molecules to confirm that there was no reaction between the D atoms and the water matrix. In addition it was confirmed that O atoms do not react with the D_2. When O and D atoms were dosed onto the water ice substrate two signals were observed, in the spectrum recorded by the QMS during the TPD, with atomic masses of 19 and 20 AMU. These signals correspond to the formation of $D_2{}^{16}O$ and $HD^{16}O$. The formation of $HD^{16}O$ occurs due to isotopic exchange between the D_2O formed during the reaction and the H_2O in the pre-deposited ASW. This H/D substitution occurs during the TPD experiment at approximately 150 K.[69] To confirm the water produced was due to the O and D atoms deposited onto the water ice, the authors repeated the reaction using ^{18}O

and D atoms. Signals in the mass spectra were observed corresponding to the formation of $D_2{}^{18}O$, $HD^{18}O$ and $H_2{}^{18}O$. The authors determine that 76 % of the ^{18}O atoms deposited onto the surface react to form the observed water isotopologues. The authors also consider the idea that they are simply observing the reaction between D atoms and undissociated O_2 from the microwave discharge. They conclude that due to their high dissociation efficiency the reaction of D atoms and O_2 can only account for 60 % of the water produced. However, they do not consider the reaction of $O + O \rightarrow O_2$ on the surface of the ASW. Although, since H atom surface diffusion is much faster than O atom surface diffusion it is likely that the O atoms primarily react with H atoms rather than one another.

Mokrane *et al.* studied the formation of water through the reaction of D atoms with O_3 on an amorphous water ice surface.[70] The ozone was produced *via* a radio-frequency electric discharge in 30 mbar of O_2 gas. Residual O_2 was pumped away whilst the ozone was frozen in liquid nitrogen. In this way a glass bulb of pure O_3 can be produced. Due to the metal surfaces in the chamber, ozone will partially dissociate into O_2 and O atoms during deposition. However, the gas was deposited onto the water ice substrate at 50 K, a temperature at which O_2 has a low sticking coefficient whilst ozone has a high sticking coefficient. Submonolayer coverages of pure ozone could therefore be deposited on the water ice surface. Following the deposition of O_3 the substrate was cooled to 10 K. The D atoms were produced using a microwave discharge with a dissociation efficiency of 60 %. After ~ 5×10^{15} D atoms cm^{-2} were deposited onto the surface the products were observed using TPD. The TPD data show the complete disappearance of O_3 from the surface and a desorption peak corresponding to HDO at 160 K. However, no D_2O is observed to desorb from the surface. The authors again attribute this to thermally activated H/D exchange which occurs at approximately 150 K.[69] However, it is interesting to note that full H/D isotopic exchange was not observed when the same group studied the reaction of O and D atoms, that is D_2O was observed.[68] The authors comment that the reaction of ozone with D atoms must be efficient on water ice surfaces since the number of D atoms dosed onto the surface is only 10 times the number of O_3 molecules on the surface. If one assumes the D atoms that do not react with O_3 react with one another to form D_2 this ratio of reactants results in more water formation than D_2 formation as in equation 1.7.2.4.

$$O_3 + 10\ D \rightarrow 3D_2O + 2D_2 \qquad (1.7.2.4)$$

The recombination of D atoms on surfaces is an efficient reaction, as discussed in Section 1.7.1, and so the reaction of O_3 and D atoms must be of a similar efficiency to account for the large quantities of water produced under these experimental conditions. Indeed, the reaction of D atoms and O_3 must be effectively barrierless at 10 K. When a reduced flux of D atoms is used, that is there are insufficient D atoms to fully hydrogenate O_3, O_2 is also observed in the TPD spectra. As

a result the authors put forward the following reaction pathway for H_2O formation including O_2 as an intermediate.

$$O_3 + D \rightarrow OD + O_2 \quad (1.7.2.5)$$

$$OD + D \rightarrow D_2O \quad (1.7.2.6)$$

$$O_2 + D \rightarrow DO_2 \quad (1.7.2.7)$$

$$DO_2 + D \rightarrow D_2O_2 \quad (1.7.2.8)$$

$$D_2O_2 + D \rightarrow D_2O + DO \quad (1.7.2.9)$$

However, the authors do not present evidence for D_2O_2 in their TPD data, as TPD spectra for mass 36 is not recorded. Evidence for this proposed formation pathway would be strengthened by observing a TPD peak for mass 36.

In 2008 two studies were published on the formation of water *via* the reaction of H atoms with O_2.[71, 72] Both studies determined the formation of water to proceed efficiently and involve the formation of H_2O_2. Miyauchi *et al.* deposited 8 ML of O_2 onto an aluminium substrate held at 10 K. H atoms were generated using a microwave discharge with a dissociation efficiency of 20 %, this generated a flux of H atoms of 2×10^{14} cm^{-2} s^{-1}.[71] The formation of H_2O and H_2O_2 were measured *in situ* using RAIRS every few minutes during the 10 minute dose of H atoms. A first order model in which H atoms diffuse to form H_2O was used to fit their results. The model showed that the capture of H atoms by O_2 is barrierless and that the formation of H_2O from H_2O_2 either possesses a small barrier of 3.6 - 4.6 kcal mol^{-1} or proceeds *via* tunnelling. In the second study, Ioppolo *et al.*, extended the reaction to a range of surface temperatures between 12 K and 28 K. A 15 ML thick O_2 ice was deposited onto a gold substrate at 15 K.[72] The ice was then heated or cooled to the desired temperature between 12 and 28 K. H(D) atoms were generated using thermal-cracking of H_2 (D_2) with a dissociation fraction of 50 %. Typically the O_2 ice was irradiated with H(D) atoms for 3 hours. Water formation was detected and quantified *via* its 1650 cm^{-1} IR absorption, since the absorption at 3430 cm^{-1} overlaps with the 3250 cm^{-1} absorption of H_2O_2. The formation of H_2O_2 was detected and quantified *via* its 1350 cm^{-1} absorption. IR spectra were acquired every few minutes during H(D) deposition and clearly show the increase in H_2O and H_2O_2 yield with increasing H(D) fluence. The initial growth of the product yields was linear and temperature independent, which corresponds to zeroth-order kinetics. This zeroth-order kinetics came as a surprise since reactions of this type are expected to involve pseudo first order kinetics due to the constant flux of H atoms in the beam.

In 2010 the Linnartz group published a two-part follow up study to extend the study described above.[73, 74] In this second study, product yields above 23 K were found to be larger than that observed in the 2008 study. This discrepancy can be explained by the different thickness of ice used in each study: 35 ML in 2010 and 15 ML in 2008. The results show that the H atoms clearly have a larger penetration depth at temperatures above 23 K than the 15 ML of O_2 ice deposited in

the first study. The increased penetration depth above 23 K increases the H atom residence time in the ice and so further reactivity with O_2 is observed. The authors were able to determine that the change in penetration depth of H atoms in O_2 ice, at different surface temperatures, is due to the temperature dependent competition between the reaction of H atoms with O_2 and further penetration of the H atoms into the ice. At low surface temperatures the reaction is favoured and at high surface temperatures penetration is favoured. The reduction in H atom reactivity with O_2 at high temperatures indicates that the capture of H atoms by O_2 may not only be barrierless but proceed *via* tunnelling. However, the primary aim of the 2010 study was to determine the origin of the zeroth-order formation kinetics observed in the 2008 study.[73] The zeroth-order formation kinetics observed in the earlier work suggests that the proposed reaction network was incomplete. The second study therefore sought to explore the interconnecting mechanisms at play when D atoms add to O, O_2 and O_3, derive a full reaction scheme and constrain rates of individual reactions.[72, 74] The experiments employ different H/O_2 ratios to probe different stages in the hydrogenation network. Four hydrogen atoms are needed to convert O_2 into H_2O. When H/O_2 = 100, full hydrogenation can occur and the IR spectra are observed to be dominated by broad H_2O and H_2O_2 bands indicating formation of bulk H_2O and H_2O_2. When H/O_2 = 1 full hydrogenation cannot occur and HO_2, H_2O_2 and OH are observed. The extensive study tracks the abundances of OH, H_2O_2, H_2O and HO_2, with respect to H atom fluence when the surface temperature and the H/O_2 ratios are varied. The authors found that OH and the H_2O_2 monomer share the same trend, the H_2O monomer and H_2O_2 bulk also share the same trend whereas HO_2 has a unique trend. Reaction 1.7.2.10 was found to be largely independent of surface temperature and so effectively barrierless. The efficiency is governed by the sticking coefficient of H atoms and efficient destruction pathways of HO_2 at low surface temperatures. This finding is in agreement with earlier studies in the Watanabe group.[71]

$$O_2 + H \rightarrow HO_2 \qquad (1.7.2.10)$$

There are four pathways in which HO_2 can undergo further hydrogenation, 1.7.2.11, 1.7.2.12, 1.7.2.13, 1.7.2.14.

$$HO_2 + H \rightarrow H_2O_2 \qquad (1.7.2.11)$$
$$HO_2 + H \rightarrow 2OH \qquad (1.7.2.12)$$
$$HO_2 + H \rightarrow H_2O + O \qquad (1.7.2.13)$$
$$HO_2 + H \rightarrow H_2 + O_2 \qquad (1.7.2.14)$$

Reaction 1.7.2.14 cannot be quantified *via* IR spectral studies since neither O_2 or H_2 is IR active. The efficiency of this pathway is therefore still unknown. However, reactions 1.7.2.11 and 1.7.2.12 were found to be effectively barrierless since the OH/H_2O_2 ratio is constant in

experiments where $H/O_2 \leq 2$. These reactions were therefore identified to be the dominant pathways for the formation of H_2O_2 and OH. Previous work had proposed that OH was primarily formed *via* the hydrogenation of H_2O_2 as in reaction 1.7.2.15

$$H_2O_2 + H \rightarrow H_2O + OH \quad (1.7.2.15)$$

However, this reaction is not in agreement with the observation that H_2O_2 and OH are formed early in the reaction and have a constant ratio. If reaction 1.7.2.15 was more efficient than reaction 1.7.2.12 one would expect the OH/H_2O ratio to be constant rather than the OH/H_2O_2 ratio. Similarly reaction 1.7.2.13 is believed to be inefficient since H_2O does not follow the same trend as OH and H_2O_2. The authors do, however, observe O_3 formation which indicates that O atoms are involved in the reaction network since O atoms react with O_2 to form O_3, as in reaction 1.7.2.17. The authors therefore propose that O atoms are produced *via* reaction 1.7.2.18 since reaction 1.7.2.13 is inefficient.

$$H + OH \rightarrow H_2O \quad (1.7.2.16)$$

$$O_2 + O \rightarrow O_3 \quad (1.7.2.17)$$

$$OH + O_2 \rightarrow HO_2 + O \quad (1.7.2.18)$$

Whilst H_2 does not react with O_2 on surfaces at low temperatures, it is possible that H_2 can react with OH and HO_2 (reactions 1.7.2.19 and 1.7.2.20).

$$H_2 + OH \rightarrow H_2O + H \quad (1.7.2.19)$$

$$H_2 + HO_2 \rightarrow H_2O_2 + H \quad (1.7.2.20)$$

Reaction 1.7.2.19 was found to be inefficient since no decrease in OH or increase in H_2O is observed when the H/H_2 ratio is decreased. However reaction 1.7.2.20 is efficient since the H_2O_2 abundance does increase when the H/H_2 ratio is decreased. It was also found that reactions 1.7.2.21 and 1.7.2.22 are inefficient pathways since HO_2 is heavy and unlikely to diffuse to find a reaction partner whilst OH is abundant and so reaction 1.7.2.21 cannot be efficient.

$$OH + OH \rightarrow H_2O_2 \quad (1.7.2.21)$$

$$HO_2 + HO_2 \rightarrow H_2O_2 + O_2 \quad (1.7.2.22)$$

The authors are able to show that the pathways for the formation of water *via* the hydrogenation of O, O_2 and O_3 are interconnected. They are also able to constrain the efficiency of several reactions, the reaction of H and O_2 is more efficient than previously thought, whilst the reaction of O + OH and H_2 + OH are less efficient. The authors predict that 30 % of the water is produced

via reaction 1.7.2.15 at early reaction times when HO_2 abundances are low, whereas 70 % of the water is produced at later times *via* reaction 1.7.2.16, since reaction 1.7.2.12 produces OH from HO_2 efficiently. As a result of these experiments the authors put forward the reaction network depicted in Figure 1.7.2.1

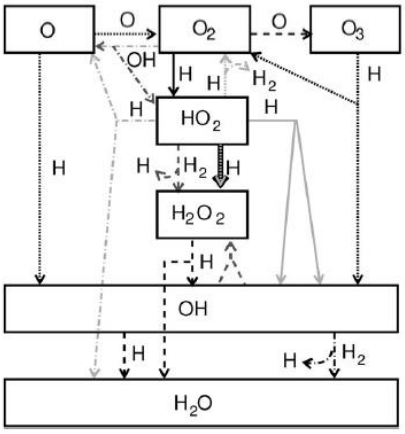

Figure 1.7.2.1: A schematic representation of the reaction network for water formation on surfaces of astrochemical interest. Four types of reactions are distinguished: efficient, effectively barrierless, reactions (solid), reactions with a barrier but with detectable efficiency (dashed), reactions of which the efficiency is below the detection limit (dash-dotted), and reactions of which the efficiency could not be determined in this study (dotted). The light grey arrows indicate the same entering channel but with different outgoing channels, and the black arrows the reactions which were in the original reaction scheme. (taken from reference 74).

1.7.3 CH_3OH Formation

Methanol is thought to be an important starting material for the formation of complex organic molecules in interstellar ices. Experimental work has shown that when solid methanol is irradiated with UV photons or cosmic rays a significant number of molecules with increased complexity are detected.[75, 76] However, methanol production *via* gas-phase ion-neutral reactions is not efficient enough to account for observed abundancies of methanol in interstellar ices.[77, 78] Surface reactions in which H atoms sequentially add to CO are thought to be the predominant formation mechanism for methanol in the ISM. This formation mechanism is not only proposed because of high H atom and CO abundances in interstellar ice but because methanol is exclusively observed in the non-polar, CO dominated, phase of interstellar ice. The first experiment to test this hypothesis irradiated an ice mixture of H_2O:CO (5:1) on an aluminium substrate with hydrogen atoms.[79] The products observed in this first study were formaldehyde and methanol. A second study used a lower flux of hydrogen atoms to irradiate a pure CO ice on a silicon substrate.[80] The only product detected in the second study was formaldehyde. A later study by Fuchs *et al.* attempted to determine the origin of this discrepancy.[81] CO was deposited onto a gold coated copper substrate

held at 10 K. The abundance of CO, H_2CO and CH_3OH were monitored as a function of H atom fluence *via* their IR absorptions (Figure 1.7.3.1). The abundance of CO follows an exponential decay function with respect to the H atom fluence. The abundance of H_2CO follows an inverse exponential growth function tracking the exponential decay of CO. The abundance of CH_3OH, however, exhibits a linear dependence on H atom fluence. Furthermore, when the flux of H atoms is reduced the appearance and disappearance of products and reactants follow the same trends. The origin of the discrepancy between the first two studies discussed above is not the flux of H atoms to the surface but rather the different fluence of H atoms. The authors conclude that the formation of methanol by successive hydrogenation of CO and H_2CO is efficient under conditions relevant to the interstellar medium. These conditions cover surface temperatures between 12 and 20 K, ice thicknesses of 1 ML to 10 ML and H atom fluxes of 0.001 ML cm^{-2} s^{-1} and 0.01 ML cm^{-2} s^{-1}. The group use Monte Carlo Simulations to extract the rates for the formation of H_2CO and CH_3OH *via* the successive hydrogenation of CO. These rates were then used in further Monte Carlo simulations under astrophysical conditions which predict H_2CO/CH_3OH ratios that are in good agreement with astronomical observations.

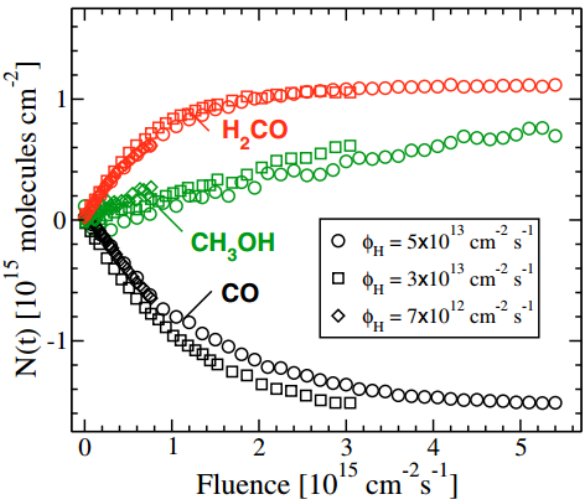

Figure 1.7.3.1: Time evolution of the surface abundance (in molecules cm^{-2}) of CO, H_2CO and CH_3OH during H-atom bombardment of CO ice at 12.0 K with three different H fluxes of 5×10^{13}, 3×10^{13}, and 7×10^{12} cm^{-2} (taken from reference 81).

.

1.8 Oxygen Atom Surface Reactivity

Oxygen is the third most abundant element in the ISM, after hydrogen and helium.[82] However, hydrogen atom surface chemistry has been the focus of laboratory and astrochemical models for decades. On surfaces H atoms readily tunnel through diffusion barriers and so easily roam the surface of interstellar dust grains until a suitable reaction partner is found. However, the work by the Linnartz group clearly demonstrates that the reaction network for the formation of water on

interstellar surfaces is influenced by O atom reactivity.[74] Coincidently, at about the same time as the study in the Linnartz group, experimental astrochemists began to study the reactivity of the oxygen atom. As a result of the work in the Price, Dulieu and Vidali groups, it is becoming more and more apparent that O atoms have a significant role to play in the surface chemistry of interstellar ices. Indeed, over the last three years the reaction of O atoms and O_2 to generate O_3 has provided the most exciting and controversial work in the field of experimental astrochemistry.

As discussed above, the addition of H atom surface reactivity to models provides important formation pathways for molecules such as water and methanol, which are inefficiently formed in the gas-phase. However, CO_2 is the second most abundant species in interstellar ice. Like water and methanol, carbon dioxide ice abundancies cannot be explained by gas-phase kinetics followed by freeze out onto grains. If only H atoms are able to roam interstellar ice surfaces one would expect methanol to be more abundant than CO_2. However, if O atoms can also diffuse on interstellar dust grains, CO_2 can be produced *via* the reaction of CO and O or OH. This scenario, in which H atoms and O atoms can diffuse on interstellar dust grains predicts that CO_2 abundancies exceed methanol abundances in interstellar ices, as is observed in astronomical observations (Figure 1.8.1).

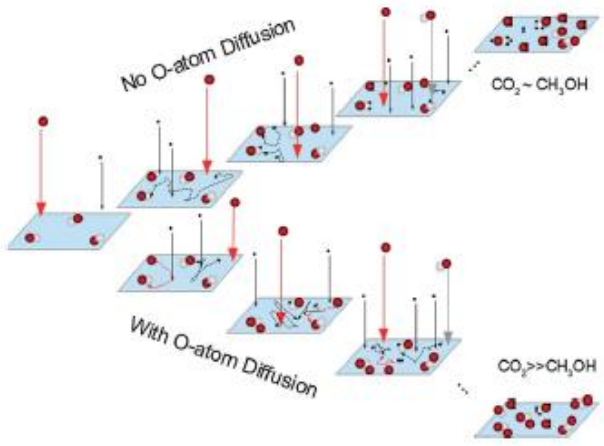

Figure 1.8.1: A schematic view of the two possible scenarios concerning the H_2O/CO_2 balance on icy grains in dense molecular clouds. If H atoms (black dots) are the only mobile species, H-addition mechanisms are dominant and the formation of water (H + OH/O/O_2/ O_3/H_2O) and other H-saturated species (e.g., CO + 3H/CH_3OH) is favoured. On the other hand, if O atoms (red circles) can also diffuse at very low temperatures, the formation of CO_2 in dense clouds may proceed *via* non-energetic reactions (CO + O and CO + OH) as well, making it possible that CO_2 is the second most abundant ice in the ISM (taken from reference 83).

Recent calculations have suggested that O atoms may become the dominant atomic species on interstellar dust grains in clouds with the highest densities. Based on these calculations, the number density of hydrogen in the interstellar medium is 1.1 cm^{-3} and is largely independent of cloud density.[84, 85] However, when cloud densities are 10^3, 10^4 and 10^5 cm^{-3}, oxygen atom densities

are 0.09, 0.75 and 7.0 cm^{-3} respectively.[84, 85] The oxygen atom density increases with increasing cloud density. The calculations use the ratio of H and O atoms in clouds of various densities to determine the mean time between the impact of two H or O atoms respectively. The calculations show that when a cloud reaches a density of 10^4 cm^{-3} H atom collisions and O atom collisions are of equal probability and so in denser clouds it is possible that O atoms are the dominant reactive atomic species (Figure 1.8.2).[83]

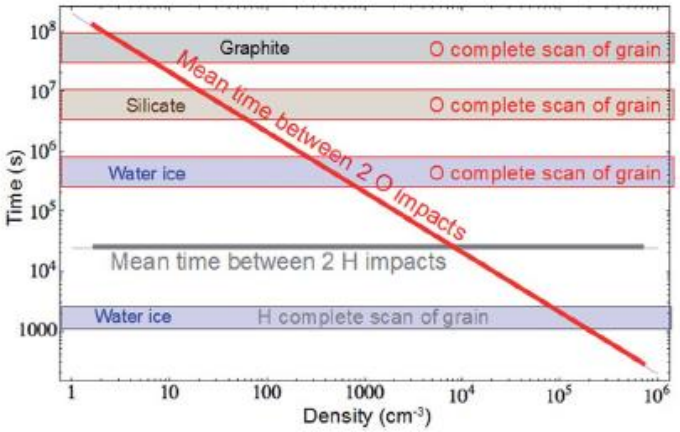

Figure 1.8.2: Time intervals between two impacts of H and O, and the times employed to scan a whole grain (shaded horizontal bands) on various surfaces of interest are plotted as a function of the density of the cloud. The time interval between two arrivals of H is constant, as the density of H atoms remains constant regardless of the density of the medium, while the abundance of O atoms increases with cloud density (taken from reference 83).

There has also been considerable recent interest in accounting for the relatively low abundance (the so-called *depletion*) of oxygen in the gas-phase in the interstellar medium.[86-88] It has been proposed that interstellar grains could act as a sink for oxygen atoms, but it appears that the necessary depletion cannot be generated simply by the incorporation of oxygen atoms into the structures of the dust grains themselves.[87] One possible additional sink for oxygen atoms is perhaps their reaction with the molecular components of the ice mantles that coat the dust grains in dense interstellar clouds.

1.8.1 O_3 Formation

Minissale *et al.* studied the reaction of O atoms and O_2 in 2013.[89] Oxygen atoms were generated with a 71 % dissociation efficiency using a microwave discharge in O_2. The beam of O/O_2 was directed towards a surface of compact amorphous solid water grown by vapour deposition on a 110 K substrate. Ozone formation was observed *via* a TPD methodology. The ozone can either be observed directly at mass 48 or *via* the O_2^+ fragment at mass 32. There are three possible reaction pathways for O atoms on the surface:

$$O + O \rightarrow O_2 \quad (1.8.1.1)$$

$$O + O_2 \rightarrow O_3 \quad (1.8.1.2)$$

$$O + O_3 \rightarrow 2O_2 \quad (1.8.1.3)$$

The experimental data shows that an almost pure O_3 ice is produced. It can be concluded that reaction 1.8.1.3 is inefficient, possessing a significant barrier, whilst reactions 1.8.1.1 and 1.8.1.2 possess small or insignificant barriers. The O_3/O_2 ratio increases with surface coverage since the O_2 rapidly reaches a steady state during dosing, whilst the O_3 yield increases linearly. As the deposition surface temperature is increased from 6.5 K to 25 K the O_3 yield increases. Since the ER mechanism, for a reaction with a small or insignificant barrier, is independent of the surface temperature, this increase in O_3 yield is indicative of the LH mechanism demonstrating that diffusion of reactive species is the limiting factor in the production of O_3. The authors use a model to extract the diffusion constant at each deposition temperature. The extracted diffusion constants, below 20 K, cannot be modelled using a traditional Arrhenius law which should describe thermal diffusion. The authors account for the extracted diffusion coefficients below 20 K by invoking O atom tunnelling through the diffusion barrier. Later publications by the same group extended this study to other surfaces such as graphite, olivine and crystalline water ice.[83, 90] O_3 was observed to form efficiently on all the surfaces of astrochemical interest that have been investigated. In these further studies, RAIRS was used to monitor the ν_3 asymmetric stretching mode of $^{16}O_3$ at 1043 cm^{-1}.[90, 91] After the deposition of O/O_2 at 6.5 K the surface was heated to 35 K and no change was observed in the absorption at 1043 cm^{-1}. This experiment confirms that the ozone produced in these experiments is not formed during the heating phase of the TPD. Further modelling also considered several scenarios to account for the yield of ozone at different surface temperatures. The models successively include (1) the ER mechanism, (2) the thermal diffusion of O atoms during the heating phase of the TPD, (3) the LH mechanism with thermal diffusion and the LH mechanism involving tunnelling through the diffusion barrier. Only the model which included O atom tunnelling of the diffusion barrier could successfully account for the O_3 produced at low surface temperatures. The authors also extracted empirical forms for the diffusion coefficient which did not vary greatly on the different surfaces studied.

It is not only the high diffusion coefficient of O atoms on surfaces that is surprising. Previously, astronomical models had assumed an O atom binding energy of 800 K (6.65 kJ mol^{-1}).[92, 93] Such a binding energy would result in oxygen atoms desorbing from the surface at approximately 28 K. However, modelling by Kimber *et al.* and He *et al.* has extracted O atom desorption energies of 14.0 ± 0.2 kJ mol^{-1} and 1760 ± 230 K (14.6 ± 1.9 kJ mol^{-1}) respectively from experimental data.[94, 95] Furthermore, the models of Hollenbach predict a high O_2 abundance in regions with very high FUV fields. This O_2 is believed to form in the gas-phase due to O atom desorption from grains. However, an O atom binding energy of at least 1200 K is required.[96] Further observations

of the Orion Bar set a stricter limit on the O_2 abundance in a high FUV region which results in an O atom binding energy prediction of 1600 K.[97] These experimental binding energies are far greater than the 800 K predicted by theory. Furthermore, the O atom binding energy determined by laboratory studies is in good agreement with the O atom binding energy predicted from astronomical observations. Together, the laboratory and astronomical observations indicate that O atoms have a stronger binding energy to interstellar dust grains than the 800 K predicted by theory.

Recently He *et al.* and Minissale *et al.* have made direct observations of the O atom desorption energy.[98, 99] In the study by He *et al.* a beam of O/O_2 was deposited onto a porous amorphous water ice held at 48 K for 480 s. The fluxes of O and O_2 were 4.8×10^{12} cm^{-2} s^{-1} and 3.3×10^{12} cm^{-2} s^{-1} respectively. The surface was cooled to 20 K and then heated linearly at a rate of 10 K min^{-1} to 70 K. A QMS was used to monitor masses 16, 32 and 48 corresponding to O, O_2 and O_3 respectively. Molecular oxygen desorption was centred at 50 K whilst ozone desorption was centred at 67 K, Figure 1.8.1.1. However there was an additional desorption peak for mass 16 centred at 57 K. This signal at 57 K is reported as direct desorption of O atoms, Figure 1.8.1.1. The TPD peak area of O direct desorption corresponds to approximately 3% of a monolayer layer. The experiment was also repeated using a silicate substrate. The binding energy of O atoms was extracted to be 1660 ± 60 K (13.8 ± 0.5 kJ mol^{-1}) and 1850 ± 90 K (15.4 ± 0.7 kJ mol^{-1}) for porous amorphous water ice and for a bare amorphous silicate film, respectively.

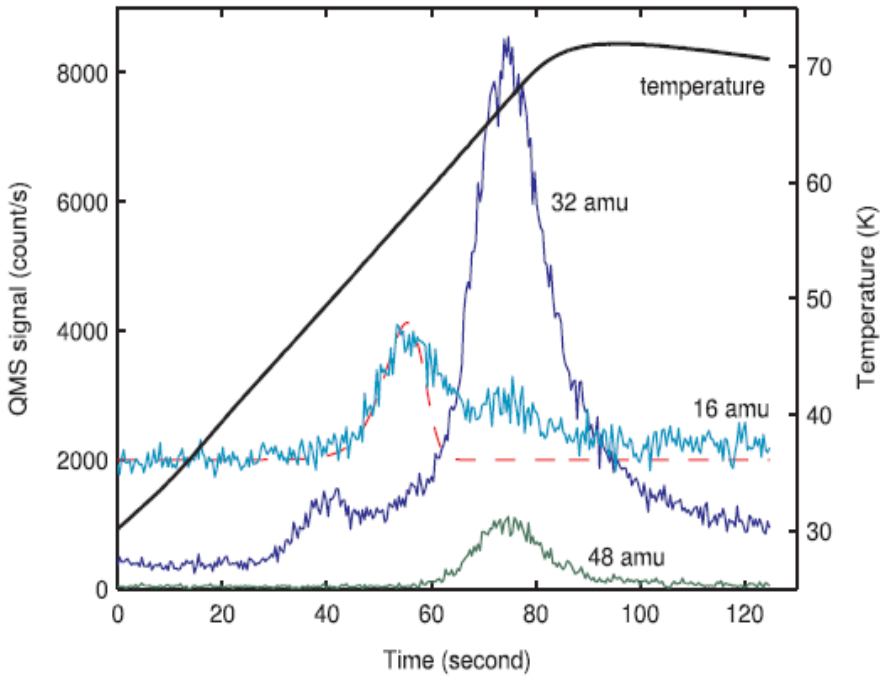

Figure 1.8.1.1: TPD trace of mass 16, 32, 48 AMU after depositing 480s of O/O_2 is deposited at 48 K on amorphous water ice. The heating ramp is 0.17 K s^{-1}. The dashed line shows a fitting of mass 16 AMU peak using $E_{des}(O)$ = 1660 K (taken from reference 98).

Meanwhile, Minissale *et al.* used a temperature programmed during-exposure desorption (TP-DED) technique, which consists of exposing the substrate to the O atom beam while slowly reducing the substrate temperature from 110 K to 10 K at a rate of 17 mK s^{-1}. When the surface temperature is above 70 K the O atoms and O_2 are scattered off the surface and enter the QMS. As the surface temperature decreases below 68 K the O atom QMS signal decreases and the O_2 signal increases (Figure 1.8.1.2). The O atoms become bound to the surface and diffuse, eventually reacting to form O_2. O_2 then desorbs from the surface due to its short residence time of 25 ms.[100] The O atom signal reaches a minimum when the surface temperature reaches 40 K. The O_2 signal starts to decrease when the surface temperature is below 54 K and reaches a minimum when the surface temperature is 30 K. A kinetic model was then used to extract an O atom desorption energy of 1475 ± 225 K (12.3 ± 1.9 kJ mol^{-1}).

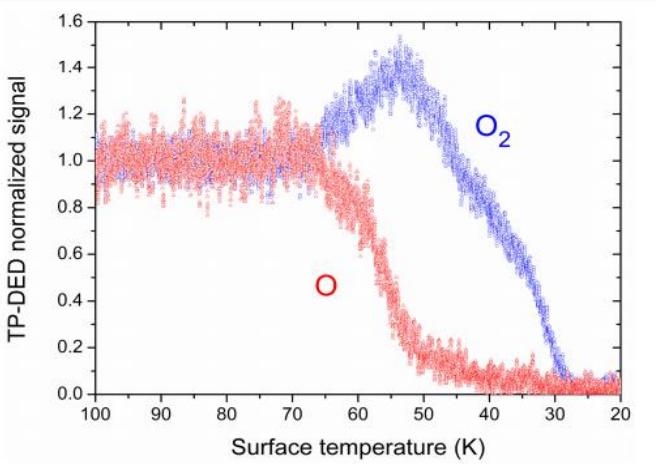

Figure 1.8.1.2: TP-DED normalised signals at mass 16 (red) and Mass 32 (blue) from compact ASW ice during exposure to the O beam. TP-DED were performed with a ramp rate of – 17 mK s^{-1} (taken from reference 99).

1.8.2 CO_2 Formation

Carbon dioxide has an abundance ranging from 10 % to 30 % of that of water in interstellar ices, despite its low gas-phase abundance.[101] CO_2 is therefore thought to form within the ice rather than from deposition from the gas-phase. As discussed previously, one postulated formation route is through O atom addition to carbon monoxide; CO is abundant in the interstellar ices. Roser *et al.* studied the addition of oxygen atoms to ^{13}CO on a copper surface at 5 K in 2001.[102] O atoms and ^{13}CO were co-deposited onto the copper substrate, however no $^{13}CO_2$ formation was observed. When an H_2O ice of an approximate thickness of 100 ML was used to cap the deposited O atoms and ^{13}CO, $^{13}CO_2$ was observed. The H_2O ice cap delays the desorption of the deposited species and so O atoms can interact with ^{13}CO at higher temperatures. The positive identification of $^{13}CO_2$ when O atoms and ^{13}CO interact at higher temperatures indicates a small barrier to the reaction which the authors estimate to be 290 K.

A second study of O atom addition to carbon monoxide in the laboratory was performed by Raut *et al.* in 2011.[103] Oxygen atoms were generated using a radio frequency (RF)-based atom source and cooled to 40 K using a Teflon coated aluminium tube. The estimated dissociation efficiency in these experiments is 40 %. The O/O_2 beam was co-deposited with ^{13}CO onto a gold substrate held at 20 K. The resulting film thickness was estimated to be 0.2 μm. This layer was then capped with a 2.5 μm thick layer of H_2O. Absorptions are observed at 2280 cm^{-1} and 1050 cm^{-1} which correspond to absorptions of $^{13}CO_2$ and O_3 respectively. When the surface temperature was raised at 1 K min^{-1} to 80 K the $^{13}CO_2$ abundance was observed to increase by 30 % indicating diffusion increases the yield of $^{13}CO_2$. The authors comment that the yield of $^{13}CO_2$ is low due to the preferential reaction of O atoms with O_2 to generate O_3. The authors attribute their ability to detect $^{13}CO_2$ without heating the surface to a higher signal to noise ratio when compared to the experiments of Roser *et al*. However, their ability to detect $^{13}CO_2$ is probably also due to the surface temperature used in their experiments which was 20 K. Roser *et al.* used a surface temperature of 5 K. Since the reaction is dependent upon O atom diffusion, a higher surface temperature will result in a larger yield of $^{13}CO_2$.

Minissale *et al.* extended this study to the submonolayer regime, on surfaces of ASW and oxidized graphite. Fixed doses of ^{13}CO (0.5 ML) and O atoms (0.5 ML) were deposited onto the surfaces at a variety of surface temperatures between 10 K and 60 K. Four peaks are observed in the TPD spectra corresponding to O_2, ^{13}CO, O_3 and $^{13}CO_2$. By performing several experiments at different dosing temperatures it was found that $^{13}CO_2$ is produced in small amounts at 10 K, the yield reaches a maximum at 35 K and becomes zero at 60 K. At low temperatures the O atoms preferentially react with residual O_2 on the surface to form O_3. At 35 K O_2 has a low residence time and so the O atoms react with ^{13}CO to generate $^{13}CO_2$. At 60 K ^{13}CO has a low residence time and so the reaction cannot proceed. The authors use a kinetic model to estimate a reaction barrier of 475 K – 780 K for the reaction of CO + O. This barrier is significantly higher than that estimated by Roser *et al*.[102]

Another pathway to form CO_2 on interstellar ice surfaces is the reaction of CO and OH. Oba *et al.* generated OH radicals using a microwave discharge in water which also generates H and O atoms.[104] The beam of radicals was cooled to 100 K and co-deposited with CO onto an aluminium surface. CO_2 was detected using RAIRS and TPD when the surface temperature was 10 and 20 K indicating there is little or no barrier to the reaction of OH and CO. The authors exclude the reaction of O atoms and CO by repeating the reaction using a microwave discharge in O_2 and do not observe CO_2 formation. In the second study, Nobel *et al.* generated OH radicals *in situ via* the hydrogenation of O_2 and O_3.[105] However, since only TPD is used in this study no *in situ* measurements of the reactive species OH were made. The authors report the formation of CO_2

when CO is deposited with their, formed *in situ*, OH radicals. However, they report a small yield of CO_2 and suggest a relatively high barrier of 400 K.

Ioppolo *et al.* have directly compared the efficiency of the two different pathways for the formation of CO_2 on interstellar dust grains.[106] The experiment compares the co-deposition of (^{13}CO + O), (^{13}CO + H), (H + O) and (^{13}CO + O + H) under the same experimental conditions. It was found that the final column density of solid $^{13}CO_2$ formed when ^{13}CO + O + H were co-dosed onto the surface was ten times higher than when only ^{13}CO + O were co-dosed onto the surface. The experiments confirmed previous predictions by models that CO_2 is formed primarily *via*:[107]

$$O + H \rightarrow OH \quad (1.8.2.1)$$

$$OH + CO \rightarrow HOCO \quad (1.8.2.2)$$

$$HOCO \rightarrow CO_2 + H \quad (1.8.2.3)$$

The OH radical is first formed through the reaction of H and O atoms. These radicals then react with CO to form the intermediate HOCO which rapidly decomposes into CO_2 and H. The advantage of the formation of CO_2 *via* the reaction of CO and OH, is that this route generates CO_2 primarily in the polar phase of interstellar ices where it is observed.

1.8.3 Oxygen Atom Addition at UCL

Figure 1.8.3.1: The structure of the three isomers of C_2H_4O

Ward *et al.* studied the reaction of O atoms with double bonds on surfaces under astrophysical conditions.[108] In separate experiments O atoms were co-dosed with either ethene or propene onto a graphite surface building a matrix approximately 1000 ML thick. Using TPD, coupled with TOFMS a single oxygen atom addition product was observed. In the case of the reaction of O atoms and ethene the oxygen addition product has three possible isomers: vinyl alcohol, acetaldehyde and ethylene oxide (Figure 1.8.3.1). The ionisation energies of these isomers are 9.33 eV, 10.23 eV and 10.56 eV respectively. By successively setting the wavelength of a dye laser such that the two-photon energy was slightly above each ionisation potential it was possible to ionise only vinyl alcohol, vinyl alcohol and acetaldehyde, or all three isomers. It was found that the predominant isomer formed on the surface was ethylene oxide with a small amount of acetaldehyde. No vinyl alcohol was observed. The Viti group were able to include this surface

reaction in their astrochemical models to qualitatively reproduce the abundances of ethylene oxide towards high-mass star-forming regions.[109] This model will be further discussed in Section 1.9.

Further experiments by Ward *et al.*, using the same apparatus observed that O atoms can readily convert CS_2 into OCS.[110] This reaction was observed to be efficient at surface temperatures between 15 K and 70 K. OCS is observed in interstellar ices and the O atom addition to CS_2 may provide a formation mechanism in dense dark clouds where UV photons are scares.

1.9 Astrochemical Models

The earliest astrochemical models designed to study the chemistry of dense interstellar clouds were devised in the 1970s by Watson,[111, 112] and Herbst and Klemperer.[113] These early models solved coupled rate equations under a steady-state and so were time-independent. The model by Herbst and Klemperer solved these coupled rate equations for 37 species and 100 reactions, a relatively small network by today's standards. The reactions included were primarily gas-phase with the exception of H_2 formation on the surface of interstellar dust grains. Nevertheless, the model was able to provide quantitative predictions of molecular abundances in interstellar clouds. Similar models by Allen and Robinson included several more surface reactions in which neutral radical species recombined on the surface of interstellar dust grains.[114] However, it was not clear at the time how molecular species heavier than H_2 would desorb from the surface replenishing gas-phase molecular abundances. For this reason subsequent models focused on developing the gas-phase reaction network.

An important development of models similar to that by Herbst and Klemperer was the extension into the time domain.[115] That is, the evolution of the abundance of molecular species could be tracked throughout the life-time of the cloud. In these first time dependent models the evolution of different species was calculated from an initial set of abundances under fixed physical conditions. Such models were later referred to as pseudo-time-dependent chemical models since in a full time-dependent model physical conditions such as temperature, density and cosmic-ray ionisation rates would also evolve with time.[116] The first pseudo-time-dependent models were devised in the late 1970s and indicated that the chemical abundances of dense interstellar clouds reach a steady state after ~10^7 years.[117, 118] Given that the estimated life-time of an interstellar cloud is 10^5 - 10^6 years these studies indicated that dense interstellar clouds may not reach a steady state before they collapse to form stars.[119, 120] These studies therefore highlighted the need for time-dependent models to be pursued further. Since the 1970s a large number of psuedo-time-dependent models have been devised, the models generally consist of only gas phase reactions with the exception of H_2 formation on the surface of dust grains. The models primary focus has been to address the question of whether gas-phase processes can account for molecular

abundancies observed in dense interstellar clouds.[121] However, as discussed previously there are molecules for which gas-phase abundances cannot be accounted for by gas-phase kinetics, the most common examples of which are CO_2 and CH_3OH. However, as discussed previously it was not clear how molecules, heavier than H_2, would desorb from the surface of the ices in dense interstellar clouds.[114] Several mechanisms for molecular desorption have been proposed but it seems the most likely candidates are heat generated *via* the exothermicity of radical recombination reactions,[122] or the impact of heavy Fe nuclei cosmic-rays.[123] To fully review the development of astrochemical models is beyond the scope of this thesis but numerous reviews can be found in the literature.[115, 124, 125]

An example of a time-dependent model applicable to the results presented in this thesis is the UCL_CHEM model.[126, 127] This code was first developed in 1999 by Viti and Williams.[126] This model has subsequently been developed to include the experimentally determined rate coefficient for the surface reaction of ethene and O atoms (discussed in Section 1.8.3).[108, 109] This particular implementation of the model simulates star formation in two steps.[128] During Phase I the gas is initially present as would be expected in a diffuse interstellar cloud and so the gas-phase species are present in their atomic form. The gas transforms into molecular matter *via* two reaction networks. The gas-phase network is based on the University of Manchester Institute of Science and Technology (UMIST) database whilst the surface reaction network includes the hydrogenation of species which adsorb onto the surface of the dust grains and the oxygen atom addition to ethene. In this first phase icy mantles form on the surface of the interstellar dust grains and the density of the cloud increases to eventually form a dense core in which a star can form. During Phase II the newly forming star heats the surrounding gas and dust causing the sublimation of icy mantles. The gas-phase and surface abundance of molecular species is determined as the cloud evolves through phases I and II. The product of the reaction of ethene and O atoms, ethylene oxide, was shown to desorb into the gas-phase during phase II. The model was able to qualitatively reproduce the abundances of ethylene oxide towards high-mass star-forming regions. This study therefore confirmed that the addition of O atoms to ethene is possible under interstellar conditions given the laboratory determined rate coefficient.

Models which solve coupled rate equations have been exceptionally successful when describing gas-phase chemistry in the interstellar medium. Models, such as UCL_CHEM, use coupled rate equations to describe surface reactions since rate equations are easily implemented into their models. However, whilst accretion and desorption onto dust grains is well described by such rate equations, calculations of molecular formation rates neglect the intrinsic stochastic nature of surface reaction kinetics.[129] This stochastic nature can be better described by Monte Carlo simulations. Rate equation models directly calculate the surface abundances of products whilst Monte Carlo simulations calculate the probability of states and so take account of statistical fluctuations. As a result Monte Carlo simulations are able to take account of the ice structure, for

example it's porosity or molecular phases. However, Monte Carlo simulations are far more computer intensive and so it is only recently that they have become viable alternatives to rate equation models. The first model to consider the surface chemistry of the interstellar medium using Monte Carlo simulations was performed by Charnley in 1998.[129] However, this model only considered grain chemistry and it wasn't until 2012 when the first Monte Carlo model considering gas and grain chemistry was published.[130] Whilst this 2012 model only considers 29 surface reactions their approach allowed them to determine the morphology of the ice, layer by layer, as a function of time, and to ascertain the environment or environments for individual molecules.

As discussed in Section 1.7.3 Monte Carlo simulations have also been used to model the experimental yields of H_2CO and CH_3OH when CO and H atoms react on surfaces in the laboratory.[81] The Monte Carlo simulations were able to determine the H atom surface abundance by taking into account the layered structure of the ice as well as the H-atom flux, diffusion, reaction and desorption. In rate equation models only the H-atom flux, diffusion, reaction and desorption are taken into account. The rate coefficients, extracted using this Monte Carlo model, were extended to simulate the same reaction under interstellar conditions, where the H atom flux is extremely low. Good agreement was found between the models predicted CH_3OH abundance and observed CH_3OH abundance in the ISM. The authors were therefore able to definitively determine that the addition of H atoms to CO is the dominant formation pathway for CH_3OH. This study highlights the advantages of Monte Carlo methods when extrapolating reactions observed in the laboratory into an interstellar context.

1.10 Summary

This Chapter describes the cycle of matter between stars and the interstellar medium. The molecules present in the interstellar medium dictate the rate of star formation and in turn star formation dictates the atoms available for molecular formation. Many molecules, such as carbon monoxide, are formed in the gas-phase. However, molecules essential for life such as water and CO_2 are inefficiently formed in the gas-phase. Laboratory work over the last two decades has transformed our understanding of thermal surface chemistry in the interstellar medium. It seems that the combination of H and O atom surface reactivity can begin to explain the large abundancies of water, methanol and carbon dioxide in interstellar ices. The recent inclusion of N atom surface reactivity, not discussed here, has led to a complex reaction network for the surface of interstellar ices. This reaction network is well summarised in Figure 1.9.1.[1] However, this reaction network is almost certainly incomplete. The reaction network in Figure 1.9.1 does not include the reactivity of more complex organic molecules. Many organic molecules are observed in the gas-phase in interstellar clouds, and their large molecular masses will result in freeze-out onto interstellar ices. The surface reactions of large interstellar molecules may be intermediate steps in the formation

of molecules such as amino acids which are essential for life. The following Chapter will discuss the experimental apparatus used at UCL. The subsequent Chapters will discuss the results of experimental investigations into the surface chemistry of oxygen atoms and the desorption of small molecules from the surface of amorphous porous dust grains.

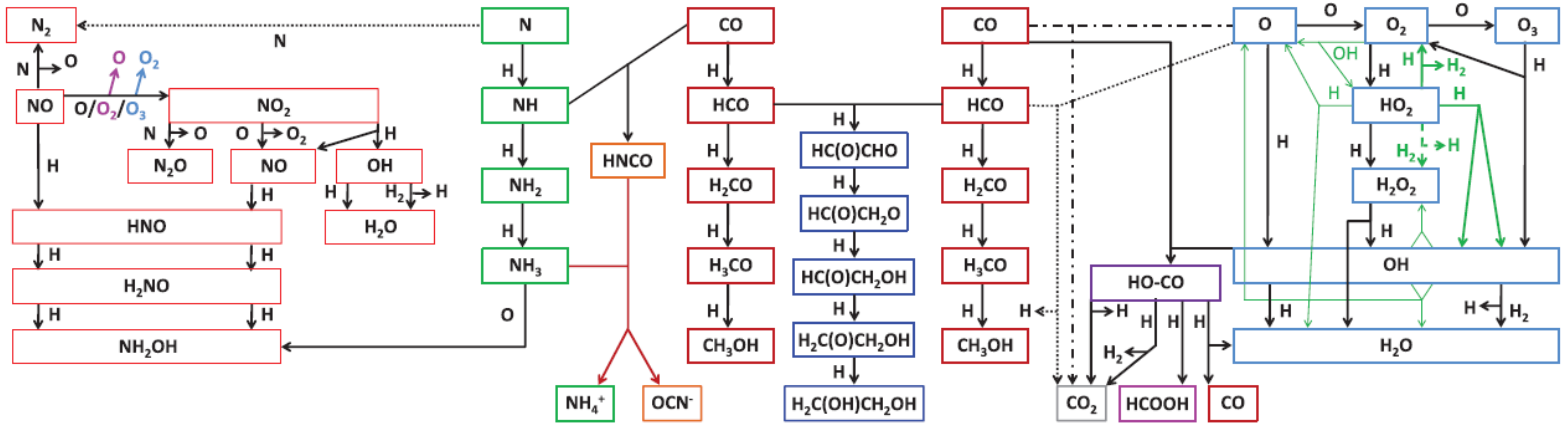

Figure 1.9.1: A summary of the atom addition reactions in the literature. The arrows indicate possible pathways, but it should be noted that their efficiency and influence on molecule abundances in space depends on a number of different parameters. Moreover, other (energetic) processes are at play as well. The take home message is that solid state chemistry is complex and that non-energetic ice processing offers pathways to form both small and abundant as well as larger and complex species (Taken from reference 1).

1.10 References

1. H. Linnartz, S. Ioppolo and G. Fedoseev, *Int. Rev. Phys. Chem.*, 2015, **34**, 205-237.
2. S. C. O. Glover, *Astrophysical Journal*, 2003, **584**, 331-338.
3. J. C. Collins and M. J. Perry, *Physical Review Letters*, 1975, **34**, 1353-1356.
4. K. A. Olive, *Science*, 1991, **251**, 1194-1199.
5. P. J. E. Peebles, *Astrophysical Journal*, 1966, **146**, 542-&.
6. R. V. Wagoner, W. A. Fowler and F. Hoyle, *Astrophysical Journal*, 1967, **148**, 3-&.
7. S. Lepp, P. C. Stancil and A. Dalgarno, *J. Phys. B-At. Mol. Opt. Phys.*, 2002, **35**, R57-R80.
8. F. Hoyle and W. A. Fowler, *Astrophys. J.*, 1960, **132**, 565-590.
9. J. E. Dyson and D. A. Williams, *The Physics of the Interstellar Medium*, Institute of Physics, Bristol, 2nd Edition edn., 1997.
10. T. P. Snow and B. J. McCall, in *Annual Review of Astronomy and Astrophysics*, Annual Reviews, Palo Alto, 2006, vol. 44, pp. 367-414.
11. J. T. Robert, *Publications of the Astronomical Society of the Pacific*, 1930, **42**, 214.
12. https://www.eso.org/public/images/eso0102a/, (accessed 16/06/2016).
13. https://www.eso.org/public/images/eso0102b/, (accessed 16/06/16).
14. S. H. Kim, P. G. Martin and P. D. Hendry, *Astrophysical Journal*, 1994, **422**, 164-175.
15. R. C. Bless and B. D. Savage, *Astrophysical Journal*, 1972, **171**, 293-&.
16. D. A. Williams and E. Herbst, *Surf. Sci.*, 2002, **500**, 823-837.
17. R. C. Bohlin, B. D. Savage and J. F. Drake, *Astrophysical Journal*, 1978, **224**, 132-142.
18. T. deGraauw, D. C. B. Whittet, P. A. Gerakines, O. H. Bauer, D. A. Beintema, A. C. A. Boogert, D. R. Boxhoorn, J. E. Chiar, H. Feuchtgruber, F. P. Helmich, A. M. Heras, R. Huygen, D. J. M. Kester, D. Kunze, F. Lahuis, K. F. Leech, D. Lutz, P. W. Morris, T. Prusti, P. R. Roelfsema, A. Salama, S. G. Schaeidt, W. A. Schutte, H. W. W. Spoon, A. Tielens, E. A. Valentijn, B. Vandenbusshe, E. F. vanDishoeck, P. R. Wesselius, E. Wieprecht and C. M. Wright, *Astronomy & Astrophysics*, 1996, **315**, L345-L348.
19. W. A. Schutte, A. Tielens, D. C. B. Whittet, A. Boogert, P. Ehrenfreund, T. deGraauw, T. Prusti, E. F. vanDishoeck and P. Wesselius, *Astronomy & Astrophysics*, 1996, **315**, L333-L336.
20. E. F. vanDishoeck, F. P. Helmich, T. deGraauw, J. H. Black, A. C. A. Boogert, P. Ehrenfreund, P. A. Gerakines, J. H. Lacy, T. J. Millar, W. A. Schutte, A. Tielens, D. C. B. Whittet, D. R. Boxhoorn, D. J. M. Kester, K. Leech, P. R. Roelfsema, A. Salama and B. Vandenbussche, *Astronomy & Astrophysics*, 1996, **315**, L349-L352.
21. D. C. B. Whittet, W. A. Schutte, A. Tielens, A. C. A. Boogert, T. deGraauw, P. Ehrenfreund, P. A. Gerakines, F. P. Helmich, T. Prusti and E. F. vanDishoeck, *Astronomy & Astrophysics*, 1996, **315**, L357-L360.
22. B. T. Draine, *Annual Review of Astronomy and Astrophysics*, 2003, **41**, 241-289.
23. J. F. McCarthy, W. J. Forrest, D. A. Briotta and J. R. Houck, *Astrophysical Journal*, 1980, **242**, 965-975.
24. C. H. Smith, C. M. Wright, D. K. Aitken, P. F. Roche and J. H. Hough, *Monthly Notices of the Royal Astronomical Society*, 2000, **312**, 327-361.
25. F. Huisken, C. Jaeger, H. Mutschke and T. Henning, *Diamond and Related Materials*, 2009, **18**, 392-395.
26. V. Mennella, L. Colangeli, E. Bussoletti, P. Palumbo and A. Rotundi, *Astrophysical Journal*, 1998, **507**, L177-L180.
27. R. Papoular, J. Conard, O. Guillois, I. Nenner, C. Reynaud and J. N. Rouzaud, *Astronomy & Astrophysics*, 1996, **315**, 222-236.
28. M. Schnaiter, H. Mutschke, J. Dorschner, T. Henning and F. Salama, *Astrophysical Journal*, 1998, **498**, 486-496.

29. M. Steglich, C. Jaeger, G. Rouille, F. Huisken, H. Mutschke and T. Henning, *Astrophysical Journal Letters*, 2010, **712**, L16-L20.
30. A. J. Adamson, D. C. B. Whittet and W. W. Duley, *Monthly Notices of the Royal Astronomical Society*, 1990, **243**, 400-404.
31. I. Butchart, A. D. McFadzean, D. C. B. Whittet, T. R. Geballe and J. M. Greenberg, *Astronomy & Astrophysics*, 1986, **154**, L5-L7.
32. J. E. Chiar, A. Tielens, D. C. B. Whittet, W. A. Schutte, A. C. A. Boogert, D. Lutz, E. F. van Dishoeck and M. P. Bernstein, *Astrophysical Journal*, 2000, **537**, 749-762.
33. C. Jaeger, S. Krasnokutski, A. Staicu, F. Huisken, H. Mutschke, T. Henning, W. Poppitz and I. Voicu, *Astrophysical Journal Supplement Series*, 2006, **166**, 557-566.
34. M. Schnaiter, T. Henning, H. Mutschke, B. Kohn, M. Ehbrecht and F. Huisken, *Astrophysical Journal*, 1999, **519**, 687-696.
35. Y. J. Pendleton and L. J. Allamandola, *Astrophysical Journal Supplement Series*, 2002, **138**, 75-98.
36. V. Mennella, G. M. M. Caro, R. Ruiterkamp, W. A. Schutte, J. M. Greenberg, J. R. Brucato and L. Colangeli, *Astronomy & Astrophysics*, 2001, **367**, 355-361.
37. L. J. Allamandola, S. A. Sandford, A. Tielens and T. M. Herbst, *Astrophysical Journal*, 1992, **399**, 134-146.
38. P. Ehrenfreund, F. Robert, L. Dhendecourt and F. Behar, *Astronomy & Astrophysics*, 1991, **252**, 712-717.
39. M. Steglich, C. Jager, F. Huisken, M. Friedrich, W. Plass, H. J. Rader, K. Mullen and T. Henning, *Astrophysical Journal Supplement Series*, 2013, **208**.
40. E. F. van Dishoeck, E. Herbst and D. A. Neufeld, *Chemical Reviews*, 2013, **113**, 9043-9085.
41. E. L. Gibb, D. C. B. Whittet, A. C. A. Boogert and A. Tielens, *Astrophysical Journal Supplement Series*, 2004, **151**, 35-73.
42. S. P. Willner, F. C. Gillett, T. L. Herter, B. Jones, J. Krassner, K. M. Merrill, J. L. Pipher, R. C. Puetter, R. J. Rudy, R. W. Russell and B. T. Soifer, *Astrophysical Journal*, 1982, **253**, 174-187.
43. D. C. B. Whittet, *Dust in the Galactic Environment* Insitute of Physics Publications, Bristol, 2003.
44. J. H. Lacy, F. Baas, L. J. Allamandola, S. E. Persson, P. J. McGregor, C. J. Lonsdale, T. R. Geballe and C. E. P. Vandebult, *Astrophysical Journal*, 1984, **276**, 533-543.
45. R. J. A. Grim, F. Baas, T. R. Geballe, J. M. Greenberg and W. Schutte, *Astronomy & Astrophysics*, 1991, **243**, 473-477.
46. J. H. Lacy, J. S. Carr, N. J. Evans, F. Baas, J. M. Achtermann and J. F. Arens, *Astrophysical Journal*, 1991, **376**, 556-560.
47. E. F. van Dishoeck, *Annual Review of Astronomy and Astrophysics*, 2004, **42**, 119-167.
48. J. E. Chiar, A. J. Adamson, T. H. Kerr and D. C. B. Whittet, *Astrophysical Journal*, 1994, **426**, 240-248.
49. J. E. Chiar, A. J. Adamson, T. H. Kerr and D. C. B. Whittet, *Astrophysical Journal*, 1995, **455**, 234-243.
50. H. Linnartz, J. B. Bossa, J. Bouwman, H. M. Cuppen, S. H. Cuylle, E. F. van Dishoeck, E. C. Fayolle, G. Fedoseev, G. W. Fuchs, S. Ioppolo, K. Isokoski, T. Lamberts, K. I. Oberg, C. Romanzin, E. Tenenbaum and J. F. Zhen, in *Molecular Universe*, eds. J. Cernicharo and R. Bachiller, Cambridge Univ Press, Cambridge, 2011, DOI: 10.1017/s1743921311025142, pp. 390-404.
51. H. J. Fraser, M. P. Collings, J. W. Dever and M. R. S. McCoustra, *Monthly Notices of the Royal Astronomical Society*, 2004, **353**, 59-68.
52. H. M. Cuppen, E. M. Penteado, K. Isokoski, N. van der Marel and H. Linnartz, *Monthly Notices of the Royal Astronomical Society*, 2011, **417**, 2809-2816.
53. J. E. Chiar, A. J. Adamson and D. C. B. Whittet, *Astrophysical Journal*, 1996, **472**, 665-672.

54. P. A. Gerakines, D. C. B. Whittet, P. Ehrenfreund, A. C. A. Boogert, A. Tielens, W. A. Schutte, J. E. Chiar, E. F. van Dishoeck, T. Prusti, F. P. Helmich and T. de Graauw, *Astrophysical Journal*, 1999, **522**, 357-377.
55. K. I. Öberg, *Chemical Reviews*, 2016, DOI: 10.1021/acs.chemrev.5b00694.
56. H. J. Fraser, M. R. S. McCoustra and D. A. Williams, *Astronomy & Geophysics*, 2002, **43**, 10-18.
57. R. Brackmann and W. L. Fite, *J. Chem. Phys.*, 1961, **34**, 1572-&.
58. R. J. Gould and E. E. Salpeter, *Astrophysical Journal*, 1963, **138**, 393-&.
59. R. J. Gould, E. E. Salpeter and T. Gold, *Astrophysical Journal*, 1963, **138**, 408-&.
60. V. Pirronello, O. Biham, C. Liu, L. O. Shen and G. Vidali, *Astrophysical Journal*, 1997, **483**, L131-L134.
61. Hollenba.D and E. E. Salpeter, *Astrophysical Journal*, 1971, **163**, 155-&.
62. V. Pirronello, C. Liu, J. E. Roser and G. Vidali, *Astronomy & Astrophysics*, 1999, **344**, 681-686.
63. J. S. A. Perry and S. D. Price, *Astrophysics and Space Science*, 2003, **285**, 769-776.
64. D. A. Williams, W. A. Brown, S. D. Price, J. M. C. Rawlings and S. Viti, *Astronomy & Geophysics*, 2007, **48**, 25-34.
65. H. C. van de Hulst, *The solid particles in interstellar space*, Utrecht, Netherlands : Drukkerij Schotanus & Jens, 1949.
66. A. Tielens and W. Hagen, *Astronomy & Astrophysics*, 1982, **114**, 245-260.
67. K. Hiraoka, T. Miyagoshi, T. Takayama, K. Yamamoto and Y. Kihara, *Astrophysical Journal*, 1998, **498**, 710-715.
68. F. Dulieu, L. Amiaud, E. Congiu, J. H. Fillion, E. Matar, A. Momeni, V. Pirronello and J. L. Lemaire, *Astronomy & Astrophysics*, 2010, **512**.
69. R. S. Smith, C. Huang and B. D. Kay, *Journal of Physical Chemistry B*, 1997, **101**, 6123-6126.
70. H. Mokrane, H. Chaabouni, M. Accolla, E. Congiu, F. Dulieu, M. Chehrouri and J. L. Lemaire, *Astrophysical Journal Letters*, 2009, **705**, L195-L198.
71. N. Miyauchi, H. Hidaka, T. Chigai, A. Nagaoka, N. Watanabe and A. Kouchi, *Chemical Physics Letters*, 2008, **456**, 27-30.
72. S. Ioppolo, H. M. Cuppen, C. Romanzin, E. F. van Dishoeck and H. Linnartz, *Astrophysical Journal*, 2008, **686**, 1474-1479.
73. S. Ioppolo, H. M. Cuppen, C. Romanzin, E. F. van Dishoeck and H. Linnartz, *Phys. Chem. Chem. Phys.*, 2010, **12**, 12065-12076.
74. H. M. Cuppen, S. Ioppolo, C. Romanzin and H. Linnartz, *Phys. Chem. Chem. Phys.*, 2010, **12**, 12077-12088.
75. S. Maity, R. I. Kaiser and B. M. Jones, *Phys. Chem. Chem. Phys.*, 2015, **17**, 3081-3114.
76. K. I. Oberg, R. T. Garrod, E. F. van Dishoeck and H. Linnartz, *Astronomy & Astrophysics*, 2009, **504**, 891-U828.
77. R. Garrod, I. H. Park, P. Caselli and E. Herbst, *Faraday Discuss.*, 2006, **133**, 51-62.
78. W. D. Geppert, R. D. Thomas, A. Ehlerding, F. Hellberg, F. Osterdahl, M. Hamberg, J. Semaniak, V. Zhaunerchyk, M. Kaminska, A. Kallberg, A. Paal and M. Larsson, in *DR2004: Sixth International Conference on Dissociative Recombination: Theory, Experiments and Applications*, eds. A. Wolf, L. Lammich and P. Schmelcher, 2005, vol. 4, pp. 26-31.
79. N. Watanabe and A. Kouchi, *Astrophysical Journal*, 2002, **571**, L173-L176.
80. K. Hiraoka, T. Sato, S. Sato, N. Sogoshi, T. Yokoyama, H. Takashima and S. Kitagawa, *Astrophysical Journal*, 2002, **577**, 265-270.
81. G. W. Fuchs, H. M. Cuppen, S. Ioppolo, C. Romanzin, S. E. Bisschop, S. Andersson, E. F. van Dishoeck and H. Linnartz, *Astronomy & Astrophysics*, 2009, **505**, 629-639.
82. S. I. B. Cartledge, J. T. Lauroesch, D. M. Meyer and U. J. Sofia, *Astrophysical Journal*, 2004, **613**, 1037-1048.
83. E. Congiu, M. Minissale, S. Baouche, H. Chaabouni, A. Moudens, S. Cazaux, G. Manico, V. Pirronello and F. Dulieu, *Faraday Discuss.*, 2014, **168**, 151-166.

84. P. Caselli, T. Stantcheva, O. Shalabiea, V. I. Shematovich and E. Herbst, *Planetary and Space Science*, 2002, **50**, 1257-1266.
85. H. H. Lee, R. P. A. Bettens and E. Herbst, *Astronomy & Astrophysics Supplement Series*, 1996, **119**, 111-114.
86. U. Hincelin, V. Wakelam, F. Hersant, S. Guilloteau, J. C. Loison, P. Honvault and J. Troe, *Astronomy & Astrophysics*, 2011, **530**.
87. D. C. B. Whittet, *Astrophysical Journal*, 2010, **710**, 1009-1016.
88. E. B. Jenkins, *Astrophysical Journal*, 2009, **700**, 1299-1348.
89. M. Minissale, E. Congiu, S. Baouche, H. Chaabouni, A. Moudens, F. Dulieu, M. Accolla, S. Cazaux, G. Manico and V. Pirronello, *Physical Review Letters*, 2013, **111**.
90. M. Minissale, E. Congiu and F. Dulieu, *J. Chem. Phys.*, 2014, **140**.
91. K. M. Bulanin, A. V. Alexeev, D. S. Bystrov, J. C. Lavalley and A. A. Tsyganenko, *Journal of Physical Chemistry*, 1994, **98**, 5100-5103.
92. R. T. Garrod, S. L. W. Weaver and E. Herbst, *Astrophysical Journal*, 2008, **682**, 283-302.
93. T. Stantcheva, V. I. Shematovich and E. Herbst, *Astronomy & Astrophysics*, 2002, **391**, 1069-1080.
94. H. J. Kimber, C. P. Ennis and S. D. Price, *Faraday Discuss.*, 2014, DOI: 10.1039/C3FD00130J.
95. J. He and G. Vidali, *Faraday Discuss.*, 2014, **168**, 517-532.
96. D. Hollenbach, M. J. Kaufman, E. A. Bergin and G. J. Melnick, *Astrophysical Journal*, 2009, **690**, 1497-1521.
97. G. J. Melnick, V. Tolls, P. F. Goldsmith, M. J. Kaufman, D. J. Hollenbach, J. H. Black, P. Encrenaz, E. Falgarone, M. Gerin, A. Hjalmarson, D. Li, D. C. Lis, R. Liseau, D. A. Neufeld, L. Pagani, R. L. Snell, F. van der Tak and E. F. van Dishoeck, *Astrophysical Journal*, 2012, **752**.
98. J. He, J. Shi, T. Hopkins, G. Vidali and M. J. Kaufman, *Astrophysical Journal*, 2015, **801**.
99. M. Minissale, E. Congiu and F. Dulieu, *Astronomy & Astrophysics*, 2016, **585**.
100. J. A. Noble, E. Congiu, F. Dulieu and H. J. Fraser, *Monthly Notices of the Royal Astronomical Society*, 2012, **421**, 768-779.
101. J. E. Chiar, Y. J. Pendleton, L. J. Allamandola, A. C. A. Boogert, K. Ennico, T. P. Greene, T. R. Geballe, J. V. Keane, C. J. Lada, R. E. Mason, T. L. Roellig, S. A. Sandford, A. G. G. M. Tielens, M. W. Werner, D. C. B. Whittet, L. Decin and K. Eriksson, *Astrophysical Journal*, 2011, **731**.
102. J. E. Roser, G. Vidali, G. Manico and V. Pirronello, *Astrophysical Journal*, 2001, **555**, L61-L64.
103. U. Raut and R. A. Baragiola, *Astrophysical Journal Letters*, 2011, **737**.
104. Y. Oba, N. Watanabe, A. Kouchi, T. Hama and V. Pirronello, *Astrophysical Journal Letters*, 2010, **712**, L174-L178.
105. J. A. Noble, F. Dulieu, E. Congiu and H. J. Fraser, *Astrophysical Journal*, 2011, **735**.
106. S. Ioppolo, G. Fedoseev, T. Lamberts, C. Romanzin and H. Linnartz, *Review of Scientific Instruments*, 2013, **84**.
107. R. T. Garrod and T. Pauly, *Astrophysical Journal*, 2011, **735**.
108. M. D. Ward and S. D. Price, *Astrophysical Journal*, 2011, **741**.
109. A. Occhiogrosso, S. Viti, M. D. Ward and S. D. Price, *Monthly Notices of the Royal Astronomical Society*, 2012, **427**, 2450-2456.
110. M. D. Ward, I. A. Hogg and S. D. Price, *Monthly Notices of the Royal Astronomical Society*, 2012, **425**, 1264-1269.
111. W. D. Watson, *Astrophysical Journal*, 1973, **183**, L17-L20.
112. W. D. Watson, *Astrophysical Journal*, 1974, **188**, 35-42.
113. E. Herbst and W. Klemperer, *Astrophysical Journal*, 1973, **185**, 505-533.
114. M. Allen and G. W. Robinson, *Astrophysical Journal*, 1977, **212**, 396-415.
115. M. Agundez and V. Wakelam, *Chemical Reviews*, 2013, **113**, 8710-8737.

116. C. M. Leung, E. Herbst and W. F. Huebner, *Astrophysical Journal Supplement Series*, 1984, **56**, 231-256.
117. E. Iglesias, *Astrophysical Journal*, 1977, **218**, 697-715.
118. S. S. Prasad and W. T. Huntress, *Astrophysical Journal Supplement Series*, 1980, **43**, 1-&.
119. L. Hartmann, J. Ballesteros-Paredes and E. A. Bergin, *Astrophysical Journal*, 2001, **562**, 852-868.
120. T. C. Mouschovias, K. Tassis and M. W. Kunz, *Astrophysical Journal*, 2006, **646**, 1043-1049.
121. A. I. Vasyunin and E. Herbst, *Astrophysical Journal*, 2013, **762**.
122. C. J. Shen, J. M. Greenberg, W. A. Schutte and E. F. van Dishoeck, *Astronomy & Astrophysics*, 2004, **415**, 203-215.
123. T. I. Hasegawa and E. Herbst, *Monthly Notices of the Royal Astronomical Society*, 1993, **261**, 83-102.
124. W. D. Watson, *Annual Review of Astronomy and Astrophysics*, 1978, **16**, 585-615.
125. E. Herbst, *Chemical Society Reviews*, 2001, **30**, 168-176.
126. S. Viti and D. A. Williams, *Monthly Notices of the Royal Astronomical Society*, 1999, **305**, 755-762.
127. S. Viti, M. P. Collings, J. W. Dever, M. R. S. McCoustra and D. A. Williams, *Monthly Notices of the Royal Astronomical Society*, 2004, **354**, 1141-1145.
128. A. Occhiogrosso, S. Viti, P. Modica and M. E. Palumbo, *Monthly Notices of the Royal Astronomical Society*, 2011, **418**, 1923-1927.
129. S. B. Charnley, *Astrophysical Journal*, 1998, **509**, L121-L124.
130. Q. Chang and E. Herbst, *Astrophysical Journal*, 2012, **759**.

Chapter 2 – Experimental Methodology and Data Analysis

2.1 Overview

The experimental apparatus at UCL is designed to study surface reactions of atoms on interstellar dust grain analogues. During the last three years, there have been several developments of the apparatus. Firstly, a Eurotherm temperature controller has been installed to facilitate linear heating during the temperature programmed desorption (TPD). Secondly, a quadrupole mass spectrometer has been installed to facilitate submonolayer experiments. Thirdly, the flux of reactants was also reduced in order to achieve submonolayer dosing. Lastly, a light bake has been incorporated into the pumping down procedure to reduce the time needed to reach the base pressure of the chamber. The results presented in this thesis are a combination of data collected before and after these changes. The results presented in Chapters Three and Four are the traditional multilayer experiments collected before changes to the chamber were made. The results presented in Chapter Five were collected after the experimental improvements to the chamber. These experimental developments will be discussed in detail in Section 2.11.

Chapters Three and Four of this thesis focus on the surface reactions of oxygen atoms. Oxygen atoms are generated using a microwave discharge in O_2 gas. The oxygen atom beam is then co-dosed with astrophysically relevant species onto a 20 mm × 10 mm × 2 mm piece of highly oriented pyrolytic graphite (HOPG). The graphite surface is held at a specific dosing temperature between 15 – 100 K. Following the deposition of reactants, in order to observe products, a temperature programmed desorption (TPD) experiment is performed. During a TPD, the surface is heated from the dosing temperature up to a temperature at which all products and reactants have desorbed from the surface into the gas-phase. When the surface temperature results in molecular thermal energies which exceed the binding energy of a particular molecule to the surface, the molecule desorbs from the surface into the gas-phase. Since each molecular species has a characteristic binding energy to the surface, each molecular species desorbs from the surface at a specific sublimation temperature. As a result, the sublimation temperature of each molecular species can aid the identification of signals in the mass spectra. In the original configuration of the apparatus, after desorbing from the surface, the reactants and products enter the source region of a time-of-flight mass spectrometer (TOFMS) which is located in front of the surface. The gas-phase reactants and products are then ionised using electron ionisation and detected. The signals in the mass spectra can then be put on an absolute scale by determining the detection efficiency of the TOFMS. Each experiment is repeated at several different dosing temperatures. The resulting data set is a profile of product yield as a function of dosing surface temperature. A model can then be used to extract kinetic data from these experimental yields, such as desorption

energies of reactants and reaction probabilities of the reactions which form the products observed. A diagram of the original configuration of the experimental apparatus can be seen in Figure 2.1.1.

Chapter Five of this thesis focuses on the desorption characteristics of small molecules from amorphous porous carbonaceous dust grains (APCDG). The APCDG were produced in laser ablation experiments and consist of nanometer sized grains of fullerene-like structures. In separate experiments each small molecule is dosed onto the surface at a range of surface coverages. The surface is then heated linearly from the dosing temperature up to 200 K in a TPD experiment. Upon desorbing from the surface, gas-phase reactants and products are ionised using electron ionisation and now identified using Quadrupole Mass Spectrometry (QMS).

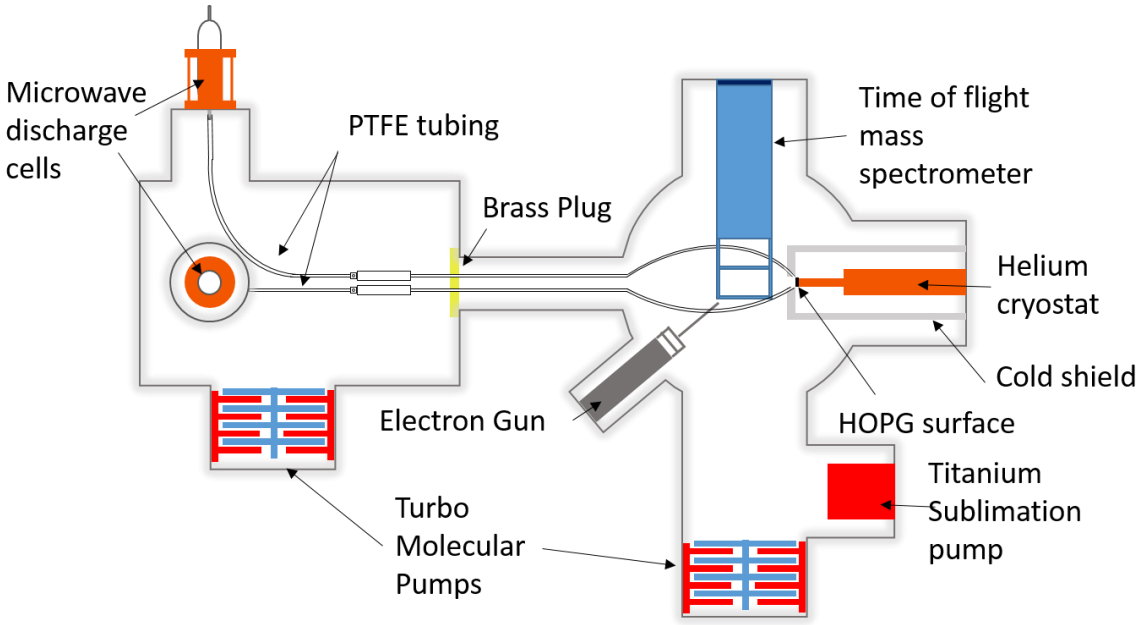

Figure 2.1.1: A schematic diagram of the experimental arrangement.

2.2 Vacuum Set-up

The experimental apparatus at UCL comprises two differentially pumped stainless steel vacuum chambers, sealed with conflat flanges. The first chamber, the source chamber, has a base pressure of 1×10^{-7} Torr where the pressure is monitored by a Penning gauge. This base pressure is maintained using a turbomolecular pump (TMP) with a pumping speed of 400 l s^{-1} for N_2, backed by a two-stage rotary pump. The function of the source chamber is to house two identical microwave discharge cells and to transport the reactants to the main chamber. During transportation, through the source chamber, the dosing lines are differentially pumped to achieve a sufficiently low flux of reactants at the target surface; a flux relevant to the interstellar medium. The differential pumping of the dosing lines raises the source chamber pressure to 1×10^{-6} Torr during dosing.

The main chamber is a UHV environment with a base pressure of 1×10^{-10} Torr, the pressure is monitored using an ion gauge. The main chamber houses a cryogenically cooled HOPG substrate mounted adjacent to a mass spectrometer. In Chapters Three and Four this mass spectrometer is a TOFMS and in Chapter Five this mass spectrometer is a QMS. UHV environments are crucial for studying surface chemistry in the laboratory, these low pressures ensure that the interaction of gas-phase species with one another and the interaction of background gas with the surface is negligible. One can therefore be sure that the reactions observed during the experiment occur on the surface, rather than in the gas-phase, and that these surface reactions are not affected by background gas accreting onto the surface during the experiment. As in the source chamber, the main chamber is pumped using a TMP, with a pumping speed of 400 l s^{-1} for N_2, backed by a two stage rotary pump. However, hydrogen is inefficiently pumped by momentum transfer pumps such as TMPs due to its low mass. In order to reduce the main chamber pressure further a titanium sublimation pump is also installed to efficiently pump hydrogen. Finally, to reach the lowest pressure possible, the chamber is baked to 60 °C to reduce the water abundance. A traditional bake of a UHV chamber raises the temperature of the chamber to 100 °C. However, the cold head mounted in the main chamber cannot be heated above 70 °C and so a traditional bake is not possible. The vapour pressure of water is an exponential function with respect to temperature and so a significant amount of water can be removed from the chamber by baking to 60 °C. During dosing the chamber pressure ranges from 1×10^{-10} - 1×10^{-8} Torr. The chamber pressure during dosing is dependent on the surface temperature and the reactants used. For example, if molecular oxygen is dosed, when the surface temperature exceeds 30 K, the dosing pressure exceeds the base pressure of the chamber. This is due to molecular oxygen's low residence time on the surface at 30 K. However, if an organic molecule such as propyne is dosed at 30 K the pressure in the main chamber will be equivalent to the base pressure. This is due to propyne desorbing from the surface at ~100 K.

For comparison, dense interstellar clouds have an approximate pressure of 1×10^{-14} Torr.[1] The pressure, in a typical UHV laboratory vacuum chamber, differs from the pressures in dense clouds for two reasons. The first is that vacuum technology available in a standard university laboratory is not quite able to reach these incredibly low pressures. The second is that even if the low pressures of dense interstellar clouds was obtainable, to maintain this low pressure, the flux of reactants to the surface, would have to be several orders of magnitudes smaller than are typically used in these types of experiments. A flux low enough to maintain the low pressures in interstellar clouds, would result in extremely slow reactions which would not be observable on a laboratory time scale. The apparatus at UCL increases the number density of reactants without approaching pressures at which three-body interactions can occur, and so, ensures that reactions relevant to the ISM can be observed on a laboratory time scale.

2.3 Oxygen Atom Generation

In Chapters Three and Four the surface chemistry of oxygen atoms is studied. The oxygen atoms are generated using a microwave discharge in molecular oxygen (O_2) (99.5%). The microwave discharge is contained within a Pyrex discharge cell measuring 260 mm long with an outer diameter of 25.5 mm. The Pyrex discharge cell is housed in the source chamber of the experimental apparatus (Figure 2.3.1). The gas flow from the cylinder, is controlled using a needle valve, and connected to a glass to metal seal at the top of the discharge cell by a Cajon fitting. The discharge cells are surrounded by a two piece copper radiator, as designed by McCullough *et al*.[2, 3] The copper radiators are designed such that there is minimum clearance between the copper radiator and the Pyrex cell. Minimum clearance between the cell and the copper radiator is required to ensure efficient coupling of the microwaves to the plasma whilst avoiding any strain on the Pyrex cells. Each half of the copper radiator has two pairs of 2 mm wide slots which link to female type-N connectors, (Figure 2.3.2). When microwaves are applied to the copper radiator a potential difference is induced across the walls of these slots. Since the centre of each 2 mm wide slot is half a wavelength from the centre of the adjacent slot the electric fields of each slot are in phase. The superposition of the potential difference from the four pairs of radiator slots gives rise to an oscillating electric field between the radiators. This arrangement of slots in the copper radiators means that no tuning of the cavity is required. The superposition of the microwaves is evident in used cells by the etching pattern (Figure 2.3.3). If a few molecules in the Pyrex cell are ionised, for example by touching the high voltage tip of a Tesla coil to the outside of the discharge cell, the free electrons oscillate in the electric field generated by the superposition of the microwaves. The oscillating electrons collide with molecules in the discharge cell causing further molecular ionisation in a 'cascade' effect. The cascade generates a plasma in the discharge cell. The plasma in the discharge cell is referred to as a 'low temperature plasma' because whilst the electrons oscillate in the electric field, the atoms and molecules are too heavy and so remain close to ambient temperatures.

The microwaves are generated by a Sairem microwave unit with a frequency of 2.45 GHz. The microwaves are guided to the copper radiators *via* two Sucoflex wave guides. The lengths of the two wave guides differ by half a wavelength and so the microwaves arrive at either side of the copper radiators 180˚ out of phase.[4] The microwave power available from the microwave generator is adjustable up to 300 W, however, the microwave power used in these experiments is 180 W. This microwave power is chosen to minimise the reflected power. Limiting reflected power is important for safe operation of the microwave discharge and to maximise the lifetime of the microwave generator. High levels of reflected power heat the magnetron and shorten its life

time, and so no more than 10 % reflected power is recommended. Typically, the reflected power achieved in these experiments is 2 % of the output power.

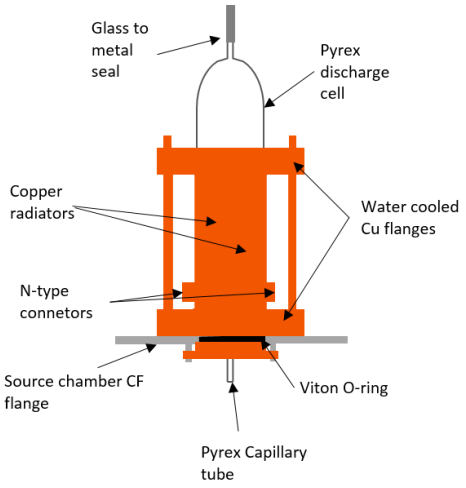

Figure 2.3.1: A diagram of the microwave discharge cell.

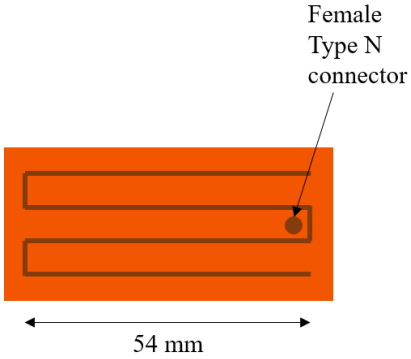

Figure 2.3.2: A schematic diagram of the inside surface of a semi-cylindrical microwave radiator.

Figure 2.3.3: A photograph of the etching pattern on a used microwave discharge cell

A diagram of the entire microwave discharge source is shown in Figure 2.3.1. The microwave cavity is water cooled by being in good thermal contact with two water cooled copper flanges at either end of the copper radiators. The water cooling of the microwave cavity increases the yield of atomic species, since atomic recombination on Pyrex surfaces is thought to become more efficient with increasing temperature.[4] The water cooling also prevents the discharge cell from overheating. Since the copper radiators are in close proximity to the Pyrex cell the heating and, therefore, expansion of the Pyrex cell can put strain on the cell. Water cooling minimises the expansion of the cell and so the cell is less likely to become damaged during operation. Before installation of a new cell, the cell is also soaked in phosphoric acid for at least 12 hours and then rinsed in distilled water. This procedure passivates the surface and further reduces the probability of atomic recombination.[5]

The precursor gas used for atomic oxygen generation was oxygen (O_2) (99.5 %). In order to remove any contamination of the discharge cell by air, the gas inlet lines are flushed several times with O_2 before being switched on. A pressure of 0.2 Torr O_2 gas is used in the discharge cell. At low pressures there are fewer collisions and so fewer recombination events. However, the pressure must be sufficient for the microwave discharge to be stable. When an O_2 pressure of 0.2 Torr is used the microwave discharge is stable and the dissociation efficiency is 20 %.[6] This pressure of O_2 is used to generate O atoms in the microwave discharge in Chapters Three and Four.

2.4 Transport of Reactants

There are two dosing lines installed in the source chamber, the first is the microwave discharge cell, described above, and the second is an identical source cell to which no microwaves are applied. The reactants from each source cell are transported to the target surface through separate dosing lines. The gas exiting the Pyrex source cells initially passes through the exit capillary of the cell (1 mm internal diameter, 40 mm long) which is attached to a ¼ inch polytetrafluoroethylene (PTFE) tube. PTFE is used for atomic and molecular transportation due to its inertness and vacuum compatibility. PTFE's inertness minimises atomic recombination and it's structure makes it a suitable flexible material for use in a vacuum chamber. The first section of the PTFE tubing transports the gas flow, in each dosing line, to separate PTFE connectors. The PTFE connectors have two 2 mm diameter pumping holes which allow a significant proportion of the gas in each dosing line to be differentially pumped. The differential pumping allows the source cell pressure to be approximately 0.2 Torr, a relatively high pressure, whilst achieving a low flux of reactants to the target surface. The differential pumping results in a source chamber pressure of ~ 1 x 10^{-6} Torr. After the pumping connectors, the reactants in each dosing line flow through separate PTFE blocks which both have diameters of 5 mm and lengths of 10 cm. The gas in each dosing line then flows separately through two identical second PTFE connectors which have exit diameters of 1 mm. These second PTFE connectors guide the gas flow in each dosing lines into two separate PTFE tubes. These PTFE tubes then pass through a brass plug into the UHV chamber, the tubes are secured in the brass plug using O-rings. The brass plug creates a barrier between the source chamber and the main chamber. This ensures that only gas from within the PTFE tubes will reach the target surface.

There are two different mounting positions for the tubes in the main chamber. One directs the reactants to the HOPG surface which is used when surface reactions are observed. Under normal operating conditions the tubes pass beneath the mass spectrometer and are held in front of the HOPG target by stiff copper wire which is mounted to the radiation shield of the coldhead. This copper wire mount holds the PTFE tubes approximately 10 mm from the target and at a 45° angle to its surface.

The second mounting of the PTFE tubing, in the main chamber, directs the gas directly into the source region of the TOFMS. This second mounting is used when the O atom dissociation efficiency is measured. In this alternative mounting, the tubes are positioned such that the gas flow can directly overlap with the electron beam. Oxygen atoms will recombine on surfaces and so can only be detected when the electron beam directly overlaps with the primary gas flow. The PTFE tubes fit into a PTFE block mounted onto the repeller plate of the TOFMS, Figure 2.4.1. The PTFE tube is held equidistant from the repeller plate and the middle plate and the electron beam intersects the gas flow before any collisions of the gas with any surfaces.

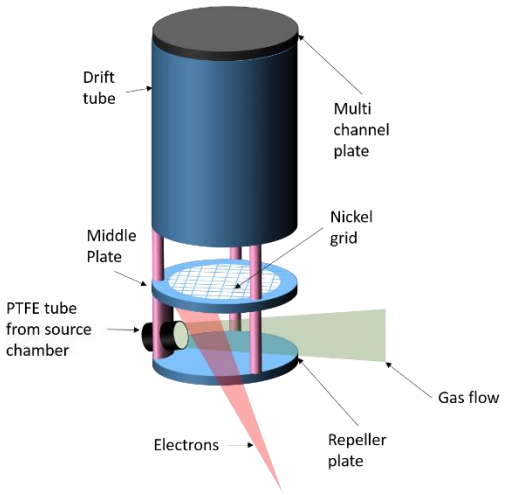

Figure 2.4.1: A diagram of the PTFE tube mounting for gas-phase detection of O atoms and the TOFMS

2.5 Coldhead and Target Mount

The reactions studied in Chapters Three and Four of this thesis occur on a HOPG surface. The graphite surface is highly ordered, with a mosaic spread of 3.5 ° ± 1.5 °, whilst carbonaceous interstellar dust is likely to be amorphous. However, it is standard practice to use ordered surfaces as targets in studies of surface astrochemistry. One advantage of using ordered surfaces is that reactions can be more directly compared with theory than reactions occurring on amorphous surfaces. A diagram of the surface mounting can be seen in Figure 2.5.1. The target mount which holds the graphite surface is mounted onto the coldhead of a closed-cycle helium cryostat. The coldhead of the closed-cycle helium cryostat can reach a minimum temperature of 8 K which results in a minimum HOPG surface temperature of 10 K – 20 K. Within the target mount is a tantalum strip heater, by passing a constant current through this heater, when the cold head is running, the graphite surface temperature can be increased up to a maximum of 500 K. The

maximum temperature of 500 K is used to clean the surface. Surface temperatures of 10 – 20 K are typical of interstellar dust grain temperatures in dense interstellar clouds. However, studying surface reactions over a wide range of temperatures allows kinetic parameters such as desorption energies of reactants and reaction probabilities to be extracted.

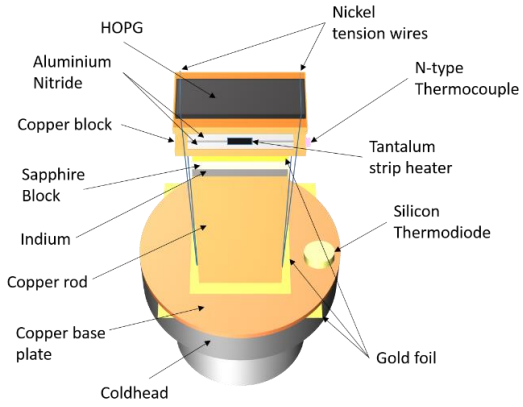

Figure 2.5.1: A diagram of the surface mounting onto the coldhead

The HOPG surface sits upon a removable hollow copper block, within this hollow copper block is the tantalum strip heater. The tantalum strip heater is held between two blocks of aluminium nitride. Aluminium nitride thermally connects the heater to the copper block and HOPG surface whilst electrically isolating the heater. Thermal contact between the HOPG surface, the copper block and the coldhead is achieved by a copper rod and a copper base plate. The copper base plate is bolted to the coldhead with a layer of gold between the pieces. Gold foil is used to make good thermal contact between surfaces since it is a good thermal conductor and a soft metal which can fill microscopic defects in the contacting surfaces. The copper rod this then bolted to the copper base plate with a layer of gold between them. Again, the layer of gold improves the thermal contact between the base plate and the rod by filling microscopic defects in the contact surfaces. The removable copper block and HOPG surface are secured to the copper rod by nickel tensioning wires. These wires are held tight by a sprung tensioning system which ensures that the HOPG surface, copper block and copper rod remain in good thermal contact, despite any thermal expansion and contraction which may take place during heating the surface. Between the copper rod and the copper block is a piece of sapphire. Sapphire is an excellent material when low temperatures and high temperatures are required on a surface. Below 50 K sapphire is an excellent thermal conductor and so efficiently thermally connects the surface to the coldhead to achieve a minimum surface temperature of 10 – 20 K. Above 200 K sapphire becomes a poor thermal conductor and so thermally isolates the surface from the cold head. Without the sapphire the thermal load from the heater, when heating to 500 K, would be unacceptably high and damage the coldhead. Between the copper block and the sapphire is a sheet of gold and between the sapphire and the copper rod is a layer of indium. Again these soft metals fill microscopic defects

and so improve thermal contact. The entire coldhead and target mount is surrounded by a cylindrical aluminium cold shield. The purpose of the cold shield is to minimise the heating of the surface *via* black body radiation given off by the walls of the chamber.

The temperature of the surface is monitored using an N-type thermocouple. The N-type thermocouple is bolted to the side of the copper block. A specific dosing temperature is maintained by passing a current through the heater. The current required is manually optimised to maintain a constant temperature reading for the N-type thermocouple. Once the reaction has occurred at a specified dosing temperature, the heater is turned off and so the surface is cooled to the minimum surface temperature (10 K - 20 K). A current of 15 A is then passed through the heater to raise the surface temperature to approximately 200 K during the TPD. The heating rate profile can be seen in Figure 2.5.2. However, developments of the experimental apparatus now allow the heating rate to be linear during the TPD (Section 2.11). Linear heating rates are used in the experiments described in Chapter 5. As the surface is heated, reactants and products sublime from the surface at different temperatures depending on their surface binding energy. When the molecules desorb from the HOPG they enter the source region of the TOFMS. The HOPG target is positioned such that it is approximately 30 mm from the centre of the source region of the TOFMS. The HOPG target's vertical position is such that it is equidistance between the planes of the repeller and middle plates of the TOFMS (Figure 2.4.1).

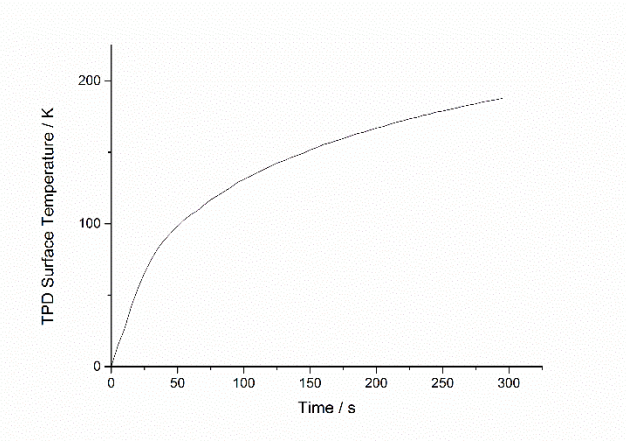

Figure 2.5.2: The heating profile during the TPD when 15 A is passed through the Tantalum strip heater

2.6 Electron Gun

In the experiments described in Chapters Three and Four of this thesis, an electron gun is used to ionise molecules in the source region of the TOFMS. The energy of the electrons produced by the electron gun, 200 eV, is larger than the ionisation potential of any molecule present. As a result the electron gun allows the simultaneous detection of all species in the source region of the TOFMS. A diagram of the electron gun can be seen in Figure 2.6.1. The electron gun consists of a V-shaped tungsten filament housed within a stainless steel cylindrical casing. The filament tip is aligned with a 2 mm diameter aperture. A current of ~ 2.5 A is continuously passed through the filament increasing the temperature sufficiently for thermionic emission of electrons to occur. The filament and its casing are both held at a potential of – 200 V. Once the electron beam emerges from the casing it enters the aperture of a brass needle. The needle is pulsed using a high voltage pulser from 0 V to – 400 V. When the needle potential is – 400 V, the electrons do not enter the needle and so do not enter the source region of the TOFMS. The application of – 400 V to the needle is called the stopping potential. The stopping potential is pulsed on prior to the repeller plate pulse of the TOFMS, this stops ions being formed after the repeller plate is pulsed and so increases the resolution in the TOFMS spectra. For a description of the repeller plate and TOFMS see Section 2.7. If the stopping potential is not applied ions, of the same mass, formed after the repeller plate pulse will have longer flight times than ions formed before the repeller plate pulse. The result would be a tailing of the mass spectral peaks thereby reducing the resolution of the spectra. A full description of the pulsing can be found in Section 2.7.

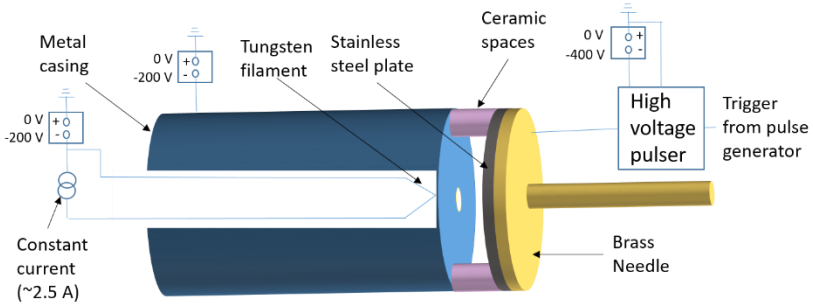

Figure 2.6.1: A diagram of the electron gun.

When the needle potential is 0 V, the electrons travel down the needle and ionise the gas in the source region of the TOFMS. Both the electron gun and target surface are positioned such that their centres are equidistant from the repeller plate and the middle plate of the TOFMS. Positioning the electron gun and target surface equidistant from the repeller plate and the middle plate ensures there is maximum overlap of the electron beam and the molecules desorbing from the target surface during the TPD. On the opposite side of the source region of the TOFMS, to the electron gun, is a Faraday cup. The primary use of the Faraday cup is to measure the current of

the electron beam using a picoammeter. Typically a current of 30 nA is used. The secondary use of the Faraday cup is to efficiently capture the electron beam, reducing the number of stray electrons in the chamber.

2.7 Time-of-Flight Mass Spectrometer

The home-built TOFMS is of a standard Wiley-McLaren design.[7] A diagram of the TOFMS can be seen in Figure 2.4.1. The TOFMS consists of a repeller plate, middle plate, drift tube and a detector made up of a pair of microchannel plates (MCPs). The repeller plate is 50 mm in diameter and held 30 mm from the middle plate using ceramic spacers. The middle plate is also 50 mm in diameter although it has an inner orifice, of diameter 32 mm. The orifice is covered with a nickel grid (90 % transmission) in order to maintain linear fields whilst still allowing the transmission of ions. The middle plate is held 30 mm from the drift tube by ceramic spacers. At the other end of the drift tube is another nickel grid. Beyond the drift tube is the MCP detector. The typical potentials used for the TOFMS are + 370 V, 0 V and -1000V for the repeller plate, the middle plate and the drift tube respectively.

Employing electron ionisation requires both the electron gun and the repeller plate to be pulsed to achieve the maximum resolution in the mass spectrum. A continuous electron beam would continue ionising molecules in the source region after the repeller plate was energised. Ions formed after the repeller plate pulse have longer flight times than expected and so produce tailing of the mass spectral peaks. Therefore pulsing both the electron gun and the repeller plate achieves the best possible peak shapes in the mass spectra. Figure 2.7.1 depicts the pulsing regime of the TOFMS. In Figure 2.7.1, t_0 denotes the beginning of the pulsing cycle. The electron gun is pulsed "on", 200 ns after t_0 by removing the stopping potential. The electron beam then passes through the source region of the TOFMS generating positive ions from the molecules present in the source region. The stopping potential is applied 1.7 μs later, turning "off" the electron beam. The repeller plate is then pulsed from 0V to - 370 V, 20 ns after the electron gun is turned off. The repeller plate voltage accelerates ions from the source region into the drift tube. The time-to-digital converter (TDC) is turned on 720 ns after the repeller plate is pulsed. Turning on the TDC starts recording ions arrival times at the MCP. The TDC stops recording arrival times 2.5 μs after being turned on and the repeller plate pulse is removed 11 μs after being applied. The cycle starts again 20 μs after t_o.

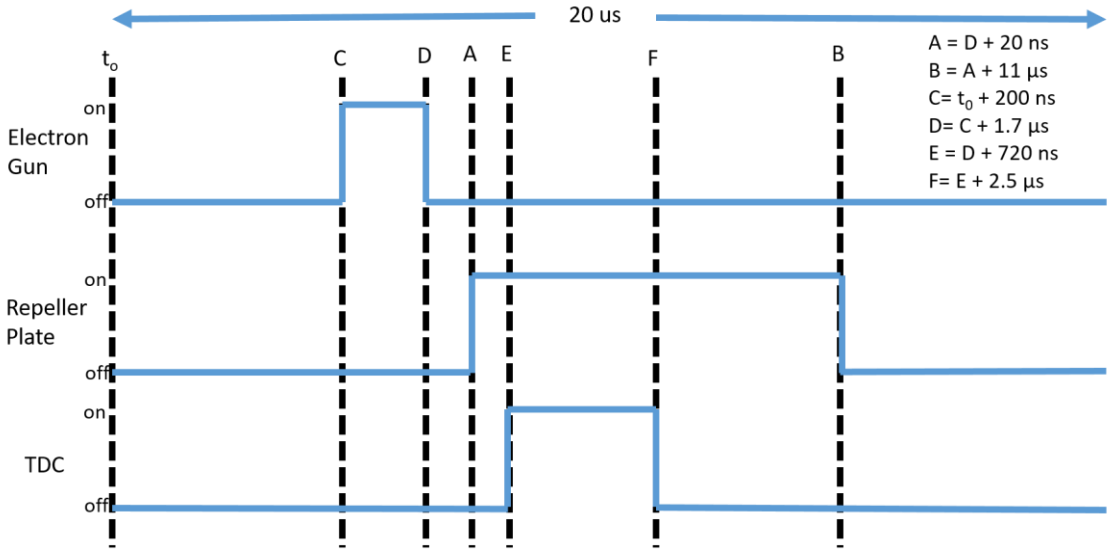

Figure 2.7.1: A diagram of the pulsing regime of the time of flight mass spectrometer.

The detector in the TOFMS is a pair of MCPs, the output from which is amplified and discriminated before being passed to the TDC. The MCPs consist of an array of 10 µm glass channels which have an extremely low work function. When an ion collides with one of the walls of the glass channels in the MCPs an electron cascade is initiated releasing approximately 10^4 electrons. Two MCPs are used so that the number of released electrons is increased to $10^7 – 10^8$ electrons for each ion and, this number of electrons produces a detectable current. The electron current is of the order of a few picoamps which is collected by a copper anode. The resulting signal from the anode first passes through an impedance matching circuit followed by a pre-amplifier, then an amplifier, before reaching a constant fraction discriminator. The constant fraction discriminator is optimised such that only electrical signals resulting from real ions hitting the MCP are passed to the TDC. Times from the TDC are recorded as a histogram of time-of-flight (resolution: 1 ns) *versus* counts in a mass spectrum.

Each ion produced in the source region of the TOFMS is subject to the same electric fields in the TOFMS. The potential energy of the fields is converted into kinetic energy of the ions. The velocity and therefore arrival time, of each ion, will depend on the mass and charge of the ion. The dependence of the arrival time on the mass to charge ratio is expressed in equation 2.7.1.

$$t = k\sqrt{\frac{m}{z}} + c \qquad (2.7.1)$$

where t is the arrival time, m is the mass, z is the charge and k and c are constants. The constant k is dependent on the magnitude of the electric fields and the length of the drift tube. The constant

c is related to the electronic timings. Equation 2.7.1 can therefore be used to convert the arrival time of each ion into their mass to charge ratio after *k* and *c* are determined in a calibration experiment.

The mass resolution of the TOFMS depends upon the spread of arrival times of ions, with a particular *m*/*z*, at the detector. The spread of arrival times is dependent upon two factors, the spread in the initial kinetic energies of the ions (energy resolution) and the initial space distribution of the ions before acceleration (space resolution). Space resolution arises due to the ionisation volume of the electron beam. The principle of space resolution can be understood by considering two ions, X^+ and Y^+, both ions have identical *m*/*z* and initial velocities. Ion X^+ is formed near the lower edge of the electron beam and so is closer to the repeller plate. Ion Y^+ is formed near the upper edge of the electron beam and so is closer to the middle plate. When the repeller plate is pulsed both ions are subject to the electric field between the middle plate and the repeller plate. Ion X^+ will have a greater potential energy and therefore acquire a larger kinetic energy than ion Y^+. As a result ion X^+ will eventually overtake ion Y^+ as they travel through the field free drift tube. Consequently, a plane will exist at which ions of the same *m*/*z* ratio and kinetic energy will arrive simultaneously regardless of their formation position in the source region. Previously, in single field TOFMSs, the spatial resolution was dependent on the geometric conditions. In the Wiley-McLaren design the ions travel through two electric fields, one between the repeller plate and the middle plate and the second between the middle plate and the drift tube. The ratio of these two fields can be tuned such that the plane, at which ion X^+ overtakes ion Y^+ is in the same plane as the detector.

Energy resolution can be understood, again, by considering two ions X^+ and Y^+. Ion X^+ and Y^+ have identical *m*/*z* and are formed at the same position in the electron beam. However, ion X^+ has an initial velocity towards the detector and ion Y^+ has an initial velocity towards the repeller plate. Upon the application of the repeller plate pulse ion X^+ is immediately accelerated towards the detector whereas ion Y^+ must first be decelerated to a velocity of zero before accelerating, in the opposite direction to its initial velocity, towards the detector. This ‘turn-around time’ causes ion Y^+ to arrive at the detector later than ion X^+. Energy resolution is also improved in the Wiley-McLaren design when compared to a single field TOFMS. In the Wiley-McLaren ions are accelerated to their maximum velocities in about 5% of their time of flight whereas in a single field TOFMS the ions reach their maximum velocity in about 50% of their time of flight. Accelerating the ions more quickly minimises the turn-around time, and so reduces energy resolution.

2.8 Data Acquisition

Each experiment discussed in Chapters Three and Four of this thesis comprises dosing reactants onto the HOPG surface held at a specific temperature. After a dosing period of one hour, the dosing lines are evacuated and the surface is cooled to the minimum surface temperature. The HOPG surface is then heated with the rate shown in Figure 2.5.2. Molecules desorb from the surface at their specific sublimation temperature and pass into the source region of the TOFMS. As the surface is heated, the time of flight of ions, formed in the source region of the TOFMS, is recorded with a duty cycle of 20 μs, as discussed in Section 2.6. Each duty cycle produces one mass spectrum which is time stamped with respect to the start of the surface heating. The count of each ion arriving at the MCP is binned in a two-dimensional matrix of time of flight (TOF) *vs* heating time. Each ions TOF corresponds to a particular *m*/*z* ratio which can be calculated using equation 2.6.1. Each heating time corresponds to a particular surface temperature. Whilst the surface temperature is not recorded in each TPD experiment, the heating time can be converted into a surface temperature using the plot in Figure 2.5.2. The two-dimensional data matrix can therefore be reported as the *m*/*z* ratios of the ions *vs* surface temperature. The two dimensional data matrix can also be plotted as a histogram of surface temperature *vs* *m*/*z*, Figure 2.8.1.

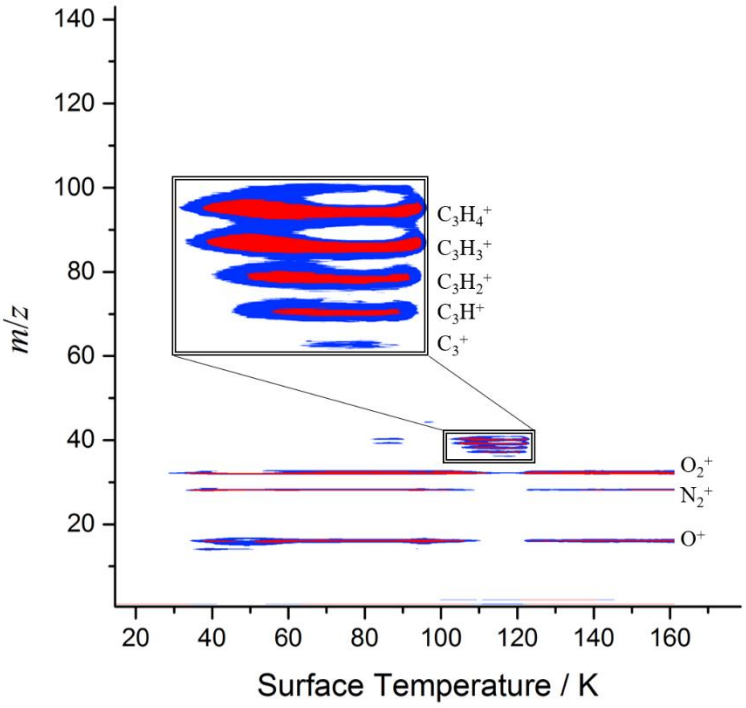

Figure 2.8.1: An example of a two dimensional histogram of ion counts recorded for the desorption of a multilayer propyne/O_2 ice from a HOPG surface. The ion fragments arising from C_3H_4 and O_2 are labelled. The insert magnifies the ion fragments arising from C_3H_4. Continuous signals can also be observed for background N_2^+.

The two dimensional matrix of *m*/*z* ratios *vs* surface temperature can be manipulated to show either the behaviour of a range of masses during the surface heating, a desorption profile, or to select a surface temperature range and extract a mass spectrum of the species desorbing at that temperature. When propyne (*m*/*z* = 40) is dosed onto the graphite surface a desorption profile for propyne can be constructed by summing the ion counts between *m*/*z* = 39.5 and 40.5, for each surface temperature during the TPD. The total counts which have a *m*/*z* ratio between 39.5 and 40.5 are then plotted as a function of surface temperature, the plot is the desorption profile of propyne (Figure 2.8.2). A desorption profile allows one to determine the surface temperature at which a molecule desorbs from the surface. From Figure 2.8.2 it can be determined that a propyne ice desorbs from a graphite surface between 90 K and 135 K. The mass spectrum of propyne can be extracted from the two-dimensional matrix by summing the ion counts between surface temperatures of 90 K and 135 K as a function of *m*/*z* ratio. The total counts recorded between a surface temperature of 90 K and 135 K are then plotted as a function of *m*/*z*, the plot is the mass spectrum of propyne, Figure 2.8.3.

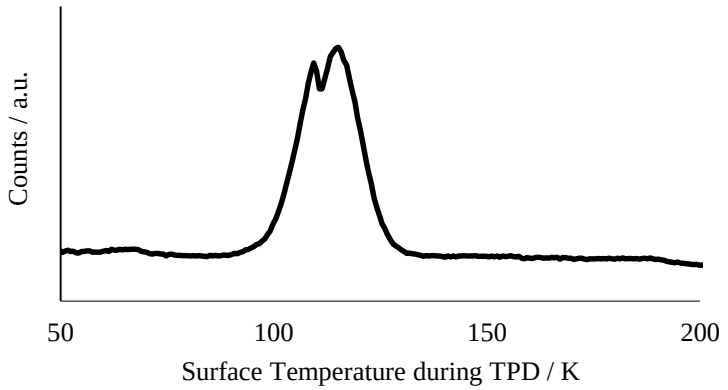

Figure 2.8.2: The desorption profile of a propyne ice deposited on a graphite surface

Desorption profiles and mass spectra enable one to identify and quantify the relative yield of products formed when O atoms react with unsaturated organic molecules on the surface. For example, if one O atom adds to propyne a signal is expected in the mass spectrum at *m*/*z* = 56. One can extract a desorption profile for *m*/*z* = 56 to determine if a molecule desorbs from the surface with this mass. If a peak is observed in the desorption profile the temperature range at which this peak desorbs from the surface can be determined. A mass spectrum over this temperature range can then be generated and the signal at *m*/*z* = 56 can be integrated to give the yield of this product. However, one must subtract a suitable background before this peak at *m*/*z* = 56 can be integrated. The background subtracted is a mass spectrum, recorded over the same temperature range in a TPD experiment, following the deposition of (in this case) propyne and O_2; an experiment in which no O atoms are present on the surface. This background subtraction procedure confirms the product signals are a result of the oxygen atoms generated in the

discharge. This integration procedure is repeated for each of the three experiments performed at each individual surface dosing temperature, and the total counts of the parent ion m/z = 56 are then averaged for the three repeats at each surface dosing temperature. The uncertainty associated with the total counts is estimated using the standard deviation of the three repeats at each surface dosing temperature. The procedure is then repeated for each dosing surface temperature studied. The result is a profile of the relative yield of product as a function of dosing surface temperature.

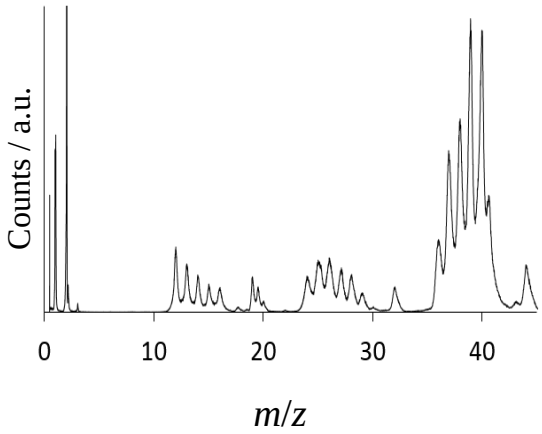

Figure 2.8.3: The mass spectrum of propyne.

2.9 Ion Signal Normalisation

The above integration procedure gives the relative ion signals of the products in terms of ion counts at the MCP detector. To compare with the kinetic model, with which we interpret our results (see Section 2.10), we require the product yields in terms of the number of molecules formed on the surface. Hence, the detection efficiency, a proportionality constant α, between ion counts detected in the TOFMS and number of molecules present, must be calculated. To carry out this transformation we first calculate the detection efficiency of the reactants dosed onto the surface. A known dose of the organic reactant and O_2 are deposited onto the surface at the minimum surface temperature, usually 15 K, in a 'blank' TPD experiment. If one assumes a sticking coefficient of unity, the dose of reactants is equal to the fluence, F_t. A sticking coefficient of unity is likely to be an excellent characterization of the interaction of a stable reactant with the 15 K surface. This assumption is supported since the main chamber pressure remains constant during dosing at this surface temperature. The fluence of reactants can be calculated by multiplying the flux of reactants, to the surface, by the dosing time. The flux of reactants can be calculated using equation 2.9.1.

$$F = \frac{P\,S}{k\,T\,A} \tag{2.9.1}$$

where F is the flux, P is pressure rise in the chamber, when the coldhead is off, and the reactant is let into the main chamber, S is the pumping speed of the chamber, k is the Boltzmann constant, T is temperature and A is the surface area. It should be noted that in the case of atomic oxygen, the flux of molecular oxygen is calculated and then the dissociation efficiency can be used to calculate the flux of atomic oxygen. The integrated ion counts for the parent ion of the reactant (m/z = 40 in the case of propyne) can then be divided by the fluence to give the detection efficiency, α.

We must now use the detection efficiencies calculated for the reactants to determine the detection efficiencies for the products. Since the detection efficiency of the reactants is calculated by integrating the parent ion, partial ionisation cross sections (PICs) of reactants and products are required to determine the detection efficiencies for the products. In the case of the reaction of O atoms and O_2 to make O_3, the detection efficiency of O_2 can be easily transformed into the detection efficiency of O_3 since both molecules' PICs for forming the relevant parent ion are readily available in the literature.[8, 9] However, there are cases where PICs are not available if either the isomer of the product is unknown, the product is a mixture of isomers or the PICs are not available in the literature. The detection efficiency will be discussed further in each individual Chapter.

When determining the number of surface reactants it is important to consider the mechanism of adsorption onto the surface. In the case of chemisorption the total number of molecules that can adsorb onto the surface is limited by the number of sites available on the surface. However, in the case of physisorption, once the first layer is filled a second layer can form. This can result in a very large number of molecules being adsorbed onto the surface. In the interstellar medium gas and dust temperatures are approximately 10 K. At these low temperatures molecules readily physisorb onto surfaces. It is therefore representative of the ISM to allow multilayer adsorption of molecules *via* physisorption during our experiments.

2.10 Kinetic Model

As discussed above, the experimental data presented in Chapters Three and Four is processed to give the yield of products as a function of the surface dosing temperature (Section 2.8 and 2.9). A simple kinetic model has been developed to account for these experimentally determined product yields at each dosing surface temperature. The model allows the surface reactions occurring during the experiment to be quantified. The model is based on a kinetic model

developed by Minissale *et al.* to account for the yield of ozone formed in the reaction of O atoms and O_2 on surfaces of astrochemical interest.[10] As discussed extensively in Section 1.6.1, when a microwave discharge is used to generate O atoms the resulting beam is a mixture of O_2 and O atoms due to dissociation efficiencies lower than 100 %. When this beam of O/O_2 is dosed onto a surface of astrochemical interest three reactions are possible:

$$O + O \rightarrow O_2 \quad (2.10.1)$$

$$O + O_2 \rightarrow O_3 \quad (2.10.2)$$

$$O + O_3 \rightarrow 2O_2 \quad (2.10.3)$$

However, experimental data shows that when a beam of O/O_2, is dosed onto surfaces of astrochemical interest, an almost pure O_3 ice is produced. It can be concluded that reaction 2.10.3 is inefficient and so possesses a significant barrier, whilst reactions 2.10.1 and 2.10.2 possess small or insignificant barriers. It has been shown that to successfully model the yield of O_3 in these experiments, reactions 2.10.1 and 2.10.2 must be effectively barrierless and the O atoms must have a high diffusion coefficient.[10, 11] It therefore follows that these two reactions will occur on the surface during the experiments discussed in Chapters Three and Four. Indeed, m/z = 48, indicative of O_3 formation, is always detected when a beam of O/O_2 and a beam of an unsaturated organic compound (Z) are co-dosed onto a surface below 50 K. Therefore, a kinetic model that seeks to understand the surface processes at play, when a beam of O/O_2 and a beam of unsaturated organic compounds (Z) are co-dosed onto a surface, must not only take account of the reaction between O atoms and the unsaturated organic compound (Z) (2.10.4) but also reactions 2.10.1 and 2.10.2.

$$Z + O \rightarrow ZO \quad (2.10.4)$$

Each of these three reactions (2.10.1, 2.10.2 and 2.10.4) is included in our kinetic model. As discussed in Section 1.4, in general reactions occurring on surfaces proceed *via* three prototypical reaction mechanisms: the Langmuir-Hinshelwood (LH) mechanism,[12] the Eley-Rideal (ER) mechanism,[12] and the hot atom mechanism (Figure 2.10.1).

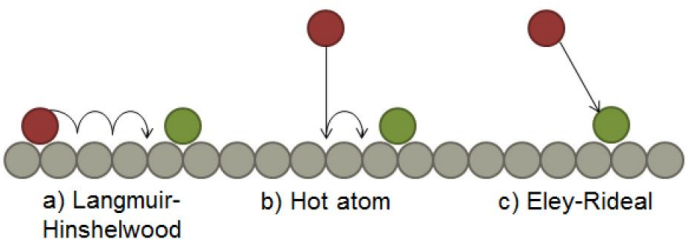

Figure 2.10.1: A diagram to show the three prototypical reaction mechanisms which occur on surfaces.

In the ER mechanism, a gas-phase species X(g) reacts with a species which is adsorbed and thermalised onto the surface, Y(ads) (2.10.5). The reaction proceeds prior to the gas-phase reactant equilibrating with the surface. The rate of the ER mechanism (r_{ER}) is a product of the rate coefficient (k_{ER}), the surface concentration of the adsorbed species ([Y](ads)) and the flux of the incident gas-phase species (F_X) (2.10.6). Since, in the experiments modelled, the reactants are co-dosed onto the surface, each reactive species can be the gas-phase reactant or the thermalized surface species, therefore two ER reactions must be modelled. The ER1 will describe the reaction where O atoms are the gas-phase reactant. The ER2 will describe the reaction where O atoms are the thermalized surface reactant.

$$X(g) + Y(ads) \rightarrow XY(ads) \quad (2.10.5)$$

$$r_{ER} = k_{ER}\,[Y](ads)\,F_X \quad (2.10.6)$$

The LH mechanism occurs when both reactants are adsorbed and thermalised on the surface. In the low temperature experiments described in this thesis, the surface species are bound *via* weak physisorption sites. The weak binding of the reactants to the surface facilitates the diffusion of light species such as the O atoms. The O atoms roam the surface until a suitable reaction partner is encountered. Upon encountering a suitable reaction partner, the reaction proceeds and the product is formed. The rate of the LH mechanism (r_{LH}) is a product of the rate coefficient (k_{LH}) and the surface concentrations of each species adsorbed on the surface ([Y](ads) and [X](ads)) (2.10.8).

$$X(ads) + Y(ads) \rightarrow XY(ads) \quad (2.10.7)$$

$$r_{LH} = k_{LH}\,[Y](ads)\,[X](ads) \quad (2.10.8)$$

The hot atom mechanism occurs when an incident gas-phase species is partially thermalized on the surface prior to encountering a suitable reaction partner. The hot atom mechanism can be thought of as half-way between the LH and ER mechanisms. However, quantifying the rate of thermalisation of species in the hot atom mechanism requires incorporating several new parameters into the model, parameters which are difficult to quantify. The inclusion of the hot atom mechanism, therefore, increases the number of free parameters in the model and so this process is not included in our modelling. Instead, the model consists of calculating the rate of reactions 2.10.1, 2.10.2 and 2.10.4 for each prototypical surface mechanism (LH, ER1 and ER2) at each experimental dosing surface temperature. The rates of reactions are numerically integrated over the dosing period of the experiment, 1 hour, with a time step of 0.001 s. This time step is chosen since no change in the product yields are observed when a finer integration grid is implemented. Traditionally rate coefficients for these reactions are evaluated using the

Arrhenius expression:

$$k_i = A_i \exp(-E_i/RT) \quad (2.10.9)$$

where k_i is the rate coefficient, A_i is the pre-exponential factor and E_i is the activation energy. However, it has been observed that the reaction of O atoms on surfaces of astrochemical interest does not obey Arrhenius type behaviour.[13] That is, it is not possible to account for the yield of ozone observed when O atoms react with O_2 on surfaces at temperatures below 20 K, when the rate constants are modelled using an Arrhenius rate coefficient. Using an Arrhenius rate coefficient consistently underestimates the yield of ozone below 20 K, even when the reaction is considered to be barrierless. It has been hypothesised that O atoms can tunnel through diffusion barriers at low surface temperatures. Indeed, models which include O atoms tunnelling through the diffusion barrier can successfully account for the yield of ozone below 20 K.[10, 11, 13] Another explanation for the high diffusion constants for O atoms below 20 K is that ices may undergo a phase change at low temperatures which alters the nature of the adsorption sites available to the O atom.[14] For example, if the ice undergoes a phase change at low temperatures, which results in lower binding energies of absorbates, the energy barrier to diffusion will also decrease. The binding energy and barrier to diffusion are directly related to one another. In both cases the molecule or atom must possess enough thermal energy to escape the potential well that binds the molecule or atom to the surface. Indeed, when the diffusion energy of a molecule is unknown it is often estimated to be 0.7 times the desorption energy.[15] When designing a model, tunnelling is simple to implement, although the barriers extracted are not always considered to be physical. On the other hand modelling a change in adsorption sites is very complicated, as many new parameters are introduced into the model. Indeed, it has been determined that modelling the rate coefficients of each reaction as reaction probabilities and using an empirical law to describe the diffusion coefficient of O atoms represents a clear quantitative fit to our experimental data without increasing the number of free parameters in the model. As a result the rates of the ER1, ER2 and LH mechanisms are modelled to be as given in equations 2.10.10, 2.10.11, 2.10.12 respectively.

$$r_{ER1} = \rho_{ER}\, C_Y(\text{ads})\ F_X \quad (2.10.10)$$

$$r_{ER2} = \rho_{ER}\, C_X(\text{ads})\ F_Y \quad (2.10.11)$$

$$r_{LH} = k_D\, \rho_{LH}\, C_Y(\text{ads})\, C_X(\text{ads}) \quad (2.10.12)$$

where ρ_{ER} and ρ_{LH} are the reaction probabilities of the ER and LH mechanisms respectively, C_Y(ads) is the fractional surface coverage of Y, F_x is the flux of X(g) to the surface in ML s^{-1} and k_D is the diffusion coefficient of an O atom in ML s^{-1}. The fractional surface coverages are calculated by dividing the surface concentration of each reactant by 1 ML, thereby cancelling the

units. For example a surface coverage of 0.5 ML has a fractional surface coverage of 0.5. By considering the surface concentrations as fractional coverages, and so unit-less, the rate constant for the reaction can be modelled as a reaction probability which is also unit-less. The units for the rate of reaction are therefore ML s^{-1}. Modelling the rate constants as reaction probabilities omits the need to invoke Arrhenius rate coefficients in the model and so no pre-exponential factors for the reactions are included, this reduces the number of free parameters in the model. The total rate of each reaction is as given in equation 2.10.13

$$r_{\text{total,i}} = r_{\text{ER1}} + r_{\text{ER2}} + r_{\text{LH}} \qquad (2.10.13)$$

The yield of each product in reactions 2.10.1, 2.10.2 and 2.10.4 is calculated by numerically integrating equation 2.10.13 for each reaction over the dosing period of the experiment. The result is a yield of product in ML. To integrate equation 2.10.12 the fractional surface coverages of O, O_2 and Z must be evaluated at each time step. To calculate the fractional surface coverages, first the surface concentration of each molecule must be evaluated in ML. The rate of change of surface concentration of each reactant ([Z](ads) / dt) is equal to the sum of the flux of the reactant to the surface, the depletion of the reactants due to the rate of desorption, depletion of reactant due to reactions and in the case of O_2 the yield of reactant due to reactions.

$$[\text{O}](\text{ads}) / \text{dt} = F_{\text{O}} + r_{\text{des,O}} - 2\, r_{\text{total,O}} \qquad (2.10.14)$$

$$[\text{O}_2](\text{ads}) / \text{dt} = F_{\text{O2}} + r_{\text{des,O2}} - r_{\text{total,O2}} + r_{\text{total,O}} \qquad (2.10.15)$$

$$[\text{Z}](\text{ads}) / \text{dt} = F_{\text{Z}} + r_{\text{des,X}} - r_{\text{total,Z}} \qquad (2.10.16)$$

The surface concentration of each reactant can be calculated by integrating equations 2.10.14, 2.10.15 and 2.10.16 at each time step. Where $r_{\text{total,O}}$ is the total rate of reaction for the reaction of two O atoms, $r_{\text{total,O2}}$ is the total rate of reaction for the reaction of O atoms and O_2 and $r_{\text{total,Z}}$ is the total rate of reaction for the reaction of O atoms with the organic species with which the O atoms are co-deposited. The model restricts the sum of the fractional coverages of each species to be 1. As a result the model assumes that the reactants do not penetrate into the ice, all the reactivity occurs on the surface. To integrate equations 2.10.14, 2.10.15 and 2.10.16 the rate of desorption ($r_{\text{des,X}}$) for each reactant (X) must be calculated. The rate of desorption can be calculated using the first-order Arrhenius equation.

$$r_{\text{des,X}} = \exp(-E_{\text{X}}/RT)\, C_{\text{X}}(\text{ads}) \qquad 2.10.17$$

where E_{X} is the activation energy of desorption. The desorption characteristics are therefore modelled as first-order desorption kinetics. However, multilayer ices, such as the ices deposited in this experiment, exhibit zero-order desorption kinetics. However, in the model desorption is

described as a first-order process since the model only considers the fractional coverages of the uppermost monolayer of reactants; the reactants can only desorb from this upper most monolayer. Furthermore, each reactant has different fractional coverages depending upon their flux to the surface, the rate of reactions and the rate of desorption. It therefore follows that to take account of the reactants fractional coverages, the desorption of each reactant must be dependent upon the reactants surface concentration.

Finally the rate of diffusion of the O atoms must be evaluated. It is possible to fit our experimental yield of products for reaction 2.10.4 using an Arrhenius diffusion coefficient, if one assumes the LH mechanism is inactive below 30 K. However, such a diffusion coefficient vastly under-predicts the yield of O_3 detected in our experiments, since the LH mechanism also becomes inactive for reactions 2.10.1 and 2.10.2. To account for the O_3 yields in our experiments, O atoms must diffuse on our surface below 30 K. This observation is in line with several previous studies.[10, 11, 13, 16] It therefore follows that if O atoms are diffusing on the surface, below 30 K, to form O_3 they must also encounter reactant Z on the surface and so reaction 2.10.4 must proceed *via* the LH mechanism. Therefore, the assumption that the LH mechanism is inactive below 30 K for reaction 2.10.4, an assumption required to fit our experimental data with an Arrhenius style O atom diffusion law, cannot be valid. The exponential function of an Arrhenius law results in a diffusion coefficient which suddenly 'switches on' at a particular surface temperature. For example in Figure 2.10.2, diffusion barriers of 200 K, 400 K and 600 K result in switch on temperatures of 9 K, 16 K and 24 K. After the switch on temperature the diffusion coefficient rises very rapidly. A diffusion barrier of approximately 200 K, which switches on the diffusion at approximately 9 K, can successfully account for the O_3 produced in our experiments at 15 K, but vastly over predicts the yield of O_3 at 30 K, and also the yield of the product in reaction 2.10.4. It is therefore apparent that an Arrhenius law cannot be used to describe O atom diffusion on our surface. Instead, the rate coefficient for the diffusion of O atoms on our surface is described using an empirical diffusion coefficient taken from a previous study by Minissale *et al*.[16] This empirical rate coefficient has been shown to successfully account for the yield of O_3 and CO_2 when CO, O_2 and O atoms are dosed onto a graphite surface.[16] The empirical law has the form:

$$k_D = k_0 (1+T^3/T_0^3) \qquad 2.10.18$$

where k_0 is 0.9 and T_0 is 10 K. A plot of the resulting rate constants at each surface temperature can be seen in Figure 2.10.2. This diffusion coefficient can successfully account for the yield of O_3 in our experiments and so is judged to be an appropriate diffusion coefficient for O atoms on our surface (Figure 2.10.3).

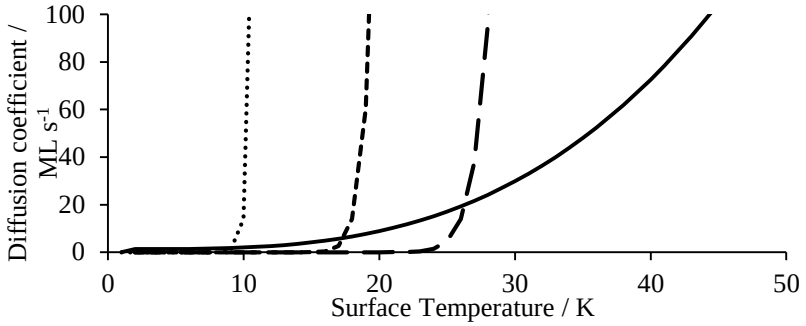

Figure 2.10.2: The form of rate coefficients solid line: the empirical rate coefficient in Equation 2.10.18, dotted line, short dash line and long dash line are all Arrhenius diffusion coefficients with barriers of 200 K, 400 K and 600 K respectively.

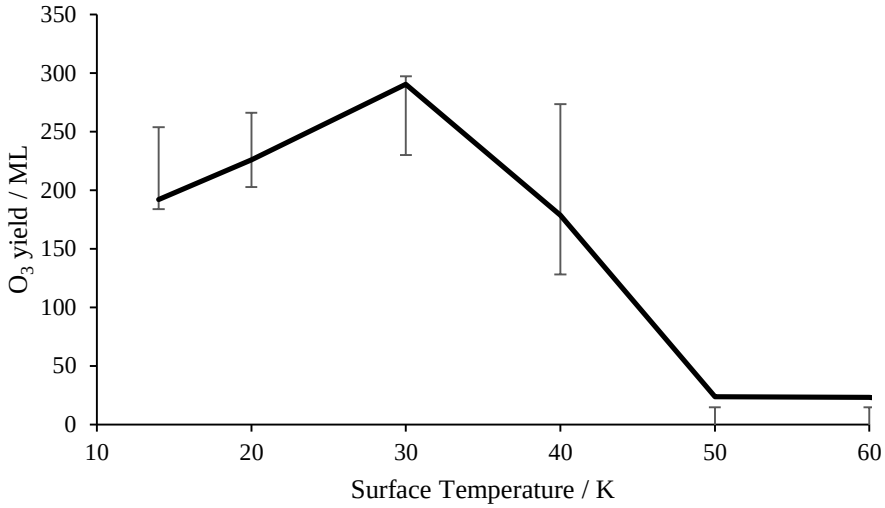

Figure 2.10.3: The fit obtained to the experimental yield of O3 using the empirical rate coefficient in equation 2.10.18

One final factor must be included in the model. When modelling the LH reaction for the reaction of an O atom with another O atom, both of the O atoms roam the surface. The diffusion of both O atoms is included in the model by multiplying the rate of diffusion by two. Physically this models one O atom as stationary and the other O atom as roaming the surface twice as fast as the O atoms which react with other stationary molecules (2.10.18). In all other cases, the rate of the LH mechanism is modelled using equation 2.10.11.

$$r_{LH,OO} = 2k_D \rho_{LH} C_Y(ads) C_X(ads) \qquad 2.10.19$$

In short, our model considers three reactions of O atoms on the surface, 2.10.1, 2.10.2 and 2.10.4. Each of these three reactions can occur *via* three prototypical surface mechanisms, the LH, the ER1 and the ER2. At each time step, the model first evaluates the fractional coverage of each reactant in the uppermost monolayer, at each surface temperature. The model then calculates the yield of O_2, O_3 and the oxygenated organic molecule, ZO, by integrating equation 2.10.12 for each product. Equation 2.10.13 is the sum of equations 2.10.10, 2.10.11 and 2.10.12. Except in

the case of the LH mechanism for the reaction of two O atoms in which case equation 2.10.12 is replaced by 2.10.19. The reaction of O atoms with one another and O_2 molecules has been shown to be a barrierless process, on surfaces of astrochemical interest, and so the reaction probabilities for these reactions are equal to one.[10, 11, 13, 16] The reaction probabilities for the reaction of O atoms with the unsaturated organic molecule and the desorption energies of O_2, O and the unsaturated organic molecule are varied until a fit is found to the experimental data. The ER1 and ER2 reaction probabilities are assumed to be equal. The model is fitted in a systematic way to ensure that results fitted to different reactions are comparable. This systematic fitting method is described below and summarised in Table 2.10.1.

Step one, in the fitting procedure, is to determine the maximum reaction probability for the ER mechanism by fitting the low temperature yield. Note, only the reaction probabilities for the reaction of O atoms and the unsaturated organic species (Z) are varied in the fit. Since the aim of this step is to determine the maximum reaction probability the desorption energy of O_2 is set to 0 k J mol^{-1} i.e. O_2 does not stick to the surface. The presence of O_2 on the surface reduces the rate of reaction since the O atoms can react with O_2 to form O_3. Similarly, the desorption of O and Z from the surface reduces the rate of reaction and so the desorption energies of the O atoms and Z are set to be infinitely high (400 k J mol^{-1}) i.e. neither desorb from the surface under the experimental conditions. In this fit the LH mechanism is presumed to be inactive and so the LH mechanism reaction probability is also set to 0. This assumption that the LH mechanism is inactive allows us to test the hypothesis that the ER mechanism alone can account for the experimental yields. However, the maximum value for the ER reaction probability is determined by the experimental yield at low temperatures, since increasing the value of the ER reaction probability further, overestimates the yield of product at these low temperatures. An optimum fit for step one can be seen in panel (a) of Figure 2.10.4.

It is clear from step one that the ER mechanism alone cannot account for the experimental yields between 40 K and 90 K (panel (a) of Figure 2.10.4). Therefore, in step two of the fitting procedure, the maximum reaction probability for the LH mechanism is determined. Again, the desorption energies of O_2, O and Z are set to 0 kJ mol^{-1}, 400 kJ mol^{-1} and 400 kJ mol^{-1} respectively. However, in this step the reaction probability for the ER mechanism is set to 0, and the reaction probability for the LH mechanism is varied, until it fits the data point at which the maximum yield of product is observed in the experimental data. In this example, the maximum yield is at 60 K (panel (b) in Figure 1.10.4). Note, this step overestimates the yield of product above 60 K and below 30 K, however, this is due to the unphysical desorption energies of the reactants which are optimised later. In step three, the LH and ER reaction probabilities are optimised together. Again, the desorption energies of O_2, O and Z are 0 kJ mol^{-1}, 400 kJ mol^{-1} and 400 kJ mol^{-1} respectively. Step three results in reducing both the reaction probabilities slightly since added together they now overestimate the yield of product at 60 K. This fit can be seen in panel (c) of Figure 2.10.4.

In step four, the desorption energy of Z is determined. The LH and ER reaction probabilities are fixed at their optimised values and the desorption energies of O_2 and O atoms remain as 0 kJ mol^{-1} and 400 kJ mol^{-1} respectively. The desorption energy of Z is reduced until the ER2 yield no longer fits the yield of product at 100 K and then the desorption energy is increased until it fits the yield at 100 K again. This fit can be seen in panel (d) of Figure 2.10.4. In step five, the desorption energy of the O atom is determined. The reaction probabilities and the desorption energy of Z are fixed at their optimised values and the desorption energy of O_2 remains at 0 kJ mol^{-1}. The O atom desorption energy is varied to reproduce the decrease in yield above a surface temperature of 60 K (panel (e) of Figure 2.10.4). In Step six, the O_2 desorption energy is determined. The reaction probabilities for the LH and ER mechanisms and the desorption energies of Z and O are fixed at their optimised values. The O_2 desorption energy is optimised to reproduce the yield of product between 15 K and 30 K. Such a fit can be seen in panel (f) of Figure 2.10.4. In step seven, each value is increased and decreased until the value no longer fits the experimental yields. This variation of each parameter provides an estimation for the uncertainty for each value extracted. The model is then optimised at increasingly small time steps until no change in the product yield is observed, the minimum time step used is 0.001 s. When no change in the product yield occurs as the time step is decreased this indicates that the time step is sufficient.

There is one final factor to consider in this fitting procedure, the desorption energy of O_2 which reproduces the rise in product yield between 30 K and 60 K does not predict the experimental yields of ozone between 30 K and 50 K. Therefore, in step eight, the desorption energy for O_2 is re-optimised to reproduce the yield of O_3 between 30 K and 60 K. As a result the uncertainty of the desorption energy for O_2 is larger than the uncertainties extracted for other desorption energies. The physical meaning of this uncertainty is discussed in the relevant Chapters.

Step	Panel in Figure 2.10.4	E_O	E_{O2}	E_Z	ρ_{LH}	ρ_{ER}
1	A	Infinite	0	Infinite	0	Optimised
2	B	Infinite	0	Infinite	Optimised	0
3	C	Infinite	0	Infinite	Optimised	Optimised
4	D	Infinite	0	Optimised	Optimised	Optimised
5	E	Optimised	0	Optimised	Optimised	Optimised
6	F	Optimised	Optimised	Optimised	Optimised	Optimised
7	G	Optimised	Optimised	Optimised	Optimised	Optimised
8	H	Optimised	Optimised	Optimised	Optimised	Optimised

Table 2.10.1: A summary of the fitting procedure and the panel in Figure 2.10.4 that each fit can be seen. Eo is the desorption energy of O atoms, E_{O2} is the desorption energy of O_2, Ez is the desorption energy of Z, ρ_{LH} is the reaction probability for the LH mechanism and ρ_{ER} is the reaction probability for the ER mechanism. All values are fixed in each step except the values in red which are optimised.

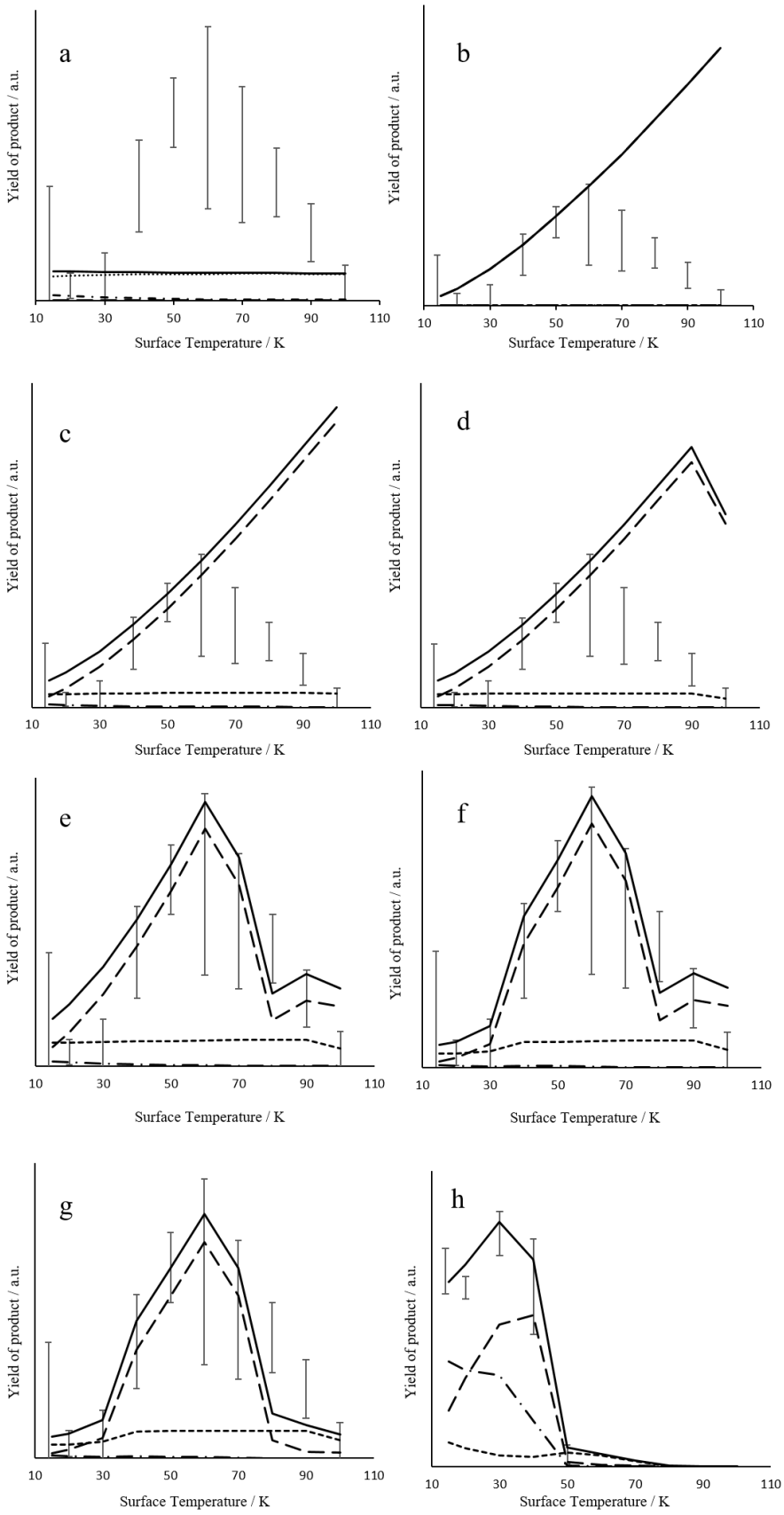

Figure 2.10.4: To show the various stages of fitting the kinetic model to the experimental data. The solid line: total yield predicted by the model, dash: LH contribution, dot: ER2, dash dot: ER1 the See Table 2.10.1 for a full description of each panel.

2.11 Experimental Developments

As discussed in Section 2.1 there has been significant development of the experimental apparatus during the last three years. These experimental developments are applicable to the experiments described in Chapter Five. The surface temperature is now determined using a silicon thermodiode, in place of the N-type thermocouple. The output from thermodiodes is of the order of a few volts and the voltage increases linearly as the temperature decreases. The output from an N-type thermocouple is of the order of a few millivolts and the output decreases exponentially as the temperature decreases. The exponential nature of the voltage output of thermocouples significantly decreases the sensitivity of N-type thermocouples below 30 K. Using a thermodiode instead of an N-type thermocouple increases the accuracy of the temperature reading, particularly at temperatures below 30 K. The voltage output from the thermodiode is read using a Lakeshore diode reader. This diode reader has an output of 0 V – 10 V which is read by a Eurotherm Nanodac temperature controller. A specific surface temperature can be maintained using the Nanodac controller. The Nanodac controller drives a power supply that heats the tantalum strip heater, in a constant voltage regime, to maintain the specified surface temperature. The Nanodac controller can also be used to heat the surface linearly during a TPD.

Another aim of the experimental development was to facilitate experiments involving the desorption of sub-monolayer doses. The TOFMS was unable to provide the sensitivity needed to detect the desorption of a submonolayer of reactants. To increase our experiment sensitivity, a Hiden 3F series RGA QMS was installed in place of the TOFMS. The mounting places the QMS is a few mm from the surface, whilst the centre of the TOFMS source region was approximately 3 cm from the HOPG surface. Furthermore, the electron gun in the QMS is capable of an output of a few hundred μA whilst the TOFMS electron gun could only produce only tens of nA. Both the close proximity of the QMS to the HOPG surface and the increased ionsing electron current of the QMS, dramatically increases the sensitivity of our apparatus. When a known quantity of O_2 is dosed onto the HOPG surface the TOFMS would typically collect ~250 counts per monolayer whereas the QMS collects ~3.4×10^5 counts per monolayer. Furthermore, the sensitivity of the QMS can be carefully controlled by varying the electron emission current.

The flux of reactants in our traditional multilayer experiments was typically 0.5 ML s^{-1}. Such a flux saturates the first monolayer within 2 s, a shorter time than the experimenter is able to reproducibly turn on and off the beam of reactants. To reduce the flux of reactants, the pressure of the gas in the source cells was reduced by an order of magnitude and the pumping holes' size was increased from 2 mm to 4 mm. Reducing the gas pressure in the source cells reduces the flux of gas which exits the source cells through the 1 mm diameter exit capillary. The gas then flows through the PTFE tubing towards the pumping holes. Increasing the diameter of the pumping holes increases the proportion of reactants which are pumped away in the source chamber, further

reducing the flux of reactants to the surface. The reduction in source cell pressure and installation of the larger pumping holes typically reduces the flux of reactants to 0.005 ML s^{-1}. The flux of reactants in our submonolayer experiments is determined by depositing the reactants for several different dosing times and observing the change in the characteristics of the TPD. For coverages of a monolayer or less, first-order desorption is observed. Conversely for multilayer desorption zero-order desorption is observed. The change from first-order to zero-order desorption can be determined by the dosing time at which the leading edge of the TPD, following an increased dose, doesn't shift to lower temperatures. The time to saturate the first monolayer can therefore be measured and used to calculate the flux of reactants.[10, 17] The method is discussed further, and the flux of O_2 is calculated, in Section 5.3.2.

The Hiden 3F series RGA QMS consists of a source region, a quadrapole mass separator and a secondary electron multiplier (SEM) detector. Molecules enter the source region and are ionised using electron ionisation. The electron energy can range from 4 – 150 eV and in this thesis 70 eV has been used. A metal grid surrounds the source region preventing electrons formed in the source region from escaping. Between the ion source and the quadrupole mass separator is a focusing plate. This focusing plate extracts ions from the source region into the quadrupole mass separator. The quadrupole mass separator consists of four parallel metal rods. Each pair of opposing rods are electrically connected. A DC offset voltage and a radiofrequency oscillating voltage are applied to each pair of rods. The electric field deflects ions in an oscillating trajectory as they migrate towards the detector. Specific oscillating radiofrequencies applied to each pair of rods are selected such that only ions with a particular mass-to-charge ratio (m/z) reach the detector. Other ions follow different trajectories and collide with the rods before reaching the detector. Here lies the main disadvantage of the QMS compared to TOFMS. In TOFMS all ions, regardless of their m/z are recorded. Whereas in the QMS the ion(s) to be monitored must be selected. To monitor several (m/z) the oscillating radiofrequency voltages are varied to select one by one each (m/z) of interest. Each time a new (m/z) is selected there is a minimum 'settle' time of 10 ms before ions can be detected. Ions can be detected for a minimum 'dwell' time of 10 ms. The cycle can therefore be repeated every 20 ms. During a typical TPD, with a heating rate of 10 K min^{-1}, molecules will desorb from the surface for ~90 s. The time a molecule desorbs from the surface provides a limit for the number of (m/z) that can be scanned in any one TPD experiment.

An advantage of QMS is the constant mass resolution. Ions with high (m/z) can be detected with the same resolution as ions with small (m/z). TOFMS has limited resolution for high (m/z). This particular QMS has a mass range of 1 AMU - 300 AMU. When an ion of the selected (m/z) reaches the SEM detector electrons are produced. These electrons undergo further collisions producing secondary electrons in a cascade effect. The current output of the SEM is recorded and this current is proportional to the ions arriving at the SEM. Unlike in the TOFMS, the QMS directly records

the surface temperature during the TPD via a 0 – 10 V output from the Nanodac controller. Therefore the counts of each *m*/*z* are recorded as a function of surface temperature.

2.12 Summary

This Chapter has provided a detailed description of the experimental apparatus employed in the experiments described in the succeeding Chapters. Furthermore, a broad overview of the kinetic modelling approach used to derive kinetic parameters from the experimental data in Chapters three and Four has been presented. The following Chapters will describe the results obtained using the experimental arrangement and data analysis procedure described here and will discuss the astrophysical implications of the results in this thesis.

2.13 References

1. D. A. Williams, *Chemistry-a European Journal*, 1997, **3**, 1929-1932.
2. D. P. Higgins, R. W. McCullough, J. Geddes, J. M. Woolsey, M. Schlapp and H. B. Gilbody, in *Advances in Engineering Materials*, eds. S. Hampshire, M. Buggy, B. Meenan and N. Brown, 1995, vol. 99-1, pp. 177-183.
3. R. W. McCullough, J. Geddes, A. Donnelly, M. Liehr, M. P. Hughes and H. B. Gilbody, *Measurement Science and Technology*, 1993, **4**, 79-82.
4. R. W. McCullough, J. Geddes, A. Donnelly, M. Liehr, M. P. Hughes and H. B. Gilbody, *Measurement Science & Technology*, 1993, **4**, 79-82.
5. A. Donnelly, M. P. Hughes, J. Geddes and H. B. Gilbody, *Measurement Science and Technology*, 1992, **3**, 528-532.
6. M. D. Ward and S. D. Price, *Astrophysical Journal*, 2011, **741**.
7. W. C. Wiley and I. H. McLaren, *Review of Scientific Instruments*, 1955, **26**, 1150-1157.
8. K. A. Newson, S. M. Luc, S. D. Price and N. J. Mason, *International Journal of Mass Spectrometry and Ion Processes*, 1995, **148**, 203-213.
9. H. C. Straub, P. Renault, B. G. Lindsay, K. A. Smith and R. F. Stebbings, *Physical Review A*, 1996, **54**, 2146-2153.
10. M. Minissale, E. Congiu and F. Dulieu, *J. Chem. Phys.*, 2014, **140**.
11. E. Congiu, M. Minissale, S. Baouche, H. Chaabouni, A. Moudens, S. Cazaux, G. Manico, V. Pirronello and F. Dulieu, *Faraday Discuss.*, 2014, **168**, 151-166.
12. H. J. Fraser, M. R. S. McCoustra and D. A. Williams, *Astronomy & Geophysics*, 2002, **43**, 10-18.
13. M. Minissale, E. Congiu, S. Baouche, H. Chaabouni, A. Moudens, F. Dulieu, M. Accolla, S. Cazaux, G. Manico and V. Pirronello, *Physical Review Letters*, 2013, **111**.
14. *Faraday Discuss.*, 2014, **168**, 571-615.
15. M. Minissale, E. Congiu and F. Dulieu, *Astronomy & Astrophysics*, 2016, **585**.
16. M. Minissale, E. Congiu, G. Manico, V. Pirronello and F. Dulieu, *Astronomy & Astrophysics*, 2013, **559**.
17. G. A. Kimmel, K. P. Stevenson, Z. Dohnalek, R. S. Smith and B. D. Kay, *J. Chem. Phys.*, 2001, **114**, 5284-5294.

Chapter 3 – Oxygen Atom Addition to Propyne

3.1 Introduction

The small unsaturated hydrocarbon, propyne, has been observed widely throughout the interstellar medium.[1, 2] Interstellar propyne was first identified in the Milky Way within the giant molecular cloud Sagittarius B2.[2, 3] Further observations, within the Milky Way, have also detected propyne in cold cloud cores and lukewarm corinos.[4] Outside of the Milky Way, across the disc of the distant Messier 82 (M82) galaxy, propyne has also been observed.[5] In M82, the propyne-to-methanol ratio ($[CH_3CCH]/[CH_3OH] > 8$) is higher than for comparable starburst galaxies such as NGC 253 ($[CH_3CCH]/[CH_3OH] \approx 1$).[6] Whilst observations and laboratory studies conclusively identify methanol in interstellar ices,[7-9] currently there is no spectral evidence for solid-phase propyne in the ISM. However, a recent paper has reviewed the reaction pathways invoked in the literature to account for the formation of propyne in the interstellar medium.[10] The authors conclude that models which only consider gas-phase reactions, cannot generate propyne abundances which are comparable to observations. Instead, propyne is thought to form *via* the successive hydrogenation of C_3 and C_3H on the surface of interstellar dust grains.[10, 11] C_3 is efficiently formed in the gas-phase and subsequently freezes out onto the surface of dust grains where hydrogenation can occur.[10] Propyne is therefore likely to have an appreciable abundance in interstellar ices. Since both propyne and methanol are believed to primarily form on the surface of dust grains, and have similar gas-phase abundances, one would expect both molecules' surface reactivity to have been studied. However, the surface chemistry of methanol has been studied extensively in the laboratory whilst that of propyne has received little attention.[12-15] It therefore follows that the surface reactivity of propyne, under interstellar conditions, appears to be overdue an investigation.

In addition to its detection in interstellar clouds, propyne has also been observed in planetary environments in our Solar System. Specifically, propyne has been detected in the stratospheres of Jupiter and Saturn, displaying column densities of $(1.5 \pm 4) \times 10^{14}$ molecules cm^{-2} and 2×10^{15} molecules cm^{-2} respectively.[16, 17] Interstellar ice composition is considered to be important when discussing the abundance of propyne in the Saturnian and Jovian atmospheres. Here, volatile molecules, such as propyne, are thought to originate from molecules trapped as clathrates in the water ice that aggregated during the formation of the planetisimals that preceded these planets.[18-23] Propyne has also recently been identified in the atmosphere of Uranus,[24] and the atmosphere of Saturn's moon Titan, where it appears enriched at northern latitudes.[25, 26]

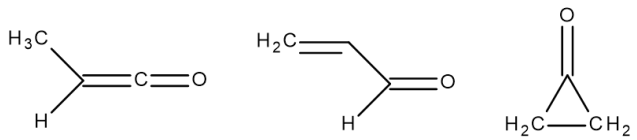

I II III

Figure 3.1.1: The structures of methyl ketene (I), propenal (II) and cyclopropanone (III).

The gas-phase reaction of propyne and O(^{3}P) atoms has been studied both experimentally and computationally.[27-34] The two most insightful studies have combined experimental and theoretical investigations, together they provide a detailed picture of the reaction at a molecular level.[28, 35] The earlier of these two studies was performed in 2004. In this study density functional theory was used to characterise the singlet and triplet potential energy surfaces for molecules with the empirical formula C_3H_4O resulting from the reaction of propyne and O atoms. The functional used was Becke's three-parameter nonlocal exchange functional with the nonlocal correlation functional of Lee, Yang, Parr (B3LYP) with the 6-311G(d, p) basis set.[36, 37] At the time, this level of theory was considered to be a good balance between computational efficiency and accuracy, for an eight atom system. By the time the second study was performed, in 2016, advances in computing made it possible to re-optimise stationary states (intermediates and transition states) with the multi-configurational second-order perturbation method, CASPT2, using the basis set aug-ccpVTZ.[38-40] Both studies agree that the gas-phase reaction of propyne and O atoms primarily proceeds *via* O atom addition rather than H atom abstraction. However, the 2016 study determined that O atom addition to the terminal acetylenic carbon atom of propyne possesses an activation energy of 1.71 kcal mol^{-1} whereas O atom addition to the central acetylenic carbon possesses an activation energy of 2.40 kcal mol^{-1}.[35] Therefore, the second study suggests that the terminal acetylenic carbon is the most facile site of attack for the O atom. When the O atom attacks the terminal C atom the initial intermediate formed is a biradical species, methyl ketocarbene (Structure I in Figure 3.1.1).[27, 28, 35] Since the O(^{3}P) atom has two unpaired electrons, the ketocarbene intermediate lies on the triplet potential energy surface. The two unpaired electrons are localised on the central carbon atom.[35] Early experimental studies observed that, in the gas-phase reaction of propyne and O atoms, vibrationally cold CO and C_2H_4 were formed.[34] Vibrationally cold CO is produced when dissociation occurs through a linear transition state.[28, 34] For such a dissociation event to occur, through this linear transition state, the molecule undergoing dissociation would possess a linear geometry. Such an intermediate would be methylketene (Structure I in Figure 3.1.1). It was therefore hypothesised that the triplet state ketocarbene would undergo intersystem crossing (ISC) to the singlet potential energy surface.[28] The singlet state ketocarbene would then isomerize to methylketene. The

2004 study supports this earlier hypothesis since ISC is the pathway, with the lowest activation energy, available to the ketocarbene on the triplet potential energy surface.[28] The 2016 study also determined that at, 300 K, 80 % of the initial triplet state ketocarbene undergoes ISC. As the temperature rises this percentage decreases to 2% at 2250 K.[35] The ISC results in a singlet ketocarbene, in which the two non-bonding paired electrons are localised on the central C atom.[35] Both studies then predict low activation energies (<5 kcal mol^{-1}) for the singlet state ketocarbene to isomerise to form methyl ketene or propenal (Figure 3.1.1).[28, 35] Both studies also predict the activation energy for the isomerisation to form methyl ketene to be slightly smaller than that of propenal. Following isomerisation, in the gas-phase, methyl ketene dissociates into C_2H_4 and CO with an activation energy of 74.7 kcal mol^{-1}.[35] On the other hand propenal can dissociate in several ways forming C_2H_3 + HCO, CH_2CHCO + H or C_2H_2 + CO + H_2 with activation energies of 95.2 kcal mol^{-1}, 90.7 kcal mol^{-1} and 84.0 kcal mol^{-1} respectively.[35] The barrier to dissociation of methyl ketene and propenal are significantly larger than the ISC activation energy and the isomerisation activation energy of the ketocarbene which forms the methyl ketene and propenal. It is therefore possible at our low temperatures that the methyl ketene and propenal will be stable. The gas-phase reactions of propyne with O(^{3}P) atoms are summarised in Figure 3.1.2.

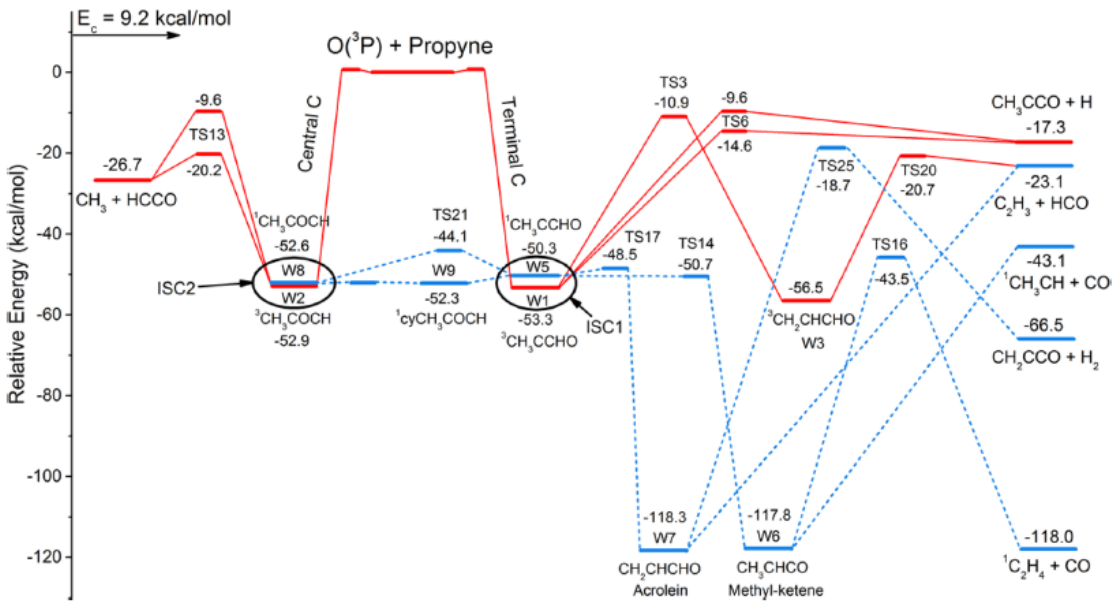

Figure 3.1.2: Schematic potential energy diagram illustrating stationary points on the triplet (red solid lines) and singlet (blue dashed lines) C_3H_4O potential energy surfaces. Taken from reference 41.

3.2 Experimental

3.2.1 Temperature Programmed Desorption Methodology

The experimental apparatus utilised in this study has been discussed in detail in Chapter Two. In this study oxygen atoms, molecular oxygen and propyne are co-dosed onto a graphite surface with fluxes of 0.13 ML s^{-1}, 0.26 ML s^{-1} and 1 ML s^{-1} respectively. The propyne was purchased from Sigma-Aldrich and has a purity of ≥99 %. The propyne was used without further purification. After a dosing period of one hour, the dosing lines were evacuated and the surface was allowed to cool to 15 K. Following this cooling a current of 15 amps was passed through a tantalum strip heater below the surface, heating the surface to approximately 200 K in a temperature programmed desorption (TPD) experiment. As the substrate temperature increases, the molecules on the surface desorb at their specific sublimation temperatures and enter the source region of the TOFMS which is located in front of the sample. It is important to note that the dosing regime is such that the graphite surface is covered within approximately 1 s. Therefore, the surface reactions we observe occurs overwhelmingly on a propyne/oxygen ice. The experiment was repeated at several different surface temperatures between 15 and 100 K. The experiment is repeated three times at each surface dosing temperature. As part of the experimental method, background spectra are also recorded. These background TPD spectra are collected for each dosing surface temperature. In each background spectra only propyne and O_2 are dosed onto the surface i.e. the microwave discharge is not used to generate O atoms, but all other experimental conditions are identical. These background spectra confirm the product signals in the experiment are due to the O atoms formed in dissociation in the source cell and not another reaction pathway.

3.2.2 Infrared Spectroscopic Methodology

The apparatus at UCL provides information about the mass of the products formed and the relative quantities of those products. Previously, when employing this apparatus multi-photon ionisation experiments have been employed to determine the specific isomer of the product formed.[42] Such experiments are not feasable if the products could be one of many possible isomers with similar ionisation potentials. To overcome this limitation, in the case of the reaction of propyne and oxygen atoms, complementary experiments were carried out at the Friedrich-Schiller-University, Jena, where the products can be identified by infrared (IR) spectroscopy. The experimental apparatus at the Friedrich-Schiller-University consists of a high vacuum (HV) chamber. Molecules and O atoms can be dosed onto a KBr substrate held at temperatures relevant

to interstellar dust. The products of the reaction can be observed using transmission IR spectroscopy.

The HV chamber, in Jena, is sealed with Klein flanges and has a base pressure of 1×10^{-7} Torr. The pressure is maintained using a turbo molecular pump (TMP) with a pumping speed of 33 L s^{-1} for N_2. The TMP is backed by a scroll pump. The chamber houses a KBr substrate mounted in a copper sample holder. The copper sample holder is then mounted on a two-stage closed helium cryostat. The surface temperature is monitored using a silicon diode and controlled using a Lakeshore 336 Cryogenic Temperature Controller. The coldhead, coupled with a Lakeshore cartridge heater, can maintain surface temperatures between 22 K and 500 K. As in the UCL apparatus, a piece of sapphire is used to thermally isolate the surface from the coldhead during heating. A diagram of the apparatus can be seen in Figure 3.2.2.1. Experiments in Jena consist of dosing propyne and O atoms onto the KBr substrate at a fixed surface temperature and using transmission FTIR spectroscopy to observe the products.

The oxygen atom source in Jena was assembled using a traditional hydrogen microwave discharge lamp and a custom-build PTFE connector. The apparatus and procedure for producing oxygen atoms in Jena was designed to be as close as possible to the apparatus and procedure used at UCL. The discharge is contained in a Pyrex tube with a constant flow of O_2 at a pressure of 0.2 Torr. Microwaves are generated using a Sairem microwave unit with a frequency of 2.45 GHz. The microwaves are coupled into the O_2 gas using an Evenson cavity.[43] The microwave power chosen was 180 W as this is the power used at UCL. The discharge is initiated by a Tesla coil. For a full description of a microwave discharge see Section 2.2. A PTFE connector fits into the end of the Pyrex discharge cell to allow atomic transport into the HV chamber. The PTFE connector has a 1 mm diameter exit capillary which allows the products of the microwave discharge to flow out of the source cell. After the exit capillary the gas flows into a 60 mm delivery line which has two pumping holes with a diameter of 2 mm. The pumping holes allow the gas to be differentially pumped using a TMP with a pumping speed of 33 L s^{-1} for N_2 backed by a rotary pump. The 60 mm delivery line then enters the HV chamber delivering the O atoms, and residual O_2, at an angle of 30° to the surface. A diagram of the microwave discharge cell can be seen in Figure 3.2.2.2. The O/O_2 beam is co-dosed onto the KBr substrate together with propyne. The propyne used has a purity of $\geq$ 99% and was used without further purification. The propyne was dosed at an angle of 30° to the surface and the flow was controlled using a needle valve.

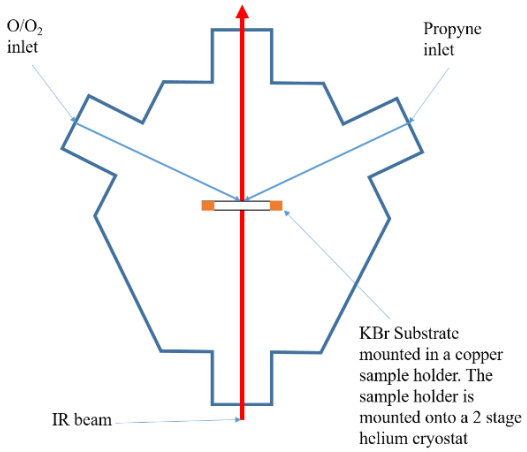

Figure 3.2.2.1: A schematic diagram of the experimental arrangement.

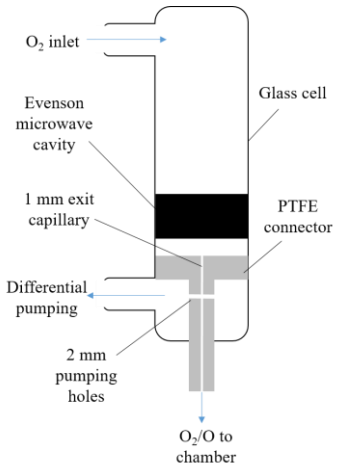

Figure 3.2.2.2: A schematic diagram microwave discharge cell.

Prior to the deposition of species, onto the KBr substrate, the cold head is turned on and the surface is heated to 100 °C to remove the water vapour on the KBr substrate. As the cold head cools to its minimum temperature the surface temperature is maintained at 200 K to prevent the deposition of chamber contaminants, such as water, CO_2 and CO, onto the surface. A surface temperature of 200 K is maintained for three hours to cryopump the chamber. The Jena experiments consist of depositing a propyne/O_2/O atom ice at a fixed surface temperature. The resulting ice has an estimated thickness of 10,000 ML. The products and reactants can be observed using transmission FTIR spectroscopy. The deposition experiment was repeated at three surface temperatures 22 K, 50 K and 80 K. Depositions lasting one hour were performed at each surface temperature. In separate experiments the dosing time was increased to two hours at 22 K and three hours at 50 K. Following the deposition of reactants the surface was then heated to 200 K, in stages, acquiring IR spectra at various temperatures. For example, following the deposition at 22 K an IR spectra was acquired. The surface was then heated at 10 K min^{-1} to 30 K where a new IR spectra was acquired. Two corresponding 'blank' spectra were also recorded. The first blank was a pure propyne ice, the second blank was a deposition of the gas emitted from the microwave discharge.

3.3 Results

3.3.1 Temperature Programmed Desorption Results

As discussed above, TPD studies were performed at UCL using the methodology described in Section 3.2.1. The results from these experiments performed at UCL are as follows: whenever propyne and O atoms are allowed to react at surface temperatures below 100 K, signals are

observed in the mass spectra , recorded during the TPD phase, with a mass-to-charge (*m*/*z*) ratio of 56 and 72 (Figure 3.3.1.2). One must first determine whether these two signals are due to the formation of two different products, or due to fragmentation in the mass spectrometer. Signals at different masses in the mass spectrum, which are simply due to fragmentation will possess identical desorption profiles. Desorption profiles track the number of counts of a particular *m*/*z* during the heating phase of the TPD. It can be seen in Figure 3.3.1.2 that the product at *m*/*z* = 56 desorbs from the surface between 80 K and 140 K. Conversely, the product at *m*/*z* = 72 is observed to desorb from the surface between 115 K and 200 K. The two signals can therefore be confirmed as distinct products, rather than fragmentations in the mass spectrometer. The two signals in the mass spectrum at *m*/*z* = 56 and 72 are consistent with the empirical formulae C_3H_4O and $C_3H_4O_2$ respectively. We, therefore, refer to these products as the single and double addition products respectively.

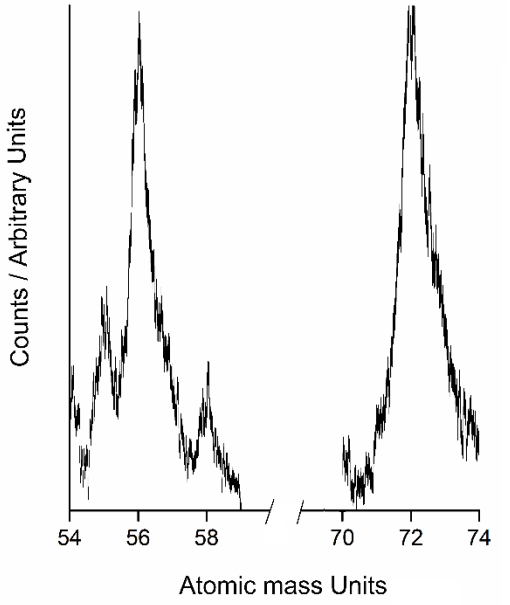

Figure 3.3.1.1: Sections of representative mass spectra recorded during the TPD phase showing peaks for *m*/*z* = 56 and *m*/*z* = 72, corresponding to the single and double addition products.

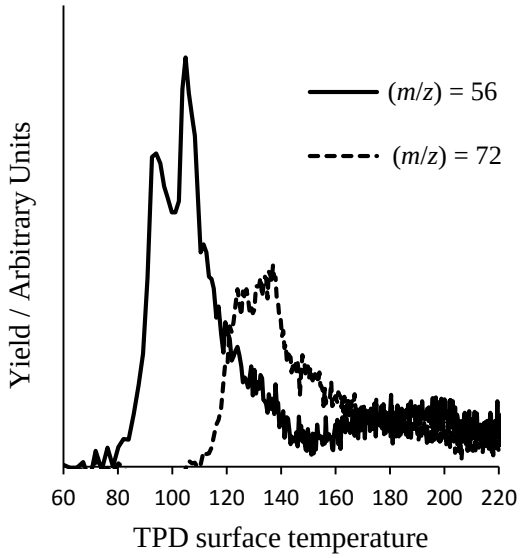

Figure 3.3.1.2: Desorption profiles recorded during the TPD for *m*/*z* = 56 and *m*/*z* = 72, corresponding to the single and double addition products.

To determine the relative yield of the single and double addition products, the mass spectra are summed over the temperatures at which each product desorbs from the surface. In the case of the single addition product the mass spectra are summed between 80 K and 140 K and the peak at *m*/*z* = 56 is then integrated. A background spectra summed over the same desorption temperatures and integrated for *m*/*z* = 56 is then subtracted from the integrated TPD signal for this mass. In the

case of the double addition product the mass spectra are summed between 115 K and 200 K and the peak at m/z = 72 is integrated. Again a background spectra summed over the same desorption temperatures and integrated for m/z = 72 is then subtracted from the raw TPD yield. This background subtraction ensures that the signal observed is solely due to the addition of O atoms. The procedure is repeated for each experiment performed at a range of different dosing surface temperatures. The above procedure yields the relative yields of each product at each surface dosing temperature.

At low dosing temperatures (15 K – 50 K) a peak at (m/z) = 48 is also observed in the mass spectra. This mass spectral signal is consistent with a molecular formula of O_3, formed from the side reaction of O atoms with undissociated O_2. As discussed in Chapter 1, it is well known that the gas resulting from a microwave discharge in O_2 will yield a beam of O atoms and O_2. When this gas is deposited onto a surface at cryogenic temperatures O_3 is formed.[44-48] This peak at (m/z) = 48 is also integrated in the same fashion as described for the (m/z) = 56 and 72 peaks.

The experimental data shows three products are observed: the single addition product, the double addition product and ozone. For each of these three products, the experimental data consists of the total counts in the mass spectra, during the TPD, at each different dosing surface temperature. To compare the yield of these three products to the kinetic model discussed in Chapter Two, one must convert the yield of products from total counts in the mass spectra to numbers of molecules. To transform the mass spectral ion counts to these absolute units, the mass spectrometer must be calibrated. To carry out this calibration, a known quantity of propyne and O_2 is dosed onto the surface at 15 K, as in the background experiments. A TPD experiment is then performed and the desorption temperatures of O_2 and propyne are determined using the desorption profiles of (m/z) = 32 and 40 respectively. The mass spectra are then summed over the temperatures at which O_2 and propyne desorb from the surface and the signals at (m/z) = 32 and 40 are integrated. Then, by dividing the number of molecules dosed onto the surface by the number of counts in the mass spectra one can determine the detection efficiency of O_2 and propyne. This procedure assumes both O_2 and propyne have a sticking coefficient of unity when the surface temperature is 15 K. During dosing, when the surface temperature is 15 K, the pressure rise in the chamber is negligible. It is therefore reasonable that a sticking coefficient of unity is a good characterization of the interaction of propyne and O_2 with the 15 K surface. The detection efficiencies measured for propyne and O_2 must now be modified to give us the detection efficiencies of the three products from the surface reaction. Total ionisation cross sections measure the total number of charged fragments that are detected when a molecule is ionised. On the other hand partial ionisation cross sections (PICs) determine the number of charged fragments with a particular m/z that are formed when a molecule is ionised. Since the integration procedure used in this Chapter only integrates the parent ion signal, the partial ionisation cross sections for

ionisation are required to transform the detection efficiencies we measure for O_2 and propyne into those for the products and O_3. This transformation is simple in the case of O_2 and O_3 since the PICs for these molecules are readily available in the literature. However, in the case of the single and double addition products the PICs and total ionisation cross sections are unknown. We must therefore assume that the total ionisation cross sections for propyne and the single and double addition products are identical. In determining these detection efficiencies we must also allow for the fact that not every molecule we ionize will result in a parent ion in the mass spectrum; we must allow for fragmentation in the ionisation process. To make this correction, for the single addition product, we used the parent to fragment ion ratio of a propenal mass spectrum measured in our apparatus. For the double addition product we estimated the fragment to parent ratio in the standard mass spectrum of methyl glyoxal from the NIST reference database.[49] The above procedure allows us to estimate the yield of the product ions on an absolute scale from our TPD spectra, and report the yield as a function of the dosing temperature. The yield of the single and double addition products as a function of dosing surface temperature is shown in Figure 3.3.1.3. These experimental results show that, below 30 K, the yield of each product gently increases with decreasing temperature. Above a surface temperature of 30 K both product yields increase to a maximum at 50 K and then decrease to zero at a surface temperature of 100 K. We also note the yields for the single and double addition products are very similar below a surface temperature of 40 K. Above a surface temperature of 40K the yield of the single addition product is much larger than that of the double addition product.

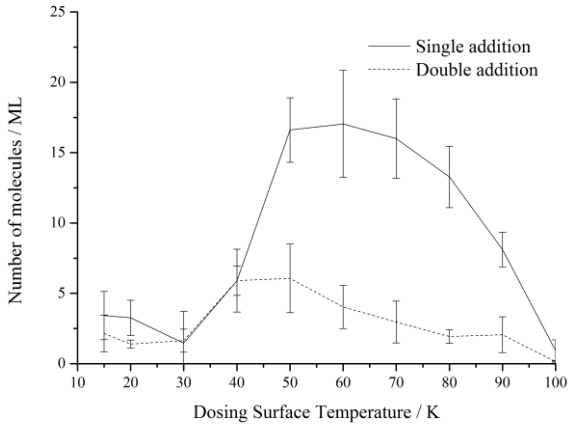

Figure 3.3.1.3: Experimental yield of the single (dashed line) and double (dotted line) addition products following the co-deposition of propyne (C_3H_4) and O atoms. The error bars associated with the experimental results represent two standard deviations from four experiments at each surface temperature. The lines linking the points serve only to guide the eye.

3.3.2 Infrared Spectroscopic Results

When a propyne ice is deposited onto a KBr substrate at 22 K, several signals are observed in the IR spectra. Several of these signals correspond to impurities such as water, CO and CO_2 since the reaction chamber is a high vacuum chamber. In a previous study, a multilayer propyne ice was deposited onto a Pd(100) surface and examined using Reflection-Absorption IR Spectroscopy (RAIRS).[50] The transmission IR spectra for the propyne ice deposited in this study are in excellent agreement with reference 50. Therefore reference 50 is used to assign the IR absorptions of propyne observed in this study. Propyne's strongest IR absorption is centred at 3266 cm^{-1}. As the surface is heated to 200 K the evolution of this band can be tracked using difference spectra. Difference spectra can be calculated by subtracting IR absorbance spectra from one another. First the transmission IR spectra must be transformed into absorbance spectra using equation 3.3.2.1.

$$A = \log_{10} (1 / \varphi) \qquad (3.2.2.1)$$

where A is absorbance and φ is transmission. One absorbance spectrum is then subtracted from another absorbance spectrum to give the difference spectrum between the two absorbance spectra. For example, in Figure 3.3.2.1, the trace labelled 22 K – 30 K is the absorbance IR spectra recorded at 30 K minus the absorbance IR spectra recorded at 22 K. The result is an IR trace in which positive absorptions, with respect to the baseline, represent an increase in absorbance as the surface is heated from 22 K to 30 K. Negative absorptions, with respect to the baseline, represent a decrease in absorbance as the surface is heated from 22 K to 30 K. As the surface is heated from 22 K to 50 K the difference spectra reveal that the intensity of the absorption at 3266 cm^{-1} increases (Figure 3.3.2.1). As the surface is heated from 50 K to 100 K the absorption further increases in intensity and the peak splits into two sharp absorptions. This increase in intensity and split into sharper peaks occurs due to the propyne ice becoming mobile and forming a more ordered, possibly crystalline, ice. As the surface is heated to 120 K, the absorption decreases in intensity as the propyne desorbs from the surface. Above 120 K no change is observed in the difference spectra for the absorption at 3266 cm^{-1}. There is a positive absorption in the trace labelled 140 K – 160 K in Figure 3.3.2.1, however, this absorption is at ~3229 cm^{-1} and is most likely due to the water impurity in the high vacuum chamber.

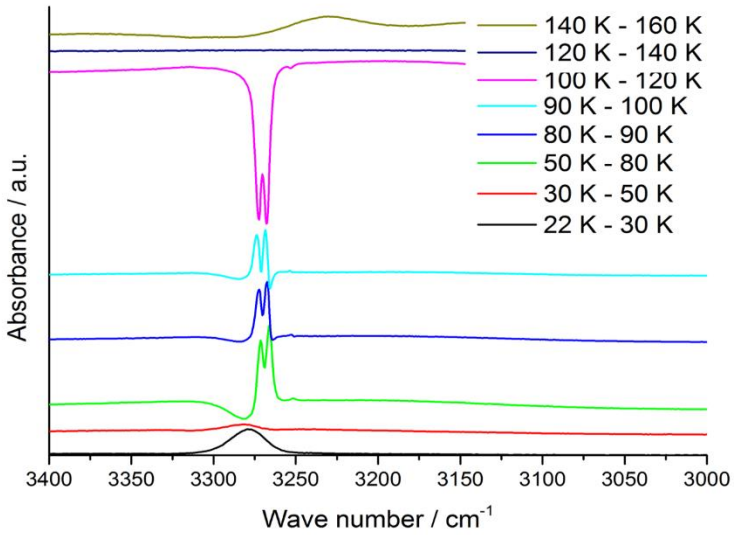

Figure 3.3.2.1: Difference absorbance spectra, between 3000 and 3400 cm^{-1}, of a propyne ice as the surface is heated from 22 K to 160 K. For example the trace labelled 22 K – 30 K is the absorbance spectrum recorded at 30 K minus the absorbance spectrum recorded at 22 K. Positive peaks, with respect to the baseline, denote and increase in absorbance whereas negative peaks denote a decrease in absorbance. The baselines of the spectra have been displaced for clarity.

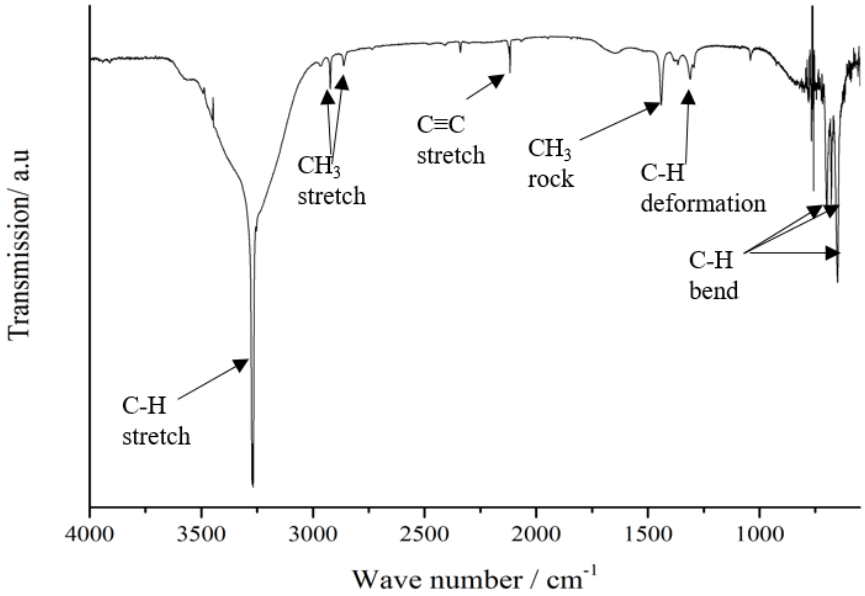

Figure 3.3.2.2: IR spectra propyne ice deposited onto a KBr substrate at 22 K and heated to 100 K. the most intense peaks have been labelled.

In order to positively identify as many propyne absorptions as possible, the spectrum used for assignment is recorded when the propyne ice, which was deposited at 22 K, is heated to 100 K (Figure 3.3.2.2). When the surface is heated to 100 K impurities such as CO and CO_2 desorb from the surface. Furthermore, heating the propyne deposit allows the ice to form a more ordered structure which results in sharper absorptions. In some cases, for example the band at 3266 cm^{-1}, broad absorptions also split into doublets. The strongest IR absorption of a propyne

ice, at 3266 cm^{-1}, is assigned to the C-H stretching mode of the acetylenic C-H bond. There are also three strong absorptions in the fingerprint region of the spectrum, 698, 479 and 650 cm^{-1}, which are assigned to C-H bending modes. The next strongest IR absorption is at 1440 cm^{-1} which is assigned to a CH_3 rock. The weak C≡C stretching mode can also be assigned to the absorption at 2117 cm^{-1}. For the full assignment of the IR absorption's observed for a propyne ice see Table 3.3.2.1.

Assignment	Peak centre / cm^{-1}
CH s str	3272(vvs)
CH a str	3267(vvs)
CH_3 d str	2966(m)
CH_3 s str	2922(s)
CH_3 a str	2862(m)
CCC def + C≡C str	2408(w)
C≡C str	2117(s)
CH_3 rock	1440(s)
CH_3 def	1381(w)
combination band	1365(m)
CH ip def	1311(s)
combination band	1295(s)
CH_3 d def	1041(m)
CH bend	698(vs)
CH bend	679(vs)
CH bend	650(vs)

Table 3.3.2.1: IR absorption band assignment for a multilayer propyne ice deposited onto a KBr substrate at 22 K and then heated to 100 K. The bands are assigned with aid of reference 50.

Peak centre / cm^{-1}	Molecular assignment
3333	H_2O
2348	$^{12}CO_2$
2278	$^{13}CO_2$
2149	^{12}CO
2140	^{12}CO
2111	^{13}CO
1874	NO
1664	H_2O
1040	O_3

Table 3.3.2.2: Molecular assignment of IR bands observed when the gas resulting from a microwave discharge in O_2 is deposited onto a KBr substrate at 22 K.

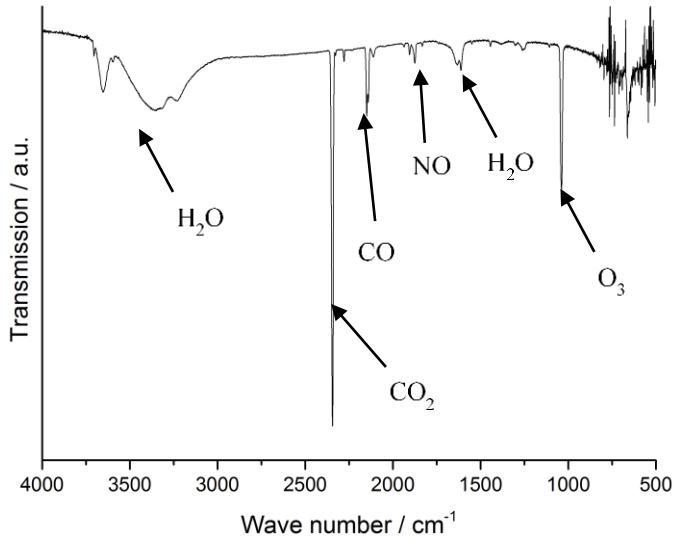

Figure 3.3.2.3: IR spectra of the gas exiting the microwave discharge. The most intense peaks have been labelled.

When the gas resulting from the microwave discharge is deposited onto a KBr substrate at 22 K, several signals are observed in the IR spectra (Figure 3.3.2.3). Again, several of these signals correspond to impurities such as water, CO and CO_2 since this is a high vacuum chamber. The strong IR absorption observed at 1040 cm^{-1} can be assigned to the ν_3 band of O_3.[51, 52] IR absorptions associated with CO_2, CO, H_2O and NO are also observed,[53-57] see Table 3.3.2.2 for full assignment. The production of O_3 and NO confirms the formation of oxygen atoms in the microwave discharge. In particular, it is well known that O_3 forms efficiently on surfaces at temperatures relevant to interstellar dust (10 – 50 K) *via* the reaction of O atoms and O_2.[46]

When propyne and O atoms react, the yield of products is typically small. At UCL approximately 3600 ML of propyne are deposited onto the graphite surface and the maximum yield of the single addition product at 50 K is 17 ± 2 ML (Figure 3.3.1.3). The maximum yield of the double addition product is even smaller (5 ± 2 ML at 50 K). The low yield of products means that IR spectra are dominated by absorptions of the reactants, mainly propyne. The domination of the IR spectra by propyne makes the identification of products difficult, since their absorptions often overlap with those of propyne. Furthermore, more than one product is formed and so absorptions of products can also overlap. Therefore, the IR data cannot provide quantitative data, for the reaction of propyne and O atoms, but rather a qualitative understanding of the isomers of the single and double addition products observed at UCL.

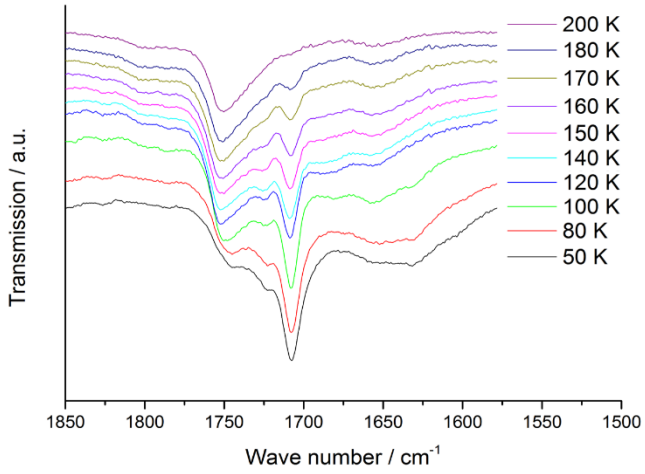

Figure 3.3.2.4: IR spectra of the carbonyl stretching region we propyne and O atoms are co-dosed onto a KBr substrate for one hour at 50 K. Each spectra represents the surface being heated to a different temperature between 50 K and 200 K. The baselines are displaced for clarity.

When propyne, oxygen atoms and molecular oxygen are co-dosed onto the KBr substrate, held at a surface temperature of 50 K for one hour, the strongest product absorption band is observed in the carbonyl stretching frequency range. This carbonyl stretching frequency is a complex convoluted band (Figure 3.3.2.4). However, it is clear that this complex band is composed of at least three absorptions, centred at approximately 1708 cm^{-1}, 1723 cm^{-1} and 1751 cm^{-1}. It is also

clear that as the surface is heated to 200 K the 1708 cm^{-1} band decreases in intensity whilst the 1751 cm^{-1} band increases in intensity.

When propyne and O atoms are dosed onto the KBr substrate at 80 K, two absorptions are observed in the carbonyl stretching region of the IR spectrum 1709 cm^{-1} and 1660 cm^{-1} (Figure 3.3.2.5). The absorbance at 1660 cm^{-1} is likely to be a water impurity.[58] As the surface is heated to 120 K the 1709 cm^{-1} peak reduces in intensity, broadens, and shifts to a slightly higher frequency of 1713 cm^{-1}. As the surface is heated further, to 160 K, the intensity decreases further and the band splits into two absorptions at 1722 cm^{-1} and 1708 cm^{-1}. When the surface is heated to 200 K a broad convoluted spectrum remains.

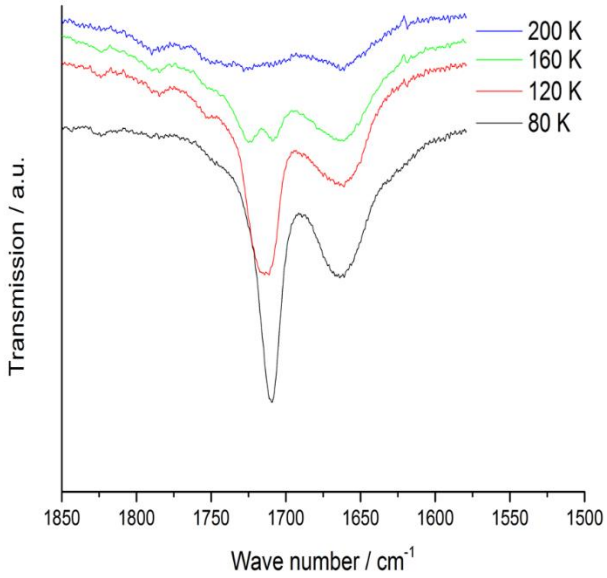

Figure 3.3.2.5: IR spectra of the carbonyl stretching region where propyne and O atoms are co-dosed onto a KBr substrate for one hour at 80 K. Each spectra represents the surface being heated to a different temperature between 80 K and 200 K. The baselines are displaced for clarity.

When propyne and O atoms are co-dosed onto a KBr substrate, at 22 K for 1 hour, no products are observed in the carbonyl stretching frequency range, of the IR spectra. However, when the dosing time is increased to two hours three absorptions can be seen in the IR spectrum at 1737 cm^{-1}, 1707 cm^{-1} and 1610 cm^{-1}. As the surface is then heated to 50 K, the absorption at 1610 cm^{-1} decreases. As this absorption at 1610 cm^{-1} decreases in intensity, a broad absorption centred at 1626 cm^{-1} is revealed. As the surface is heated from 22 K to 120 K the centres of the absorptions at 1737 cm^{-1} and 1707 cm^{-1} shift in frequency. The absorption at 1707 cm^{-1} shifts to a lower frequency and is centred at 1695 cm^{-1} at 120 K. The absorption at 1737 cm^{-1} shifts to a higher frequency and is centred at 1743 cm^{-1} at 120 K.

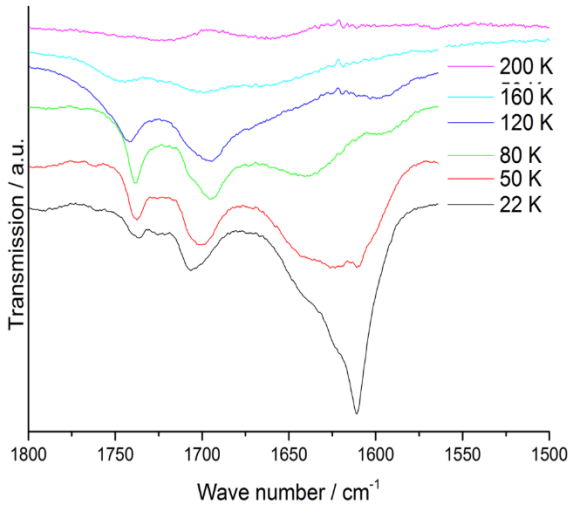

Figure 3.3.2.6: IR spectra of the carbonyl stretching region where propyne and O atoms are co-dosed onto a KBr substrate for two hour at 22 K. Each spectra represents the surface being heated to a different temperature between 22 K and 200 K. The baselines are displaced for clarity.

To increase the signal to noise ratio propyne and O atoms were also co-dosed onto the KBr substrate at 50 K for 3 hours, Figure 3.3.2.7. These spectra closely resemble the data collected when propyne is co-dosed with O atoms for 1 hour. The three most distinct bands are centred at 1708 cm^{-1}, 1724 cm^{-1} and 1747 cm^{-1}. It is also clear that as the surface is heated to 200 K the 1708 cm^{-1} band decreases in intensity whilst the 1747 cm^{-1} band increases in intensity. It is not easy to tell whether the intensity of the band at 1724 cm^{-1} changes upon heating due to the convolution of the peaks.

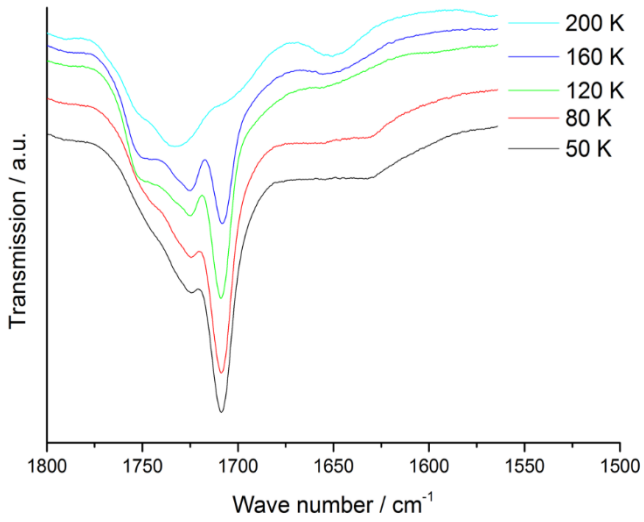

Figure 3.3.2.7: IR spectra of the carbonyl stretching region we propyne and O atoms are co-dosed onto a KBr substrate for three hour at 50 K. Each spectra represents the surface being heated to a different temperature between 50 K and 200 K. The peaks are displaced for clarity.

The depositions at each temperature (22K, 50K and 80 K) share one key feature, a carbonyl stretching frequency at 1708 ± 1 cm^{-1}. This C=O stretching frequency is often broad and when the surface temperature is 50 K, a distinct shoulder can be seen at 1726 cm^{-1}. The intensity of this band is smallest at 22 K and approximately 10 times larger at 50 K and 7 times larger at 80 K when compared to 22 K. These ratios of products, at 22 K, 50 K and 80 K, are the approximate ratios expected for the single addition product observed in the TPD experiments at UCL (Figure 3.3.1.3). It is therefore likely that this absorption at 1708 ± 1 cm^{-1} is due to the single addition product. There are two possible isomers of the single addition product which contain carbonyl stretching frequencies, cyclopropanone (Structure III in Figure 3.1.1) and propenal (Structure II in Figure 3.1.1). The strained nature of the cyclopropanone ring gives rise to a carbonyl stretching frequency of 1850 cm^{-1} in an aqueous solution.[59] Therefore, it is unlikely that cyclopropanone can be the carrier of the 1708 cm^{-1} absorption observed in this study. On the other hand, when propenal is deposited in an argon matrix, two C=O stretching frequencies are observed between 1700 cm^{-1} and 1730 cm^{-1}.[60] A comparison between reference 60 and the data from this study, after 3 hours of dosing at 50 K, can be seen in Figure 3.3.2.8. The carbonyl stretching frequency observed at 1708 cm^{-1}, in this study, is in good agreement with the carbonyl stretching frequency of propenal in an argon matrix. Propenal is therefore identified as the isomer of the single addition product formed in the reactions at UCL. However, it should be noted that at 50 K there are clearly additional carbonyl stretching frequencies at higher wave numbers which are not due to propenal.

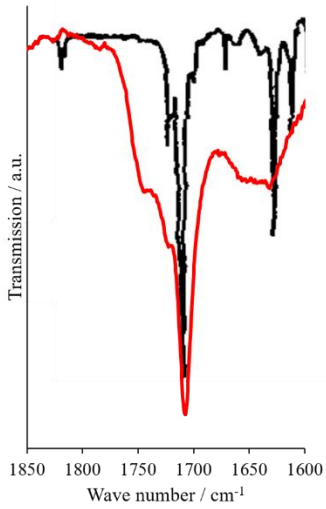

Figure 3.3.2.8: A comparison of the carbonyl stretching frequency observed at 1708 cm^{-1} when propyne and O atoms are dosed onto a KBr substrate at 50 K (red trace) and the carbonyl stretching frequency of propenal in an argon matrix (black trace). The spectra of the carbonyl stretching frequency of propenal in an argon matrix is taken from reference 60.

As discussed in Section 3.1, when propyne and O atoms react in the gas-phase, methylketene and propenal are expected to be intermediates. Methyl ketene has two IR absorptions at 2129 and

2125 cm^{-1}.[55, 61] This region of the IR spectrum contains an absorption of the C≡C bond in propyne at 2117 cm^{-1} and a C≡O stretch of carbon monoxide at 2136 cm^{-1}.[50, 56, 62] However, when a difference spectra between the propyne blank and propyne + O is taken a peak is revealed in the difference spectrum at 2123 cm^{-1} (Figure 3.3.2.9). This difference spectra is constructed by subtracting the IR absorbance spectrum for a pure propyne ice from an absorbance spectrum of a propyne ice which was co-deposited with O atoms. The absorbance spectra are calculated from the transmission spectra using equation 3.2.2.1. This difference spectrum allows one to remove the IR absorptions which are due to propyne from the spectrum recorded when propyne and O atoms are co-deposited. It is possible that this peak at 2123 cm^{-1} is due to $^{12}C^{17}O$, since $^{12}C^{17}O$ absorbs at 2123 cm^{-1}.[62] However, the natural abundance of ^{17}O is < 0.04%, given the intensity of the $^{12}C^{16}O$ absorption at 2136 cm^{-1} it is not possible that the peak at 2123 cm^{-1} is due to $^{12}C^{17}O$. The isotopic species with the highest abundance is $^{13}C^{16}O$ which absorbs at 2092 cm^{-1} and so this isotopologue can also not be responsible for the absorption at 2123 cm^{-1}.[62] It has been reported that CO can form dimers and trimers which can shift the CO absorption frequency. However, shifts due to $(CO)_x$ reported in the literature result in shifts to higher wavenumbers than 2136 cm^{-1}.[62] We therefore assign the absorption observed at 2123 cm^{-1} to the C=C=O asymmetric stretch of methylketene.[61] The absorption at 2123 cm^{-1} is observed when propyne and O atoms are dosed onto a KBr substrate at 22 K and 50 K. The absorption is not observed when propyne and O atoms are dosed onto the KBr substrate at 80 K. Since this absorption at 2123 cm^{-1} is only observed when the surface temperature is 22 K and 50 K, methyl ketene is likely to only be a product at low surface temperatures in the ISM.

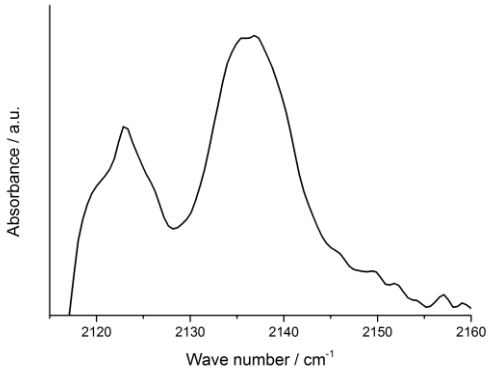

Figure 3.3.2.9: A difference spectra taken when spectrum 1 is subtracted from spectrum 2. Spectrum 1 is taken when propyne is deposited onto the KBr substrate at 22 K and heated to 80 K. Spectrum 2 is taken when propyne and O atoms are co-dosed onto the surface at 22 K and then heated to 80 K. The positive absorbance shows two absorption that are only present when O atoms are dosed with propyne. The absorption at 2136 cm^{-1} is due to CO and the absorption at 2123 cm^{-1} is due to methyl ketene.

From the data at UCL it is clear that at a low surface temperature of 22 K, one expects a similar quantity of single and double addition products to be produced (Figure 3.3.1.3). However, the yield of the single addition product is far greater than the yield of double addition product when the surface temperature is 50 K. One would therefore expect the carbonyl stretching frequency for the single addition product to dominate the spectra when the surface temperature is 50 K. When the IR spectra at 22 K are examined it is clear there is a second carbonyl stretching frequency at 1737 cm^{-1}. The stretching frequency of 1737 cm^{-1} is at higher frequency than the 1708 cm^{-1} absorption assigned to propenal. In general, a shift in the carbonyl absorption to higher wavenumbers is indicative of a more saturated molecule. There are six isomers of the double addition product which contain carbonyl groups: propenoic acid, propiolactone, methyl glyoxal, propanedial, formic acid ethenyl ester and glycidaldehyde (Figure 3.3.2.10). The double addition product is unlikely to be propenoic acid or formic acid ethenyl ester since these are unsaturated molecules and so their carbonyl stretching frequencies are at lower wavenumbers than 1737 cm^{-1}. Propiolactone can also be ruled out due to the strained nature of the ring the carbonyl group is bonded to, which generally shifts carbonyl stretching frequencies to wavenumbers higher than 1800 cm^{-1}. However, it is clear from the literature, that the carbonyl stretching frequencies of the other three molecules are not different enough to allow us to make a firm identification of the double addition product. The carbonyl frequencies of these products are often in coincidence with one another and their solid phase IR spectra are not always available in the literature. Since the yield of the double addition product is low, identification *via* weaker bands is also not possible. However, if the double addition product is the result of an O atom addition to propenal, the O atom addition is likely to occur at the double bond. Previous work at UCL has shown that the primary product when an O atom adds to a double bond is the epoxide.[42] If an O atom adds to the double bond in propenal to form an epoxide the resulting molecule would be glycidaldehyde. We therefore predict that the most likely isomer of the double addition product is glycidaldehyde. However, the solid phase IR spectrum of glycidaldehyde is not available in the literature to confirm this prediction.

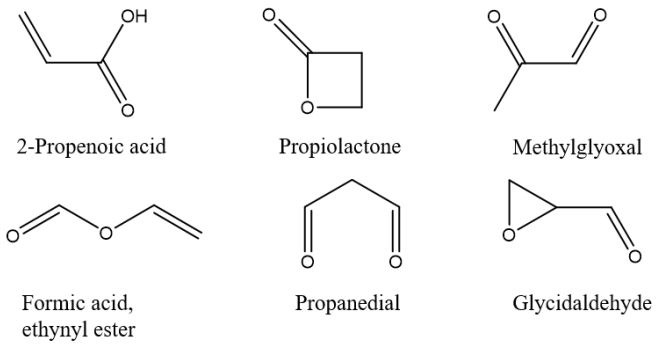

Figure 3.3.2.10: Possible isomers of the double addition product with carbonyl groups.

Whilst the double addition product was not able to be identified unambiguously, the experiments in Jena did reveal an unexpected result. After dosing propyne, O_2 and oxygen atoms onto a KBr substrate the surface was left overnight, under vacuum, to warm to room temperature. The next day a residue with a broad absorption centred at 1733 cm^{-1} was observed, Figure 3.3.2.11. The molecule responsible for the bands observed in this residue, at room temperature under vacuum, must have a significantly larger molecular mass than propyne. The implications of this result will be discussed in Section 3.5.2. In summary, there are several IR bands observed when propyne and O atoms are dosed onto a KBr substrate at surface temperatures relevant to the interstellar medium. Three bands in particular can be assigned to the single and double addition products, observed at UCL. The band at 1737 cm^{-1} is assigned to the double addition product and is possibly due to glycidaldehyde. Two bands observed at 1708 cm^{-1} and 2123 cm^{-1} are assigned to the single addition product. The 1708 cm^{-1} band is assigned to propenal and is observed at all three surface temperatures studied. The 2123 cm^{-1} band is assigned to methyl ketene, however, this band is only present when the surface temperature is 22 K or 50 K. Finally, a residue is observed when the surface is allowed to heat over night to room temperature. This residue must be due to a molecule with a significantly larger molecular mass than propyne.

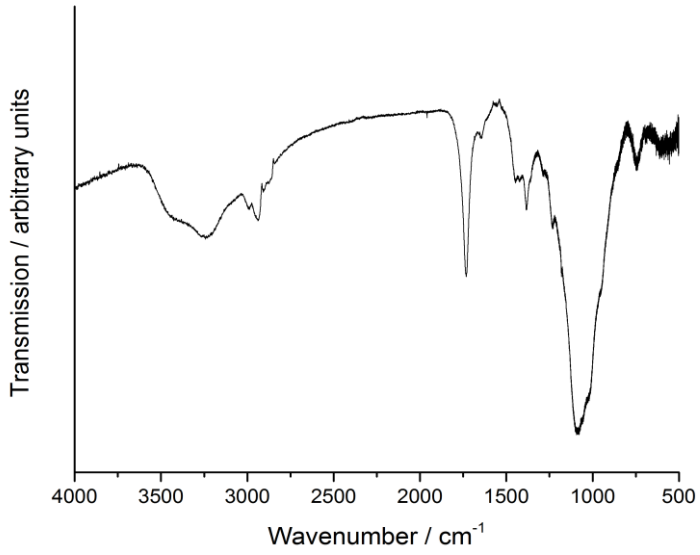

Figure 3.3.2.11: The IR spectrum of the residue which was observed on the KBr substrate when propyne and O atoms were dosed onto the surface at 50 K and the surface was left to warm to room temperature overnight.

3.4 Temperature Programmed Desorption Data Analysis

To account for the yield of the single and double addition products observed at UCL (Figure 3.3.1.3), a simple model is used to extract kinetic parameters. This model is described extensively

in Chapter Two. However, since in the case of propyne reacting with O atoms there are two products, the model must be extended to include the reaction that forms the double addition product. The model assumes that the O atoms add sequentially to propyne. The addition of the first oxygen atom generates the single addition product. The single addition product then reacts with another oxygen atom to form the double addition product. If all of the double addition product is formed from the O atom addition to the single addition product then the true yield of the single addition product is the sum of the single addition product and the double addition product. The model is therefore fitted to the sum of the single addition product and the double addition product rather than just the yield of the single addition product. In the model used in this Chapter, the O atoms can undergo the three reactions described in Section 2.10. The O atoms can react with themselves to form O_2 (reaction 3.4.1), O atoms can also react with O_2 to form O_3 (reaction 3.4.2) and finally O atoms can react with propyne to form the single addition product (reaction 3.4.3). In addition to these three reactions O atoms can also add to the single addition product to form the double addition product (reaction 3.4.4).

$$O + O \rightarrow O_2 \quad (3.4.1)$$

$$O_2 + O \rightarrow O_3 \quad (3.4.2)$$

$$C_3H_4 + O \rightarrow C_3H_4O \quad (3.4.3)$$

$$C_3H_4O + O \rightarrow C_3H_4O_2 \quad (3.4.4)$$

Each of the above reactions can proceed *via* two prototypical mechanisms, the Langmuir-Hinshelwood (LH) and the Eley-Rideal (ER) reactions. The LH mechanism proceeds when both reactants are adsorbed and thermalised on the substrate. In this case the O atoms diffuse on the surface where they either react with another mobile O atom or with immobile species such as O_2 or propyne. The rate coefficient for the LH mechanism is a product of the reaction probability and the diffusion coefficient. As discussed in Section 2.10, it is possible to fit the yield of the single and double addition products using an Arrhenius diffusion coefficient if one assumes the LH mechanism is inactive below 30 K. However, such a diffusion coefficient vastly under predicts the yield of O_3 detected in the experiment. Therefore, the rate coefficient for the diffusion of O atoms on the surface is described using an empirical rate coefficient that successfully describes the yield of ozone. [63] What is more, if O atoms diffuse on the surface, which results in O_3 production below 30 K, it follows that the diffusing O atoms can also react with propyne. Therefore, the assumption that the LH mechanism is inactive below 30 K for the reaction of O atoms and propyne, an assumption required to fit the data with an Arrhenius O atom diffusion barrier, cannot be valid.

The ER mechanism occurs, when an adsorbed species undergoes a reaction with a gas-phase partner. Since, in the present experiment, the reactants are co-dosed, either reactant can be the adsorbed species or the gas-phase partner, therefore two ER reactions must be included in the

model. ER1 will describe the reaction where O atoms are the gas-phase reactant. ER2 will describe the reaction where O atoms are the thermalized surface reactant. In the case of O atom addition to the single addition product discussed later, only the ER1 mechanism is active since there is no flux of the single addition product to the surface.

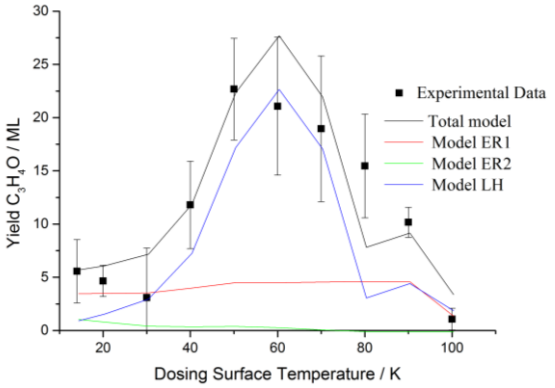

Figure 3.4.1: The sum of the yield of C_3H_4O and $C_3H_4O_2$, formed following the co-deposition of propyne (C_3H_4) and O atoms, as a function of surface temperature. Squares: experimental data; black line: total model; red: ER1 mechanism; green ER2 mechanism; blue LH mechanism. The error bars associated with the experimental results represent two standard deviations from three repeats at each surface temperature.

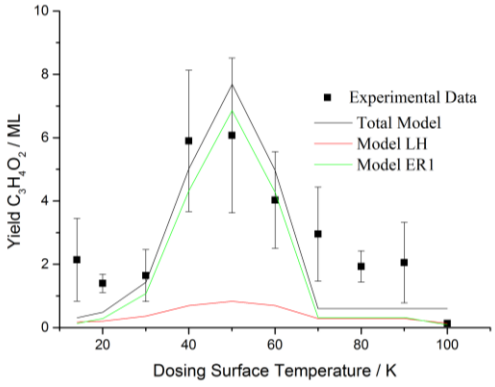

Figure 3.4.2: Yield of $C_3H_4O_2$, formed following the co-deposition of propyne (C_3H_4) and O atoms, as a function of surface temperature. Squares: experimental data; black line: total model; green: ER1 mechanism; red LH mechanism. The error bars associated with the experimental results represent two standard deviations from three repeats at each surface temperature.

The surface concentration of each reactant is calculated from the flux of the reactant to the surface, the depletion of the reactant due to reactions and the depletion of the reactant due to desorption. In this way the fractional coverage of each species can be evaluated at each dosing temperature. The model restricts the sum of the fractional coverages of each species to be 1. As a result the model assumes that the reactants do not penetrate into the ice; that is, all the reactivity occurs on the surface. The rate of each ER reaction is the product of the reaction probability, the fractional coverage of the surface reactant and the flux of the gas phase reactant. Whereas, the rate of each LH reaction is the product of the reaction probability, the diffusion coefficient and the fractional coverage of the reactants. The rates of reaction are then integrated over the time of the experiment, with a time step of 0.001 s, to give the total yield of product for each deposition temperature. A time step of 0.001 s is chosen since no change in product yield is observed when a smaller time step is used. These total yields are then compared to the experimental data. The model is first fitted to the sum of the single and double addition product yields. The model is fitted by varying the desorption energies of the reactants and the reaction probabilities of each prototypical reaction

mechanism (LH, ER1 and ER2) for the reaction of O atoms with propyne. The model is then fitted to the double addition product yield by varying the ER1 and the LH reaction probabilities for reaction 3.4.4. Note since there is no flux of the single addition product to the surface the ER2 mechanism is not active. The fits of the model to our experimental data can be seen in Figure 3.4.1 and 3.4.2 for the sum of the single and double addition products and double addition product respectively. The kinetic parameters used in these fits can be seen in Table 3.4.1.

Parameter	Value
O_2 desorption energy	8.7 ± 1.0 kJ mol^{-1}
O desorption energy	14.2 ± 0.3 kJ mol^{-1}
Propyne desorption energy	22.3 ± 0.5 kJ mol^{-1}
Reaction probability ER addition of the first O atom	0.01 ± 0.005
Reaction probability LH addition of the first O atom	0.003 ± 0.001
Reaction probability ER addition of the second O atom	0.2 ± 0.1
Reaction probability LH addition of the second O atom	0.1 ± 0.1

Table 3.4.1: Kinetic parameters characterizing the reaction of O atoms to propyne as a function of surface temperature. As discussed in the text, these parameters have been extracted by fitting a kinetic model to the experimental data we record for this surface reaction.

Previously in the literature reaction probabilities have been used to estimate reaction barriers.[63] Reaction probabilities have the same physical meaning as a rate constant and so a normalised Arrhenius equation (3.4.5) can be used to estimate the activation energy of the reaction:

$$E_x = - T \ln (\rho_x) \tag{3.4.5}$$

where E_x is the activation energy in Kelvin, T is the temperature in Kelvin and ρ_x is the reaction probability. In the case of the LH mechanism, the temperature is simply the surface temperature. However, in the case of the ER mechanism, the gas phase species has an approximate temperature of 300 K. One must therefore take account of the thermal energy of the gas phase species and calculate an 'effective' temperature of the encounter. The effective temperature for the ER mechanism can be calculated using equation 3.4.6:[63]

$$T_{eff} = \mu \left(\frac{T_s}{m_s} + \frac{T_g}{m_g} \right) \tag{3.4.6}$$

The effective temperature for the ER1 and ER2 mechanisms can be calculated at each surface temperature. The effective temperature for the ER mechanism ranges from 219 K to 259 K which estimates an activation energy of 9.19 ± 0.78 kJ mol^{-1}. Conversely, the barrier estimated for the LH mechanism is 2.68 ± 2.05 kJ mol^{-1}. The significance of these barriers will be discussed in the following Section.

3.5 Discussion

3.5.1 Temperature Programmed Desorption Discussion

The fit obtained with the kinetic model to the single addition product yield shows that the dominant mechanisms for the addition of an O atom to propyne are the LH and ER1. The ER1 mechanism occurs between a gas-phase O atom and a thermalized surface propyne molecule. The ER2 mechanism is significantly less active than the ER1 since [O(ads)] << [C_3H_4(ads)]. There are two factors effecting the relative fractional coverages of the O atoms and propyne. Firstly the fluxes of propyne and O atoms to the surface are 1 ML s^{-1} and 0.13 ML s^{-1}, the flux of O atoms is approximately an order of magnitude smaller than propyne. Secondly, at surface temperatures below 40 K, O atoms react with O_2 in the ice to eventually form O_3, this reaction further reduces the O atoms fractional coverage. Our model predicts that [O(ads)] and [C_3H_4(ads)] reach a steady state fractional coverage of approximately 0.03 and 0.76 respectively after 1.5 s when the surface temperature is 20 K. The rate of the ER1 mechanism is proportional to the product of the fractional surface coverage of propyne and the flux of O atoms to the surface, whilst the rate of the ER2 mechanism is proportional to the product of the fractional surface coverage of O atoms and the flux of propyne to the surface. This difference results in a larger rate of reaction for the ER1 mechanism, when compared with the rate of the ER2 mechanism. However, this reasoning does assume that the reaction probabilities of the ER1 mechanism and the ER2 mechanism are equal. However, the reaction probability of the ER2 mechanism would need to be approximately 10 times the ER1 mechanism reaction probability to result in comparable rates of reaction. One might therefore expect the LH mechanism to also be relatively inactive, since the rate of reaction is proportional to the product of the fractional surface coverages of propyne and O atoms. However, it is clear from the kinetic model that it is not possible to fit the single addition product yield with the ER1 mechanism and the ER2 mechanism alone. If the ER1 and ER2 reaction probabilities are increased to fit the data points between 40 K and 60 K, the predicted yields between 14 K and 30 K become too large. Furthermore, since O atoms have been shown to have a high diffusion coefficient on surfaces of astrochemical interest, it follows that the LH mechanism is active in this experiment.[46]

The model shows that at a dosing temperature of 100 K propyne ices can form on the graphite surface. When gas-phase O atoms impinge the propyne ice, the ER1 mechanism produces the single addition product. When the surface temperature is 70 K and below oxygen atoms can also adsorb onto the surface and so the LH mechanism becomes active. The activation of the LH mechanism increases the yield of the single addition product. At surface temperatures of 30 K and below O_2 can also adsorb onto the surface. The presence of O_2 in the ice opens up a competing pathway for O atom reactivity: the oxygen atoms can now react with O_2 to generate O_3. This

competing reaction is barrierless and so the yield of the single addition product is reduced below 30 K.[63]

The propyne desorption energy extracted using our kinetic model is 22.3 ± 0.5 kJ mol^{-1}. Previous work has shown that the desorption energy of propene is 21.4 ± 0.3 kJ mol^{-1} from a propene ice.[42] Propyne has a similar molecular mass to propene and so their desorption energies are expected to be similar. However, it is usually expected that alkynes will have smaller desorption energies than that of its alkene equivalent.[64] Specifically, the work of Rubes *et al.*[64] shows that ethene's desorption energy from a graphite (0001) surface is 17.36 ± 0.0361 kJ mol^{-1} whilst acetylene's desorption energy from the same surface is 14.67 ± 0.0273 kJ mol^{-1}. However, the uncertainty associated with the desorption energies extracted from our experimental data do not exclude the desorption energy of propyne being smaller than that of propene. Furthermore, the desorption energies we extract are not the desorption energies of propene and propyne on a graphite surface. Infact, our experiments probe the desorption kinetics of propyne and propene from multilayer ices of propyne and propene respectively.

There is a larger uncertainty associated with the desorption energy extracted for molecular oxygen compared to the uncertainty in other desorption energies extracted from this data set. The desorption energy of molecular oxygen is crucial to predicting the increase in yield of C_3H_4O and $C_3H_4O_2$ observed between 30 K and 50 K. The yield of C_3H_4O and $C_3H_4O_2$ increases because, as O_2 desorbs from the surface, the only reactive pathway for the O atoms are then to sequentially add to propyne to form C_3H_4O and $C_3H_4O_2$. The lower bound of the desorption energy represents the desorption energy needed to predict this increase in C_3H_4O and $C_3H_4O_2$ yield. The upper bound of the desorption energy represents the desorption energy needed to model the yields of ozone observed in this experiment. In reality, it is likely of course that there are a range of desorption energies of O_2. Noble *et al.* have shown that the desorption energy of O_2, on surfaces of astrochemical interest, is dependent upon surface coverages.[65] A multilayer ice of O_2 has a desorption energy of 7.6 ± 0.5 kJ mol^{-1}.[65] When the surface coverage of O_2 is decreased to 0.1 ML the O_2 desorption energy increases to as high as 9.65 kJ mol^{-1}, 9.55 kJ mol^{-1} and 10.44 kJ mol^{-1} on non-porous amorphous water ice, crystalline water ice and non-porous amorphous silicates respectively. The molecular oxygen binding energy, to the surface, is more dependent upon the surface coverage rather than the substrate onto which the ice is deposited. At low coverages, the molecules will occupy the highest energy binding sites. As the dose is increased these high energy binding sites become fully occupied and so the molecules must bind to lower energy adsorption sites. This range of desorption energies can be modelled by a single desorption energy with a large uncertainty. The kinetic model used in this Chapter to analyse the experimental results predicts a steady state O_2 surface coverage of 0.17 ML at 20 K after 1.5 s. The desorption energy

of a 0.2 ML O_2 ice on an amorphous porous water substrate has been extracted to be 9.00 kJ mol^{-1},[65] and so the value of 8.7 ± 1.0 kJ mol^{-1}, extracted here, is in good agreement with the literature data.

The interaction energy of an oxygen atom and pyrene (representative of a bridge site in graphite) has been calculated to be 11.6 kJ mol^{-1}.[66] It is generally accepted now that the desorption energy of O atoms observed experimentally is larger than this calculation.[67, 68] The desorption energy of O atoms obtained from the fit to the experimental data presented in this Chapter is 14.2 ± 0.3 kJ mol^{-1}. This is in good agreement with the value of 13.8 ± 0.5 kJ mol^{-1} determined by He *et al*. for the atom desorption energy on amorphous porous water.[45, 67]

As discussed in Chapter Two, it is not possible to fit the rate coefficients of the reaction between propyne and O atoms with Arrhenius reaction barriers. It has been hypothesised that this may be due to oxygen atoms tunnelling at these low temperatures, although this is controversial.[46] Another explanation is that the morphology of ices changes at very low temperatures which alters the nature of the absorption sites available.[69] For example, if the ice undergoes a phase change at low temperatures which results in lower binding energies of absorbates, the energy barrier to diffusion will also decrease. The binding energy and barrier to diffusion are directly related to one another since both processes require the molecule or atom to possess enough thermal energy to escape the potential well that binds the molecule or atom to the surface. Indeed, when the diffusion energy of a molecule is unknown it is often estimated to be 0.7 times the desorption energy.[67] Practically, whatever the origin of the non-Arrhenious behaviour of the diffusion coefficient, modelling a change in the rate constant with temperature is far simpler to implement when compared with a change in O atom adsorption energy. Quantum tunnelling only requires new parameters to describe the barrier through which the O atoms tunnel, whereas a change in O atom adsorption energy requires many new free parameters to describe the change in adsorption sites at each dosing surface temperature. However, the barriers required to fit a model, which includes tunnelling, are not always considered to be physical. We therefore use an empirical rate coefficient to describe O atom diffusion and reaction probabilities to account for the rate of reactions. Using an empirical rate coefficient for O atom diffusion and reaction probabilities allows a clear quantitative fit to our experimental data without increasing the number of free parameters in the model. The reaction probabilities extracted for the addition of the first O atoms to propyne generating the single addition product, ρ_{LH} = 0.003 ± 0.001 and ρ_{ER}=0.01 ± 0.005, show that the reaction is more facile than the recently reported reactivity of O atoms and carbon monoxide. This is expected since the reaction of an O atom with carbon monoxide occurs at a polar triple bond whilst this reaction is occurring at a non polar C≡C bond.

The fit of the kinetic model to the yield of double addition product is not as successful as the fit to the sum of the single and double addition products. The less successful fit to the double addition data is unsurprising as the fit to the double addition data relies upon the fit to the sum of the single

and double addition data. The model calculates the surface concentration of the single addition product based on the yields predicted by the fit to the sum of the single and double addition product yields. There is therefore more error associated with the fit to the double addition data than the fit to the single addition data. However, the model successfully qualitatively fits the general trends in double addition yield. The yield is low between 15 K and 20 K, the yield rises to a maximum at 50 K and reduces again as the temperature increases to 100 K. The model also successfully quantitatively fits the increase in the yield of the double addition product between 30 K and 60 K. However, the model predicts the yield between 70 K and 90 K to be smaller than the experimental yields. Generally, the fit to the double addition product yield shows that the reaction of O atoms with the single addition product requires much larger reaction probabilities than the reaction probabilities for the addition of an O atom to propyne. An increased reaction probability of the O atom addition to the single addition product, when compared with the addition of an O atom to propyne, is an indication that the barrier to the addition of the second O atom to propyne is smaller than the addition of the first atom. It is possible that the intermediate that forms the double addition product is a reactive, possibly strained, species; in this case, a large reaction probability is expected.

3.5.2 Infrared Spectroscopy Discussion

As discussed previously the IR spectral data can help identify the precise structural forms of the single and double addition products. Previously, at UCL, laser ionisation has been employed to determine the structure of the product when ethene and oxygen atoms react on surfaces at low temperatures. Determination of the product isomer by laser ionisation is feasible when there are a small number, of possible isomers with well separated ionisation potentials. The three possible isomers with the empirical formula C_2H_4O, relevant for the reaction of O atoms with ethene, are ethylene oxide, acetaldehyde and vinyl alcohol (Figure 3.5.2.1). It was found that, in the case of $O + C_2H_4$, the dominant product was the epoxide, ethylene oxide, with a small yield of acetaldehyde. In the case of the reaction between propyne and oxygen atoms the single and double addition products have many possible structural isomers. It is therefore not possible to use laser ionisation to determine the precise structural form of the products.

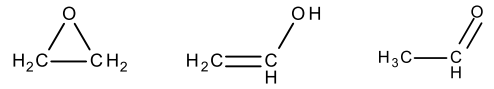

Ethylene oxide Vinyl alcohol Acetaldehyde

Figure 3.5.2.1: Organic structures relevant the reaction between ethene and O atoms.

If oxygen atoms react with ethene to form ethylene oxide, the analogous reaction of oxygen atoms with propyne would generate methyloxirene (Structure II in Figure 3.5.2.2). However, the stability of oxirenes is heavily debated. Different computational methods predict oxirenes to be either a transition state or a discrete intermediate during the isomerisation of ketocarbenes. As discussed earlier, a computational study determined that when O atoms react with propyne, in the gas-phase, two triplet state methyl ketocarbenes are formed (Structures I and III in Figure 3.5.2.2).[35] The methyl ketocarbene formed is dependent upon whether the O atom attacks the terminal or central acetylenic carbon in propyne. If the site of O atom attack is the terminal acetylenic carbon the two unpaired electrons are localised on the central C atom (Structure III in Figure 3.5.2.2). Conversely, if the site of O atom attack is the central C atom the two unpaired electrons are localised on the terminal C atom (Structure I in Figure 3.5.2.2). Both these methyl ketocarbenes undergo ISC to the singlet potential energy surface where they can isomerise to one another, *via* a methyl oxirene intermediate. The activation energy required to isomerise between the two ketocarbenes is 2 kcal mol^{-1}. The ketocarbene in which the paired electrons are localised on the central C atom can isomerise to form propenal and methyl ketene. There is evidence in our IR spectra for the formation of propenal and methyl ketene. The carbonyl stretching frequency observed at 1708 cm^{-1}, when the surface temperature is 22 K, 50 K and 80 K, is in good agreement with the carbonyl stretching frequency of propenal in an argon matrix.[60] The stretching frequency observed at 2123 cm^{-1} is in good agreement with the stretching frequency of methyl ketene in an argon matrix.[55, 61] Whilst the identification of the band at 2123 cm^{-1}, assigned to methyl ketene, is only possible in difference spectra, of a blank dose of propyne and a dose of propyne and O atoms at 22 K, ketene has been observed to be stable under experimental conditions relevant to the ISM.[56] Specifically, ice mixtures were grown on a metal substrate (aluminium and gold) held at 10 K for 1 hour. The resulting ice had an estimated thickness of 2.0 μm – 3.0 μm. The ices were then irradiated with 0.8 MeV protons to initiate radiation-chemical changes at surface temperatures of 10 – 20 K. In separate experiments ices were also irradiated using far-UV photolysis. Several ice mixtures were studied, which all consisted of a simple organic, such as acetylene or ethene, and either H_2O, CO_2 or O_2. Ketene's strongest IR feature, a C=C=O asymmetric stretch, is almost coincident with the intense fundamental vibration of solid CO near 2136 cm^{-1} and CO was also observed to be a product of these reactions. The authors were able to use isotopic labelling to separate the most intense CO and ketene features to unequivocally

identify the formation of ketene. Substituted ketenes are expected to be more stable than ketene and so if ketene is stable under similar experimental conditions it seems likely that methyl ketene will also be stable in our experiments.

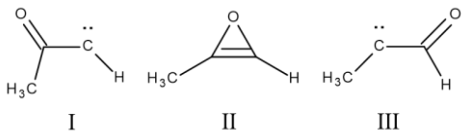

I II III

Figure 3.5.2.2: Chemical structures of I: the ketocarbene formed when the O atom attacks the central acetylenic carbon pf propyne, II: methyl oxirene, III: the ketocarbene formed when the O atom attacks the terminal acetylenic carbon of propyne.

In the gas-phase, methyl ketene and propenal dissociate to form C_2H_4 + CO, C_2H_3 + HCO, CH_2CHCO + H and C_2H_2 + CO + H_2. However, as discussed in Section 3.1, the activation energies for the dissociation of propenal and methyl ketene are at least an order of magnitude larger than the activation energies required to form propenal and methyl ketene from propyne and O atoms.[35] Furthermore, no conclusive evidence is found in our IR or TPD spectra, to show the formation of CO, C_2H_4, C_2H_2 or CH_2CHCO. CO is observed in the IR studies, however, since the chamber is only a high vacuum chamber it is very likely that this CO signal is due to accretion of the background gas in the chamber onto the cold substrate. Furthermore, no CO is identified in the TPD spectra recorded at UCL. It is therefore concluded that propenal and methyl ketene are the isomers of the single addition product observed at UCL. Unlike the gas-phase reaction, propenal and methyl ketene appear to be stable on surfaces at temperatures relevant to the ISM. This observation that methyl ketene and propenal are stable on surfaces at low temperatures is chemically intuitive, since the barriers for these molecules to dissociate, in the gas-phase, are at least an order of magnitude larger than the barriers which formed these molecules from O atoms and propyne. When the reaction probabilities extracted, at UCL, for the first O atom addition to propyne are used to estimate the activation energies of the reaction, the activation energies for the LH and ER mechanism are 2.68 ± 2.05 kJ mol^{-1} and 9.19 ± 0.78 kJ mol^{-1} respectively. Interestingly, the theoretically determined gas phase barriers for the ISC from the triplet state methyl ketocarbene to the singlet state methyl ketocarbene is 13 kJ mol^{-1}, the barrier for the formation of methyl ketene from this singlet state ketocarbene is 1.7 kJ mol^{-1} and the barrier for the formation of propenal from this singlet state ketocarbene is 7.5 kJ mol^{-1}.[35, 41] The barriers extracted in this study are comparable to the gas phase barriers which indicates that the mechanism for O atom addition on our surface is similar to the mechanism in the gas-phase.

In Section 3.3.2 it was postulated that the most likely structure for the double addition product was glycidaldehyde. There are six possible isomers of the double addition product which contain carbonyl groups: propenoic acid, propiolactone, methyl glyoxal, propanedial, formic acid ethenyl ester and glycidaldehyde (Figure 3.3.2.10). Propenoic acid and formic acid ethenyl ester were

ruled out since they are unsaturated molecules and so their carbonyl stretching frequencies are more similar to the unsaturated carbonyl stretching frequency of the single addition product, propenal (1708 cm^{-1}). The double addition product appears to have a carbonyl stretching frequency at 1737 cm^{-1}. Propiolactone can also be ruled out due to the strained nature of the ring the carbonyl group is bonded to which generally shifts carbonyl stretching frequencies to wave numbers higher than 1800 cm^{-1}. Glycidaldehyde was put forward as the most likely candidate out of the three remaining molecules since an O atom addition to the single addition product, propenal, is likely to occur at the C=C bond. At UCL it has been shown that an O atom addition to a C=C bond, on surfaces at low temperatures, results in an epoxide.[42] If an O atom adds to the double bond in propenal to form an epoxide the resulting molecule is glycidaldehyde. Interestingly, the reaction of propenal and O atoms has been studied in the gas-phase,[70] and this study shows that the primary process for oxygen atom addition to propenal is the addition of the O atom to the C=C bond. The addition of the O atom to the C=C bond accounts for 90 % of the reactivity. The other 10 % of the reactivity proceeds *via* H atom abstraction from the CHO group. The active intermediates formed by the O atom addition to the C=C bond form glycidaldehyde, CO + CH_3CHO and a polymeric species. So, this gas-phase study suggests that the double addition product isomer in our work is indeed glycidaldehyde. Since previous work at UCL indicates that an O atom addition to the double bond in propenal will result in the epoxide, glycidaldehyde, and the gas-phase study also shows that glycidaldehyde is a product when an O atom adds to propenal it seems very likely that the double addition product is indeed glycidaldehyde. However, there is no experimental data for the solid phase IR spectrum of glycialdehyde in the literature to help us definitively identify this species in the Jena IR spectra.

Perhaps the most interesting observation in the IR spectral data is the detection of a product which remains on the surface at room temperature under high vacuum. Following the deposition of propyne and O atoms, onto the KBr substrate at 50 K, the surface was left to warm overnight to room temperature. The following day IR spectral peaks were observed at 2936 cm^{-1}, 1733 cm^{-1}, 1384 cm^{-1}, 1233 cm^{-1} and 1091 cm^{-1}, Figure 3.3.2.11. It should be noted that the strong broad absorption at 1091 cm^{-1} is assigned to a silicate material which is believed to be formed from the glass in the discharge cell.[71] This band is not present in the first residue detected when propyne and O atoms were dosed onto the KBr substrate at 50 K for one hour, however, the data for 3 hours is shown because the other bands are more easily identifiable after a three hour dose. It is therefore believed that over time the O atoms etch the microwave discharge cell generating this silicate deposit. Nevertheless, for an organic molecule to remain on the surface under vacuum at room temperature means the molecule must have a significantly larger molecular mass than propyne. We therefore propose that this residue is formed *via* an extensive polymerisation reaction. It is known in organic chemistry that the presence of an acyl radical can initiate polymerisation of unsaturated carbon bonds.[72] Furthermore, in the gas-phase study, the polymeric species formed, when O atoms add to propenal, was found to be the dominant reaction product.[70]

The gas-phase study found that the polymeric species was a white deposit found in the reaction chamber. The deposit was insoluble in water, acetone or methanol, and could not be removed by heating with concentrated H_2SO_4. However, when the polymer was heated in concentrated NaOH solution, it could be easily removed from the walls of the reaction chamber. The authors conclude that these tests suggest that this substance is an ester-type polymer. It is suggested in the gas-phase study that β-propiolactone is a possible precursor for this ester-type polymer. The radical-initiated polymerisation of propenal has also been observed in other studies.[73, 74] However, these studies do not use O atoms as the radical and so different polymers are formed. The IR absorption peaks of the residue, in our experiments, are broad which is typical of non-crystalline polymers.[75] The broad absorptions arise from side chains vibrating in different chemical environments. The IR absorption spectra of the residue, in our experiments, resembles the IR spectra, in the literature, of poly-vinyl esters for example Poly(methyl methacrylate) (PMMA).[76] In the IR spectra of PMMA the absorptions at 2950 cm^{-1}, 1732 cm^{-1}, 1380 cm^{-1} and 1242 cm^{-1} can be assigned to asymmetric CH_3 stretching, C=O ester stretching, CH_3 asymmetric bending and –C-C(=O)-O bending respectively. The IR absorptions of our residue at 2936 cm^{-1}, 1733 cm^{-1}, 1384 cm^{-1} and 1233 cm^{-1} can therefore be assigned to the asymmetric CH_3 stretching, C=O ester stretching, CH_3 asymmetric bending and –C-C(=O)-O bending respectively. The polymer in our experiments is unlikely to be PMMA since the empirical formula of PMMA is $(C_5O_2H_8)_n$. If the polymer in our experiments is formed due to an O atom addition to propenal, as is observed in the gas-phase study, one would expect a polymer with the empirical formula $(C_3O_2H_4)_n$. A polymer with this empirical formula is poly(β-propiolactone). The absorptions of the residue formed in our study are in reasonably good agreement with the IR spectra of poly(β-propiolactone).[77] However, since the IR spectra of this polymer is dependent upon sample preparation, a firm identification of the polymer in our experiment is difficult. Nevertheless, the carbonyl stretching frequencies of poly-lactones such as poly(β-propiolactone) are observed at approximately 1730 cm^{-1}.[78] Another polymer with the empirical formula $(C_3O_2H_4)_n$ is poly(acrylic acid). However, the carbonyl stretching frequency of poly(acrylic acid) is 1713 cm^{-1}.[79] A carbonyl stretching frequency of 1713 cm^{-1} is not in agreement with the carbonyl stretching frequency of our residue which is at 1733 cm^{-1}. Furthermore, if the polymerisation reaction observed in this study, is analogous to the reaction observed in reference 70 then the polymer formed is not water soluble. Poly(acrylic acid) is water soluble and so cannot be the polymer formed in reference 70. It therefore follows that the most likely candidate for the residue formed in our experiments is poly(β-propiolactone).

3.6 Astrophysical Implications

The experiments discussed in this Chapter show that on interstellar dust grain analogues, under UHV conditions and at low temperatures, oxygen atoms can readily add to the carbon-carbon triple bond of a propyne molecule. The reaction is detectable at surface temperatures of 14 K and above, and is most efficient at 50 K. The O atom flux used in the experiments at UCL are equivalent to approximately 10^5–10^6 years of O atom exposure in an interstellar cloud.[34,36,42] It is therefore possible that this pathway is active in interstellar clouds. The IR spectral data indicates that there are two single addition products, with the empirical formula C_3H_4O, methyl ketene and propenal. Propenal has been observed in the gas-phase towards the star-forming region Sagittarius B2(N).[80] In the same study propanol and propynal were also observed. The authors suggest that hydrogenation of propynal, on the surface of dust grains, will produce propenal and propanol under astrophysical conditions. However, the results presented in this Chapter suggest that propenal can also be produced *via* the single oxygen atom addition to propyne. Hydrogen atom addition reactions are limited to surface temperatures below 20 K since above this surface temperature H atoms have a low residence time on surfaces of astrochemical interest. The desorption energy extracted in this study for O atoms is 14.2 ± 0.3 kJ mol^{-1}. Such a desorption energy is significantly larger than the desorption energy of H atoms. As a result O atom addition is likely to occur on interstellar dust grains at temperatures up to approximately 70 K. In the warm up phase of interstellar clouds the surface temperature rises at approximately 1 K $century^{-1}$.[65] O atom addition on surfaces can therefore take place for a longer time period during the warm up phase of an interstellar cloud.[81]

The detection of an organic refractory residue at room temperature under vacuum indicates that radical initiated polymerisation reactions may occur on the surface of dust grains. In this case the O atoms initiate the polymerisation of propenal which is likely to form the polymer poly(β-propiolactone). It is well known that carbonaceous dust grains are efficiently destroyed in the interstellar medium.[82] The polymerisation of propenal on the surface of interstellar dust grains represents a cold condensation method for synthesising carbonaceous dust grains in the interstellar medium. However, further studies are required to investigate if this polymerisation reaction is unique to the addition of O atoms to propenal.

3.7 Summary

The experiments presented in this Chapter show that when propyne reacts with O atoms, on surfaces at temperatures relevant to the ISM, three products are formed. At UCL the TPD studies show two reaction products with the empirical formulae C_3H_4O and $C_3H_4O_2$. The reaction products at UCL are detectable between temperatures of 15 K and 100 K. Modelling of the UCL experimental yields of C_3H_4O and $C_3H_4O_2$ indicate that the LH mechanism is significantly active

under our experimental conditions. Since the LH mechanism is the most active surface mechanism in the ISM it is likely that the reactions which form these products under our experimental conditions can occur on the surface of dust grains. The IR studies in Jena indicate that the product with the empirical formula of C_3H_4O is likely to be a mixture of propenal and methyl ketene below 80 K and only propenal above 80 K. The IR studies also show that the product with the empirical formula $C_3H_4O_2$ has a carbonyl stretching frequency at 1737 cm^{-1}. This carbonyl stretching frequency, of the double addition product, possibly indicates that glycidaldehyde forms, when an O atom addition occurs at the C=C bond in propenal. The IR studies in Jena show a third product is formed which is a residue which remains on the surface under vacuum at room temperature. This residue is believed to be formed *via* an O atom radical initiated polymerisation reaction and a likely polymeric structure is poly(β-propiolactone). Consequently, these experiments show that thermal heterogeneous pathways can contribute to the formation of C_3H_4O and $C_3H_4O_2$ isomers in interstellar clouds whilst the polymeric species may contribute to the carbonaceous dust in interstellar clouds. Propyne and propenal have already been observed within the giant molecular cloud Sagittarius B2.[2, 3, 80] A confirmed identification of glycialdehyde in the same regions of the ISM, as propyne and propenal, would provide an observational signature of the addition of O atoms to propyne occurring on dust grains.

3.8 References

1. B. E. Turner, E. Herbst and R. Terzieva, *Astrophysical Journal Supplement Series*, 2000, **126**, 427-460.
2. S. Martin, R. Mauersberger, J. Martin-Pintado, C. Henkel and S. Garcia-Burillo, *Astrophysical Journal Supplement Series*, 2006, **164**, 450-476.
3. E. Churchwell and J. M. Hollis, *Astrophysical Journal*, 1983, **272**, 591-608.
4. E. Herbst and E. F. van Dishoeck, in *Annual Review of Astronomy and Astrophysics, Vol 47*, eds. R. Blandford, J. Kormendy and E. VanDishoeck, Annual Reviews, Palo Alto, 2009, vol. 47, pp. 427-480.
5. A. Fuente, S. Garcia-Burillo, M. Gerin, D. Teyssier, A. Usero, J. R. Rizzo and P. de Vicente, *Astrophysical Journal*, 2005, **619**, L155-L158.
6. R. Mauersberger, C. Henkel, C. M. Walmsley, L. J. Sage and T. Wiklind, *Astronomy & Astrophysics*, 1991, **247**, 307-314.
7. R. J. A. Grim, F. Baas, T. R. Geballe, J. M. Greenberg and W. Schutte, *Astronomy & Astrophysics*, 1991, **243**, 473-477.
8. J. E. Chiar, A. J. Adamson and D. C. B. Whittet, *Astrophysical Journal*, 1996, **472**, 665-672.
9. H. M. Cuppen, E. M. Penteado, K. Isokoski, N. van der Marel and H. Linnartz, *Monthly Notices of the Royal Astronomical Society*, 2011, **417**, 2809-2816.
10. K. M. Hickson, V. Wakelam and J.-C. Loison, *Molecular Astrophysics*, 2016, **3–4**, 1-9.
11. C. Walsh, T. J. Millar, H. Nomura, E. Herbst, S. W. Weaver, Y. Aikawa, J. C. Laas and A. I. Vasyunin, *Astronomy & Astrophysics*, 2014, **563**.
12. K. Hiraoka, N. Mochizuki and A. Wada, in *Astrochemistry: From Laboratory Studies to Astronomical Observations*, eds. R. I. Kaiser, P. Bernath, Y. Osamura, S. Petrie and A. M. Mebel, 2006, vol. 855, pp. 86-99.
13. T. Kasamatsu, T. Kaneko, T. Saito and K. Kobayashi, *Bulletin of the Chemical Society of Japan*, 1997, **70**, 1021-1026.
14. Y. Dede and I. Ozkan, *Phys. Chem. Chem. Phys.*, 2012, **14**, 2326-2332.
15. Y. Takano, H. Masuda, T. Kaneko and K. Kobayashi, *Chemistry Letters*, 2002, DOI: 10.1246/cl.2002.986, 986-987.
16. T. Fouchet, E. Lellouch, B. Bezard, H. Feuchtgruber, P. Drossart and T. Encrenaz, *Astronomy and Astrophysics*, 2000, **355**, L13-L17.
17. T. deGraauw, H. Feuchtgruber, B. Bezard, P. Drossart, T. Encrenaz, D. A. Beintema, M. Griffin, A. Heras, M. Kessler, K. Leech, E. Lellouch, P. Morris, P. R. Roelfsema, M. RoosSerote, A. Salama, B. Vandenbussche, E. A. Valentijn, G. R. Davis and D. A. Naylor, *Astronomy and Astrophysics*, 1997, **321**, L13-L16.
18. Y. Alibert, O. Mousis and W. Benz, *Astrophysical Journal*, 2005, **622**, L145-L148.
19. Y. Alibert, O. Mousis, C. Mordasini and W. Benz, *Astrophysical Journal*, 2005, **626**, L57-L60.
20. D. Gautier, F. Hersant, O. Mousis and J. I. Lunine, *Astrophysical Journal*, 2001, **559**, L183-L183.
21. D. Gautier, F. Hersant, O. Mousis and J. I. Lunine, *Astrophysical Journal*, 2001, **550**, L227-L230.
22. F. Hersant, D. Gautier and J. I. Lunine, *Planetary and Space Science*, 2004, **52**, 623-641.
23. O. Mousis, Y. Alibert and W. Benz, *Astronomy & Astrophysics*, 2006, **449**, 411-415.
24. M. Burgdorf, G. Orton, J. van Cleve, V. Meadows and J. Houck, *Icarus*, 2006, **184**, 634-637.
25. A. Coustenis, B. Bezard, D. Gautier, A. Marten and R. Samuelson, *Icarus*, 1991, **89**, 152-167.
26. N. A. Teanby, P. G. J. Irwin, R. de Kok, A. Jolly, B. Bezard, C. A. Nixon and S. B. Calcutt, *Icarus*, 2009, **202**, 620-631.
27. C. A. Arrington and D. J. Cox, *Journal of Physical Chemistry*, 1975, **79**, 2584-2586.
28. S. L. Zhao, W. Q. Wu, H. M. Zhao, H. Wang, C. F. Yang, K. H. Liu and H. M. Su, *J. Phys. Chem. A*, 2009, **113**, 23-34.
29. G. Y. Adusei, A. S. Blue and A. Fontijn, *Journal of Physical Chemistry*, 1996, **100**, 16921-16924.

30. E. N. Aleksandrov, I. V. Dubrovina and S. N. Kozlov, *Kinet. Catal.*, 1981, **22**, 394-396.
31. J. M. Brown and B. A. Thrush, *Transactions of the Faraday Society*, 1967, **63**, 630-&.
32. K. H. Homann and C. Wellmann, *Ber. Bunsen-Ges. Phys. Chem. Chem. Phys.*, 1983, **87**, 527-532.
33. J. R. Kanofsky, D. Lucas, F. Pruss and D. Gutman, *Journal of Physical Chemistry*, 1974, **78**, 311-316.
34. G. Q. Xing, X. Huang, X. B. Wang and R. Bersohn, *J. Chem. Phys.*, 1996, **105**, 488-495.
35. I. Gimondi, C. Cavallotti, G. Vanuzzo, N. Balucani and P. Casavecchia, *The Journal of Physical Chemistry A*, 2016, DOI: 10.1021/acs.jpca.6b01564.
36. A. D. Becke, *J. Chem. Phys.*, 1993, **98**, 5648-5652.
37. C. T. Lee, W. T. Yang and R. G. Parr, *Physical Review B*, 1988, **37**, 785-789.
38. H. J. Werner, *Molecular Physics*, 1996, **89**, 645-661.
39. P. Celani and H. J. Werner, *J. Chem. Phys.*, 2000, **112**, 5546-5557.
40. D. E. Woon and T. H. Dunning, *J. Chem. Phys.*, 1995, **103**, 4572-4585.
41. G. Vanuzzo, N. Balucani, F. Leonori, D. Stranges, V. Nevrly, S. Falcinelli, A. Bergeat, P. Casavecchia and C. Cavallotti, *The Journal of Physical Chemistry A*, 2016, DOI: 10.1021/acs.jpca.6b01563.
42. M. D. Ward and S. D. Price, *Astrophysical Journal*, 2011, **741**.
43. Fehsenfe.Fc, K. M. Evenson and H. P. Broida, *Review of Scientific Instruments*, 1965, **36**, 294-&.
44. J. He and G. Vidali, *Faraday Discuss.*, 2014, **168**, 517-532.
45. J. He, D. Jing and G. Vidali, *Phys. Chem. Chem. Phys.*, 2014, **16**, 3493-3500.
46. E. Congiu, M. Minissale, S. Baouche, H. Chaabouni, A. Moudens, S. Cazaux, G. Manico, V. Pirronello and F. Dulieu, *Faraday Discuss.*, 2014, **168**, 151-166.
47. M. Minissale, E. Congiu and F. Dulieu, *J. Chem. Phys.*, 2014, **140**.
48. M. Minissale, E. Congiu, S. Baouche, H. Chaabouni, A. Moudens, F. Dulieu, M. Accolla, S. Cazaux, G. Manico and V. Pirronello, *Physical Review Letters*, 2013, **111**.
49. N. M. S. D. Center and d. S.E. Stein, in *NIST Chemistry WebBook, NIST Standard Reference Database Number 69, Eds. P.J. Linstrom and W.G. Mallard*, National Institute of Standards and Technology, Gaithersburg MD, 20899, http://webbook.nist.gov, (retrieved December 4, 2013). .
50. J. P. Camplin, J. K. Eve and E. M. McCash, *Phys. Chem. Chem. Phys.*, 2000, **2**, 4433-4440.
51. C. Ennis and R. I. Kaiser, *Astrophysical Journal*, 2012, **745**.
52. B. Sivaraman, C. S. Jamieson, N. J. Mason and R. I. Kaiser, *Astrophysical Journal*, 2007, **669**, 1414-1421.
53. P. A. Gerakines, W. A. Schutte, J. M. Greenberg and E. F. Vandishoeck, *Astronomy & Astrophysics*, 1995, **296**, 810-818.
54. M. Minissale, G. Fedoseev, E. Congiu, S. Ioppolo, F. Dulieu and H. Linnartz, *Phys. Chem. Chem. Phys.*, 2014, **16**, 8257-8269.
55. D. E. Johnstone and J. R. Sodeau, *Journal of the Chemical Society-Faraday Transactions*, 1992, **88**, 409-415.
56. R. L. Hudson and M. J. Loeffler, *Astrophysical Journal*, 2013, **773**.
57. A. S. Bolina, A. J. Wolff and W. A. Brown, *Journal of Physical Chemistry B*, 2005, **109**, 16836-16845.
58. S. Ioppolo, H. M. Cuppen, C. Romanzin, E. F. van Dishoeck and H. Linnartz, *Phys. Chem. Chem. Phys.*, 2010, **12**, 12065-12076.
59. R. Breslow and G. Ryan, *Journal of the American Chemical Society*, 1967, **89**, 3073-&.
60. C. E. Blom, R. P. Muller and H. H. Gunthard, *Chemical Physics Letters*, 1980, **73**, 483-486.
61. J. A. Harrison and H. Frei, *Journal of Physical Chemistry*, 1994, **98**, 12142-12151.
62. H. Dubost, *Chem. Phys.*, 1976, **12**, 139-151.
63. M. Minissale, E. Congiu, G. Manico, V. Pirronello and F. Dulieu, *Astronomy & Astrophysics*, 2013, **559**.
64. M. Rubes, J. Kysilka, P. Nachtigall and O. Bludsky, *Phys. Chem. Chem. Phys.*, 2010, **12**, 6438-6444.

65. J. A. Noble, E. Congiu, F. Dulieu and H. J. Fraser, *Monthly Notices of the Royal Astronomical Society*, 2012, **421**, 768-779.
66. H. Bergeron, N. Rougeau, V. Sidis, M. Sizun, D. Teillet-Billy and F. Aguillon, *J. Phys. Chem. A*, 2008, **112**, 11921-11930.
67. M. Minissale, E. Congiu and F. Dulieu, *Astronomy & Astrophysics*, 2016, **585**.
68. J. He, J. Shi, T. Hopkins, G. Vidali and M. J. Kaufman, *Astrophysical Journal*, 2015, **801**.
69. *Faraday Discuss.*, 2014, **168**, 571-615.
70. M. Sadayuki, *Bulletin of the Institute for Chemical Research, Kyoto*

University 1981, **59**, 128-141.
71. B. T. Draine, *Annual Review of Astronomy and Astrophysics*, 2003, **41**, 241-289.
72. C. Chatgilialoglu, D. Crich, M. Komatsu and I. Ryu, *Chemical Reviews*, 1999, **99**, 1991-2069.
73. W. Kern, R. C. Schulz and D. Braun, *Journal of Polymer Science*, 1960, **48**, 91-99.
74. D. H. Volman and R. K. Brinton, *The Journal of Chemical Physics*, 1952, **20**, 1764-1768.
75. D. Bower and Maddams, *The Vibrational Spectroscopy of Polymers*, Cambridge University Press 1989.
76. G. Duan, C. Zhang, A. Li, X. Yang, L. Lu and X. Wang, *Nanoscale Research Letters*, 2008, **3**, 118-122.
77. S. Okamura, T. Higashimura, A. Tanaka, R. Kato and Y. Kikuchi, *Die Makromolekulare Chemie*, 1962, **54**, 226-229.
78. H. R. Kricheldorf, M. Berl and N. Scharnagl, *Macromolecules*, 1988, **21**, 286-293.
79. L. J. Kirwan, P. D. Fawell and W. van Bronswijk, *Langmuir*, 2003, **19**, 5802-5807.
80. J. M. Hollis, P. R. Jewell, F. J. Lovas, A. Remijan and H. Mollendal, *Astrophysical Journal*, 2004, **610**, L21-L24.
81. A. Occhiogrosso, S. Viti, M. D. Ward and S. D. Price, *Monthly Notices of the Royal Astronomical Society*, 2012, **427**, 2450-2456.
82. A. P. Jones, N. Ysard, M. Koehler, L. Fanciullo, M. Bocchio, E. Micelotta, L. Verstraete and V. Guillet, *Faraday Discuss.*, 2014, **168**, 313-326.

Chapter 4 – Reaction of Acrylonitrile with Oxygen Atoms

4.1 Introduction

Acrylonitrile (CH_2CHCN), also known as vinylnitrile and propenitrile, was the first molecule with a C=C double bond to be observed in the ISM.[1, 2] The positive identification of acrylonitrile was made possible due to its well-characterised microwave spectrum.[1, 3] In early studies, upper limits for the abundance of acrylonitrile were calculated for Sgr B2.[1, 2] In 1983 acrylonitrile was also detected in the dark dense cloud TMC-1, *via* four rotational transitions, and found to have a column density of 3×10^{12} cm^{-2}.[4] The following year a spectral scan of the molecular cloud Orion A and the carbon star IRC+ 10216 was published.[5] This paper reported an estimated column density of 1×10^{14} cm^{-2} for acrylonitrile in Orion A. In 2005 the column densities of several molecules containing a cyanide or isocyanide functional group were evaluated in Sgr B2(N). Acrylonitrile was found to have a column density of 3.72×10^{14} cm^{-2}. As a result of these studies it is clear that acrylonitrile is present in a range of interstellar environments.

Dense clouds have two main phases to their life cycle, a cold phase and a warm up phase. In the cold phase, gas and dust temperatures are approximately 10 – 20 K. As a result of the cold temperatures molecular species accrete onto the surface of the dust present forming icey mantles. Once a cold phase cloud reaches a critical density the cloud will start collapsing under its own gravitational field. The contraction of the cloud causes a rise in temperature of approximately 1 K $century^{-1}$. This phase in which the temperature rises is called the warm up phase and the contraction eventually results in the formation of a protostar. Acrylonitrile is yet to be observed in the solid phase in ices present in the ISM. However, recently acrylonitrile's desorption energy has been determined to be 35 kJ mol^{-1} from a pure acrylonitrile ice.[6] A desorption energy above 10 kJ mol^{-1} results in little to no thermal desorption from a surface of 10 K - 20 K. Since acrylonitrile is observed in the gas-phase and it has a desorption energy larger than 10 kJ mol^{-1} it is likely that acrylonitrile will be present in interstellar ices.

In addition to its detection in the ISM, acrylonitrile has also been observed in comets and in Titan's atmosphere. Since the temperature of Titan's surface is 94 K,[7] the reactions in this Chapter are not only relevant to the ISM but also relevant to Titan. Studying the reactivity of acrylonitrile also provides a direct comparison between the reactivity of C=C and C≡N bonds on surfaces under interstellar conditions. Both of these functional groups are contained in many of the molecules detected in the interstellar medium. The cyanide group can be found in simple radicals such as CN, small molecules such as HCN, as well as long chain cyanopolyynes.[8-10] For this reason it is important to establish the reaction pathways available to acrylonitrile on ice surfaces.

Acrylonitrile may also be important in the process of forming prebiotic molecules, since hydrogenation of the cyanide group results in a C-N single bond. This C-N bond is often considered the most important bond in nature due, to its presence in amino acids and, therefore, in proteins. The deuteration of the CN radical has been studied under astrophysical conditions,[11] where the CN radical was produced using a microwave discharge in N_2/HCN (50/1). The gas resulting from the discharge was co-deposited onto a gold plated copper substrate target with D atoms. The reaction was repeated at three different dosing temperatures: 10, 15 and 20 K. Using IR spectroscopy, the only product detected below 20 K was DCN, no hydrogenation of the C≡N bond was detected. Above 20 K, DCN was not detected, presumably due to the low residence time of the D atoms. In 2011, the hydrogenation of the C≡N bond was revisited. The hydrogenation of hydrogen cyanide, HC≡N, was studied on a copper surface at 15 K.[10] A HCN ice was deposited onto the copper substrate and irradiated with a fluence of 10^{18} cm^{-2} H atoms. The authors attempted to detect the products of the reaction using IR spectroscopy, however, no products were identified. It was only when TPD, a more sensitive technique, was used that methylamine, CH_3NH_2, was detected from the reaction of H atoms and HCN. The reaction of H atoms with the C≡N bond in the cyanide radical and hydrogen cyanide is therefore concluded to be a slow reaction. The reaction of the C≡N bond with O atoms has not been studied on surfaces under astrophysical conditions.

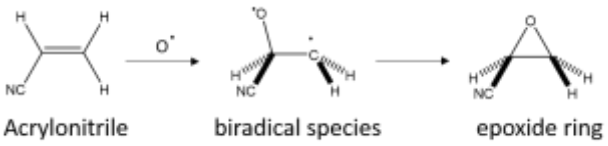

Figure 4.1.1: The reaction pathway of acrylonitrile and oxygen atoms in the gas-phase.[12]

In the gas-phase reaction of acrylonitrile and $O(^3P)$, the major channel is thought to involve the formation of a biradical species which subsequently undergoes fragmentation or stabilisation to an epoxide ring (Figure 4.1.1).[12] Minor fragmentation channels were also observed, preceding *via* an H atom or a CN moiety extraction by the incident O atom.[12] Conventional transition state theory was used to estimate an activation energy of 855 K (7.4 kJ mol^{-1}) for the reaction of acrylonitrile and O atoms.[12] The accuracy of conventional transition state theory is verified by a plot of activation energy *vs* ionisation potential. In general as the ionisation potential increases the activation energy increases linearly. This linear relationship occurs since the O atom must extract an electron from the highest occupied molecular orbital to form a bond generating the biradical intermediate. However, when the activation energy of several alkenes' reactions with O atoms is plotted as a function of the alkene's ionisation potential, acrylonitrile is a clear outlier from the line of best fit. The activation energy appears to be lower than would be predicted by the line of best fit for the ionisation potentials and activation energies of several other alkenes. The

authors, therefore, conclude that an activation energy of 885 K (7.4 k J mol^{-1}) is likely to be an underestimate. It can be estimated from the linear plot of ionisation potentials *vs* activation energies that a more appropriate activation energy would be ~9.6 kJ mol^{-1}. Nevertheless, the results in Chapter Three indicate that a reaction with an activation energy of 9.6 kJ mol^{-1} can proceed under our experimental conditions (Section 3.4 and 3.5.2). It is therefore likely that O atoms will readily react with acrylonitrile on surfaces under astrophysical conditions.

4.2 Experimental

The experimental apparatus utilised in this study has been discussed in detail in Chapter Two. In this study oxygen atoms, molecular oxygen and acrylonitrile are co-dosed onto a graphite surface with fluxes of 0.266 ML s^{-1}, 0.534 ML s^{-1} and 0.656 ML s^{-1} respectively, where 1 ML = 1 x 10^{15} molecules. It is important to note that the dosing regime is such that the graphite surface is covered within approximately 1 s. Therefore, the surface reaction we observe occurs overwhelmingly on an acrylonitrile/oxygen ice. The experiment was repeated at several different surface temperatures between 14 and 100 K. After a dosing period of one hour, the dosing lines were evacuated and the surface was allowed to cool to 14 K. Following this cooling a current of 15 amps was passed through a tantalum strip heater below the surface to heat the surface to approximately 200 K in a TPD experiment. Products and reactants desorbing from the surface were detected using time of flight mass spectroscopy (TOFMS). The experiment is repeated three times at each surface dosing temperature. As part of the experimental method, suitable background spectra are also recorded. These background TPD spectra are collected for each dosing surface temperature. In each background spectra only acrylonitrile and O_2 are dosed onto the surface i.e. no microwave discharge is used to generate O atoms, but all other experimental conditions are identical. These background spectra confirm the product signals in the experiment are due to the O atoms formed in the source cells and not another reaction pathway.

The acrylonitrile was purchased from Sigma-Aldrich and has a purity of ≥99 %. Volatile impurities were removed from the liquid by subjecting it to a series of freeze-thaw cycles. The acrylonitrile was then taken from the vapour pressure of the purified liquid acrylonitrile held at room temperature. Commercial samples of acrylonitrile contain 35-45 ppm monomethyl ether hydroquinone to inhibit polymerisation. However, since the concentration is extremely low and the vapour pressure of monomethyl ether hydroquinone is also low, this impurity does not affect the experiment. The acrylonitrile was also protected from light activated polymerisation by shielding the sample vial in aluminium foil.

4.3 Results

Whenever acrylonitrile and O atoms are co-dosed onto the graphite surface below 100 K, a signal is observed in the mass spectra during the TPD phase with a mass-to-charge (*m/z*) ratio of 69 (Figure 4.3.1). No other product signals corresponding to the reaction of O atoms with acrylonitrile are observed. This signal is consistent with an empirical formula of C_3H_3NO indicating addition of a single oxygen atom to acrylonitrile.

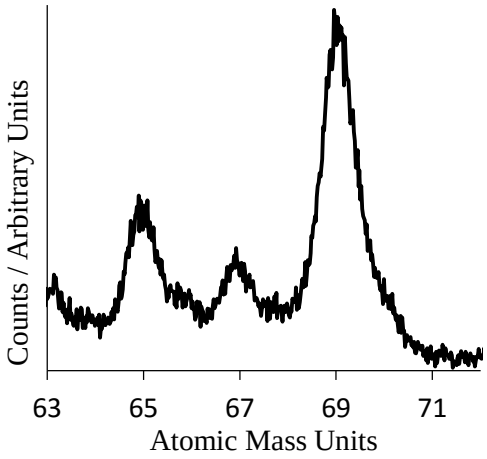

Figure 4.3.1: Sections of representative mass spectra recorded during the TPD phase showing peaks for *m/z* = 69, corresponding to the additions of one oxygen atom. See text for details.

To determine the yield of product (*m/z* = 69), the temperature of desorption is first determined by observing the number of counts at *m/z* = 69 during the heating phase of the TPD (Figure 4.3.2). Such a plot is referred to as a desorption profile. From the desorption profile for *m/z* = 69 (Figure 4.3.2) it can be seen that molecules with *m/z* = 69 desorb from the surface between 135 K - 200 K. The desorption profile has two peaks, a smaller low temperature peak centred at ~ 140 K and a larger high temperature peak centred at ~ 180 K The mass spectra between 135 K - 200 K are summed and the peak at *m/z* = 69 is integrated. A background spectra summed over the same desorption temperatures and integrated for *m/z* = 69 is then subtracted. This ensures that the background subtracted signal observed is solely due to the addition of O atoms. The procedure is repeated for each experiment performed at a range of different dosing surface temperatures. The above procedure yields the relative yields of product at each dosing temperature.

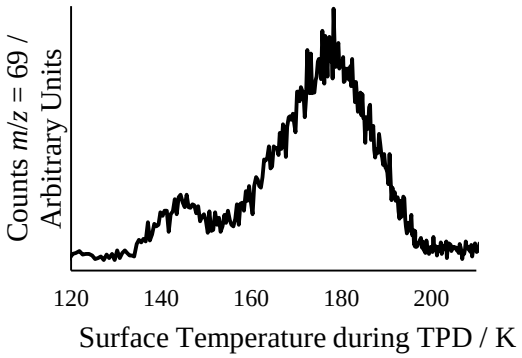

Figure 4.3.2: A desorption profile for *m*/*z* = 69 during the TPD heating phase.

At low temperatures (14 K – 50 K) a peak at (*m*/*z*) = 48 is also observed in the mass spectra. This mass spectral signal is consistent with a molecular formula of O_3 formed from the side reaction of O atoms with undissociated O_2. As discussed in Chapter 1, it is well known that the gas resulting from a microwave discharge in O_2 will yield a beam of O atoms and O_2. When this gas is deposited onto a surface of astrophysical interest O_3 is formed.[13-17] This peak at (*m*/*z*) = 48 is also integrated in the same fashion as described for the (*m*/*z*) = 69 peak.

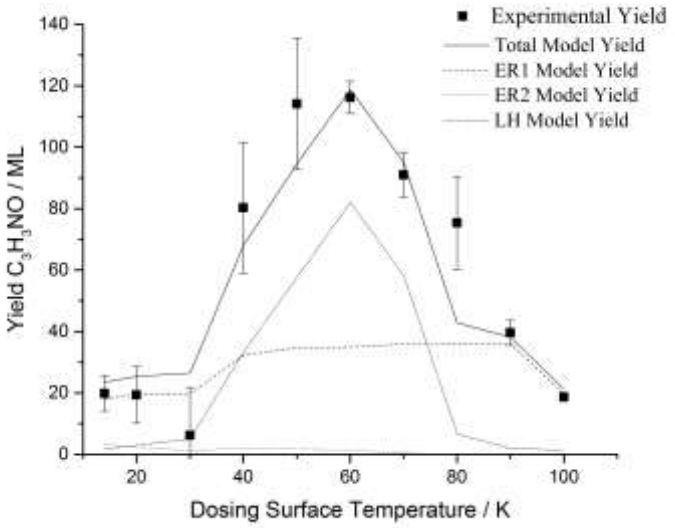

Figure 4.3.3: Yield of C_3H_3NO, formed following the co-deposition of acrylonitrile (C_3H_3N) and O atoms, as a function of surface temperature. Squares: experimental data; solid line: model; long dash ER1 mechanism; dot ER2 mechanism; short dash LH mechanism. The error bars associated with the experimental results represent two standard deviations from three repeats at each surface temperature.

As discussed in Chapter Two, a kinetic model can be used to extract reaction probabilities from the experimental data. To compare the experimental data to the model, the number of counts in the mass spectra must be converted to number of molecules. This transformation is carried out by integrating the mass spectral signals at (m/z) = 53 and (m/z) = 32 from a known dose of acrylonitrile and O_2 respectively, when the surface is held at 14 K. The integrated signal of (m/z) = 53 and (m/z) = 32 allows us to determine a proportionality constant between the number of counts in the mass spectral signals and molecular abundance for acrylonitrile and O_2 respectively. The proportionality constant represents the detection efficiency of the parent ion when acrylonitrile or O_2 is ionised in our TOFMS. Determining the detection efficiency assumes a sticking probability of unity in the calibration experiment. Such a sticking coefficient is likely to be an excellent characterization of the interaction of acrylonitrile and O_2 with the 14 K surface since the pressure rise in the chamber during this dosing is negligible. These detection efficiencies for O_2 and acrylonitrile must now be modified to characterise the detection efficiencies of the products observed at m/z = 69 and m/z = 48. To relate the detection efficiency of O_3 to that of O_2 is straight-forward since partial ionisation cross sections are readily available in the literature. However, the partial and total ionisation cross sections of acrylonitrile and the product observed at m/z = 69 are not available, and so the total ionisation cross sections of acrylonitrile and the product observed at m/z = 69 are assumed to be equal. In determining these detection efficiencies we must also allow for the fact that not every molecule we ionize will result in a parent ion in the mass spectrum; we must allow for fragmentation in the ionisation process. To make this correction, for the product observed at m/z = 69 the fragment to parent ratio is estimated from the standard mass spectrum of acetyl cyanide from the NIST reference database.[18] The above procedure allows the yield of C_3H_3NO and O_3 to be estimated on an absolute scale from the TPD spectra. The yield is reported as a function of surface temperature. The total yield of C_3H_3NO and O_3 at each dosing surface temperature can be seen in Figure 4.3.3 and 4.3.4 respectively. The yield of C_3H_3NO is relatively low at a surface temperature of 100 K. The yield increases as the surface temperature is decreased and reaches a maximum at 60 K. As the surface temperature decreases to 30 K from 60 K the yield is nearly zero. As the temperature decreases further to 14 K, the yield rises to the same yield as at 100 K. The yield of O_3 is approximately zero at 60 K. As the surface temperature decreases, the yield increases and reaches a plateau at 40 K. The O_3 yield is, within the uncertainty of the data, constant as the surface temperature is decreased to 14 K.

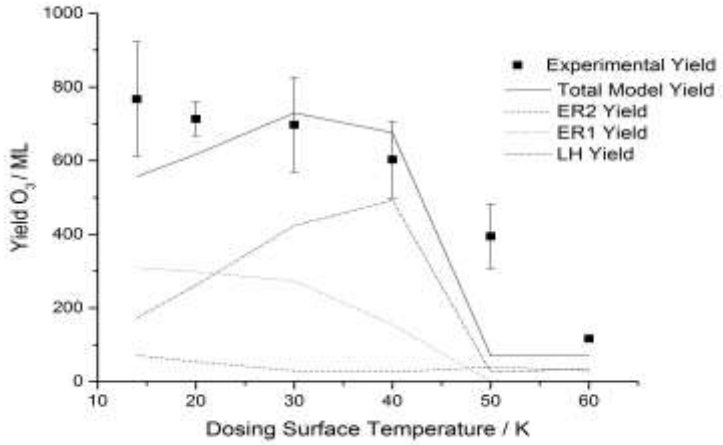

Figure 4.3.4: Yield of O_3 formed following the co-deposition of acrylonitrile (C_3H_3N) and O atoms, as a function of surface temperature. Squares: experimental data; solid line: model; long dash ER1 mechanism; dot ER2 mechanism; short dash LH mechanism. The error bars associated with the experimental results represent two standard deviations from three repeats at each surface temperature.

4.4 Data analysis

A simple kinetic model can be used to extract kinetic parameters from the experimental data. Since this model is well described in Chapter Two, only the key features concerning the modelling of experimental data described in this Chapter are outlined here. The O atoms can undergo three different reactions on the surface: O atoms can either react with themselves or O_2 in a 'side reaction', equations 4.4.1 and 4.4.2 respectively. O atoms can also react with acrylonitrile to form the observed product at m/z = 69 equation 4.4.3.

$$O + O \rightarrow O_2 \quad (4.4.1)$$

$$O_2 + O \rightarrow O_3 \quad (4.4.2)$$

$$C_3H_3N + O \rightarrow C_3H_3NO \quad (4.4.3)$$

Each of the above reactions can proceed *via* two prototypical mechanisms, the Langmuir-Hinslewood (LH) and the Eley-Rideal (ER) reaction. The LH mechanism proceeds when both reactants are adsorbed and thermalised on the substrate. In this case the O atoms diffuse on the surface where they either react with another mobile O atom or with immobile species such as O_2 or acrylonitrile. As discussed in Chapter Two the O atom diffusion coefficient does not seem to obey an Arrhenious law and so is evaluated using equation 4.4.4.[19]

$$k_{diff} = k_0 (1 + T^3/T_0^3) \quad (4.4.4)$$

The ER mechanism occurs, when an adsorbed species undergoes a reaction with a gas-phase partner. Since in the present experiment, the reactants are co-dosed, either reactant can be the adsorbed species or the gas-phase partner, therefore two ER reactions must be modelled. The ER1 will describe the reaction where O atoms are the gas-phase reactant. The ER2 will describe the reaction where O atoms are the thermalized surface reactant.

The fractional coverage of each reactant is calculated from the flux of the reactant to the surface, the depletion of the reactant due to reactions and depletion of the reactant due to desorption. In this way the surface concentrations can be evaluated at each dosing temperature. The model also assumes that the reactants do not penetrate into the ice; that is all the reactivity occurs on the surface. As a result the model restricts the total surface concentration of all the reactants to be 1 ML (1×10^{15} cm^{-2}). The rate of each reaction can be evaluated using the calculated fractional coverages. The rates of reaction are then integrated to give the total yield of product for each deposition temperature. These total yields are then compared to the experimental data. The model is fitted to the experimental data by varying the desorption energies of acrylonitrile, molecular oxygen and atomic oxygen as well as the reaction probabilities of each prototypical reaction mechanism (LH, ER1 and ER2) for the reaction of O atoms with acrylonitrile. The fit obtained using our model can be seen in Figure 4.3.3 and 4.3.4. The kinetic parameters used in the fit can be seen in Table 4.4.1.

Parameter	Value
O_2 desorption energy	8.5 ± 0.8 kJ mol^{-1}
O desorption energy	14.2 ± 0.2 kJ mol^{-1}
Acrylonitrile desorption energy	22.7 ± 0.2 kJ mol^{-1}
Reaction probability ER	0.038 ± 0.002
Reaction probability LH	0.0060 ± 0.0002

Table 4.4.1: Kinetic parameters characterizing the reaction of O atoms to acrylonitrile, to C_3H_3NO, as a function of surface temperature. As discussed in the text, these parameters have been extracted by fitting a kinetic model to the experimental data we record for this surface reaction.

As discussed in Section 3.4, previously in the literature experimentally determined reaction probabilities have been used to estimate reaction barriers using equation 4.4.5.[19]

$$E_x = - T \ln (\rho_x) \qquad (4.4.5)$$

where E_x is the activation energy in Kelvin, T is the temperature in Kelvin and ρ_x is the reaction probability. In the case of the LH mechanism the temperature is simply the surface temperature, however, in the case of the ER mechanism, the gas phase species has an approximate temperature of 300 K. One must therefore take account of the thermal energy of the gas phase species and

calculate an 'effective' temperature of the reaction. The effective temperature for the ER mechanism can be calculated using equation 3.4.6:[19]

$$T_{eff} = \mu\left(\frac{T_s}{m_s} + \frac{T_g}{m_g}\right) \tag{3.4.6}$$

The effective temperature for the ER1 and ER2 mechanisms can be calculated at each surface temperature. The effective temperature for the ER mechanism ranges from 219 K to 259 K which estimates an activation energy of 6.79 ± 0.41 kJ mol^{-1}. Conversely, the barrier estimated for the LH mechanism is 2.4 ± 1.8 kJ mol^{-1}. The significance of these barriers will be discussed in the following Section.

4.5 Discussion

The fit obtained with the kinetic model shows that the dominant prototypical mechanisms are the LH and ER1. The ER1 mechanism occurs between a gas-phase O atom and a thermalized surface acrylonitrile molecule. The ER2 mechanism occurs between gas-phase acrylonitrile and a thermalized surface O atom. The ER2 mechanism is significantly less active than the ER1 because [O(ads)] << [C_3H_3N(ads)] despite their fluxes to the surface being of the same order of magnitude. This low surface coverage of O atoms is due to O atom's reaction with other O atoms and O_2 molecules. The model predicts that [O(ads)] and [C_3H_3N(ads)] reach steady state fractional coverages of approximately 0.03 and 0.5 respectively after 1 s when the surface temperature is 20 K. It should be noted that it is not possible to fit the experimental data with a pure ER model. If the ER1 and ER2 reaction probabilities are increased to fit the data points between 40 K and 60 K the predicted yields between 14 K and 30 K become too large. Furthermore, since O atoms have been shown to have a high diffusion coefficient on surfaces of astrochemical interest, it follows that the LH mechanism should be active in this experiment.[15]

Our model shows that at a surface temperature during dosing of 100 K, and below, acrylonitrile can adsorb onto the surface. When gas-phase O atoms impinge the acrylonitrile ice, a reaction occurs generating C_3H_3NO *via* the ER1 mechanism. As the surface temperature decreases to 70 K, O atoms can also adsorb onto the surface and so the LH mechanism becomes active, increasing the yield of C_3H_3NO. As the surface temperature begins to approach 30 K, O_2 can also adsorb onto the surface. The adsorption of O_2 onto the surface opens up a competing pathway for O atoms. Specifically, the O atoms can now react with O_2 to generate O_3, this is a barrier-less reaction.[15] This competing pathway reduces the yield of C_3H_3NO below 40 K.

There is a larger uncertainty associated with the desorption energy extracted for molecular oxygen compared with the uncertainty in other desorption energies extracted from this data set. The desorption energy of molecular oxygen is crucial to predicting the increase in yield of C_3H_3NO observed between 30 K and 50 K. The yield of C_3H_3NO increases because as O_2 desorbs from the surface the O atoms can only react with acrylonitrile to form C_3H_3NO. The lower bound of the desorption energy represents the desorption energy needed to predict this increase in C_3H_3NO yield. The upper bound of the desorption energy represents the desorption energy needed to predict the yields of ozone observed in this experiment. In reality it is likely that there are a range of desorption energies of O_2. Noble *et al.* has shown that the desorption energy of O_2, on surfaces of astrochemical interest, is dependent upon surface coverages.[20] A multilayer ice of O_2 has a desorption energy of 7.6 ± 0.5 kJ mol^{-1}.[20] When the surface coverage of O_2 is decreased to 0.1 ML the O_2 desorption energy increases to as high as 9.65 kJ mol^{-1}, 9.55 kJ mol^{-1} and 10.44 kJ mol^{-1} on non-porous amorphous water ice, crystalline water ice and non-porous amorphous silicate respectively. The oxygen ice binding energy is more dependent upon the surface coverage rather than the substrate the ice is deposited onto. At low coverages, the molecules will occupy the highest energy binding sites. As the dose is increased these high energy binding sites become fully occupied and so the molecules must bind to lower energy adsorption sites. This range of desorption energies can be modelled by a single desorption energy with a large uncertainty. Our kinetic model, used in this Chapter, to analyse the experimental results predicts a steady state O_2 surface coverage of 0.47 ML at 20 K after 1 s. The desorption energy of a 0.5 ML O_2 ice on an amorphous porous water substrate has been extracted to be 8.08 kJ mol^{-1} and so the value of 8.5 ± 0.8 kJ mol^{-1}, extracted here, is in good agreement with the literature data. This value is also in good agreement with the desorption energy extracted for O_2 in Chapter Three (8.7 ± 1.0 kJ mol^{-1}).

The interaction energy of an oxygen atom and pyrene (representative of a bridge site in graphite) has been calculated to be 11.6 kJ mol^{-1}.[21] However, as discussed in Chapters One and Three, the desorption energy of O atoms observed experimentally is larger than this calculation.[22] The desorption energy of O atoms obtained from the fit to the experimental data presented in this Chapter is 14.2 ± 0.2 kJ mol^{-1} which is in line with the value extracted in Chapter Three (14.2 ± 0.3 kJ mol^{-1}).[23] This desorption energy for O atoms also agrees with a previous estimation by He *et al.* of 13.8 ± 0.5 kJ mol^{-1} on amorphous porous water,[14] and also agrees with experiments by Minissale *et al.*[22]

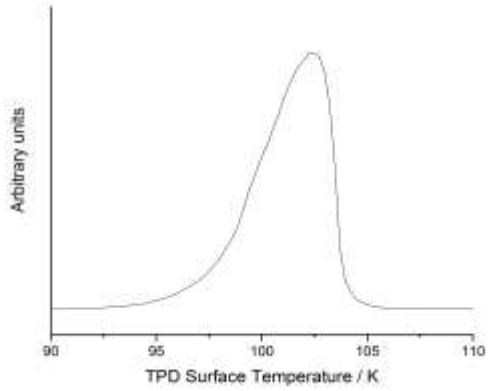

Figure 4.5.1: A desorption profile for acrylonitrile following the deposition of an acrylonitrile-oxygen ice.

The desorption energy extracted for acrylonitrile is 22.7 ± 0.2 kJ mol^{-1}. This agrees nicely with desorption energies extracted for propene,[24] 21.4 ± 0.3 kJ mol^{-1} and propyne, 22.3 ± 0.5 kJ mol^{-1} (determined in Chapter Three). The desorption energy of acrylonitrile is expected to be slightly larger than propene and propyne due to its increased mass. However, this extracted desorption energy of acrylonitrile, 22.7 ± 0.2 kJ mol^{-1}, is significantly smaller than the previous estimation of 35 kJ mol^{-1} from a pure acrylonitrile ice by Toumi et al.[6] The desorption energy extracted in this Chapter is essential for fitting the reduction in yield of C_3H_3NO between 90 K – 100 K. If acrylonitrile does not start to desorb from the surface at 95 K the ER1 mechanism will continue to generate C_3H_3NO above 100 K. This is not in line with the experimental results in this Chapter. Furthermore, the desorption energy of a molecule is directly related to the temperature at which the molecule desorbs from the surface during a TPD experiment. It has previously been determined that water desorbs from a pure ice between 160 K -180 K.[25] In the same study the desorption energy of water was extracted to be 36.2 kJ mol^{-1}. In our study acrylonitrile desorbs from the surface between 95 K – 105 K (Figure 4.5.1) and so its desorption energy must be lower than that of water. One could argue that during our experiments, at low temperatures (15 – 30 K), the ice deposited is an acrylonitrile/O_2 ice which one might expect to have a smaller desorption energy than a pure acrylonitrile ice, however at high temperatures (70 – 100 K) O_2 and O atoms no longer have a high sticking coefficient. As a result ices deposited above 70 K, in our experiments, generate a nearly pure acrylonitrile ice, since there is only a low concentration of C_3H_3NO in the ice. However, the desorption profile for acrylonitrile does not vary significantly when our experiment is performed at different deposition temperatures and so we believe the desorption profile of acrylonitrile observed in this experimental data is representative of a pure acrylonitrile ice. If acrylonitrile's binding energy to a pure acrylonitrile ice was 35 kJ mol^{-1}, one would expect acrylonitrile to desorb between approximately 140 – 160 K. We therefore conclude that a more appropriate desorption energy for acrylonitrile from a pure acrylonitrile ice is 22.7 ± 0.2 kJ mol^{-1}. Toumi et al. comment that an amorphous-crystalline phase change is observed at 94

K for an acrylonitrile ice as so it is possible we are observing desorption of an amorphous ice whereas Toumi et al. observe the desorption of a crystalline ice.

As discussed in Chapters Two and Three, it is not possible to fit the rate coefficients for of the reaction between acrylonitrile and O atoms with Arrhenius reaction barriers. It has been hypothesised that this may be due to oxygen atoms tunnelling at these low temperatures, although this is controversial.[15] Another explanation is that the morphology of ices changes at very low temperatures which alters the nature of the absorption sites available.[26] For example, if the ice undergoes a phase change at low temperatures which results in lower binding energies of absorbates, the energy barrier to diffusion will also decrease. The binding energy and barrier to diffusion are directly related to one another since both processes require the molecule to possess enough thermal energy to escape the potential well that binds the molecule to the surface. Indeed, when the diffusion energy of a molecule is unknown it is often estimated to be 0.7 times the desorption energy.[22] When designing a model, tunnelling is simple to implement although the barriers extracted are not always considered to be physical. Additionally, the change in adsorption sites is complicated as many new parameters are introduced into the model. The rates of reaction are therefore modelled as reaction probabilities which represent a clear quantitative fit to our experimental data without increasing the number of free parameters in the model. The reaction probabilities extracted, ρ_{LH} = 0.006 ± 0.0002 and ρ_{ER}=0.038 ± 0.002 (see equations 2.10.10, 2.10.11 and 2.10.12 for the definitions of ρ_{LH} and ρ_{ER}), show that the reaction between acrylonitrile and O atoms is more facile than the recently reported reactivity of O atoms and carbon monoxide.[19] The reaction is also more facile than the reaction observed in Chapter Three for the first O atom addition to propyne.

Acrylonitrile has two unsaturated centres, the C=C bond and the cyanide group and so if full saturation of acrylonitrile was achieved in the reaction, one would expect the addition of three oxygen atoms. There is no evidence for such a product in our experimental data, only the addition of one oxygen atom. We believe this single oxygen atom addition occurs at the C=C bond rather than the C≡N bond for three reasons. Firstly, if this single oxygen atom addition occurred at the C≡N bond one might expect the addition of a second oxygen atom, as in the case of oxygen atom addition to the triple bond in propyne (Chapter Three). Secondly, when oxygen atoms are deposited onto a methyl cyanide or cyanide ice, under the same experimental conditions as described in this Chapter, no reaction was observed within the detection limits of our experimental apparatus. Thirdly, the reaction probabilities extracted for this O atom addition to acrylonitrile are larger than the reaction probabilities extracted for the O atom addition to C≡O,[19] and also larger than the reaction probabilities extracted in Chapter Three for the first O atom addition to the C≡C bond in propyne. Reaction probabilities relate to the relative activation energies of a reaction, the smaller the activation energy the larger the reaction probability. The activation energy for an O atom addition to a triple bond is generally dependent on the strength of the bond

and the bond strength is largely dependent on the polarity of the bond. The polarity of these three bonds is C≡O > C≡N > C≡C and so the expected reaction probabilities for each bond is C≡O < C≡N < C≡C. Since our kinetic model extracts reaction probabilities for O atom addition to acrylonitrile, which are larger than the O atom addition to a C≡O bond and a C≡C bond, we conclude that the O atom addition occurs at a weaker bond in acrylonitrile, the C=C bond.

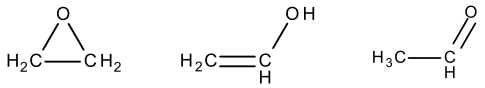

Ethylene oxide Vinyl alcohol Acetaldehyde

Figure 4.5.2: Organic structures relevant to the reaction between ethene and O atoms

As discussed in Section 1.8.3, a previous study by Ward *et al.* has shown that when ethene, the simplest molecule with a C=C bond, is dosed onto a graphite surface, in the same fashion as the experiment described in this Chapter, a single oxygen addition is observed.[24] Since, in the case of ethene reacting with O atoms, there are only three possible isomers of the product (Figure 4.5.2) laser ionisation could be employed to identify the specific isomer formed. The overwhelming majority of the product was found to be ethylene oxide with a small amount of acetaldehyde. The experimental data presented in this Chapter appears to be analogous to the reaction observed between ethene and O atoms, since two peaks are observed in the desorption profile for (*m/z*) ratio of 69. Two desorption peaks in desorption profiles indicate different molecular binding energies to the surface. A binding energy of a molecule, at a fixed surface coverage, is dependent upon the molecule and the environment the molecule is bound. For example, different phases of ice represent different surface environments and so can lead to different desorption profiles for the different phases of the ice. However, during TPD experiments, ices often have time to crystallise during the heating phase and so different phases of the ice are difficult to observe. Another case which can lead to two peaks in desorption profiles can be the formation of two different isomers of the product. Since two isomers are formed when the double bond in ethene reacts with O atoms, it seems likely that two isomers are formed when the double bond in acrylonitrile reacts with O atoms. It is therefore predicted that the isomer of the product with the empirical formula C_3H_3NO is cyanoethylene oxide and a small yield of acetyl cyanide. This prediction is in line with the gas-phase reactivity for the reaction of O atoms and acrylonitrile where the major product is thought to form *via* a biradical species which subsequently undergoes stabilisation to an epoxide ring.[12] Interestingly, the activation energy extracted from our experimental data for the ER mechanism is 6.8 ± 0.4 kJ mol^{-1} which is in agreement with the gas phase barrier of 7.4 kJ mol^{-1} for the O atom addition to acrylonitrile. This agreement further confirms that the reaction we observe on our surface is analogous to the gas phase and so the most likely isomer of the product is cyanoethylene oxide.

4.6 Astrophysical Implications

The results presented in this Chapter show that oxygen atoms can readily add to acrylonitrile on interstellar dust grain analogues under UHV conditions. The fluence of oxygen atoms used in this experiment has been previously determined to be equivalent to 10^5–10^6 years of exposure to O atoms in an interstellar cloud.[24] A typical life time of an interstellar cloud is also approximately 10^5–10^6 years. It is therefore possible that this pathway for the destruction of acrylonitrile is active on the surface of dust grains in the ISM. This pathway is not only relevant to dense dark clouds where grain temperatures are 10 K – 20 K, but also to the warm-up phase of these clouds since acrylonitrile can remain on surfaces up to approximately 100 K. The results of this Chapter allow us to hypothesise that during the warm-up phase of a cloud, when dust temperatures approach 140 - 200 K, cyanoethylene oxide and or acetyl cyanide will be observed in the gas-phase. Specifically, it is expected that acetyl cyanide desorption will peak at a temperature of approximately 145 K and cyanoethylene oxide desorption will peak at approximately 180 K. Although these peak desorption temperatures may be altered due to the slow heating rate in the ISM. A confirmed detection would provide further support for the reaction of acrylonitrile and O atoms being an active pathway on interstellar dust grain analogues.

The LH mechanism is of particular relevance to grain chemistry in the ISM, since the ER mechanism is believed to have a low cross section. Our model confirms that the LH mechanism is significantly active under our experimental conditions. The low yields of C_3H_3NO between 15 – 30 K are artificially supressed due to high O_2 surface concentrations. Whilst acrylonitrile is likely to have low surface concentrations on dust grains, the reaction probability for the reaction of acrylonitrile with O atoms is larger than that of the reaction between O atoms and CO. Therefore, it is possible, that even at low ice abundances the reaction of O atoms with acrylonitrile may be efficient enough to take place on the surface of icey mantles in the ISM.

Prior to recent experimental studies on the surface chemistry of oxygen atoms it was assumed that hydrogen surface chemistry was the route to molecular complexity within interstellar ices. The recent experiments from the Price group, the Vidali group and the Dulieu group show that oxygen atoms have a larger desorption energy than had been previously predicted by theory.[14, 22, 23, 27] This large desorption energy allows oxygen atoms to have an appreciable surface coverage up to a surface temperature of 70 K. Therefore, surface chemistry of O atoms can continue on grain surfaces during the first part of the warm up phase of the ISM. At these elevated dust grain temperatures (20 – 70 K) all hydrogen atoms have desorbed from the grains and so O atoms will be the dominant reactive species.[28]

4.7 Summary

The results presented in this Chapter report the first laboratory study of the heterogeneous reactions of acrylonitrile and oxygen atoms at low temperatures relevant to the ISM. The data shows that a single oxygen atom can add to acrylonitrile efficiently on surfaces below 100 K. As the surface temperature decreases the yield of product reaches a maximum at 60 K. The yield then falls to a minimum at 30 K. The minimum at 30 K is a result of the experimental conditions allowing a competitive pathway rather than due to a decrease in reactivity of O atoms with acrylonitrile. At 30 K O_2 has an appreciable residence time on the surface and so ozone is generated *via* O atom reactions with themselves and molecular oxygen. At temperatures of 14 K and 20 K, relevant to the surface chemistry of cold dust grains, there is still an appreciable amount of oxygen atom addition to acrylonitrile. It is proposed that the major isomer of the product observed is cyanoethylene oxide.

4.8 References

1. M. C. L. Gerry, K. Yamada and G. Winnewisser, *Journal of Physical and Chemical Reference Data*, 1979, **8**, 107-123.
2. F. F. Gardner and G. Winnewisser, *Astrophysical Journal*, 1975, **195**, L127-L130.
3. M. C. L. Gerry and Winnewis.G, *J. Mol. Spectrosc.*, 1973, **48**, 1-16.
4. H. E. Matthews and T. J. Sears, *Astrophysical Journal*, 1983, **272**, 149-153.
5. L. E. B. Johansson, C. Andersson, J. Ellder, P. Friberg, A. Hjalmarson, B. Hoglund, W. M. Irvine, H. Olofsson and G. Rydbeck, *Astronomy and Astrophysics*, 1984, **130**, 227-256.
6. A. Toumi, N. Piétri, T. Chiavassa and I. Couturier-Tamburelli, *Icarus*, DOI: http://dx.doi.org/10.1016/j.icarus.2014.10.042.
7. R. L. Hudson and M. H. Moore, *Icarus*, 2004, **172**, 466-478.
8. M. B. Bell, P. A. Feldman, M. J. Travers, M. C. McCarthy, C. A. Gottlieb and P. Thaddeus, *Astrophysical Journal*, 1997, **483**, L61-L64.
9. M. B. Bell, J. K. G. Watson, P. A. Feldman and M. J. Travers, *Astrophysical Journal*, 1998, **508**, 286-290.
10. P. Theule, F. Borget, F. Mispelaer, G. Danger, F. Duvernay, J. C. Guillemin and T. Chiavassa, *Astronomy & Astrophysics*, 2011, **534**.
11. K. Hiraoka, S. Ushiama, T. Enoura, H. Unagiike, N. Mochizuki and A. Wada, *Astrophysical Journal*, 2006, **643**, 917-922.
12. H. P. Upadhyaya, P. D. Naik, U. B. Pavanaja, A. Kumar, R. K. Vatsa, A. V. Sapre and J. P. Mittal, *Chemical Physics Letters*, 1997, **274**, 383-389.
13. J. He and G. Vidali, *Faraday Discuss.*, 2014, **168**, 517-532.
14. J. He, D. Jing and G. Vidali, *Physical Chemistry Chemical Physics*, 2014, **16**, 3493-3500.
15. E. Congiu, M. Minissale, S. Baouche, H. Chaabouni, A. Moudens, S. Cazaux, G. Manico, V. Pirronello and F. Dulieu, *Faraday Discuss.*, 2014, **168**, 151-166.
16. M. Minissale, E. Congiu and F. Dulieu, *J. Chem. Phys.*, 2014, **140**.
17. M. Minissale, E. Congiu, S. Baouche, H. Chaabouni, A. Moudens, F. Dulieu, M. Accolla, S. Cazaux, G. Manico and V. Pirronello, *Physical Review Letters*, 2013, **111**.
18. N. M. S. D. Center and d. S.E. Stein, in *NIST Chemistry WebBook, NIST Standard Reference Database Number 69, Eds. P.J. Linstrom and W.G. Mallard*, National Institute of Standards and Technology, Gaithersburg MD, 20899, http://webbook.nist.gov, (retrieved December 4, 2013). .
19. M. Minissale, E. Congiu, G. Manico, V. Pirronello and F. Dulieu, *Astronomy & Astrophysics*, 2013, **559**.
20. J. A. Noble, E. Congiu, F. Dulieu and H. J. Fraser, *Monthly Notices of the Royal Astronomical Society*, 2012, **421**, 768-779.
21. H. Bergeron, N. Rougeau, V. Sidis, M. Sizun, D. Teillet-Billy and F. Aguillon, *J. Phys. Chem. A*, 2008, **112**, 11921-11930.
22. M. Minissale, E. Congiu and F. Dulieu, *Astronomy & Astrophysics*, 2016, **585**.
23. H. J. Kimber, C. P. Ennis and S. D. Price, *Faraday Discuss.*, 2014, DOI: 10.1039/C3FD00130J.
24. M. D. Ward and S. D. Price, *Astrophysical Journal*, 2011, **741**.
25. A. S. Bolina, A. J. Wolff and W. A. Brown, *Journal of Physical Chemistry B*, 2005, **109**, 16836-16845.
26. *Faraday Discuss.*, 2014, **168**, 571-615.
27. J. He, J. Shi, T. Hopkins, G. Vidali and M. J. Kaufman, *Astrophysical Journal*, 2015, **801**.
28. E. Herbst, *Faraday Discuss.*, 2014, **168**, 617-634.

Chapter 5 – The Desorption of O_2 and CO_2 from Amorphous Porous Carbonaceous Interstellar Dust Grain Analogues

5.1 Introduction

As discussed in Chapter One, dense interstellar clouds are the precursors to stars. As a result young stars are often embedded within the cloud of gas and dust from which they were formed. Molecules in relatively close proximity to a young star absorb the UV radiation emitted by the star and, therefore, become energised.[1] The energy is redistributed amongst the molecules' vibrational and rotational energy levels and so the molecules emit infrared radiation. This infrared radiation, emitted by the molecules, in relatively close proximity to a young star, act as a heat source for the surrounding gas and dust. The efficiency of this heat source is directly related to the timescale over which the star is formed and this timescale is dependent upon the stellar mass. [1] The surrounding gas and dust in close proximity to this heat source is heated more efficiently than gas and dust at a larger distance. There is therefore a radial temperature dependence for the gas and dust surrounding a young star. This radial temperature dependence leads to observed 'snow lines' at specific distances from the newly forming star. Snow lines refer to the radial distance at which molecules present in the ices, on the surface of interstellar dust, sublime from the surface into the gas-phase where they can be observed. However, to make predictions about the stellar mass one must know the temperature of the observed snow lines. Molecules desorb from the surface of the ices when the thermal energy is sufficient to overcome the binding energy of the molecules to the surface. Therefore, if the binding energy of a molecule desorbing from the ices at a particular snow line is known, the temperature of the gas and dust can be estimated. The heating of an interstellar cloud can be simulated in the laboratory by a TPD experiment, albeit on a laboratory time scale. The heating rate in the ISM is typically 1 K century^{-1} whereas heating rates in the laboratory are typically a few K min^{-1}.[2] Nevertheless, TPD experiments, coupled with the Polanyi-Wigner equation, have been used extensively in the laboratory to extract binding energies of many small interstellar molecules. These binding energies can then be used in simulations to estimate the temperature of the snow lines observed in the ISM and, therefore, the stellar mass of the newly forming star.

The most abundant molecular component of interstellar ice is water.[3] The desorption kinetics of water on a graphite surface have been studied by Bolina *et al.*[4] In these experiments water was deposited onto a graphite substrate held at 92 K. RAIRS was then used to observe the water ice *in situ* and then a TPD experiment was performed. The surface was heated at 0.5 Ks^{-1} and the desorbing water was detected using QMS, as described in Chapter Two. When submonolayer coverages of water were deposited onto the substrate, water was observed to desorb between 135 K and 155 K. When multilayer coverages of water were deposited onto the substrate, desorption

peaks were observed at slightly higher temperatures between 140 K and 180 K. Intermolecular bonding of water is clearly a stronger interaction than water binding to the graphite surface, which is unsurprising due to the strong hydrogen bonding between water molecules. The multilayer ice deposited at 92 K is not crystalline.[4] However, multilayer ASW undergoes a phase transition at 135 K, during the TPD, to form cubic crystalline ice.[5] The authors therefore extract a binding energy of 39.9 ± 0.8 kJ mol^{-1} for a crystalline water multilayer ice deposited on a HOPG surface. This binding energy was then used to estimate the temperature of water snow lines in the ISM by simulating a 950 ML thick ice, with a binding energy of 39.9 ± 0.8 kJ mol^{-1}, desorbing from a surface when the heating rate was 1 K $century^{-1}$, a heating rate characteristic of the ISM. The ice was shown to desorb from the surface under interstellar conditions between surface temperatures of 70 K and 90 K.[1] Pure water snow lines in the ISM are therefore expected to be a signature of gas and dust temperatures of 70 K – 90K.

Desorption energies for O_2, CO and CO_2 have also been determined by Noble *et al.*[6] These small molecules were deposited, in separate experiments, onto three different surfaces: non-porous ASW (H_2O(np)), crystalline ice (H_2O(c)) and amorphous silicate (SiO*x*) for a range of coverages between 0.08 ML to 20 ML. The Polyani-Wigner equation was then used to extract multilayer and submonolayer binding energies which can be seen in Table 5.1.1. Noble *et al.* observed that when a 20 ML thick ice of O_2, CO or CO_2, was deposited onto each surface (H_2O(np), H_2O(c) or SiO*x*), within the reported uncertainty the binding energies extracted for these multilayer ices was independent of the substrate onto which the ice was deposited.[6] In a 20 ML thick ice the vast majority of the molecules do not interact with the underlying substrate and so desorb from the surface when the thermal energy is sufficient to overcome the intermolecular forces within the multilayer ice. However, the desorption energies extracted for the submonolayer depositions were dependent upon the three substrates (H_2O(np), H_2O(c) or SiO*x*). In a submonolayer ice the molecules are in direct contact with the surface and so will desorb when the thermal energy is sufficient to overcome the interaction between the molecule and the substrate and so the desorption energy becomes substrate dependent. In addition, the sub monolayer desorption energies extracted for each molecule were also observed to increase as the surface coverage decreased. Unless the surface is perfectly crystalline there will be a distribution of binding energies available to the adsorbates. At low coverages, provided there is enough thermal energy for the molecules to diffuse, the molecules will occupy the highest energy binding sites and desorb at relatively high temperatures. If the deposition surface temperature is too low to facilitate diffusion during dosing, this diffusion to occupy the highest energy binding sites may occur during the TPD. As the dose is increased these high energy binding sites become fully occupied and so the molecules must bind to lower energy adsorption sites. The molecules bound to lower energy adsorption sites will desorb from the surface at lower surface temperatures. The larger binding energies extracted for submonolayer ices indicates that O_2, CO and CO_2, in contrast with water, have stronger interactions with the surfaces than one another. O_2, CO and CO_2 cannot

hydrogen bond and so it is unsurprising that their intermolecular binding is relatively weak. In the same paper the authors use their extracted binding energies at different surface coverages, to simulate desorption of each molecule under astrophysical conditions. They assume 2 ML of each molecule is present on the dust grains and that the heating rate is 1 K century^{-1}.[2] If only multilayer binding energies are used in the model CO completely desorbs from the surface at a surface temperature of 17 K, which corresponds to a heating time of 7×10^3 years. If submonolayer desorption energies are included in the model CO completely desorbs from the surface at a surface temperature of approximately 30 K which corresponds to a heating time of 2×10^4 years. Hence, the desorption time is underestimated by approximately 10^4 years when only multilayer binding energies are considered. Similar desorption characteristics are observed for O_2 and CO_2 under interstellar conditions. This study by Noble *et al.* highlights the need to extract submonolayer desorption energies for use in astrochemical models which predict temperatures of snow lines surrounding newly forming stars.

	Multilayer binding energy /kJ mol^{-1}			One monolayer (1 ML) Binding energy /kJ mol^{-1}			Submonolayer (0.1 ML) Binding energy /kJ mol^{-1}		
	H_2O(np)	H_2O(c)	SiO*x*	H_2O(np)	H_2O(c)	SiO*x*	H_2O(np)	H_2O(c)	SiO*x*
O_2	7.46 ± 0.25	7.78 ± 0.33	7.44 ± 0.30	7.60	8.06	7.73	9.65	9.55	10.4
CO	6.88 ± 0.23	7.06 ± 0.46	6.91 ± 0.33	7.18	8.39	7.21	10.9	11.1	11.8
CO_2	18.8 ± 0.59	19.6 ± 0.69	18.9 ± 0.67	18.6	19.6	18.9	19.5	20.9	25.0

Table 5.1.1: Data taken from reference 6 showing the binding energies of O_2, CO and CO_2 on surfaces of astrochemical interest.

As discussed in Section 1.2, dust grains are thought to be largely amorphous and porous in nature. However, in general, laboratory studies of the surface chemistry relevant to the ISM use ordered substrates as interstellar dust grain analogues. The advantages of using ordered substrates are that data are more easily compared to theory, and reactions between the dust analogue and the adsorbates do not occur. Furthermore, in the case of multilayer experiments, the ice binding energy, and therefore possibly its structure, appears to be independent of the ordered surface onto which the ice is deposited.[6] The ordered substrates are often graphite or silicates, but can be metal surfaces such as gold or aluminium. Often, amorphous water ices are grown on the surface of these substrates to mimic the amorphous nature of the ice that coats interstellar dust grains. However, it is possible that the amorphous and porous structure of dust grains may affect the ice layer that grows on its surface. As discussed in Section 5.1 binding energies extracted from these ordered surfaces are key for determining the desorption characteristics of molecules under

interstellar conditions. The desorption characteristics can be used to estimate the temperature of the gas and dust at snow lines which can then be used to predict the stellar mass of a newly forming star. These desorption characteristics, under interstellar conditions, therefore determine upper temperature limits for each molecules surface reactivity on interstellar dust grains by defining a temperature at which molecule's residence time is too low for reactions to occur. Furthermore, in cases where diffusion coefficients are not available, the thermal diffusion coefficient is often estimated to be 0.7 times the desorption energy.[7] Desorption energies therefore also provide a lower temperature limit for reactivity which relies on molecular or atomic thermal diffusion. Whilst the study by Noble *et al* determined the binding energies of O_2, CO_2 and CO from an amorphous silicate surface,[6] dust grains are likely to also be porous. Furthermore, dust grains are also partially composed of carbonaceous material which is also likely to be amorphous and porous. Given the range of chemical structures carbon can form (diamond, graphite, fullerenes, nanotubes and graphene) and the amorphous porous nature of interstellar dust grains, it is quite possible that molecular desorption from interstellar carbonaceous grains may not be well-represented by desorption characteristics of molecules from a graphite surface. The experiments presented in this Chapter investigate the effect of an amorphous porous fullerene-like surface on the desorption characteristics of O_2 and CO_2 under conditions relevant to the ISM.

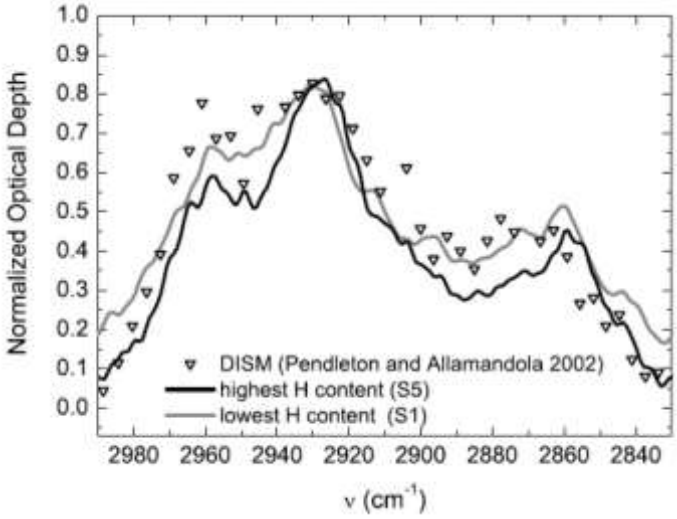

Figure 5.1.1: Comparison of the 3.4 μm profile of carbonaceous grains produced in laser ablation experiments. Taken from reference 8.

It is generally assumed that most of the primary cosmic carbonaceous material is formed *via* gas-phase condensation in envelopes of carbon rich asymptotic giant branch (AGB) stars.[9] The grains are believed to consist of nano and subnanometer-sized particles, but their precise chemical structure is yet to be confirmed. The chemical structure is likely to depend upon the condensation temperature of the grains. However, the exact carbon condensation temperatures in AGB stars is also unclear, since estimations of the temperature are highly dependent upon mass loss rates and gas density outflow velocities. Models have estimated temperatures to be between 2500 K and

4000 K.[10] Jäger *et al.* have used laser pyrolysis and laser ablation in rare gas atmospheres to replicate interstellar dust condensation in the laboratory.[11] Laser pyrolysis of ethene was performed using a laser power of 850 W cm^{-2}. A pyrometer determined the gas temperature to be ~ 1000 K. The material resulting from the pyrolysis of ethene consisted of a complex mixture of PAHs. When laser pyrolysis of ethene and benzene was performed with a higher laser power of 5200 W cm^{-2} (1500 K) the resulting material consisted of graphene-like soot and 33 % PAH's. When the same laser power was applied to a mixture of ethene and acetylene the PAH content of the deposit reduced to 14 %. When an increased laser power of 6400 W cm^{-2} (1700 K) was applied to ethene and benzene the PAH content was 17 %. As the condensation temperature increases the yield of PAHs decreases. This observation is in agreement with predictions that PAHs are most efficiently produced in AGB stars when the effective temperature is between 900 K and 1100 K.[12-14] When higher laser powers of $10^7 – 10^9$ W cm^{-2} (≥3500 K) are applied to ethene, acetylene and benzene, fullerene-like soot and fullerenes are produced. The fullerene-like soot is also produced in laser ablation experiments which evaporate graphite, where laser powers are $10^8 – 10^9$ W cm^{-2} (≥4000 K).[8] The IR spectra of these fullerene-like soot deposits have been shown to match the 3.4 μm band profile and intensity pattern observed in the interstellar medium (Figure 5.1.1). As discussed in Section 1.4, this 3.4 μm band is observed along lines of sight in the diffuse interstellar medium where large quantities of dust grains are expected to be present. This absorption feature is now commonly attributed to the CH stretching of an organic refractory material primarily composed of hydrocarbons, and so these bands are attributed to carbonaceous dust grains.[15-19] However, the weak oscillator strength for the IR absorptions of these fullerene-like grains requires all the carbon present in the ISM to be in this fullerene-like form to account for the intensity of the 3.4 μm band observed in the ISM.[8] It is unlikely that all the carbon in the ISM is in this structural form and so these fullerene-like dust particles are unlikely to be the true form of carbonaceous dust in the ISM. However, the chemical structure of the dust in the ISM is likely to have similar characteristics to this fullerene-like soot produced in the laboratory. The fullerene-like dust deposit also does not exhibit a distinct UV band due to (π-π*) transitions. Carbon (π-π*) transitions are thought to be responsible for the pronounced bump in the extinction curve in the ISM (Figure 1.2.4). Again, since this fullerene-like soot does not seem to exhibit (π-π*) transitions which can account for the bump in the UV extinction curve, it is unlikely that the soot is the true form of carbonaceous dust in the ISM. However, to date this fullerene-like dust is one of the most promising structures, produced in the laboratory, which can reproduce some of the astronomical observations believed to be signatures of carbonaceous interstellar dust. Carbonaceous dust is heavily processed in the interstellar medium and its final chemical structure in interstellar clouds is elusive. However, the near-spherical structure and closed-shell electron configuration of fullerenes results in very high stabilities with respect to dissociation and prolonged exposure to heat.[20] These fullerenes are therefore likely to be more stable under interstellar conditions, when compared to hydrogenated carbonaceous species. Indeed, fullerenes

have been positively identified in many different astrochemical environments in close proximity to stars.[21-24] Recent models predict the carbonaceous grains in dense interstellar clouds to be composed of hydrogen poor, aromatic material, although a specific chemical structure is not described.[25] The temperatures at which this fullerene-like soot is produced in the laboratory, by Jäger *et al.*, are comparable to the predicted carbon condensation temperatures in AGB stars.[11] The fullerene-like soot particles are therefore likely to represent the dust particles formed in very early stages of carbon condensation in the AGB stars.

As with the discovery of graphene, fullerenes were a popular material to study following their identification in 1985,[26] for example it was hoped that they would provide surfaces for gas storage. Schlögl and coworkers dosed O_2 onto a C_{60} surface at 400 K. The surface was then cooled to 300 K and then heated linearly at 1 K s^{-1}. O_2 was observed to readily react with C_{60} to form CO and CO_2. The onset temperature for the reaction was determined to be 370 K.[27] Rao and co-workers also dosed O_2 onto a C_{60} surface.[28] In this work photoelectron spectroscopy showed evidence for a reactive interaction, an O(1s) feature observed at 532.5 eV when the surface was 300 K. The authors comment that this interaction is likely to be due to O_2^- chemisorbed on the surface of the C_{60} deposit. However, this feature was not observed when the surface temperature was below 200 K. It is therefore believed that for O_2 to chemisorb to a C_{60} surface the temperature must be above 200 K.

Several IR active small molecules have also been dosed onto fullerene surfaces. When CO is dosed onto a C_{60} surface, at 77 K, two overlapping bands are observed at 2135 cm^{-1} and 2128 cm^{-1}.[29] The appearance of two bands suggest two sites of adsorption. The strong shift in frequency when compared with the gas-phase (2153 cm^{-1}) suggest there a strong interactions between the CO and C_{60}. The authors also comment that CO does not interact with graphite at a surface temperature of 77 K, which further confirms that CO-C_{60} binding must be a stronger interaction than CO graphite physisorption. CO_2 has also been dosed onto the surface of C_{60} with similar results. Specifically, the gas-phase IR absorption of CO_2, observed at 2349 cm^{-1}, shifts to 2341 cm^{-1} on graphite and 2328 cm^{-1} on C_{60}.[30] This increased shift is indicative of a stronger interaction of CO_2 with fullerenes than graphite.

The structure of fullerenes is closely related to single-walled carbon nanotubes (SWCNT). Both structures consist of sp^2 hybridised carbon sheets with high curvature. Fullerenes are spherical structures in which the carbons are arranged into hexagons and pentagons. SWCNTs are composed of a cylindrical graphene layer and so the carbons are arranged in hexagons. The interaction energies of a range of molecules, such as oxygen, nitrogen, methane, xenon, carbon dioxide, ammonia, methanol, water and ethanol, have also been studied on the surface of SWCNT.[31] Each small molecule was dosed at multilayer and submonolayer coverages, onto graphite. A TPD experiment was then used to observe the desorption characteristics of each molecule. The same molecules were then deposited onto a SWCNT surface at submonolayer

coverages. When the TPD spectra of each molecule on graphite or SWCNT surfaces were compared it was found that all desorption features, with the exception of water, were significantly broadened and shifted to higher temperatures on SWCNTs compared to graphite. The authors also observed additional broadening of the TPD peaks for species which can hydrogen bond, for example methanol and ethanol, but with the exception of water. They attribute this 'delayed' desorption of molecules, when compared to graphite, to the porosity of the surface and stronger binding energies.

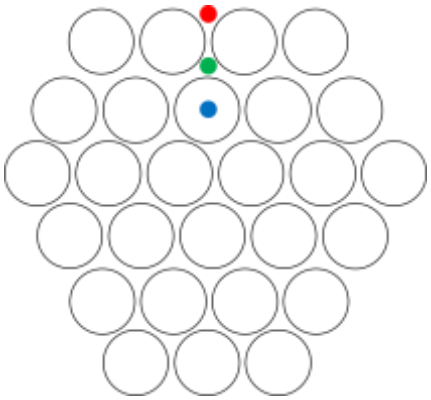

Figure 5.1.2: The binding sites available to O_2 on a bundle of single walled carbon nanotubes (SWCNT). The black hollow circles represent SWCNT end on. The red circle represents a groove site, the green circle presents an interstitial site and the blue circle represents an endohedral site.

An earlier study by the same authors used molecular mechanics calculations to determine if the strong interaction of O_2 and SWCNTs can be attributed to physisorption.[32] It is well known that O_2 physisorbs rather than chemisorbs onto a graphite surface. This physisorption is evident in electron energy loss studies, which reveal that the stretching frequency of adsorbed O_2 is largely unchanged when compared to the gas-phase.[33] Furthermore, *ab initio* studies have shown no evidence for chemisorbed O_2 on a graphite surface.[34] Ulbricht *et al.* used Van der Waals potentials to predict a binding energy of 8.1 kJ mol^{-1} for O_2 physisorption on a graphite surface. This model was then extended to determine the desorption energy of O_2 from the surface of SWCNT. The binding energies are calculated for various orientations and sites for O_2 on a rigid, close-packed (9,9)SWCNT bundle with a fixed lattice constant of 15.6 Å. There are three sites for O_2 adsorption onto the SWCNT bundle: the groove site, the interstitial channel, and the endohedral site (Figure 5.1.2). The groove site is on the outside of the SWCNT bundle, the interstitial site is between three SWCNTs and the endohedral site is inside one of the SWCNT. When O_2 is oriented parallel to the SWCNTs, binding energies of 14.9, 14.3, and 15.4 kJ mol^{-1} are obtained for adsorption in the groove, interstitial channel, and endohedral sites, respectively. A binding energy of 12.9 kJ mol^{-1} is obtained for perpendicular orientation in groove sites. The authors conclude that the O_2 must orient itself parallel to the SWCNT in their experiments at low temperatures and low coverages. Their calculations predict an increase in O_2 binding energy on SWCNTs of 30 – 50 %

when compared to graphite. This calculation is in line with their experimental results where a 55 % increase in binding energy is observed. The interaction between O_2 on the surface of SWCNTs can therefore be explained by strong physisorption sites. Due to the close chemical similarity of SWCNTs and fullerenes it is likely that O_2 will also have strong physisorption sites on the surfaces of fullerenes.

It is clear that the interaction energies of small molecules on different allotropes of carbon can vary significantly. Since the true chemical form of carbonaceous dust grains is unknown, using graphitic interaction energies may be an over-simplification of small molecule desorption from carbonaceous grains in the ISM. This Chapter presents experimental data to determine the desorption characteristics of O_2 and CO_2 from the surface of fullerene-like soot. The soot was produced in laser ablation experiments where condensation temperatures are ≥4000 K. The fullerene-like soot represents a possible structure of the amorphous porous carbonaceous interstellar dust grains produced in AGB stars.

5.2 Experimental

5.2.1 Generation of Amorphous Porous Carbonaceous Dust Grains

The fullerene-like amorphous porous carbonaceous dust grains (APCDG), that were used in the experiments described in this Chapter, were produced at the Friedrich-Schiller-University, Jena as part of a collaboration between UCL and the Max-Plank Institute for Astronomy. The apparatus used to generate the dust grains consists of three differentially pumped stainless steel high vacuum chambers (Figure 5.2.1.1). The base pressure of each chamber is 1×10^{-6} Torr. This base pressure of each chamber is achieved using turbomolecular pumps backed by rotary pumps. The first ablation chamber houses a rotating platform on which the ablation target is placed. For the purpose of producing interstellar dust grains, the target is generally graphite for carbonaceous grains and olivine for producing silicate dust grains. However, in this case, amorphous ^{13}C was used as the ablation target. A ^{13}C target was prepared to allow us to determine if the dust grains were incorporated into surface reaction products at UCL. Whilst the target rotates, the second harmonic of a pulsed Nd:YAG laser is focused onto the surface of the target. The duration of the laser pulses was 10 ns which generates pulse energies of 250 mJ. The incident laser beam vaporises the surface of the ^{13}C target generating a laser-induced plasma with an approximate height of 3 cm. The plasma height can be seen during the experiment as an area that glows red above the surface. Previously a pyrometer has been used to determine the temperature of the plasma to be 4000 K.[11] The laser-induced plasma consists of a high concentration of highly reactive clusters and atoms. Condensation of dust grains occurs just outside the laser induced

plasma, in the quenching gas. In the case of carbonaceous dust grains the composition of the quenching gas determines the degree of hydrogenation of the grains produced. In this case the quenching gas was 10 Torr helium and so the grains contain relatively low quantities of hydrogen. However, one can add hydrogen or water to the quenching gas, to increase the hydrogen content of the grains.[8] In the condensation zone the quenching gas is supersaturated and so dust particles form by surface growth or coagulation. The target is positioned such that a nozzle, with an orifice of 0.8 mm, is adjacent to the laser induced plasma in the condensation zone. Particles formed in the condensation zone are adiabatically extracted through the nozzle into the second 'expansion' chamber. During dust deposition the expansion chamber has a pressure of 10^{-3} Torr. The expansion that occurs during the particles extraction from the first chamber into the second chamber, decreases the number density of the particles and so prevents further growth of the grains. A second extraction is performed through a skimmer into a third 'deposition' chamber with a pressure of 10^{-5} Torr. The beam of particles in the deposition chamber has an approximate diameter of 1 cm and the flux of material can be calibrated by deposition onto a quartz microbalance. The beam of carbon particles was deposited onto a 1 cm x 2 cm graphite surface. Since the diameter of the beam was 1 cm the result is a 1 cm x 2 cm graphite surface with a 1 cm diameter circular deposit of carbon grains in the centre. The quartz microbalance was used to determine that the carbon deposit was 300 nm thick.

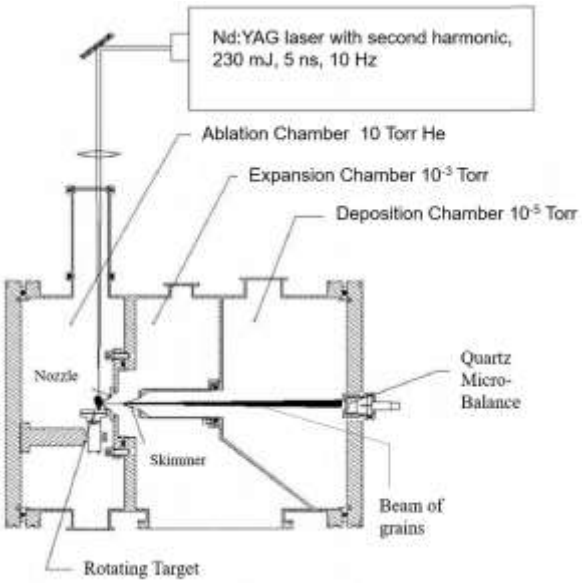

Figure 5.2.1: The laser ablation experimental apparatus. Reproduced from reference 8.

In an identical experiment, the APCDG were deposited onto a KBr substrate to allow IR spectroscopy, Field Emission Scanning Electron Microscopy (FESEM) and High Resolution Transmission Electron Microscopy (HRTEM). The FESEM data is performed using a Zeiss LEO 1530 Gemini microscope. The resolution of the microscope is dependent upon the material, but can be as good as 2 nm. The FESEM data can be obtained without destruction of the film.

Conversely, the HRTEM data requires some of the deposit to be scratched off the film and dispersed in toluene. Infrared spectra of the grains were acquired by placing the dust grains, which were deposited onto the KBr window, into the chamber described in Section 3.2.2. An IR spectra was acquired of the deposit in the high vacuum chamber at room temperature. The deposit was then heated to 475 K for 90 minutes. A second IR spectra was acquired at 475 K. The deposit was then cooled to room temperature where a further IR spectra was acquired.

5.2.2 Desorption of O_2 and CO_2 from Amorphous Porous Carbonaceous Dust Grains

The fullerene-like APCDG deposits on the graphite surface were then transported to UCL and inserted into the UHV chamber described in Chapter Two. Since the grains have been transported outside of a vacuum chamber it is necessary to clean the surface to desorb absorbents and cleave surface oxygen bonds. To this end the grains were heated to 475 K for 90 minutes. At this temperature the surface can be cleaned without annealing the thin film. Typically if one wants to anneal thin films of fullerenes for X-ray diffraction a temperature of 523 K is required for 10 hours.[35]

O_2 or CO_2 were then deposited onto the APCDG at 15 K at several different submonolayer surface coverages. The flux of CO_2 or O_2 can be altered by changing the pressure in the source cell. The pressure in the horizontal source during all these experiments was 0.05 torr which results in a flux to the surface of 4.2×10^{12} molecules cm^{-2} s^{-1}. When this flux is deposited onto a graphite surface the first monolayer is saturated after 238 s. However, since the surface area of the APCDG is much larger than graphite the first monolayer on the APCDG is not saturated after 238 s. After the adsorbate exposure, the surface was then heated at a rate of 10 K min^{-1} to a temperature of 200 K. During the heating phase the QMS monitored the parent ions (CO_2^+ and O_2^+) intensities as a function of surface temperature as described in Section 2.9. Identical experiments where O_2 was deposited on a graphite surface were carried out for comparison and flux calibration. O_2 was also dosed onto the APCDG surface at a temperature of 70 K for eight minutes.

5.3 Results

5.3.1 Dust grains

The electron microscopy is in excellent agreement with previous studies in the Jäger group.[8, 36] The FESEM data provides a better understanding of the morphology of the APCDG surface. The micrograph confirms that the grains are arranged in an amorphous manner with many large pores between them (Figure 5.3.1.1). The HRTEM micrographs show the surface is composed of dense agglomerates of very small carbon particles (Figure 5.3.1.2). The particles are a few nm in size and consist of strongly bent graphite-like layers. The deposit is referred to as fullerene-like since the grains are composed of symmetric, elongated, open and caged fullerenes. The IR spectra in

panel (b) of Figure 5.3.1.3 show that upon heating to 475 K for 90 minutes the absorption at 1725 cm^{-1} reduces in intensity. This absorption is attributed to a small number of C=O bonds which form upon exposure of the carbonaceous film to air.[11] The reduction in intensity demonstrates thatheating the carbonaceous film removes a large proportion of these C=O bonds. Panel (a) of Figure 5.3.1.3 shows several IR bands in the 2600 cm^{-1} – 3000 cm^{-1} range. Upon heating several of these bands diminish in intensity, but some are persistent. These persistent signals are characteristic of aliphatic C-H stretching bands. It has been shown in the Jäger group that these absorptions are in good agreement with the 3.4 μm absorption feature observed in regions of the diffuse interstellar medium where dust grains are believed to be present (Figure 5.1.1).[8, 37]

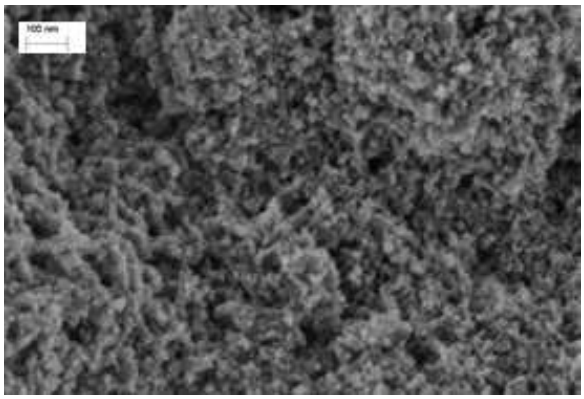

Figure 5.3.1.1: FESEM 13C dust grains

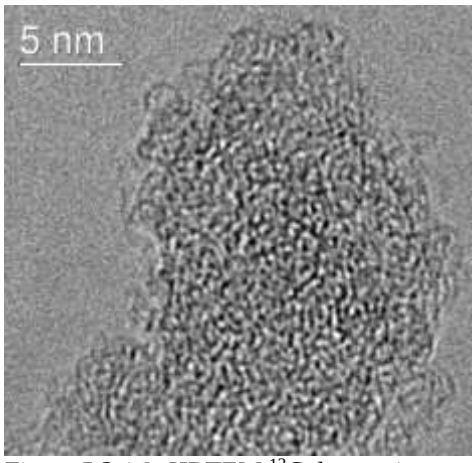

Figure 5.3.1.2: HRTEM ^{13}C dust grains

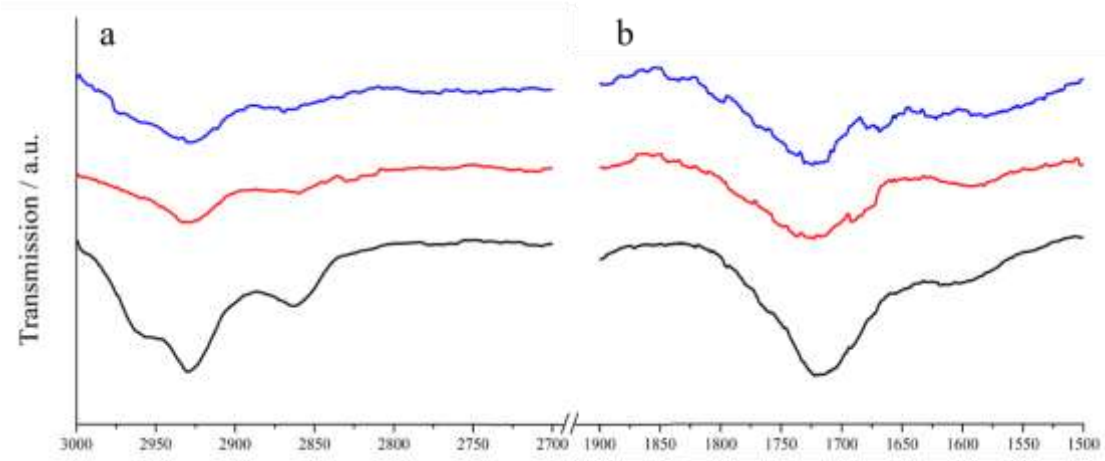

Figure 5.3.1.3: IR spectra ^{13}C dust grains panel a shows between 2700 cm^{-} and 3000 cm^{-1} and panel b shows between 1500 cm^{-1} and 1900 cm^{-1}. The black spectra is taken at room temperature under vacuum. The red spectra is taken at 475 K after the surface has been heated to this temperature for 90 minutes. The blue spectra was taken after the heating to 475 K but after the deposit had cooled to room temperature.

5.3.2 Desorption experiments

Whenever O_2 is dosed onto a graphite surface at 15 K a single peak is observed for the parent ion fragment (O_2^+ 32 AMU) in the TPD-QMS spectra. Depending upon the coverage, O_2 is observed to desorb between 24 K and 38 K. When O_2 is dosed onto the graphite surface at low coverages (< 4 minutes) the TPD peak is symmetrical. As the dose is increased, in this low dosing regime, the leading edge of the TPD shifts to lower surface temperatures. At the lowest doses O_2 occupies the strongly bound sites which desorb at higher temperatures. As the dose increases these strongly bound sites become filled and so O_2 occupies lower energy binding sites which desorb at lower temperatures. The shifting of the leading edge to lower surface temperatures is indicative of first order desorption. For high coverages (>4 minutes) the leading edge remains at the same temperature and the peak shape gains a shoulder on the low temperature side. This shoulder represents zero order desorption and indicates the deposition of a multilayer ice. The flux of O_2 to the graphite surface can be calibrated by determining the dose of O_2 at which the leading edge no longer shifts to lower temperatures.[38] At this dose all the graphite sites are occupied and so the first monolayer is full. From Figure 5.3.2.1 it can be seen that the leading edge no longer shifts to lower temperatures for doses above four minutes. The flux is therefore calculated to be 0.0042 ML s^{-1}. If one assumes 1 ML = $1x10^{15}$ molecules cm^{-2} the flux can be calculated to be 4.2×10^{12} molecules cm^{-2} s^{-1}. The flux to the surface can be controlled by altering the pressure in the source cell, when O_2 or CO_2 was deposited onto the surface of the APCDG grains the pressure in the horizontal source was kept constant and so the fluxes are assumed to be equal. However, since the APCDG surface is amorphous and porous the surface area is much larger than the graphite surface. As a result the four minute dose which saturates the first monolayer on the graphite surface will result in a submonolayer coverage on the APCDG surface and so all coverages on the APCDG surface are assumed to be << 1 ML. Attempts to saturate the first monolayer of the APCDG surface were made. When O_2 is deposited at 35 K no multilayer O_2 ice can form and so once the first monolayer is full, dosing for a longer time should result in the same intensity of the TPD peak. However, even when the dose of O_2 onto the APCDG surface was increased to 2 hours (3×10^{16} molecules cm^{-2}) the intensity of the TPD peak increased monotonically. Since the TPD peak intensity still increased it is clear that the first monolayer was not filled by a dose of 3×10^{16} molecules cm^{-2}. The surface area of the APCDG surface is therefore at least 30 times larger than a graphite surface area.

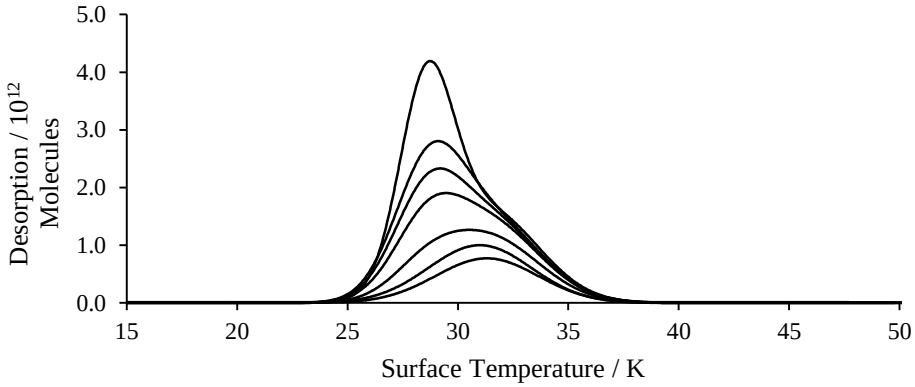

Figure 5.3.2.1: TPD of O_2 deposited onto a graphite surface for 1, 2, 3, 4, 5, 6, 7 minutes in order of intensity.

When O_2 is dosed onto the APCDG surface a more complex TPD spectra for the parent ion fragment (O_2^+ 32 AMU) is observed (Figure 5.3.2.2). Furthermore, O_2 is observed to desorb between 25 K and 90 K, a wider desorption temperature range than when O_2 is dosed onto graphite. Independent of the dose, the TPD spectra consist of a sharp peak between 25 K and 40 K. This first peak is overlapped by a second broad peak between 40 K and 90 K. This second broad peak reaches a maximum at 55 K and has a shoulder on the tailing edge. At doses above four minutes TPD spectra share leading edges which suggests zero order desorption, usually associated with multilayer ices. However, the second broad peak does not seem to share a leading edge, although this is difficult to confirm due to the convolution of the peaks. The TPD spectra for each dosing time can be fitted with a minimum of three Gaussians as in Figure 5.3.2.3. The fits for each dosing time are tabulated in Table 5.3.2.1. The average peak centres for the three Gaussians at each dosing time are 32.6 ± 0.5 K, 55.1 ± 0.5 K and 75.1 ± 0.5 K, the errors represent one standard deviation of the peak centres for each dose. As the dose is increased the peak centres shift to lower surface temperatures however, this shift is no more than 1 K. Each Gaussian's average weighting is 18 ± 1.1 %, 68 ± 0.9 % and 14 ± 0.6 % respectively, again the errors represent one standard deviation of the weighting at each dosing time.

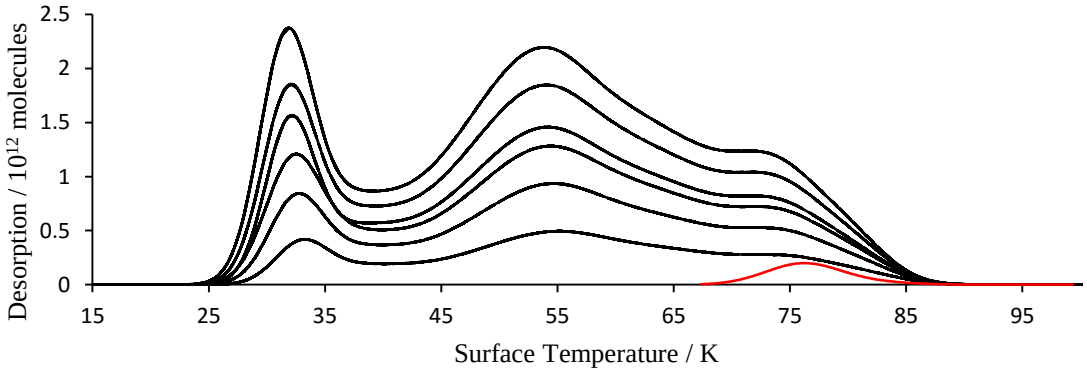

Figure 5.3.2.2 : Black traces TPD of O_2 deposited onto a APCDG at 15 K for 4, 5, 6, 7, 8, 9 minutes in order of intensity. Red traces O_2 desposites APCDG at 70 K for 8 minutes.

Experiment	T_1 / K	T_2 / K	T_3 / K	W_1 / %	W_2 / %	W_3 / %
4 min	33.5	55.8	75.8	16.4	68.9	14.7
5 min	33.0	55.3	75.4	17.9	67.9	14.2
6 min	32.7	55.0	75.0	18.8	66.4	14.8
7 min	32.3	54.9	75.0	18.3	68.4	13.3
8 min	32.2	54.7	74.8	18.7	67.2	14.1
9 min	32.0	54.5	74.6	19.6	67.0	13.5
Average	32.6	55.1	75.1	18.3	67.7	14.1
SD	0.5	0.5	0.4	1.1	0.9	0.6

Table 5.3.2.1: The peak maximum temperatures (T_x) and weights (W_x) of the Gaussians fitted to the TPD spectra when O_2 is dosed onto APCDG

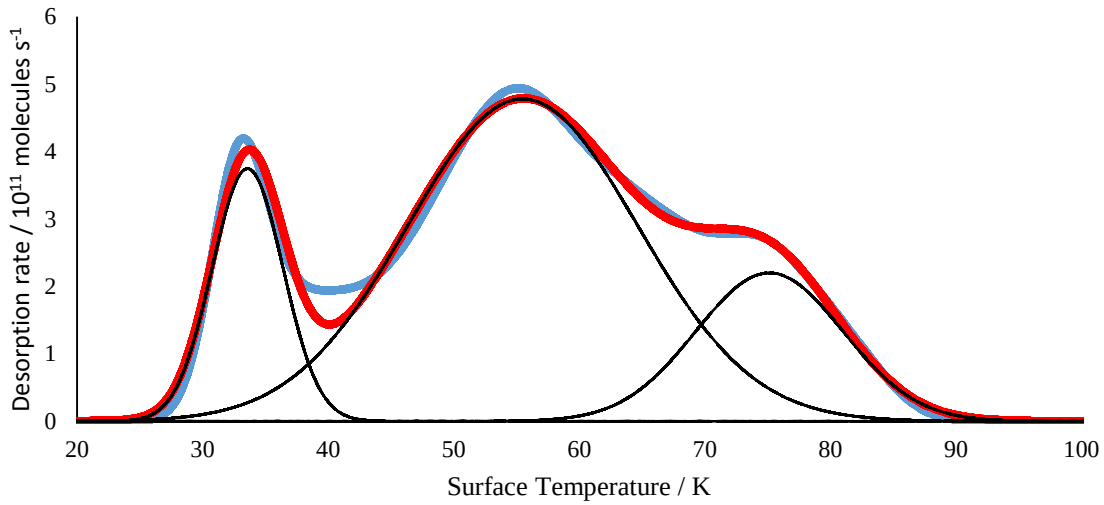

Figure 5.3.2.3: O_2 deposited onto the amorphous porous carbonaceous surface for 4 minutes fitted with three Gaussian functions centred at 33.6 K, 55.5 K and 75.2 K.

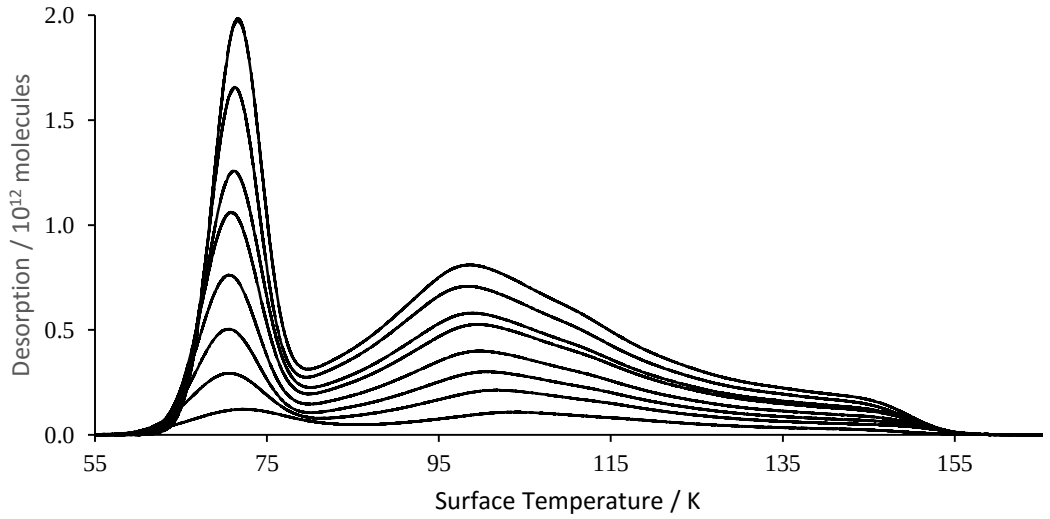

Figure 5.3.2.4 : TPD of CO_2 deposited onto a APCDG for 4, 5, 6, 7, 8, 9, 10, 11 minutes in order of intensity.

Experiment	T_1 / K	T_2 / K	T_3 / K	W_1 / %	W_2 / %	W_3 / %
4 min	72.1	105.1	136.5	28.3	59.9	11.8
5 min	70.5	103.3	137.5	26.2	60.5	13.2
6 min	70.4	102.1	136.3	26.6	60.2	13.2
7 min	70.6	101.3	135.4	27.8	59.1	13.1
8 min	70.8	101.0	135.1	27.9	59.0	13.1
9 min	71.1	100.4	134.4	28.5	58.3	13.2
10 min	71.2	99.8	133.7	28.2	58.3	13.4
11 min	71.6	100.0	133.8	28.7	57.9	13.4
Average	71.1	101.6	135.3	27.8	59.2	13.1
SD	0.6	1.8	1.4	0.9	1.0	0.5

Table 5.3.2.2: The peak maximum temperatures (T_x) and weights (W_x) of the Gaussians fitted to the TPD spectra when CO_2 is dosed onto APCDG

When CO_2 is dosed onto the APCDG surface, similarly, a complex TPD spectra for the parent ion fragment (CO_2^+ 44 AMU) is observed (Figure 5.3.2.4). Typically CO_2 is observed to desorb from a graphite surface between 78 K and 92 K.[39] However, CO_2 is observed to desorb from the APCDG surface between 61 K and 155 K. The TPD spectra at each dosing time again consist of two peaks. The first sharp peak desorbs between 60 K and 80 K. The first peak is overlapped by a second broad peak between 85 K and 160 K. The second broad peak reaches a maximum at 100 K and has a shoulder on the tailing edge. At all doses the TPD spectra share leading edges which suggests zero order desorption usually associated with multilayer ices. However, again the second broad peak does not seem to share a leading edge, although the convolution of the peaks makes this difficult to confirm. The TPD spectra can be fitted with a minimum of three Gaussians, as in Figure 5.3.2.5. The fits for each dosing time are tabulated in Table 5.3.2.2. The average peak centres for the three Gaussians at each dosing time are 71.1 ± 0.6 K, 101.6 ± 1.8 K and 135.3 ± 1.4 K, the errors represent one standard deviation of the peak centres for each dose. Again the peak centres shift to lower surface temperatures as the dose is increased. For the Gaussian centres at 71.1 ± 0.6 K and 135.3 ± 1.4 K this shift is approximately 1 K. However, the shift for the Gaussian at 101.6 ± 1.8 K can be as large as 5 K between the smallest and largest doses. Each Gaussian's average weighting is 28 ± 0.9 %, 59 ± 1.0 % and 13 ± 0.5 % respectively, again the errors represent one standard deviation.

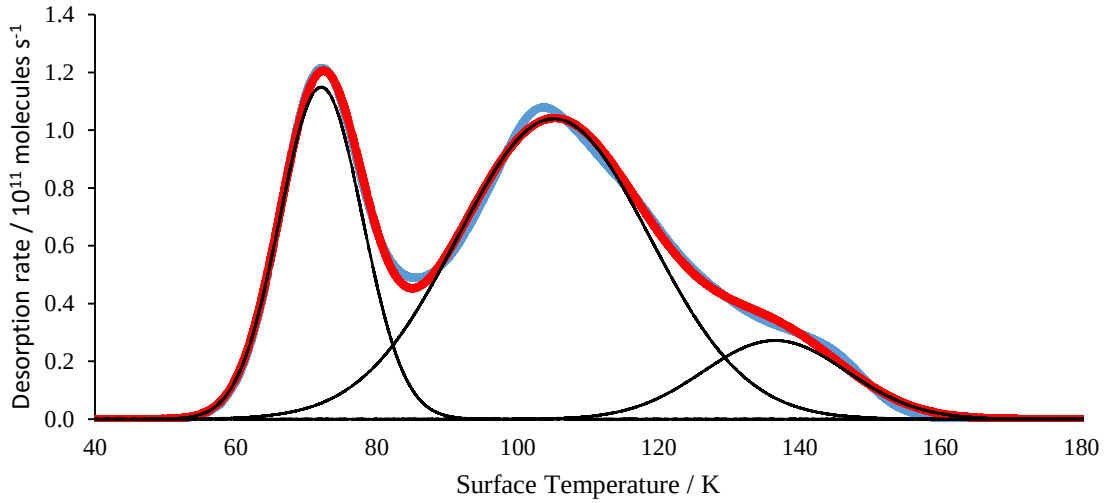

Figure 5.3.2.5: CO_2 deposited onto the amorphous porous carbonaceous surface for 4 minute fitted with three Gaussian functions centred at 72.1 K, 105.1, and 136.5 K.

5.4 Data Analysis

To provide a meaningful interpretation for the different desorption characteristics of O_2 and CO_2 on graphite and the APCDG, it is necessary to extract surface binding energies. The rate of thermal desorption is described by the Polanyi-Wigner equation 5.4.1.

$$d\theta/dt = -\nu\, \theta^{n} \exp(-E_A/kT) \qquad (5.4.1)$$

where θ is the coverage, n is the order of desorption, ν the pre-exponential factor, E_A the activation energy for desorption, k the boltzmann constant and T the surface temperature. In this study the desorption energies have been extracted using Redhead's maximum peak method.[40] This method can be applied to desorption which follows first order kinetics. Setting the first derivative of 5.4.1 to zero gives:

$$E_A/RT_m^2 = (\nu/\beta) \exp(-E_A/RT_m) \qquad (5.4.2)$$

where T_m is the temperature of the peak maximum and β is the heating rate. Plots of E_A against T_m, when (ν/β) is between 10^8 and 10^{13} K^{-1}, are approximatley linear. The linear plot can be fitted using equation 5.4.3.

$$E_A = RT_m[\ln(\nu T_m/\beta) - 3.46] \qquad (5.4.3)$$

One can therefore use the temperature of peak maxima in TPD spectra in equation 5.4.3 to extract binding energies of desorbing molecules. For the Redhead's maximum peak method to be used one must confirm first order desorption kinetics and obtain good estimates of the pre-exponential factors. By rearraging and taking the log of equation 5.4.1:

$$\ln[d\theta/dt] = n \ln[\nu\theta] - [E_A/kT] \qquad (5.4.4)$$

Equation 5.4.4 shows that when $\ln[d\theta/dt]$ is plotted against $\ln[\theta]$ at a fixed desorption temperature the gradient will be equal to the order of desorption. Practically one selects a particular temperature during the TPD, in the case of O_2 on graphite 30 K. The temperature selected is dependent upon the TPD peak one wishes to determine the order of desorption. In the case of O_2 and CO_2 desorption from the APCDG surface the temperatures selected were 55.1 K and 101.6 K respectively. These temperatures represent the average peak temperature for the desorption from the APCDG grains. The low temperature peaks at 32.6 K and 71.1 K are assigned to the desorption of O_2 and CO_2 respectively from the graphite surface which the APCDG is deposited onto. For each initial coverage the intensity of the TPD is recorded ($I(T)$), this is proportional to $[d\theta/dt]$, the relative coverage (θ_{rel}) can then be calculated by summing ($I(T)$) between the temperature of interest and the tailing edge of the TPD. One can then plot $\ln[I(T_x)]$ against $\ln[\theta_{rel}]$ and the gradient will give the order of desorption. In the case of O_2 adsorbed onto a graphite surface the order is 1.05 ± 0.07 as in Figure 5.4.1. The order is slightly higher at 1.1 ± 0.1 for O_2 adsorbed onto an APCDG surface although within the uncertainty still shows first order desorption kinetics (Figure 5.4.2). The order is 1.03 ± 0.09 for CO_2 adsorbed onto the APCDG surface and exhibits first order desorption kinetics (Figure 5.4.3). Since in all three cases (O_2 on graphite, O_2 on APCDG and CO_2 on APCDG) first order desorption kinetics are observed, the use of the Redhead's maximum peak method to extract binding energies is appropriate.

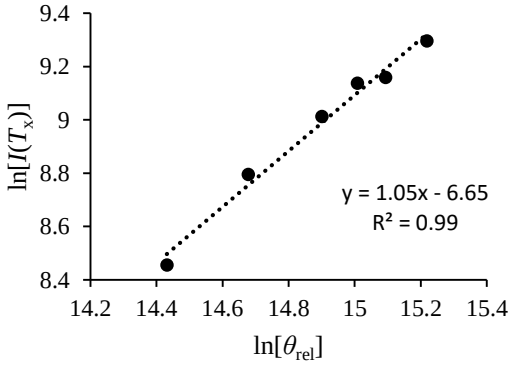

Figure 5.4.1: A plot of $\ln[I(T_x)]$ against $\ln[\theta_{rel}]$ to determine the order of desorption

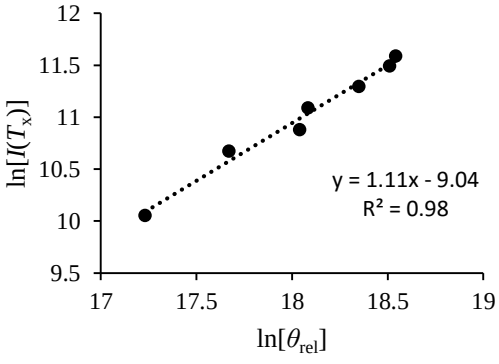

Figure 5.4.2: A plot of $\ln[I(T_x)]$ against $\ln[\theta_{rel}]$ to determine the order of desorption

when O_2 is deposited onto graphite, (T_x = 30 K).

when O_2 is deposited onto APCDG, (T_x = 55.1 K).

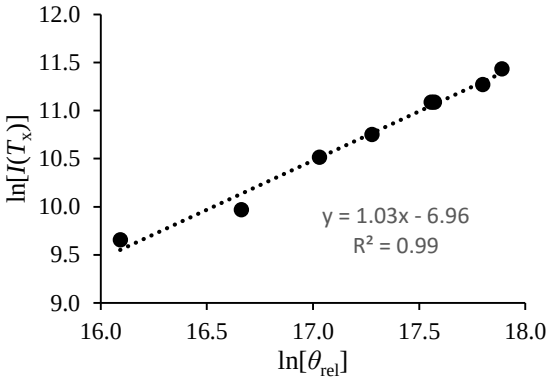

Figure 5.4.3: A plot of ln[I(Tx)] against ln[θrel] to determine the order of desorption when CO_2 is deposited onto APCDG, (T_x = 101.6 K).

A large proportion of the error associated with using the Redhead's maximum peak method to calculate the surface binding energy of adsorbates is associated with inaccurate pre-exponential factors.[31] In the case of first order kinetics the pre-exponential factor can be thought of as the attempt frequency of desorption. The binding energy and the temperature determine the success rate. Desorption of small molecules from surfaces tend to be described by pre exponential factors between 10^{12} s – 10^{15} s. However, the pre-exponential factors must at least be the correct order of magnitude to provide reliable results when using the Redhead's maximum peak method to extract binding energies.[31] Ulbricht *et al*. have previously determined suitable pre-exponential factors for O_2 and CO_2 which were used in the Redhead's maximum peak method.[31, 41] The pre-exponential factor (ν) can be calculated using equation 5.4.6:

$$\nu = s\, p_0 / \sigma \sqrt{(2\pi m k T)} \qquad (5.4.6)$$

where s is the sticking coefficient, σ is the number of adsorbates per unit area, m is the mass of the adsorbate, k is the boltzmann constant, T is the temperature and p_0 is the vapour pressure at $T = \infty$. p_0 can be evaluated by integrating the Clausius-Clapeyron equation from (p_0, T_0) to (p_1,T_1):

$$\ln (p_1/p_0) = \Delta H_{sub}/k\, ((-1/T_1)-(-1/T_0)) \qquad (5.4.7)$$

where ΔH_{sub} is the enthalpy of sublimation. Since $T_0 = \infty$, the equation can be simplified to:

$$p_1 = p_0 \exp(-\Delta H_{sub}/kT_1) \qquad (5.4.8)$$

and so p_0 can be evaluated from a plot of $\ln(p_1)$ *vs* $1/T_1$. However, vapour pressure data in the literature is not available at temperatures in the vicinity of monolayer desorption from surfaces. The literature vapour pressure must therefore be extrapolated using Antoine's expression:

$$p = \exp(A - (B/(T+C)))\text{kPa} \qquad (5.4.9)$$

where *A*, *B*, and *C* are constants. p_0 can then be evaluated from the ordinate intercept of the tangent to the plot of $\ln(p_1)$ *vs* $1/T_1$ when T_1 is the surface temperature at which a single monolayer is observed to desorb from the surface. Using this method the authors calculate pre-exponential factors for O_2 and CO_2 to be 8×10^{13} s^{-1} and 6×10^{14} s^{-1} respectively.[31] The calculated pre-exponential factor for CO_2 on a graphite surface is in good agreement with a previously extracted value of $9.9 \times 10^{14\pm0.9}$ s^{-1}.[39] The pre-exponential factor for O_2 on a graphite surface has been extracted to be 1.1×10^{13} s^{-1} which is in reasonable agreement with the value calculated by Ulbricht.[32]

The desorption energy for O_2 on graphite and the amorphous porous dust grains can be determined using equation 5.4.3. In the case of O_2 on graphite T_m is taken to be 31.3 ± 0.2 K since this is the average peak centre during submonolayer dosing. The resulting desorption energy is 8.8 ± 1.5 kJ mol^{-1}. In the case of O_2 deposited onto APCDG three desorption energies have been extracted for each Gaussian fitted to the TPD spectra. For each desorption energy T_m is taken to be 32.6 ± 0.5 K, 55.1 ± 0.5 K and 75.1 ± 0.5 K, which give desorption energies of 9.2 ± 1 kJ mol^{-1}, 15.7 ± 1 kJ mol^{-1} and 21.6 ± 1 kJ mol^{-1}. In the case of CO_2 deposited onto APCDG the three desorption energies extracted are for each of the Gaussians fitted to the TPD spectra. For each Gaussian T_m is taken to be 71.1 ± 0.6 K, 101.6 ± 1.8 K and 135.3 ± 1.4 K, which give desorption energies of 20.5 ± 1 kJ mol^{-1}, 29.5 ± 1 kJ mol^{-1} and 39.7 ± 2 kJ mol^{-1}.

5.5 Discussion

The desorption energy extracted in this Chapter for O_2 on a graphite surface, 8.8 ± 1.5 kJ mol^{-1}, is in good agreement with literature data. As discussed previously, the desorption energy of O_2 has been studied on other interstellar dust grain analogues. Specifically, O_2 was found to have monolayer binding energies of 914 K (7.6 kJ mol^{-1}), 969 K (8.1 kJ mol^{-1}) and 930 K (7.7 kJ mol^{-1}) on non-porous water, crystalline water and amorphous silicates respectively.[6] In 1987, Bojan *et al.* extracted an O_2 graphite binding energy of 10 kJ mol^{-1}.[42] However, more recently Ulbricht *et al*. have used the same "Redhead's maximum peak" method to extract a value of 12 ± 1 kJ mol^{-1}.[31] Within the uncertainty of our experiment, the binding energy we extract for O_2 on a graphite surface is in agreement with Bojan *et al*. However, our value is smaller than the value extracted

by Ulbricht *et al*. The discrepancy between the value extracted here and the value extracted by Ulbricht *et al*. occurs due to different values of T_m. In our study, a value of 31.3 ± 0.2 K was observed whereas a value of 41 K was observed by Ulbricht *et al.* The desorption energy extracted here more closely resembles desorption energies for multi-layer O_2 ice. However, it is clear from Figure 5.3.2.1 that we do indeed observe the transition from monolayer to multilayer ice. The desorption energy extracted for submonolayer depositions is strongly dependent upon the coverage. Unless the surface is perfectly crystalline the available binding sites will have an energy distribution. At extremely low coverages the molecules will roam the surface during the TPD experiment and become trapped in the deepest potential wells. As a result the molecules will desorb from the surface at higher temperatures. As the dose increases these highest energy binding sites will become fully occupied and so molecules will adsorb in lower energy binding sites. The molecules in lower energy binding sites will desorb at lower temperatures. Furthermore, surface molecular orientation will also affect the binding energy of the adsorbates. In the case of O_2 on a graphite surface, at low coverages O_2 will adsorb with the bonding axis parallel to the surface. [43, 44] As the dose increases the surface can no longer accommodate a higher number of parallel O_2 molecules. The O_2 molecules orient themselves perpendicular to the surface in order for more O_2 to adsorb onto the graphite surface. This perpendicular interaction is weaker than the parallel configuration but stronger than the O_2 intermolecular forces. Different coverages lead to a different proportion of parallel and perpendicular orientations. When a TPD experiment is performed one is observing the average interaction of the O_2 molecules with the surface and so the binding energy extracted is dependent upon the surface coverage. The different energies extracted for different coverages is evident in the work of Noble et al. where O_2 binding energies have a range of 2 kJ mol^{-1} for different surface coverages on a non-porous water surface.[6] Therefore, one must assume that our value represents a high coverage monolayer binding energy and the value extracted by Ulbricht *et al.* represents a low coverage submonolayer binding energy. Indeed, this is the reasoning used by Ulbricht *et al.*to explain their high value compared to Bojan *et al*.[32]

In our study there have been three desorption energies extracted for O_2 on the surface of APCDG: 9.2 ± 1 kJ mol^{-1}, 15.7 ± 1 kJ mol^{-1} and 21.6 ± 1 kJ mol^{-1}. The desorption energy of 9.2 ± 1 kJ mol^{-1} is characteristic of the desorption energy extracted for O_2 on a graphite surface. Since the APCDG surface is 1 cm in diameter and deposited onto a graphite substrate it is very likely that this desorption observed at 9.2 ± 1 kJ mol^{-1} is O_2 desorbing from the graphite surface rather than the APCDG. Furthermore, as stated previously the first peak in the TPD spectra exhibits zero order desorption kinetics and so could even be desorption from an O_2 multilayer ice on the surface of the graphite. However, the desorption energies of 15.7 ± 1 kJ mol^{-1} and 21.6 ± 1 kJ mol^{-1} are not observed for O_2 on a graphite surface. These high energy desorptions clearly indicate that O_2 has a much stronger interaction with our fullerene-like APCDG surface than graphite. As discussed previously, Schlögl and coworkers have observed strong interactions of O_2 on a C_{60}

surface at room temperature.[27] In their 1997 study they observe that O_2 desorbs from a C_{60} surface when the surface temperature is approximately 450 K. The interaction observed in Schlögl's study cannot be the same interaction observed in our study since O_2 is observed to desorb between 50 K and 90 K in our experiments. The interaction observed by Schlögl and coworkers is at a strongly bound chemisorption site, whereas at cryogenic surface temperatures the barrier to chemisorption cannot be overcome and so adsorbates physisorb to the surface. Indeed, Rao *et al.* observed that the 532.5 eV O(1s) feature in their photoelectron spectroscopy experiments, which was assigned to chemisorbed O_2^- on a C_{60} surface, was not present when the surface temperature was 200 K or below.[28] This observation by Rao *et al.* indicates that at a surface temperature below 200 K there is insufficient thermal energy for O_2 to overcome the barrier to chemisorption on a C_{60} surface. We therefore believe that O_2 must physisorb onto our APCDG surface.

Similar physisorption sites have been observed for O_2 on the surface of SWCNT at cryogenic temperatures.[31] O_2 was observed to desorb from the surface of SWCNTs between surface temperatures of 45 K – 80 K, almost coincident with the temperatures observed for O_2 desorption from our APCDG surface. The APCDG deposit used in this study and the SWCNT surface used by Ulbricht *et al.* are not only chemically different to graphite but also have different surface morphologies. Graphite surfaces are relatively ordered and non-porous, whereas the APCDG surface used in this study is undoubtedly amorphous and porous. Ulbricht *et al.* also comment that their SWCNT surface is porous. [31] One might therefore argue that the high temperature desorption of O_2 from our APCDG surface and the SWCNT surface used by Ulbricht *et al.* is due to the porosity of the materials rather than high energy binding sites. When molecules are bound to a non-porous surface, such as graphite, and a TPD experiment is performed, upon the surface temperature reaching the molecule's sublimation temperature the molecules desorb from the surface into the gas-phase where they can be detected. Conversely, when molecules are bound to a porous surface and a TPD experiment is performed, upon the surface temperature reaching the molecule's sublimation temperature the molecules must first diffuse out of the pores of the material before they can be observed in the gas-phase. The molecules diffusing out of the pores may exhibit 'artificially delayed' desorption. It is possible that the molecules observed to desorb at high surface temperatures from our APCDG surface, and the SWCNT surface used by Ulbricht *et al.*, are exhibiting artificially delayed desorption rather than coming from high energy physisorption sites. However, when O_2 was deposited onto our APCDG surface at 70 K for 8 minutes, a clear signal was observed in the TPD spectra (red trace in Figure 5.3.2.2). O_2 must therefore have an appreciable residence time on our APCDG surface at 70 K. If the O_2 observed in the TPD spectra was simply due to artificial delayed desorption, and not high energy binding sites, then O_2 would have a low residence time on the surface at 70 K and so would not be able to get trapped in the pores of the material. Furthermore, it is unlikely that the porosity of our APCDG surface and the SWCNT surface used by Ulbricht *et al.* are comparable, yet the desorption temperatures observed for O_2 on these two surfaces are nearly identical. We therefore conclude

that the porosity of the material is not responsible for the high desorption temperatures observed. As discussed in Section 5.1, Ulbricht *et al.* have successfully modelled the interaction of O_2 and SWCNT bundles.[32] Their molecular mechanics simulations show that Van der Waals forces can account for, and predict, the binding energies observed for O_2 on a SWCNT surface. When O_2 is oriented parallel to the SWCNTs binding energies of 14.9, 14.3, and 15.4 kJ mol^{-1} are obtained for adsorption in the groove, interstitial channel, and endohedral sites, respectively (Figure 5.1.1). A binding energy of 12.9 kJ mol^{-1} is obtained for O_2 in a perpendicular orientation in a groove site. The authors conclude that the O_2 must orient itself parallel to the SWCNT in their experiments at low temperatures and low coverages. Their calculations predict an increase in O_2 binding energy on SWCNTs of 30 – 50 % when compared to graphite. This is in line with their experimental results where a 55 % increase in binding energy is observed. The interaction between O_2 on the surface of SWCNTs can therefore be explained by strong physisorption sites. Due to the close chemical nature of SWCNTs and fullerenes we assign the binding energy of 15.7 ± 1 kJ mol^{-1} for O_2 on our APCDG surface to parallel physisorption of O_2 in groove, interstitial channel or endohedral-like sites. However, we also observe a higher energy binding site of 21.6 ± 1 kJ mol^{-1}. Since our APCDG surface is composed of symmetric, elongated, open and caged fullerenes there is likely to be a larger variation in the binding sites available on our APCDG surface when compared to a SWCNT surface. For example, consider an O_2 molecule physisorbed inside an open fullerene (Figure 5.5.1) this O_2 molecule is likely to have a higher binding energy than an O_2 bound to an endohedral site of a SWCNT since the O_2 molecule in the open fullerene is surrounded by the carbon structure in three dimensions.

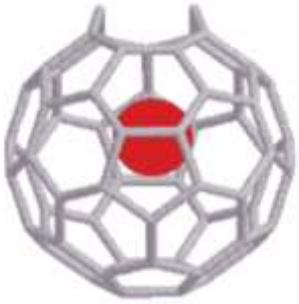

Figure 5.5.1: A molecule contained within an open fullerene structure.

When CO_2 is deposited onto the surface of the APCDGs, at 15 K, the TPD trace can be fitted with three Gaussians (Figure 5.3.2.4). Using Redhead's maximum peak method desorption energies of 20.5 ± 1 kJ mol^{-1}, 29.5 ± 1 kJ mol^{-1} and 39.7 ± 1 kJ mol^{-1} can be extracted. As with the O_2 data it is likely that the first desorption peak is due to CO_2 desorbing from the exposed graphite surface on which the APCDGs are deposited. Previously, the desorption energy of CO_2 on a graphite surface has been extracted to be 20.2 ± 2.3 kJ mol^{-1}.[39] However, high energy binding sites of 29.5 ± 1 kJ mol^{-1} and 39.7 ± 2 kJ mol^{-1} are not observed when CO_2 is deposited onto graphite. As discussed previously, studies have observed that when CO_2 is dosed onto a graphite or C_{60} surface

the IR gas-phase absorption observed at 2349 cm^{-1} is shifted to 2341 cm^{-1} and 2328 cm^{-1} respectively.[30] The larger shift observed when CO_2 is dosed onto the C_{60} surface is characteristic of a stronger binding interaction than that observed for a graphite surface. However, the authors only observed one IR absorption indicating that CO_2 has only one type of binding site available on C_{60}. In the case of our APCDG surface the fullerenes are not a pure film of C_{60} but rather a collection of different sized fullerenes along with open, elongated and caged structures. We therefore propose that the highest energy binding site observed at 39.7 ± 0.4 kJ mol^{-1} could be due to a CO_2 molecule physisorbed inside an open fullerene.

5.6 Astrophysical Implications

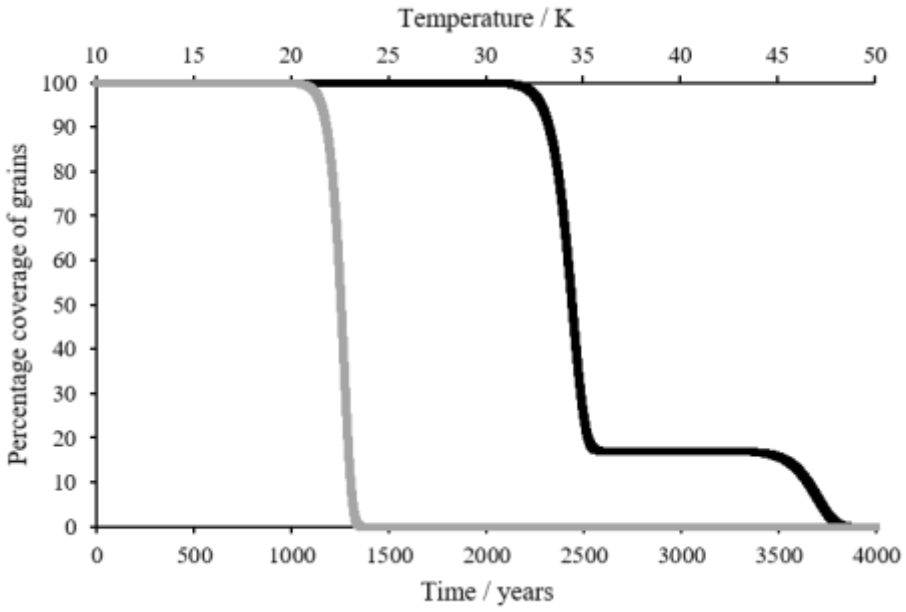

Figure 5.6.1 : The desorption of O_2 from the surface of graphite (grey) and a fullerene-like surface (black) on an astronomical time scale.

The chemical structure of interstellar carbonaceous grains is still unclear. Despite this the most popular carbonaceous dust grain analogue for laboratory studies is still graphite. This Chapter uses fullerene-like grains, condensed at approximately 4000 K, to demonstrate that TPD spectra of small molecules such as O_2 and CO_2 desorption from APCDG can be vastly different to those observed when the same molecules are dosed onto graphite. The TPD data reveals states with binding energies which are in some cases more than double those extracted from the surface of graphite. A simple kinetic model can be used to demonstrate the effect of high energy binding of O_2 to the surface of fullerene type grains, under interstellar conditions. The model numerically integrates equation 5.4.1 over a period of 4000 years. The grain surfaces are initially 10 K and are heated at a rate of 1 K per century.[2] The first model assumes all surface molecules have a graphite binding energy of 10 kJ mol^{-1}, since this value represents the average binding energy of a

monolayer of graphite.[42] In the second model 83 % of the molecules have a binding energy of 15.7 kJ mol^{-1} and 17 % of the molecules have a binding energy of 21.6 kJ mol^{-1}. These percentages are the average weighting of the two Gaussians fitted to the high energy binding sites observed in the TPD spectra recorded in our experiments. It is these two high energy binding sites that are associated with the desorption from the APCDG surface. The Gaussian centred at ~30 K is assigned to O_2 desorption from graphite. The model shows that complete desorption from fullerene type dust grains would take ~3.0×10^3 years longer than from the surface of graphite like dust grains (Figure 5.6.1).

The model can also be applied to CO_2 (Figure 5.6.2). Equation 5.4.1 is integrated over a period of 8 000 years. The grain surfaces are initially 10 K and are heated at a rate of 1 K per century.[2] The first model assumes all surface molecules have a graphite binding energy of 20.2 kJ mol^{-1}. In the second model 82 % of the molecules have a binding energy of 29.5 kJ mol^{-1} and 18 % of the molecules have a binding energy of 39.7 kJ mol^{-1}. Again these percentages are chosen based on the weighting of the Gaussians fitted to the TPD spectra. The Gaussian fitted to the first peak in the TPD spectra is omitted as it is assigned to CO_2 desorption from graphite. The model shows that complete desorption from fullerene type dust grains would take 3.5×10^3 years longer than from the surface of graphite like dust grains, Figure 5.6.2.

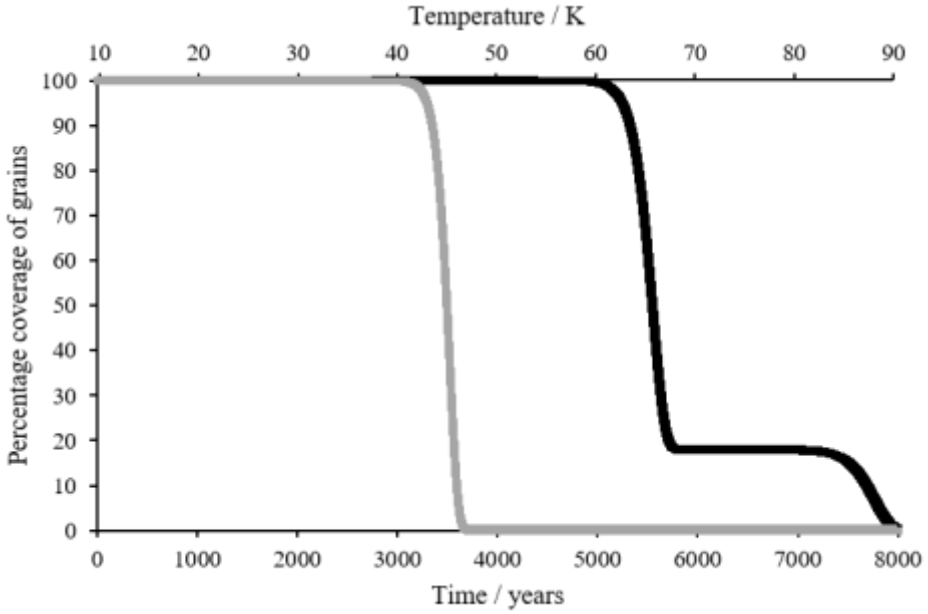

Figure 5.6.2 : The desorption of CO_2 from the surface of graphite (grey) and a fullerene-like surface (black) on an astronomical time scale.

Interstellar clouds have typical lifetimes of $10^5 - 10^6$ years, and so if desorption of small molecules from fullerene-like dust grains takes ~3.5×10^3 years longer than from a graphite surface this time represents between 100th and 1000th of a clouds life time. Therefore, this desorption from

fullerene-like grains will not be insignificant on an astronomical time scale. Furthermore, in our kinetic model (in which the heating rate is 1 K century^{-1}) the temperature at which 50 % and 100 % of the molecules desorb from the surface is increased by 30 % and 50 % respectively when the molecules desorb from an APCDG surface when compared to a graphite surface (Table 5.6.1). If molecules have stronger binding energies to carbonaceous interstellar dust grains, than have been extracted from graphite surfaces, then gas and dust temperatures determined by molecular species present in the gas-phase may not be accurate. Furthermore, the work of Ulbritch *et al.* suggests that the increased binding energy does not affect all molecules in the same way. For example water physisorption seems to be unchanged on SWCNT surfaces when compared to graphite. The result could be that molecules desorb from carbonaceous dust grains in a different order to silicate dust grains. For example, polar molecules such as ammonia, methanol and ethanol are observed to desorb between 160 K and 400 K from a SWCNT surface whereas water desorbs at approximately 150 K. The spatial resolution of ALMA may make it possible to identify regions of interstellar clouds which contain fullerene-like carbonaceous dust grains based on the snow lines observed for water and alcohols.

% coverage	O_2			CO_2		
	Graphite /K	APCDG / K	% increase	Graphite / K	APCDG/ K	% increase
50	22.5	34.4	34.6	45.0	65.6	31.4
100	23.6	48.2	51.0	47.2	90.2	47.7

Table 5.6.1: Data to compare the time taken for 50 % and 100 % the desorption characteristics of O_2 and CO_2 under interstellar conditions when graphite and APCDG binding energies are used in the kinetic model. The table shows the temperature at which 50 % and 100 % of the molecules desorb from the surface and compares the desorption from graphite and APCDG surfaces in the form of a % increase in temperature.

It is not only the desorption characteristics that will be affected by higher energy binding sites. For molecules to diffuse on surfaces they must either thermally hop from site to site or, if light enough, they may tunnel diffusion barriers. Diffusion barriers are directly related to binding energies. For molecules to thermally hop from site to site it is the same attractive forces that must be overcome as when a molecule desorbs from the surface. It is customary in models when diffusion barriers are unknown to define the diffusion barrier as 0.7 times the size of the desorption energy.[7] Higher energy binding on carbonaceous dust grains will alter the temperature at which molecular species are most reactive. Molecules will remain on their surfaces for longer and only diffuse at higher temperatures.

5.7 Summary

The experimental data reported in this Chapter highlights the different desorption characteristics of O_2 and CO_2 from a fullerene-like APCDG surface when compared to a graphite surface. Binding energies for O_2 and CO_2 adsorbed onto the APCDG surface are extracted and in some cases are double the binding energies extracted from a graphite surface. Since the true chemical nature of carbonaceous dust grains is still unknown, the results in this chapter suggest that using graphite binding energies in models may be an oversimplification of the interaction of molecules with carbonaceous dust grains in the ISM.

5.8 References

1. D. A. Williams, W. A. Brown, S. D. Price, J. M. C. Rawlings and S. Viti, *Astronomy & Geophysics*, 2007, **48**, 25-34.
2. S. Viti and D. A. Williams, *Monthly Notices of the Royal Astronomical Society*, 1999, **305**, 755-762.
3. D. C. B. Whittet, *Dust in the Galactic Environment* Insitute of Physics Publications, Bristol, 2003.
4. A. S. Bolina, A. J. Wolff and W. A. Brown, *Journal of Physical Chemistry B*, 2005, **109**, 16836-16845.
5. Y. P. Handa and D. D. Klug, *Journal of Physical Chemistry*, 1988, **92**, 3323-3325.
6. J. A. Noble, E. Congiu, F. Dulieu and H. J. Fraser, *Monthly Notices of the Royal Astronomical Society*, 2012, **421**, 768-779.
7. M. Minissale, E. Congiu and F. Dulieu, *Astronomy & Astrophysics*, 2016, **585**.
8. C. Jager, H. Mutschke, T. Henning and F. Huisken, *Astrophysical Journal*, 2008, **689**, 249-259.
9. T. Henning and F. Salama, *Science*, 1998, **282**, 2204-2210.
10. C. Jager, H. Mutschke, T. Henning and F. Huisken, *Analogs of Cosmic Dust*, 2009.
11. C. Jaeger, F. Huisken, H. Mutschke, I. L. Jansa and T. H. Henning, *Astrophysical Journal*, 2009, **696**, 706-712.
12. T. Allain, E. Sedlmayr and S. Leach, *Astronomy & Astrophysics*, 1997, **323**, 163-176.
13. I. Cherchneff, Y. H. Le Teuff, P. M. Williams and A. Tielens, *Astronomy & Astrophysics*, 2000, **357**, 572-580.
14. M. Frenklach and E. D. Feigelson, *Astrophysical Journal*, 1989, **341**, 372-384.
15. A. J. Adamson, D. C. B. Whittet and W. W. Duley, *Monthly Notices of the Royal Astronomical Society*, 1990, **243**, 400-404.
16. I. Butchart, A. D. McFadzean, D. C. B. Whittet, T. R. Geballe and J. M. Greenberg, *Astronomy & Astrophysics*, 1986, **154**, L5-L7.
17. J. E. Chiar, A. Tielens, D. C. B. Whittet, W. A. Schutte, A. C. A. Boogert, D. Lutz, E. F. van Dishoeck and M. P. Bernstein, *Astrophysical Journal*, 2000, **537**, 749-762.
18. C. Jaeger, S. Krasnokutski, A. Staicu, F. Huisken, H. Mutschke, T. Henning, W. Poppitz and I. Voicu, *Astrophysical Journal Supplement Series*, 2006, **166**, 557-566.
19. M. Schnaiter, T. Henning, H. Mutschke, B. Kohn, M. Ehbrecht and F. Huisken, *Astrophysical Journal*, 1999, **519**, 687-696.
20. E. R. Micelotta, A. P. Jones, J. Cami, E. Peeters, J. Bernard-Salas and G. Fanchini, *Astrophysical Journal*, 2012, **761**.
21. D. A. Garcia-Hernandez, F. Cataldo and A. Manchado, *Monthly Notices of the Royal Astronomical Society*, 2013, **434**, 415-422.
22. M. Otsuka, F. Kemper, J. Cami, E. Peeters and J. Bernard-Salas, *Monthly Notices of the Royal Astronomical Society*, 2014, **437**, 2577-2593.
23. D. A. Garcia-Hernandez and J. J. Diaz-Luis, *Astronomy & Astrophysics*, 2013, **550**.
24. S. Kwok and Y. Zhang, *Astrophysical Journal*, 2013, **771**.
25. A. P. Jones, N. Ysard, M. Koehler, L. Fanciullo, M. Bocchio, E. Micelotta, L. Verstraete and V. Guillet, *Faraday Discuss.*, 2014, **168**, 313-326.
26. H. W. Kroto, J. R. Heath, S. C. Obrien, R. F. Curl and R. E. Smalley, *Nature*, 1985, **318**, 162-163.
27. M. Wohlers, H. Werner, T. Belz, T. Ruhle and R. Schlogl, *Mikrochimica Acta*, 1997, **125**, 401-406.
28. V. Vijayakrishnan, A. K. Santra, T. Pradeep, R. Seshadri, R. Nagarajan and C. N. R. Rao, *Journal of the Chemical Society-Chemical Communications*, 1992, DOI: 10.1039/c39920000198, 198-199.
29. http://voyager.jpl.nasa.gov/, (accessed 20 May, 2015).
30. M. Fastow, Y. Kozirovski and M. Folman, *Journal of Electron Spectroscopy and Related Phenomena*, 1993, **64-5**, 843-848.
31. H. Ulbricht, R. Zacharia, N. Cindir and T. Hertel, *Carbon*, 2006, **44**, 2931-2942.
32. H. Ulbricht, G. Moos and T. Hertel, *Physical Review B*, 2002, **66**.

33. R. E. Palmer, P. J. Rous, J. L. Wilkes and R. F. Willis, *Physical Review Letters*, 1988, **60**, 329-332.
34. D. Lamoen and B. N. J. Persson, *J. Chem. Phys.*, 1998, **108**, 3332-3341.
35. M. M. El-Nahass, H. A. M. Ali, A. S. Gadallah, M. A. Khedr and H. A. Afify, *European Physical Journal D*, 2015, **69**.
36. F. Huisken, C. Jaeger, H. Mutschke and T. Henning, *Diamond and Related Materials*, 2009, **18**, 392-395.
37. Y. J. Pendleton and L. J. Allamandola, *Astrophysical Journal Supplement Series*, 2002, **138**, 75-98.
38. M. Minissale, E. Congiu and F. Dulieu, *J. Chem. Phys.*, 2014, **140**.
39. J. L. Edridge, K. Freimann, D. J. Burke and W. A. Brown, *Philosophical Transactions of the Royal Society a-Mathematical Physical and Engineering Sciences*, 2013, **371**.
40. A. M. Dejong and J. W. Niemantsverdriet, *Surf. Sci.*, 1990, **233**, 355-365.
41. R. Zacharia, H. Ulbricht and T. Hertel, *Physical Review B*, 2004, **69**.
42. M. J. Bojan and W. A. Steele, *Langmuir*, 1987, **3**, 1123-1127.
43. R. D. Etters, R. P. Pan and V. Chandrasekharan, *Physical Review Letters*, 1980, **45**, 645-648.
44. W. A. Steele, *Langmuir*, 1996, **12**, 145-153.

Chapter 6 - Conclusions and Further Work

6.1 Conclusions

6.1.2 Oxygen Atom Surface Reactions

Chapters Three and Four of this thesis present results of laboratory experiments studying the reactions of oxygen atoms with astrophysically relevant molecular ices under interstellar conditions. Specifically, the temperature dependences of the product yields have been recorded and used to derive estimates of the reaction probabilities for these reactions. The key finding of these two Chapters confirms recent laboratory studies which predict that O atoms have a significantly larger binding energy than the 800 K which was previously assumed in astrochemical models.[1-4] The binding energy extracted is 14 ± 0.3 kJ mol^{-1} which results in O atoms having an appreciable residence time on our surfaces up to surface temperatures of approximately 70 K. In contrast it has been previously shown that, under similar experimental conditions, H atoms have a low residence time at surface temperatures above 20 K.[5, 6] It therefore follows that O atom reactivity will continue to occur on the surface of interstellar dust grains during the warm up phase of a cloud, after H atoms have desorbed from their surfaces. Furthermore, the elevated surface temperatures of the dust will increase the thermal energy available to overcome activation energies. It therefore seems likely that the formation of oxygenated species on the surface of dust grains will increase during the early stages of the warm up phase of an interstellar cloud.

In Chapter Three the reaction of propyne and O atoms on a low temperature surface was shown to generate a single addition product, a double addition product and a polymer. The single addition product was identified to be composed of two isomers, methyl ketene and propenal. In the gas-phase the reaction of propyne and O atoms generates propenal and methyl ketene which dissociate into CO and C_2H_4. However, no CO or C_2H_4 was detected in our experimental studies. Detailed computational studies have shown that the activation energies of the reactions which form methyl ketene and propenal in the gas-phase have an approximate height of 10 kJ mol^{-1} whereas the barriers to dissociation have a minimum height of 310 kJ mol^{-1}.[7, 8] A comparison between our results and studies in the gas-phase, without the aid of the detailed computational study, may have presumed that the formation of different products (methyl ketene and propenal in our experiments and CO and C_2H_4 in the gas-phase) was a signature of different reaction pathways. When in fact, it appears that different products are formed since the barriers for methyl ketene and propenal to dissociate are too large to be overcome at low temperatures and so propenal and methyl ketene are stable under our experimental conditions. Indeed, the ER mechanism's reaction probability extracted from our experimental data indicate that the activation energy for a single O atom to

add to propyne is 9.1 ± 0.77 kJ mol^{-1} which is comparable to the maximum activation energy required to produce propenal and methyl ketene in the gas-phase. Our study highlights the errors that can occur by assuming that gas-phase reactions and low temperature surface reactions yield the same products and require the same activation energy to proceed. Clearly, in the gas-phase the rate determining step is the dissociation of propenal and methyl ketene to form CO and C_2H_4. Conversley, at low temperatures, on surfaces, propenal and methyl ketene are stable since this barrier to dissociation is far too large to be overcome. The rate determining step for the surface reaction is likely to be the isomerisation of methyl ketocarbene to form methyl ketene or propenal. Furthermore, since on the surface propenal and methyl ketene are stable a second oxygen atom addition can occur. The addition of a second O atom to propenal is likely to result in glycidaldehyde and a polymeric species which is likely to be poly(β-propiolactone). Again, gas-phase studies of the O atom addition to propyne would not predict these products.

In Chapter Four a single oxygen atom was shown to add to an acrylonitrile molecular ice at low temperatures. The reaction of acrylonitrile and O atoms provides a direct comparison between the reactivity of C=C and C≡N bonds under interstellar conditions. The O atom addition to acrylonitrile is believed to occur at the C=C bond rather than the C≡N bond. In separate experiments O atoms were co-dosed with HCN or methyl cyanide and no products were observed within the detection efficiency of our apparatus. Since no reaction between O atoms and HCN or methyl cyanide was observed it seems that the C≡N is stable with respect to O atom addition under interstellar conditions. Previous studies in the Price group have shown that an O atom addition to a double bond results in an epoxide,[9] and so the product of the reaction between acrylonitrile and O atoms is believed to be cyanoethylene oxide. There is more agreement between the surface reaction of acrylonitrile and O atoms in this study and previous gas-phase studies. The gas-phase reaction is believed to proceed *via* the formation of a biradical species which subsequently undergoes stabilisation to an epoxide ring.[10] The activation energy extracted in this gas-phase study is 7.1 kJ mol^{-1} which is comparable to the barrier extracted using the reaction probability of the ER mechanism in our study of 6.7 ± 0.41 kJ mol^{-1}.

More generally both the reactions studied in Chapters Three and Four indicate that O atoms readily add to C=C and C≡C but not C≡N bonds on surfaces under interstellar conditions. The formation of products suggests that thermal reactions on interstellar dust grain surfaces may play a significant role in the formation of complex organic molecules. As discussed in Section 1.9, previously, the rate coefficient for the surface reaction of ethene and O atoms to form ethylene oxide has been incorporated into the rate equation astrochemical model UCL_CHEM.[11, 12] These studies were able to confirm that O atoms can add to ethene under interstellar conditions. In a similar way the rate coefficients for the reaction of O atoms with propyne and acrylonitrile could also be included in such models. In the case of the reaction of propyne and O atoms it would be interesting to determine whether the dominant formation pathway of propenal is the addition of

H atoms to propynal or the addition of propyne to O atoms. One could also determine whether either or both pathways can account for the observed abundances of propenal. More generally it would be interesting to determine if under interstellar conditions a significant degree of oxidation can occur during the warm up phase of an interstellar cloud. As discussed previously H atoms will have a low residence time above 20 K in the ISM and so will desorb from the surface of interstellar dust grains almost immediately during the warm up phase of an interstellar cloud. Conversely, the large binding energy of O atoms under interstellar conditions will result in an appreciable O atom surface abundance above 20 K. Furthermore, the elevated surface temperatures will result in larger diffusion and reaction coefficients. It therefore seems likely that there may be a period of time in the warm up phase of an interstellar cloud where a significant degree of oxidation can occur. Further astrochemical modelling will be able to determine the feasibility of these pathways under interstellar conditions.

6.1.2 Small Molecule Desorption of Amorphous Porous Carbonaceous Dust Grains

In Chapter Five the desorption characteristics of O_2 and CO_2 from a surface of a fullerene-like amorphous porous carbonaceous dust grain were presented. Both molecules were found to have binding energies which were up to twice as large as their binding energies to a graphite surface. These higher energy binding sites were shown to increase the time taken for a monolayer of O_2 and CO_2 to desorb from the surface of interstellar grains by 3.0×10^3 years 3.5×10^3 years respectively when compared to binding energies extracted from a graphite surface. The results highlight the need for the desorption characteristics of small molecules to be studied on the surfaces of other prototypical carbonaceous dust grains. Carbonaceous dust grains clearly evolve in the ISM and so desorption characteristics of small molecules in different regions of the ISM may provide an indication of the chemical structure of grains in each region.

6.2 Further Work

6.2.1 Further Studies of the Reactions of Atoms on Surfaces

The installation of the QMS into the experimental chamber at UCL has dramatically increased the sensitivity of the apparatus. As discussed in Section 2.9 the TOFMS typically collected ~250 counts per monolayer whereas the QMS collects ~ 340000 per monolayer. The increased sensitivity will enable a submonolayer coverage of reactants, such as propyne or acrylonitrile, to be deposited onto the surface which can then be irradiated with atomic species, rather than having to co-deposit the reactants with the atomic species as in the experiments described in Chapters Three and Four. This dosing regime has several advantages. Firstly it will enable the ER and LH

mechanisms to be observed in separate experiments. In the experiments described in this thesis the LH and ER mechanisms contributions to the overall reaction can only be determined by modelling. If the atomic species is highly mobile such as in the case of the O atom, the LH mechanism is largely dependent upon the surface temperature. Conversely, the ER mechanism is largely dependent upon the surface coverage. By performing experiments at a fixed surface temperature and varying the surface coverage one can more precisely quantify the contribution of the ER mechanism to the overall reaction. Secondly, depositing the propyne or acrylonitrile onto the surface prior to irradiating the molecules with the atomic species means that only one ER mechanism must be modelled since only the atomic species can be the gas-phase reactant. Thirdly the dose of the atomic species which fully oxygenates the submonolayer coverage of propyne or acrylonitrile can be determined. The dose of the atomic species needed to fully oxygenate a submonolayer coverage of propyne or acrylonitrile would provide a more precise measurement of the reaction probability. Fourthly, several reactions have been studied at UCL for which no products were observed within the detection efficiency of the TOFMS. For example CO + O, however this reaction was observed to proceed in other research groups and so revisiting reactions with the new increased sensitivity of the apparatus may reveal new reaction pathways on interstellar dust grains. Lastly, there are two delivery lines installed into the chamber at UCL. In the experiments described in Chapters Three and Four, one delivery line was used to generate the O atoms *via* a microwave discharge in O_2 and one was used to co-deposit the propyne or acrylonitrile. However, if the propyne or acrylonitrile is pre-deposited onto the surface, it will be possible to use the second dosing line to introduce another atomic species, for example H atoms *via* a microwave discharge in H_2, and so O atoms and H atoms can be co-deposited onto the pre-deposited propyne or acrylonitrile ice. Preliminary experiments at UCL have shown that propyne and acrylonitrile also react with H atoms on surfaces, under astrophysical conditions. Co-depositing O and H atoms onto pre-deposited acrylonitrile or propyne would provide a direct comparison between these two atomic species. One would also be able to observe the reaction of propyne or acrylonitrile with reactive species formed when H and O atoms are co-deposited onto surfaces at low temperature, such as OH, HO_2 and H_2O_2.

Whilst O atoms are the third most abundant species in the ISM, N atoms have an abundance approximately 10 times smaller than O atoms in the ISM. It would therefore be a logical step forward to generate N atoms in a microwave discharge in N_2. Efforts have already been made to produce N atoms. However, the N≡N bond is an extremely strong bond and so the dissociation efficiency was found to only be a few percent. McCullough *et al.* show that an enhanced dissociation efficiency can be obtained by applying an axial magnetic field to the discharge cell.[13] Therefore, in order to obtain the maximum possible flux of N atoms, a current could be passed through a coil of wire which was wrapped around the discharge cell to produce an axial magnetic field.

The QMS has not only increased the sensitivity of the apparatus but also the mass range of products that can be observed. Previously, the TOFMS had a mass range of 0 – 120 AMU, whereas the QMS has a mass range of 1-300 AMU. In preliminary studies, a single oxygen atom addition has been observed to toluene. However, due to the large mass of toluene, potential double addition and triple addition products were unable to be observed. The addition of the Eurotherm controller into the experimental apparatus has enabled linear heating during the TPD experiment. One can therefore perform several TPD experiments and use the Polyani-Wigner equations to determine the desorption energy of each reactant from the surface. Determining the desorption energy of each reactant would reduce the number of free parameters in our kinetic model. A final development of the studies presented in Chapters Three and Four would be to develop a Monte Carlo model to describe the experimental results. Monte Carlo simulations take account of the structure of the ice and include statistical fluctuations. Indeed, it has been shown that Monte Carlo models can provide a more accurate extrapolation of reactions observed in the laboratory into reactions occurring in the interstellar medium.[14]

6.2.2 Further Studies of the Reactions of Atoms on Surfaces using Scanning Tunnelling microscopy.

As discussed throughout this thesis the high diffusion coefficient of oxygen atoms on the surface of interstellar dust grain analogues is observed indirectly *via* the production of high yields of O_3. However, to confirm this high diffusion coefficient, direct observation of O atom diffusion is required. Such experiments could be performed *via* scanning tunnelling microscopy (STM).[15-18] Previously, the diffusion of O atoms has been studied on a Ni(100) surface.[19] In this case O_2 was deposited onto a clean Ni(100) surface and annealed to 330 °C. The O_2 underwent dissociative adsorption onto the Ni(110) surface resulting in O atoms bound to the nickel surface. Upon inspection of the surface, the authors observed spikes in the STM traces caused by transient O atoms in the tunnelling region of the STM. The authors determined a jump frequency of 2×10^4 s^{-1} and a diffusion coefficient of 6×10^{12} $cm^2\,s^{-1}$ at a surface temperature of 353 K. However, the O atoms bound to the Ni(100) surface represent chemisorption sites on a metal surface and so are not astrophysically relevant. To determine the O atom diffusion coefficient relevant to astrochemistry one would need to observe the hopping rate of O atoms on an interstellar dust grain analogue at cryogenic temperatures, where the O atoms reside in physisorption sites. In these experiments O atoms would be dosed onto the surface of an interstellar dust grain analogue at a surface temperature at which the O atom diffusion is effectively negligible and so the O atoms would be immobile. Indirect observations of the O atom diffusion coefficient on a silicate surface indicates this surface temperature, at which O atoms would be immobile, is close to 5 K (Figure 6.2.2.1).[20] One would then raise the surface temperature and determine the change in O atom hopping rate and diffusion constant at a series of fixed surface temperatures. To maintain surface

temperatures between 5 K (the temperature at which O atoms are immobile) and 70 K (the approximate temperature at which O atoms desorb from the surface) the interstellar dust grain analogue would need to be mounted onto a helium cryostat coupled with a heater. Since O atoms have been shown to have similar diffusion coefficients on several different interstellar dust grain analogues,[20] it may be favourable to first observe O atom diffusion from physisorption sites on a metal surface. Whilst a metal surface is not representative of interstellar dust grains electron microscopy on metal surfaces is experimentally more feasible on atomically flat conducting materials.

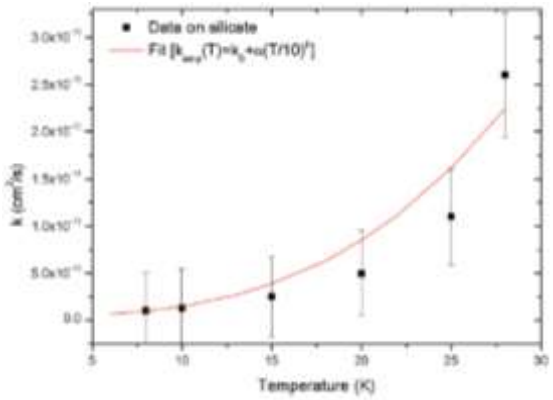

Figure 6.2.2.1: Black squares represent diffusion constants of O atoms on amorphous silicate as a function of temperature. The red solid line is a best fit of diffusion constant vs. temperature. Taken from reference 20.

6.2.2 Further Studies of Thermal Desorption from Amorphous Porous Interstellar Dust Grains

The experiments presented in Chapter Five clearly demonstrate that the desorption of small molecules from the surface of graphite may not be representative of the desorption of small molecules from carbonaceous interstellar dust grains. During the experiments, discussed in Chapter Five, there were clear signs in the TPD data that O_2 and CO_2 were desorbing from the graphite surface onto which the APCDGs were deposited. Hence, the experiments would be improved by depositing the APCDG across the entire graphite surface to determine if there are 'graphitic like' absorption sites for these molecules on the surface or if indeed as we expect, we are seeing adsorption sites on the uncovered graphite surface. Since these surfaces are fullerene-like and not a pure deposit of fullerenes, it would be interesting to note the difference in desorption behaviour from our surfaces and a pure C_{60} deposit. This experiment would determine if it is indeed the chemical nature of fullerenes that enables these high energy binding sites to exist or whether it is the 'broken' structure of the amorphous fullerenes in our deposit. It would also be

advantageous to perform Van der Waals calculations, similar to those performed by Ulbritch *et al.* to investigate the binding energy sites available on a fullerene surface.[21]

Preliminary experiments on the surface of the APCDG also show that N_2, O_3, and CO also find high energy binding sites on the APCDG surface. However, H_2O was not observed to exhibit higher energy binding sites. This is in line with the observations by Ulbritch *et al.* where water was not observed to have high energy binding sites on the surface of SWCNTs. Preliminary experiments also suggest that O_2 may react with the surface to form CO and CO_2, although further experiments are needed to confirm this. Preliminary experiments were also performed in which O atoms and O_2 were deposited onto the APCDG, we observed that the yields of O_3 were significantly smaller than on a graphite surface which possibly implies that the O atoms are consumed by the surface. However, since the surface area of the APCDG surface is unknown this low yield may also be due to extremely low surface coverages. Finally, preliminary experiments also show that when propene (C_3H_6) and O atoms are dosed onto the APCDG a product is observed with the empirical formula (C_4H_6O) indicating that CO formed on the surface can add to C=C bonds.

6.3 Summary

This chapter has provided an overview of some of the potential future directions for the work presented in this thesis. Some of this work would continue to identify O atom addition reactions occurring on molecular ices and then extend this to include the co-deposition of H and O atoms. The increased sensitivity and mass range of the mass spectrometer will also enable a wider range of reactions to be studied. However, the reactivity and desorption kinetics from the surface of different APCDG surfaces would provide a unique future direction for this project. Whatever the future direction of this project the unprecedented spatial resolution of the new telescopes the Atacama Large Millimetre Array (ALMA) and the James Webb Space Telescope (JWST), will undoubtedly provide an unpresidented number of new queries to be addressed by laboratory astrochemists.

6.4 References

1. R. T. Garrod, S. L. W. Weaver and E. Herbst, *Astrophysical Journal*, 2008, **682**, 283-302.
2. T. Stantcheva, V. I. Shematovich and E. Herbst, *Astronomy & Astrophysics*, 2002, **391**, 1069-1080.
3. J. He, J. Shi, T. Hopkins, G. Vidali and M. J. Kaufman, *Astrophysical Journal*, 2015, **801**.
4. M. Minissale, E. Congiu and F. Dulieu, *Astronomy & Astrophysics*, 2016, **585**.
5. R. J. Gould and E. E. Salpeter, *Astrophysical Journal*, 1963, **138**, 393-&.
6. R. J. Gould, E. E. Salpeter and T. Gold, *Astrophysical Journal*, 1963, **138**, 408-&.
7. G. Vanuzzo, N. Balucani, F. Leonori, D. Stranges, V. Nevrly, S. Falcinelli, A. Bergeat, P. Casavecchia and C. Cavallotti, *The Journal of Physical Chemistry A*, 2016, DOI: 10.1021/acs.jpca.6b01563.
8. I. Gimondi, C. Cavallotti, G. Vanuzzo, N. Balucani and P. Casavecchia, *The Journal of Physical Chemistry A*, 2016, DOI: 10.1021/acs.jpca.6b01564.
9. M. D. Ward and S. D. Price, *Astrophysical Journal*, 2011, **741**.
10. H. P. Upadhyaya, P. D. Naik, U. B. Pavanaja, A. Kumar, R. K. Vatsa, A. V. Sapre and J. P. Mittal, *Chemical Physics Letters*, 1997, **274**, 383-389.
11. A. Occhiogrosso, A. Vasyunin, E. Herbst, S. Viti, M. D. Ward, S. D. Price and W. A. Brown, *Astronomy & Astrophysics*, 2014, **564**.
12. A. Occhiogrosso, S. Viti, M. D. Ward and S. D. Price, *Monthly Notices of the Royal Astronomical Society*, 2012, **427**, 2450-2456.
13. D. P. Higgins, R. W. McCullough, J. Geddes, J. M. Woolsey, M. Schlapp and H. B. Gilbody, in *Advances in Engineering Materials*, eds. S. Hampshire, M. Buggy, B. Meenan and N. Brown, 1995, vol. 99-1, pp. 177-183.
14. G. W. Fuchs, H. M. Cuppen, S. Ioppolo, C. Romanzin, S. E. Bisschop, S. Andersson, E. F. van Dishoeck and H. Linnartz, *Astronomy & Astrophysics*, 2009, **505**, 629-639.
15. B. S. Swartzentruber, *Physical Review Letters*, 1996, **76**, 459-462.
16. L. J. Lauhon and W. Ho, *Physical Review Letters*, 2000, **85**, 4566-4569.
17. L. J. Lauhon and W. Ho, *Physical Review Letters*, 2002, **89**.
18. T. Mitsui, M. K. Rose, E. Fomin, D. F. Ogletree and M. Salmeron, *Surf. Sci.*, 2003, **540**, 5-11.
19. G. Binnig, H. Fuchs and E. Stoll, *Surf. Sci.*, 1986, **169**, L295-L300.
20. E. Congiu, M. Minissale, S. Baouche, H. Chaabouni, A. Moudens, S. Cazaux, G. Manico, V. Pirronello and F. Dulieu, *Faraday Discuss.*, 2014, **168**, 151-166.
21. H. Ulbricht, G. Moos and T. Hertel, *Physical Review B*, 2002, **66**.